# CRRES ONR-307 Experiment Data Analysis

W. L. Imhof
H. L. Collin
J. Mobilia
J. B. Cladis
M. Walt
R. W. Nightingale
H. D. Voss
R. M. Robinson
J. M. Quinn
R. R. Vondrak

Space Sciences Laboratory, Dept. H1-11, Bldg. 252
Lockheed Martin Advanced Technology Center
3251 Hanover Street
Palo Alto, CA 94304

April 29, 1997

**Final Report**

**Period Covered: May 4, 1994 - February 28, 1997**

**Approved for public release, distribution unlimited**

**Prepared for :**

The Office of Naval Research
800 North Quincy Street
Arlington, Virginia 22217

**Under Contract No. N00014-94-C-0042**

19970509 052

DTIC QUALITY INSPECTED 1

# REPORT DOCUMENTATION PAGE

*Form Approved*
*OMB No. 0704-0188*

Public reporting burden for this collection of information is estimated to average 1 hour per response, including the time for reviewing instructions, searching existing data sources, gathering and maintaining the data needed, and completing and reviewing the collection of information. Send comments regarding this burden estimate or any other aspect of this collection of information, including suggestions for reducing this burden, to Washington Headquarters Services, Directorate for Information Operations and Reports, 1215 Jefferson Davis Highway, Suite 1204, Arlington, VA 22202-4302, and to the Office of Management and Budget, Paperwork Reduction Project (0704-0188), Washington, DC 20503.

**1. AGENCY USE ONLY** *(Leave blank)*

**2. REPORT DATE**
April 29, 1997

**3. REPORT TYPE AND DATES COVERED**
Final Report May 4, 1994-February 28, 1997

**4. TITLE AND SUBTITLE**
CRRES ONR-307 Experiment Data Analysis

**5. FUNDING NUMBERS**
Contract
N00014-94-C-0042

**6. AUTHOR(S)**

W.L. Imhof J.B. Cladis H.D. Voss* R.R. Vondrak†
H.L. Collin M. Walt R.M. Robinson**
J. Mobilia R.W. Nightingale J.M. Quinn***

**7. PERFORMING ORGANIZATION NAME(S) AND ADDRESS(ES)**

Lockheed Martin Advanced Technology Center
Space Sciences Laboratory (Dept. H1-11, Bldg. 252)
3251 Hanover Street
Palo Alto, CA 94304-1191

**8. PERFORMING ORGANIZATION REPORT NUMBER**

**9. SPONSORING/MONITORING AGENCY NAME(S) AND ADDRESS(ES)**

Office of Naval Research
Dept. of the Navy
800 North Quincy Street
Arlington, Virginia 22217-5000

Contract Manager
Dr. R. McCoy

**10. SPONSORING/MONITORING AGENCY REPORT NUMBER**

**11. SUPPLEMENTARY NOTES**

†NASA GSFC, Code 690, Greenbelt MD 29771
*Taylor University, Physics Dept., 500 W. Reade Ave., Upland, IN 46989-1001
**National Science Foundation, 4201 Wilson Blvd., Rm., 775, Arlington VA 22230
***Univ. of New Hampshire, Space Science Center, Morse Hall, Durham, NH 03824

**12a. DISTRIBUTION / AVAILABILITY STATEMENT**

Approved for public release; distribution unlimited

**12b. DISTRIBUTION CODE**

**13. ABSTRACT** *(Maximum 200 words)*

A number of scientific results have been obtained from analysis of the CRRES ONR-307 energetic particle and ion data, concentrating on three key areas of investigation: particle precipitation and wave-particle interactions, radiation belt and ring current modeling, and dynamic event studies. Utilizing the ONR-307 particle data together with plasma wave data from other instrumentation on CRRES, we have studied, for the first time from the same spacecraft in the outer belt region, the simultaneous nature of waves and precipitating electrons near the equator, both for trapped particles and narrow particle dropouts. These studies showed that there is a general correlation between wave intensities and electron fluxes. Investigation of the ion composition data during the large magnetic storm of March 1991 revealed detailed structure of the ring current, allowed mapping of the structure for the first time, and showed dynamic transport of hydrogen, helium, and oxygen ions to lower L-shells. The low-energy ion mass spectrometers observed new phenomena near the equator where pitch-angle distributions are asymmetric for long periods of time during geomagnetic storms. These distributions were caused by parallel electric fields that appear to be induced by increasing Birkeland currents and by decreasing tail currents.

**14. SUBJECT TERMS**

Radiation Belts, Ring Current, Particle Precipitation, Wave-Particle Interactions

**15. NUMBER OF PAGES**

**16. PRICE CODE**

| 17. SECURITY CLASSIFICATION OF REPORT | 18. SECURITY CLASSIFICATION OF THIS PAGE | 19. SECURITY CLASSIFICATION OF ABSTRACT | 20. LIMITATION OF ABSTRACT |
|---|---|---|---|
| Unclassified | Unclassified | Unclassified | SAR |

NSN 7540-01-280-5500

Standard Form 298 (Rev 2-89)
Prescribed by ANSI Std Z39-18
298-102

# Contents

## Summary

A number of scientific results have been obtained from the continued study of the ONR-307 energetic particle and ion composition experiment data acquired onboard the Combined Release and Radiation Effects Satellite (CRRES). Under a previous contract excellent data were obtained from the instrumentation and analysis was performed on the 14 months of data obtained from CRRES. This is the final report for the CRRES ONR-307 Experiment Data Analysis follow-on contract.

The overall objectives of the ONR-307 experiments were to obtain necessary data on the earth's radiation belt and plasma environment, to understand the physical processes responsible for the sources and losses of energetic particles, and to improve the existing models of the radiation belts and ring current. Plasma composition data for ions from 0.1 to 1000 keV, electrons from 50 eV to 5000 keV, and energetic protons from 500 keV to 100 MeV were measured by the ONR-307 experiment with high pitch-angle resolution.

Our data analysis and scientific research using these data have concentrated on three key areas of investigation: particle precipitation and wave-particle interactions, radiation belt and ring current modeling, and dynamic event studies. Utilizing the ONR-307 particle data together with plasma wave data measured by other instrumentation on CRRES, we have studied, for the first time from the same spacecraft in the outer radiation belt region, the simultaneous nature of waves and precipitating electrons near the equator, both for trapped particles and narrow particle dropouts. These latter studies showed that there is a general correlation between wave intensities and electron fluxes. The sudden, short electron dropouts usually include both electrons and ions, as well as thermal plasma. Hiss and chorus are usually enhanced near the boundaries of the particle dropouts. Because of the rapid loss of the particles during these events, it is concluded that these dropouts cannot be caused by the mechanism of plasma waves scattering the particles into the atmospheric loss cone.

Investigation of the ion composition data during the large magnetic storm of March 1991 revealed the detailed structure of the ring current, allowed mapping of the structure for the first time, and showed dynamic transport of the hydrogen, helium, and oxygen ions to lower L-shells.

The ONR-307 low-energy ion mass spectrometers observed new phenomena near the equator where the ion pitch-angle distributions are asymmetric for long periods of time during geomagnetic storms. These observations reveal important interaction of the solar wind with the magnetosphere, and they imply significant inter-hemispheric asymmetry and dynamics. All of these events occurred after the IMF turned southward and while $B_z$ was increasing with time. A computer simulation of these events reveals that these asymmetric distributions were caused by parallel electric fields that generally increase with time and extend from one hemisphere to the other. The electric field appears to be induced by increasing Birkeland currents and by decreasing tail currents.

# Introduction

The primary objectives of the Combined Release and Radiation Effects Satellite (CRRES) were: to improve existing models of the inner and outer radiation belts of the earth, to correlate radiation effects on microelectronics with in situ radiation measurements, and to study the nature of wave-particle interactions that cause radiation belt particles to precipitate into the atmosphere. The ONR-307 experiment provided an important set of measurements toward the accomplishment of the overall CRRES mission objectives. The ONR-307 observations complemented measurements provided by other laboratories to obtain a significant improvement in our understanding of radiation belt physics.

The CRRES orbit and the comprehensive measurements made by the ONR-307 instrumentation enabled us to address the objectives stated above. This is schematically illustrated in Figure 1, which shows the CRRES orbit at an inclination of 18° from the geographic equator. The geomagnetic equator is offset from the geographic equator by ~11°, and hence, the orbital plane "wobbles" through the radiation belts at low inclinations as the earth rotates underneath. The high altitude of apogee (~ 6.6 earth radii) permitted sampling of all of the geomagnetic field lines containing the threatening doses to DoD satellite missions.

One of the most important life-limiting elements of DoD reconnaissance, communication and manned platforms in space is the radiation environment. Current program requirements demand operational spacecraft lifetimes of 5 to 10 years in near-earth orbit. Such long operational lifetimes require that considerable attention be given to shielding and radiation-hardening of electronic parts. Military space systems must also be designed to survive the even more extreme radiation effects from nuclear weapon bursts in space. Radiation shielding creates significant weight and cost impacts on many DoD missions. Uncertainties in the amount of shielding required leads to conservative design practices that adversely impact available payload weight capability.

Electron precipitation from the radiation belts into the atmosphere entails ionospheric effects that have important consequences for radiowave propagation. It has been demonstrated that energetic electron precipitation events may cause an enhancement or degradation of ELF signal waves, depending upon where the disturbance is occurring along the path. At VLF frequencies long-lived phase disturbances can be explained by excess D region ionization caused by energetic electron precipitation. The precipitation of energetic electrons from the earth's radiation belts can cause degradation or blocking out of critical U. S. Navy Communication and Navigation links operating at HF, VLF, and ELF frequencies. Precipitating particles play a significant role in atmospheric chemistry through the production, destruction and transport of reactive nitrogen, oxygen and hydrogen species.

Existing data indicate that electrons are precipitated from the radiation belts both by natural mechanisms such as lightning and plasmaspheric hiss, and by man-operated VLF transmitters. The precipitation involves both electrons precipitating directly in the bounce loss cone and

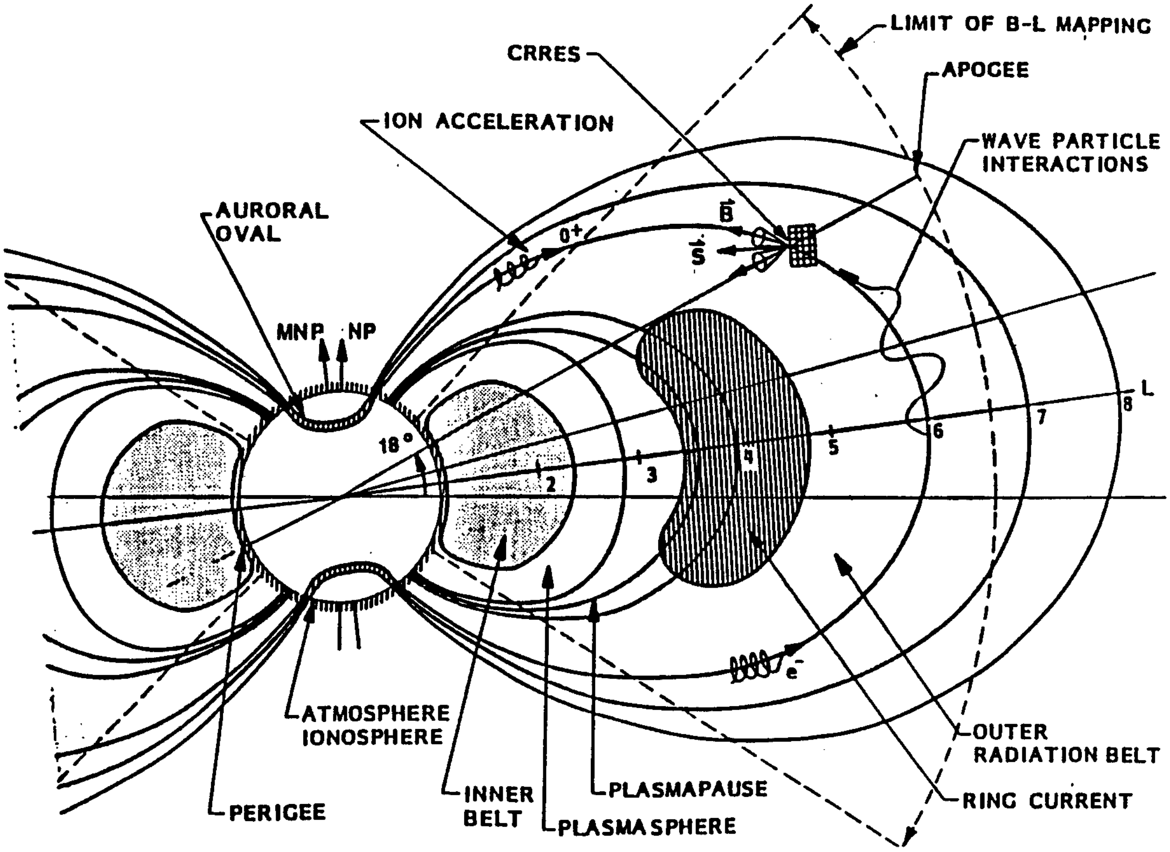

Figure 1. Illustration of the combined release and radiation effects satellite (CRRES) orbit plane with respect to the relevant magnetosphere particle trapping and precipitation regions. The spin vector S is always pointing towards the sun.

electrons that mirror at altitudes above 100 km at most longitudes and below 100 km, in which case they precipitate into the atmosphere, after they have drifted to the vicinity of the South Atlantic Anomaly.

Our present understanding of the earth's radiation belts, based on three decades of measurements, has been synthesized by the National Space Science Data Center and others into models of the electron and proton populations that provide the principal threat to satellites. For several reasons the accuracy of these models in defining the environment that a particular satellite mission will encounter is only good to a factor of 3, i.e., a 200 percent uncertainty. Of the many factors responsible for this large uncertainty, the most significant are the dynamics of the radiation belts with solar activity, the limited region of space and temporal duration covered by the measurements, and the variability in the capabilities and accuracy of the measuring instrumentation. To significantly improve on the current radiation belt models, therefore, all of these limitations must be improved upon. The unique orbit of the CRRES mission and the comprehensive set of measurements it made provide great promise for substantial improvements in radiation belt modeling.

It is important to clearly understand the elements necessary for the improvement of radiation modeling for DoD purposes. The first of these elements involves the type of orbits used by the military for photo and electromagnetic observatories. These orbits and their relationship to the earth's inner and outer trapped radiation belts are depicted in Figure 2. The principal orbit used for land and ocean reconnaissance is the low-altitude polar orbit, designated as LEO in the figure. Communications from earth-to-satellite heavily utilize the synchronous (SYNC) and high-earth orbits (HEO). The radiation dose received in each of these orbits comes from different regions of the trapped radiation belts. The type and energy of the particles providing the dose is also different in the respective orbits. For example, the principal natural threat to a SYNC orbit vehicle is from the intense flux of electrons, while the principal threat to the LEO orbit comes from the very energetic protons in the inner radiation belt in the vicinity of the South Atlantic Anomaly. The radiation intensity increases with altitude on a given field line and the maximum intensity is reached at the geomagnetic equator. In Figure 2 notice that the HEO orbit transits the same magnetic field lines as the SYNC orbit but at lower altitude and hence lower flux levels. On the other hand, the HEO orbit transits the inner belt at higher altitudes than the LEO orbit. The HEO orbit is therefore very complex in terms of the radiation environment and the modeling effects on spacecraft systems.

Because of the variety of orbits used by the DoD and the complexity of the radiations encountered it is essential that a comprehensive radiation-measuring payload include:

1) Discrimination of the various particle types and masses, i.e., electrons, protons, and heavy ions.

2) Measurement of the energy spectra of the various particle species since this directly translates into the penetrating power through shielding.

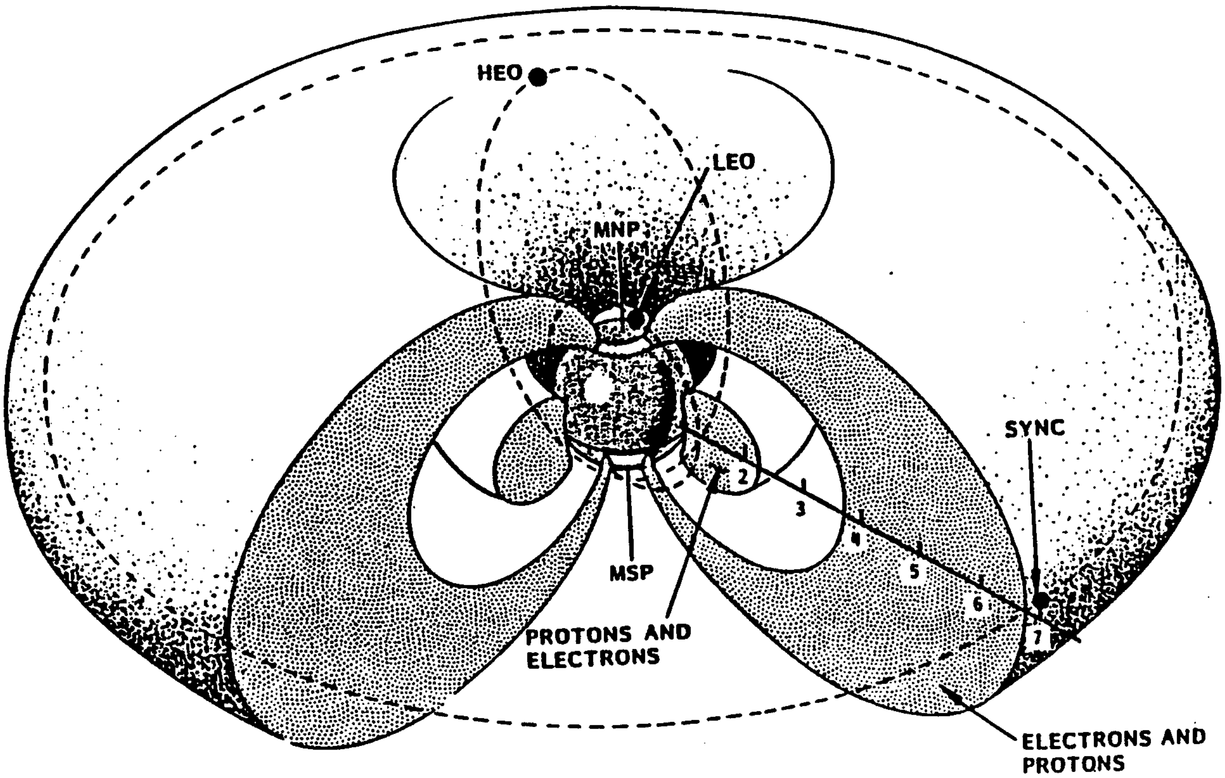

Figure 2. The earth's radiation belts showing the inner and outer portions and the principal particles responsible for providing life-limiting radiation doses to the key satellite orbits used by the DoD. The distances are to scale and shown in earth radii. LEO, HEO and SYNC refer to low-earth-orbit, high-earth-orbit and synchronous orbit, respectively.

3) Complete pitch-angle coverage with good angular resolution because this provides the ability to map particles down the field lines from the point of observation. Measurements of the complete pitch-angle distribution at the geomagnetic equator from 0° (along the field line) to 90° (perpendicular to the field line) with good angular resolution completely define the entire particle population on that field line at all altitudes.

4) The ability to sample all of the magnetic field lines as close to the geomagnetic equator as possible since this will define the environment of the entire radiation belts.

In addition to the primary objective of acquiring an accurate data base for radiation belt modeling, there are other important scientific objectives of the ONR-307 experiment related to our understanding of radiation belt physics. It is well known that the solar wind plasma is the primary source of the particles observed in the trapped radiation belts. The sub-kilovolt particles from the sun are energized and radially transported inward toward the earth by the electric and magnetic forces in the magnetosphere. In recent years it has been recognized that the ionosphere at higher latitudes is also a major source of energetic particles. The cold ionospheric ions are accelerated in energy by electric fields created parallel to the magnetic field and are transported up the field lines where a significant fraction are permanently trapped in the radiation belts. The region around the field line is, therefore, a "source cone" for the radiation belts at mid- and high-latitudes. The Space Sciences Laboratory of Lockheed Martin Missles & Space Advanced Tecnology Center has made major contributions to this field since the original discovery on an ONR satellite in 1972. To study this source and its contributions to the earth's ring current portion of the radiation belts requires good mass discrimination with high angular resolution. The ONR-307-8 instrumentation is capable of providing the necessary measurements, as can be seen in the studies presented below.

Equilibrium is reached with the various sources of particles in the radiation belt principally through loss processes that precipitate particles into the atmosphere. Particles are precipitated by being diffused in pitch angle into the "loss cone", the narrow angular region centered along a magnetic field line. A principal mechanism for diffusing particles in pitch angle is wave-particle interactions between electrostatic and electromagnetic waves of natural and man-made origin and the various particle species in the belts. In the highly-successful SEEP program for the ONR [Imhof et al., 1986; Voss et al., 1984] it was clearly demonstrated that VLF waves from ground-based transmitters were diffusing energetic electrons into the atmospheric loss cone. The SEEP satellite payload measured the precipitation near the foot of the field line. The ONR-307-3 instrument on CRRES studied these wave-particle interactions for the first time in the near-equatorial interaction regions where the waves are resonating with the particles. The high angular resolution and good energy resolution of the ONR-307-3 spectrometer provided major new information on the microphysics involved in the interaction processes. Complementary wave and plasma measurements aboard CRRES provided all of the key ingredients necessary to make major studies in our understanding of the wave-particle interaction processes. The precipitation of particles into the atmosphere/ionosphere creates disturbances to vital U.S. Navy communication links operating from ELF to HF. Understanding the precipitation processes improves our capabilities to predict communication disruptions and blackout under both natural and nuclear disturbed conditions.

The ONR-307 instrumentation, which is briefly described in the next section, provides both good energy and pitch-angle resolution over the entire energy range of importance to radiation belt modeling and studies. The ONR-307 instruments were operated essentially continuously for the mission lifetime. During the period from launch, until the satellite failure 14 months later, CRRES apogee moved through 19 hours in local time, thus providing excellent altitude-local time coverage of the earths radiation belts and inner plasma sheet.

The present final report provides a description of the investigations conducted under the current ONR contract. The basis for these studies was obtained during the data analysis performed under the original ONR-307 contract. The studies described below involve data analysis and scientific research using the ONR-307 data in three key areas of investigation: (1) particle precipitation and wave-particle interactions, (2) radiation belt and ring current modeling, and (3) dynamic event studies.

## Methods, Assumptions and Procedures

The overall objective of the ONR-307 experiment was to obtain necessary data to construct predictive models, suitable for engineering purposes, of the energetic particle and plasma environment in those regions of space of primary interest to the Department of Defense satellite operations. Accurate and comprehensive measurements are crucial to this objective. This includes a quantitative understanding of the sources and losses of radiation belt particles, as well as developing an accurate and comprehensive engineering data base on particle intensities, composition, energy spectra, and pitch-angle distributions. As our knowledge of the microphysics involved in particle injections, acceleration, transport, and losses improves we will be in a much better position to predict effects on the spacecraft systems of the future. The accurate and complete particle data base can be used to interpret observed degradation effects on electronics and solar cell packages as well as for the survivability analysis and design of future operational spacecraft missions.

To achieve the objectives of this investigation, energetic electron and ion measurements of the entire particle distribution function must be utilized. The data must provide good mass, temporal, spatial and energy resolution. As part of our previous ONR contract (N00014-83-C-0476), which began in 1983, the Lockheed Martin Space Sciences Laboratory designed, developed, tested, and delivered a set of instruments referred to as ONR-307. The ONR-307 instrumentation is shown in Figure 3 before being installed on the CRRES spacecraft. The present ONR contract is a follow-on to the previous one, and as such, the analysis of the data is a continuation with some overlap of that reported under the previous contract. The instruments were integrated on the spacecraft and launched on an Atlas-Centaur rocket on July 25, 1990. Operations of these instruments over a 14 month period obtained an excellent data set with which to address the investigation's objectives.

The measurement capabilities of the ONR-307 instruments are summarized in Table 1. The three instruments are described briefly in the following subsections and in more detail in the published instrument papers referenced therein.

Table 1: ONR-307 Payload Summary

| Instruments | Measured Quantity | Energy | Sensor Angle to Spacecraft Spin Axis |
|---|---|---|---|
| ONR-307-3<br>SEP | Electrons<br>Protons | 40 - 5000 keV<br>0.5 - 100 MeV | 40°, 60°, 80° |
| ONR-307-8-1,2<br>IMS-LO | Ion Composition<br>Electrons | $E/q = 0.1 - 35$ keV<br>0.05 - 25 keV | 45°, 75° |
| ONR-307-8-3<br>IMS-HI | Ion Composition | $EM/q^2 = 10 - 2000$ keV-AMU/$e^2$ | 75° |

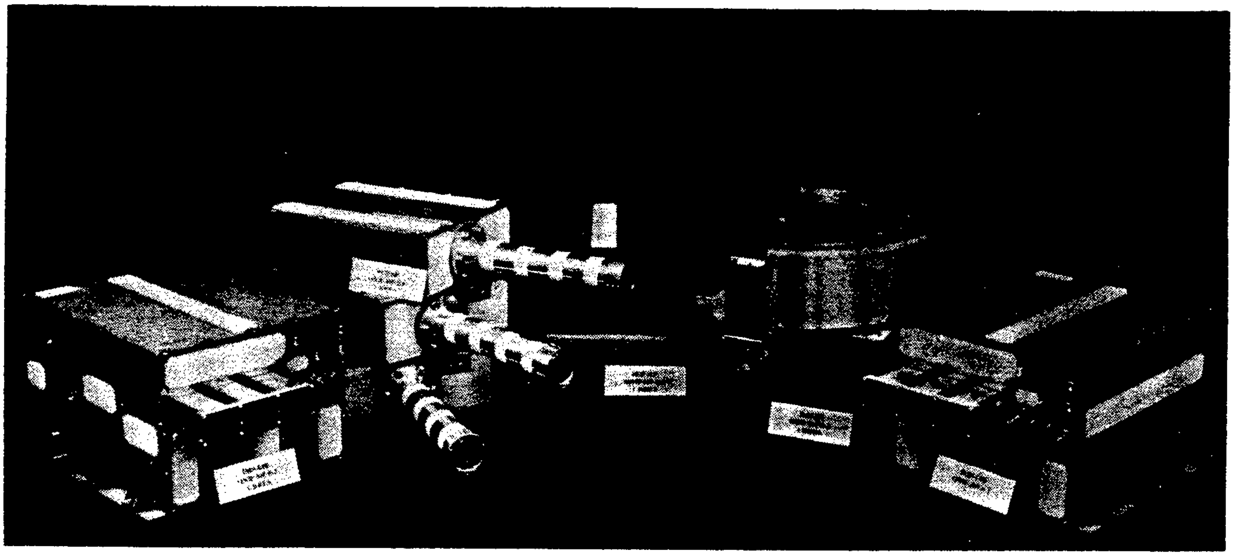

Figure 3. A picture of the ONR-307 instruments prior to mounting on the spacecraft.

### ONR-307-3 Spectrometer for Electrons and Protons (SEP)

The Spectrometer for Electrons and Protons (SEP), designated ONR-307-3, measured electrons in the energy range 40-5000 keV and protons in the range 0.5 - 100 MeV. The energy ranges were covered with fine, programmable energy resolution. Very good pitch-angle resolution was provided by 3° FWHM collimation. In order to obtain nearly complete pitch-angle coverage over the CRRES orbit, the instrument used three identical particle telescopes, mounted at carefully optimized angles to the spacecraft spin axis. Each telescope used a stack of surface-barrier silicon detectors with active anticoincidence shielding. Various logic combinations of the detector elements determined the particle types and energy ranges that were measured. The SEP instrument was based on the highly successful SC-3 instrument developed for ONR and flown on SCATHA. A more detailed description of the SEP instrument and its capabilities can be found in Nightingale et al. [1992].

### ONR-307-8-1,2 Low Energy Ion Mass Spectrometer (IMS-LO)

The Low Energy Ion Mass Spectrometers (IMS-LO), designated ONR-307-8-1 and ONR-307-8-2, were two identical instruments that measured ion composition in the energy range E/q = 0.1 -35 keV/e. The two instruments were mounted at different angles to the spacecraft spin axis in order to optimize pitch-angle sampling. The IMS-LO instruments used crossed electric and magnetic field Wien filters, followed by 180° electrostatic analyzers and channeltron sensors to determine ion energy/charge and mass/charge. Three parallel analyzers were used within each instrument to cover different segments of the full energy range. The instruments could be commanded to sweep through the full mass range, to alternately lock on any four selected masses, or to alternate between the two modes. In addition to the ion measurements, IMS-LO used magnetic analyzers to measure the electron background fluxes at eight energy steps between 50 eV and 25 keV. The IMS-LO instruments were derived from the extremely successful instruments developed for the Office of Naval Research for flight on S3-3 and SCATHA. The instrument has been described in more detail by Collin et al. [1992].

### ONR-307-8-3 Medium Energy Ion Mass Spectrometer

The Medium Energy Ion Mass Spectrometer (IMS-HI), designated ONR-307-8-3, measured ion composition in the energy range $EM/q^2 = 10 - 2000$ keV-AMU/$e^2$. The instrument was a novel design based on ion momentum separation in a magnetic field. The ions were dispersed onto an array of six passively cooled silicon solid-state detectors. Energy and mass defect analysis were performed in the parallel processing electronics, allowing simultaneous measurements by each of the detectors. The instrument could be operated in two basic modes, providing full mass coverage every eight seconds or sampling of four selected ions every half second. A detailed description of the instrument is contained in Voss et al. [1992].

## Results and Discussion

Utilizing the data sets from the above instrumentation, specific investigations, which can be put into three areas, have been studied in support of the overall ONR-307 objectives. First is the investigation of particle precipitation. This includes wave-particle interactions, which are critical to pitch-angle scattering and particle precipitation. The second area is the study of radiation belt and ring current populations towards the development of quantitative, parameterized models. The third area is the study of dynamic events of special interest. The investigations in each of these area are described in the following subsection.

### Particle Precipitation & Wave-Particie Interactions

The synergy between trapped particles in the magnetosphere and various types of plasma waves has been a dominant theme of space plasma physics for decades. Early theoretical work of Dungey [1963] raised the issue of wave effects on trapped particle populations and the classic paper of Kennel and Petschek [1966] brought out the fact that a non-isotropic particle population would generate waves. Since these pioneering papers appeared, a continuous series of experimental and theoretical analyses have focused on these processes. Nevertheless, detailed understanding of the mechanisms by which particle distributions generate waves has not yet been achieved, although a general association of wave types with particle distributions and locations have been tabulated (i.e., Shawhan, [1979] ). Measurements from the CRRES satellite help fill a void in the serious lack of simultanaeous wave and electron data near the equator where the bulk of the wave-particle interactions in the outer radiation belt are believed to take place.

#### *Simultaneous Measurements of Waves and Precipitating Electrons*

The fluxes and energy spectra of particles trapped in the slot region ($L = 2\text{-}3.5$) of the radiation belts are very dynamic. This region of the radiation belts is a source of significant precipitation of particles into the atmosphere. Despite its importance the source and loss mechanisms of the trapped particles are still not well understood. Evidence exists for electron precipitation by a variety of mechanisms involving VLF chorus, plasmaspheric hiss, and lightning. Our knowledge of these loss mechanisms is limited by the lack of experimental data. Evidence for the importance of plasmaspheric hiss came from a coordinated wave-electron investigation [Imhof et al., 1982] that was limited by the fact that the waves and electrons were measured from different satellites at widely differing altitudes. Studies of precipitation by chorus and lightning were subsequently conducted from the SEEP payload [Imhof et al., 1986; Voss et al., 1984].

An investigation ( Imhof et al., [1994] ) of wave-particle interactions was made using several simultaneous electron and wave measurements performed at near-equatorial positions from the CRRES satellite. Bursts of electron precipitation were observed, most frequently at local times near dawn. The changes of the precipitating fluxes were generally less pronounced at the lowest energies. On the basis of electron-cyclotron resonant calculations using cold plasma densities and ambient magnetic fields taken from the CRRES measurements it was found that the wave frequencies and precipitating electron energies were generally consistant with those expected from electron resonance with parallel propagating whistler waves. The electron data of principal concern here were acquired in and about the loss cone with narrow angular resolution covering the energy range 340 eV to 5 MeV. The wave data included electric field measurements spanning frequencies from 5 Hz to 400 kHz and magnetic field measurements from 5 Hz to 10 kHz.

The results of this investigation provided new insights into the nature of the transient precipitation events previously reported by Imhof et al., [1992]. Several events were studied in great detail to see if they could be understood in the context of the Kennel and Petschek [1966] theory. Our investigation provides support for the Kennel-Petschek theory for pitch-angle scattering of energetic electrons into the atmospheric loss cone. The electron flux measurements show enhancements in fluxes near the loss cone relative to the trapped fluxes. When higher-frequency waves are present, the flux enhancements are seen at lower electron energies in agreement with the theory. In general, the best correlation between waves and particles is seen for wave frequencies near 256 Hz and for electron energies near 50 keV. The spatial distribution of the electron bursts is consistent with that expected from energetic electrons injected near midnight in association with auroral substorms. An example of the flux variations acquired between L-shell values of 5 and 6 near the dusk magnetic local time is shown in Figure 4 for 10 April 1991. Two isolated enhancements at 0° pitch angle with no corresponding variations at 10°. Each flux enhancement in Figure 4 is accompanied by correlated enhancements in the electric-field wave measurements. A reprint of the published work is in Appendix B.

### *Association of Plasma Waves with Changes in Trapped Particle Fluxes*

In the present study several features of the wave-particle associations were investigated, making use of the comprehensive set of particle detectors and a broad frequency range plasma wave receiver onboard the CRRES spacecraft. Special emphasis was placed on times when particle and wave distributions changed suddenly. In particular, cases of narrow (<30 min) flux dropouts were examined to see if unusual wave activity was associated with changes in the particle distributions. This work is the first such study that was able to include detailed measurements of the wave fields, as well as the particle fluxes. A preprint of a paper describing this investigation entitled, "Association of Waves with Narrow Particle Dropouts in the Outer Radiation Belt," by Imhof et al. [1997], can be found in the Appendix B.

The particle data used for this work were acquired with the CRRES ONR-307 instruments. The SEP electron data used covered the energy range of 40 keV to 5 MeV, while that from IMS-LO were centered in energy bands at 1.7, 3.9, and 8.9 keV. IMS-HI proton measurements were utilized in the energy range 18 - 360 keV. The particle data used for this work were acquired with the CRRES ONR-307 instruments. Figure 5 shows an orbit of selected electron data from 10 October 1990 (orbit 186). A survey of the electron dropout events was made using the SEP

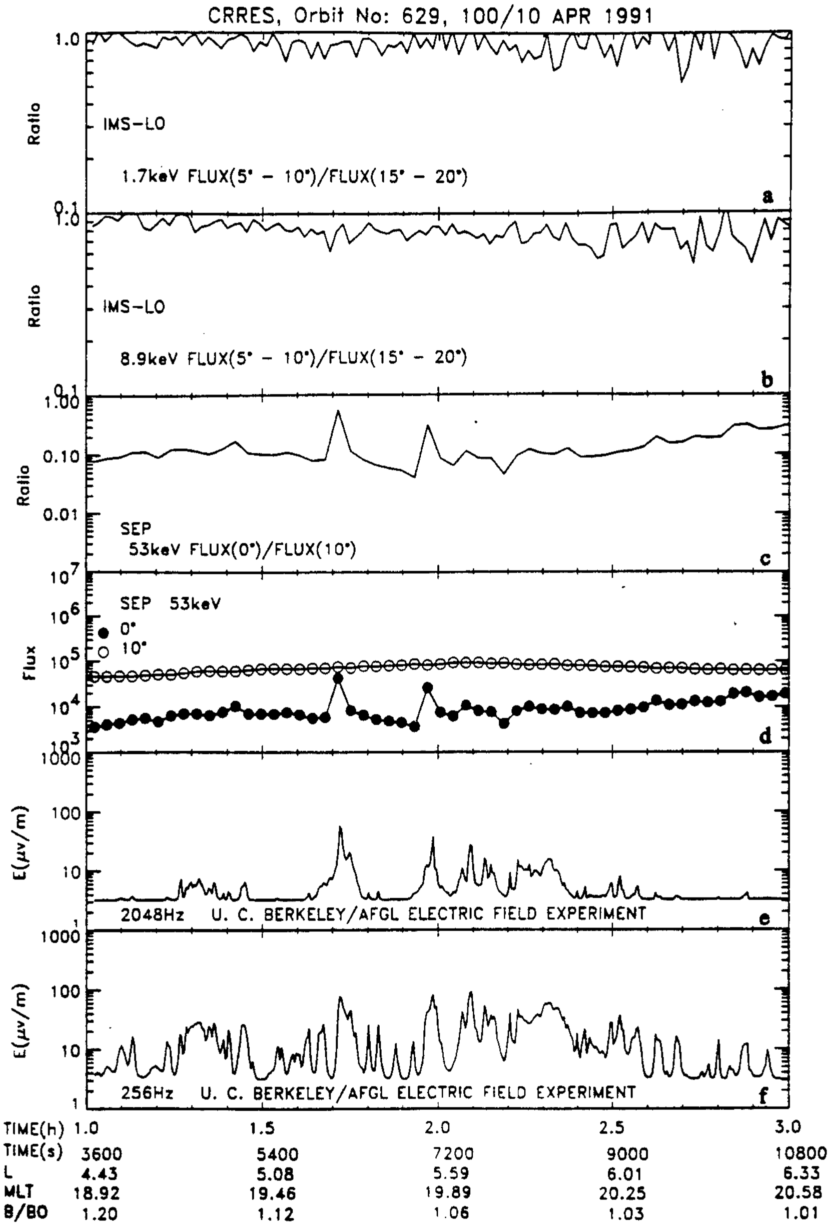

Figure 4. Fluxes and ratios of various energy electrons at different pitch angles.

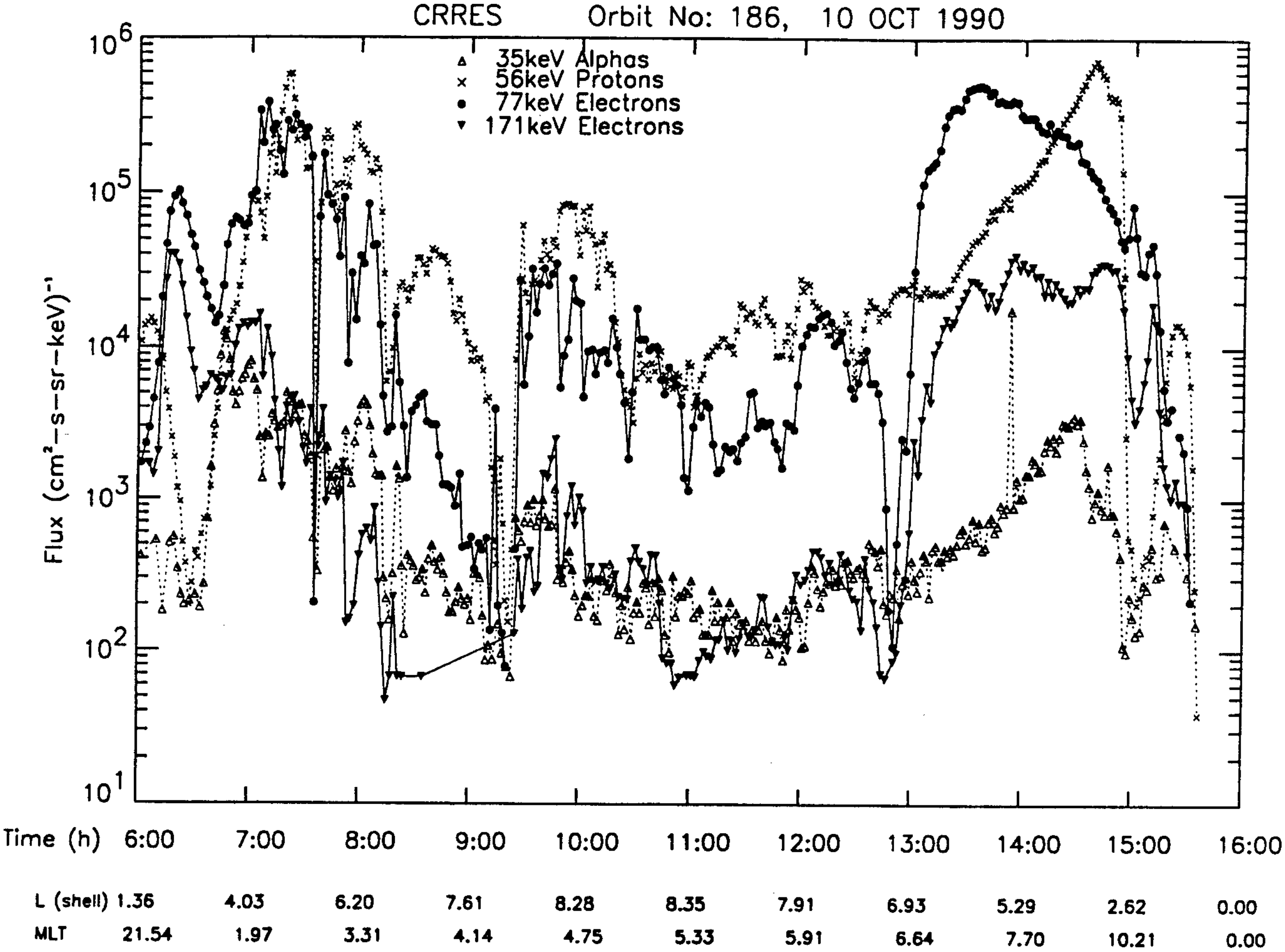

Figure 5. Flux variations of various energy electron, protons, and alpha particles for orbit 186 on October 10, 1990.

data set, followed by an intercomparison of the events with the IMS-HI and IMS-LO data. Examples of the flux dropouts used in the study can be found at 07:37 and 12:46 UT.

The electric and magnetic field wave data used in this study were provided by the onboard University of Iowa/Air Force Geophysics Laboratory (AFGL) Plasma Wave Experiment and the University of California at Berkeley/AFGL Electric Field/Langmuir Probe Experiment. The Iowa/AFGL instrument included a Sweep Frequency Receiver (SFR) and Multichannel Spectrum Analyzer (MCA) that together provided electric field wave measurements from 5 Hz to 400 kHz and magnetic field measurements from 5 Hz to 10 kHz. [Anderson et al., 1992]. The Berkeley/AFGL experiment [Wygant et al., 1992] measured electric and magnetic waveforms over frequencies ranging from quasistatic to 40 kHz. The instrument also provided continuous monitoring at several samples per second of the wave amplitudes measured throught 3 broadband filters with maximum responses at frequencies of 32 Hz, 256 Hz, and 2048 Hz.

Two typical examples of CRRES particle and wave data are presented in Figure 6, which shows a number of quantities as a function of time during orbits 279 and 542, which took place on November 17, 1990 and March 5, 1991, respectively. For both orbits the lowest panel indicates the spectral density of the electric field the power spectral density scale on the left of each spectrogram. Above the spectrogram are the electric field intensities in a series of frequency bands. The multichannel electric field data are complementary to the multichannel magnetic field information provided at the top of the figure. Proton and electron fluxes at a number of energies are plotted between the magnetic and electric field charts.

All these data exhibit a rich morphology and a wealth of detail about particles and waves in the magnetosphere. Transits through the radiation belts and slot region can be identified in the particle fluxes. The wave spectrograms usually show the plasmapause crossings (such as at 11:45 UT on November 17 and at 9:30 UT on March 5) where low-frequency plasmaspheric hiss ends and chorus commences. The thin vertical lines and arrows below the spectrograms denote times of abrupt, temporary reductions in electron flux. These reductions are to be contrasted with those observed at the outer boundary of the electron radiation belt [Imhof et al., 1993], investigated under the previous contract. In both cases enhanced wave energy occurred at the edges of the dropouts, as shown by the vertical dark lines within the white areas at the bottom of the spectrograms. At other times increases in electron fluxes were accompanied by increased wave activity (such as at 12:00 UT on March 5). On November 17 as the electron flux decreased near 1:30 UT, wave intensities also decreased. An interesting band of chorus is apparent also on this day between about 17:00 and 19:00 UT This band increases systematically in frequency from 1 kHz to about 10 kHz as the satellite moves inward through the outer radiation belt. The chorus band ends as the satellite crosses the plasmapause.

At the high-frequency region of the bottom spectrogram, above $10^5$ Hz, sporatic enhancements of wave emissions are seen, often at the same time as increases in the lower frequency waves. The high-frequency component, known as auroral kilometric radiation, or

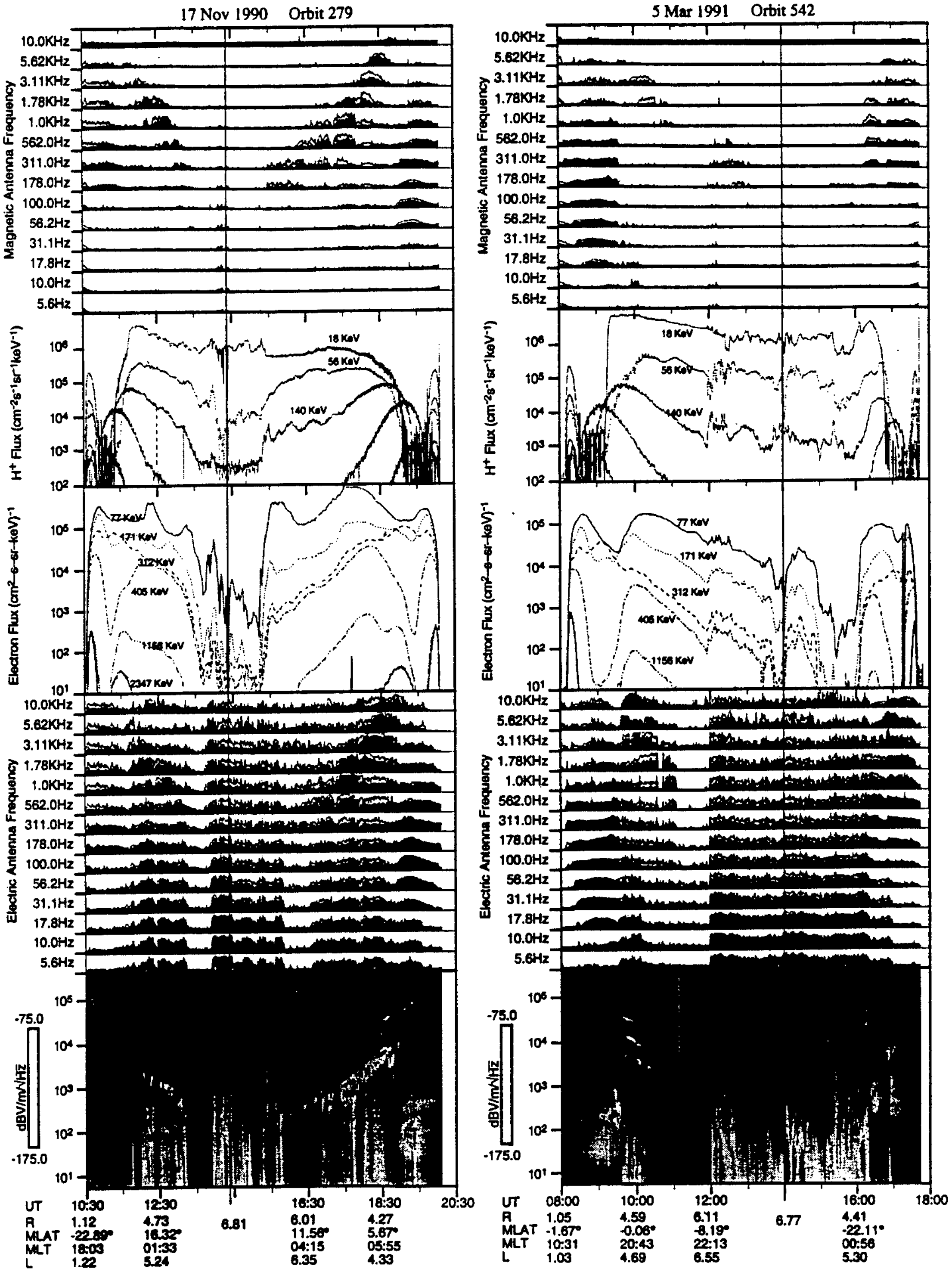

Figure 6. Charge particle and wave data for orbits 279, November 17, 1990, and 542, March 5, 1991. The bottom two sections contain frequency spectrograms while the next two contain plots of fluxes of protons and electrons at various energies. In the upper section the magnetic component of the wave data is plotted.

AKR, is believed to be produced by a loss-cone distribution of auroral electrons and is indicative of substorm activity.

As part of the present study the wave fields associates with the narrow electron flux decreases were studied for 17 cases similar to those shown in Figure 6. The conclusions of this work are summarized below.

a. There is a general correlation between wave intensities and electron fluxes. Higher fluxes accompany higher wave intensities.

b. The sudden, short electron dropouts usually, but not always, include both electrons and ions, as well as the thermal plasma.

c. Hiss and chorus are usually enhanced near the boundaries of the particle dropouts or where particle gradients are large. However, similar wave enhancements are sometimes seen without particle dropouts. Presumably in those cases a flux gradient exists somewhat removed from the satellite, and the waves generated at the gradient propagate to the satellite location.

d. On short time scales (<30 min) features in the wave and particle profiles are sometimes correlated, but frequently are independent. Again the localized nature of the particle characteristics compared to the more widespread wave fields may be responsible for the lack of detailed correlation.

e. Because of the rapid loss of particles during dropouts, it is concluded that these dropouts cannot be caused by the mechanism of plasma waves scattering the particles into the atmospheric loss cone. At the L-shell values considered the loss cone is so small that even with strong diffusion, a particle requires many bounces to enter the atmosphere through the loss cone.

### *Narrow Proton Flux as Short as One Second*

During several of the short duration (<30 min) proton flux dropouts in the outer radiation belt examined in the above study, one to three brief enhancements occurred with rise times, durations and fall times as short as one second. We have recently begun to analyze these particular events, for which examples are shown in Figure 7. Sometimes the 56 keV protons displayed much narrower enhancements than did protons with 18 keV energy. Such short rise times for proton flux changes in the outer radiation belt are to be contrasted with the measurements by Kaufman et al. [1972] of protons at similar positions in the radiation belt. They found that the >100 keV proton fluxes require several seconds to change by large factors. The observations were interpreted in terms of temporal and/or spatial variation in the magnetic field. The observed perturbations were found to be neither purely temporal nor purely spatial. At the time of each of the flux enhancements observed in the present investigation the CRRES magnetometer data recordings are being examined to find evidence for motion of a flux gradient. Further investigation of those cases with narrow flux enhancements having a repetition rate consistent with the satellite spin period of ~30 seconds would require scanning the data for flux variations at specific pitch angles.

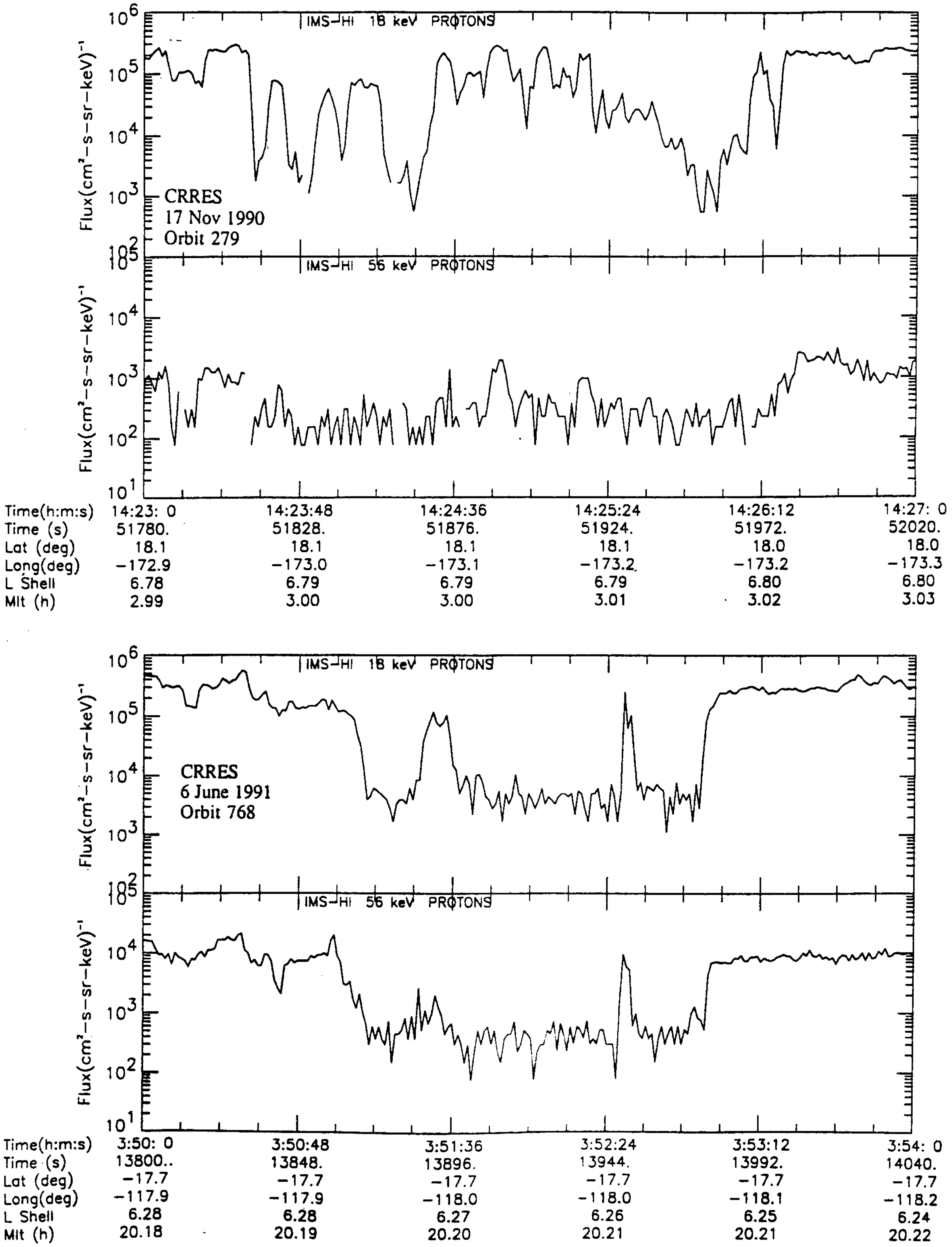

Figure 7. Short duration enhancements observed from CRRES by ONR-307.

*Cross Correlations Between Electrons and Waves Onboard CRRES*

Another, unique, perspective on the physics of wave particle interactions is available on CRRES through the onboard wave-particle correlations capabilities. The University of Sussex Particle Correlator Experiment performed real time cross correlations between electrons and waves onboard CRRES. It was in operation for several months of the CRRES mission. Observations of strong correlations have indicated that wave-particle interactions were occurring locally to CRRES. Confirmation that the interactions were local removes uncertainties resulting from the propagation of the waves and particles from distant, and perhaps independent, interaction regions.

In collaboration with the University of Sussex we have examined the IMS-LO electron data when strong cross correlations were observed. At the times of the correlations the electron distributions were found to develop shoulders on the flanks of trapped distributions at certain energies indicating that electrons were being selectively diffused towards the loss cone. In one case, correlations were observed at frequencies between 1/3 and 1/2 of the electron gyrofrequency for approximately one hour. At the same time the University of Iowa plasma wave experiment measured chorus emissions at approximately 1/3 the electron gyrofrequency, and IMS-LO observed an apparent velocity dispersion event between 770 eV and 20 keV. Some of the results of the investigations with the wave particle correlator have been presented at the MIT Workshop on Space Plasma Physics by Watkins et al., [1994] entitled, "Observations of Possible Wave-Particle Interactions Identified by the CRRES Particle Correlator: Preliminary Comparison with Kennel-Petschek Theory." A preprint can be found in Appendix B. Results were also reported at COSPAR and a reprint by Watkins et al., [1996] entitled, "Suspected Wave-Particle Interactions Coincident with a Pancake Distribution as Seen by the CRRES Spacecraft," also appears in Appendix B.

## Radiation Belt and Ring Current Modeling

The magnetic storm of March 1991 produced dramatic changes in the fluxes of energetic electrons and ions in the magnetosphere. In the L-shell range from 2.5 to 3.5 the fluxes of electrons with energies between 30 keV and 2 MeV increased during several orbits after the main storm compression at 03:42 UT on March 24. The ion flux also increased at storm onset; the enhancement in the $O^+$ fluxes was more dramatic than $H^+$ fluxes. During the later part of March 25 CRRES was on field lines whose ionospheric footprints were over Canada and the central United States. At this time, low-latitude aurora were observed at some locations in the Unitied States. The precipitating particles measured from CRRES may have been responsible for those auroral events. The dynamic structure of the ion composition during the storm time ring current is discussed below.

The ring current ions are thought to be responsible for 1) the current that reduces the earth's horizontal magnetic field (*D*st), 2) the generation of energetic neutrals that may be used to probe the magnetosphere, 3) the source of the equatorward proton and ion aurora and mid-latitude ion precipitation zone, and 4) the radial diffusion of energetic ions into the radiation belts. The early detection of these particles was without charge or composition information. Only recently have measurements been made of the bulk of the ring current ions during a magnetic storm but with relatively low sensitivities [Gloeckler et al.,1987, Hamilton et al., 1988]. By understanding the injection, acceleration, and transport within the radiation belts the assumptions for modeling algorithms can be improved.

The March 24, 1991 Magnetic storm was investigated using the IMS-HI and IMS-LO instruments on the CRRES satellite. This storm shows considerable variation. Figure 8a is a plot of the flux vs. time (L-shell) for protons of various energies before the storm commencement. Hydrogen in the ring current was mapped continuously between 15 and 2000 keV by the IMS-HI instrument. Before the storm, energetic 18 keV protons were found to have a sharp cutoff at L=3.5 in which the flux dropped by over two orders of magnitude into the background. Figure 8b shows the energy spectra at 6 L shells for the March 23 orbit 586 for 18 keV protons. One day after the SSC when the *D*st was near its minimum (-300 nT) the protons pushed inward with a cutoff at L~1.7, a peak near L~2.6, and fluxes less than pre-storm for L>4. The lower cutoff stayed at about L~2.0 for several days after the storm with the peak fluxes near L~ 2.6 to ~ 3.2. Energetic $O^+$, $O^{++}$, and $He^+$ were observed to penetrate and also peak near L~2.6 one day after the SSC and near *D*st minimum. The decay rates are consistent with ion loss due to charge exchange.

While the pre-storm ion distributions are fairly well understood the dynamics of the storm time ion distributions are still difficult to model. The results from the high-sensitivity CRRES IMS-HI instrument provide new insights into the ring current energy flow. In Figures 9a and 9b the hydrogen flux for differential energies of 18, 56, 140, 360, and 1200 keV is plotted as a function of L shell for inbound and outbound passes on orbits 587 through 592, March 23 - 26. Each orbit is offset by constant value to help follow the storm development and reduce plot overlap. These plots provide a dramatic picture of the ring current ion composition during a large magnetic storm. The pre-storm ion flux for orbit 587 is shown in the upper panel of each figure. Noteworthy for this orbit is the relatively low fluxes, the similarity of the outbound and inbound passes, the relatively high L shell of the ion flux maximum or centroid, the composition dominated by hydrogen, and the absence of particle flux fine structure. The modulation of the 360 and 1200 keV hydrogen flux is the result of pitch-angle variations. The similarity of outbound and inbound passes indicates that the ions have diffused in their drift motion about the earth. For example, both 140 keV hydrogen peaks are observed on the inbound and outbound passes. Note again that the peak or centroid flux for hydrogen moves toward lower L with increasing energy while for helium it has a tendency to move to higher L with increasing energy. For March 24, 1991 storm the *Kp* reached 9-.

At the time of the sudden commencement CRRES was in the slot region at L~2.5 at about 03:00 UT. Immediately after the sudden commencement on the outbound pass (orbit 588) the 18 and 56 keV hydrogen, the 90 and 300 keV helium, and the 75 and 106 keV oxygen particle

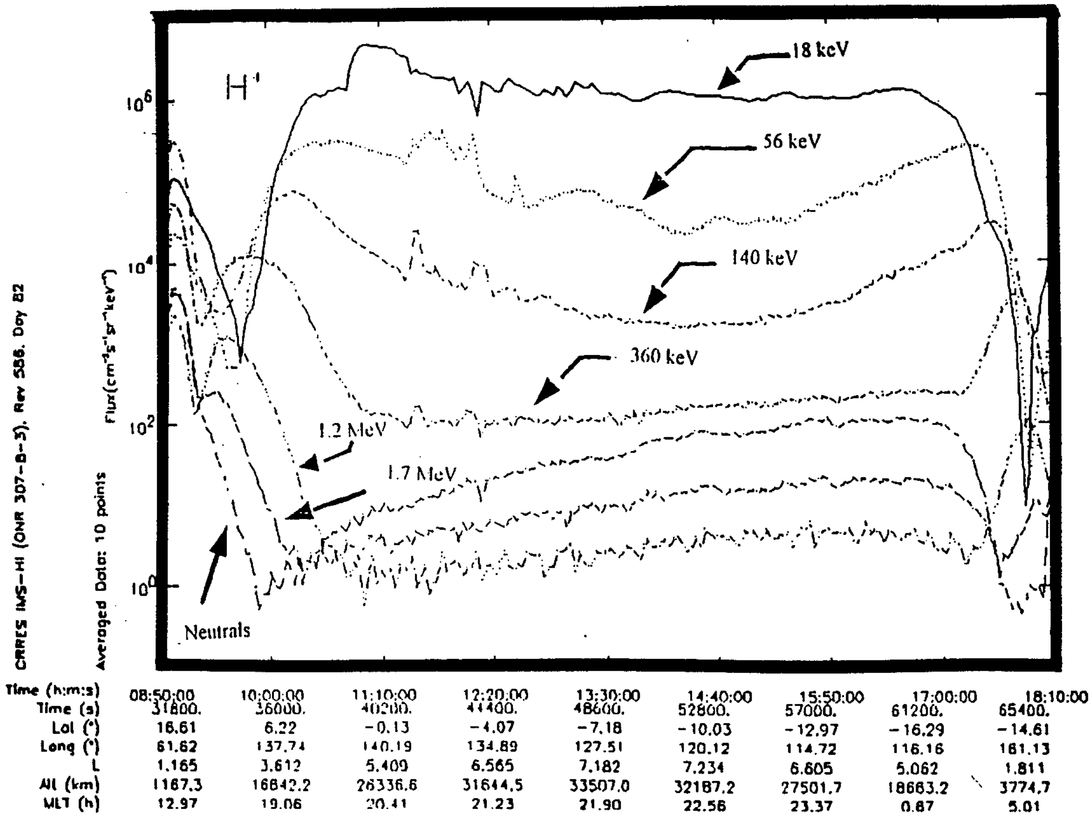

Figure 8a. Pre-storm proton flux measured with IMS-HI for orbit 586 on March 21, 1991.

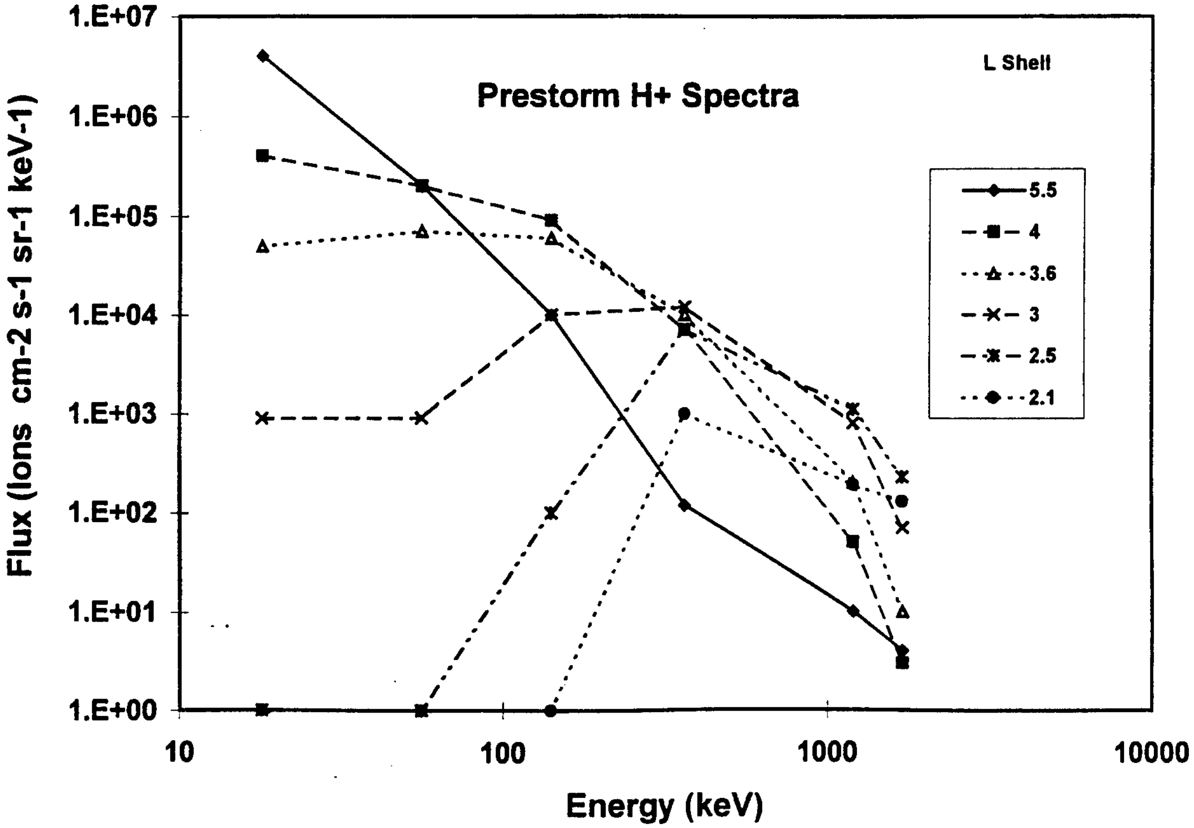

Figure 8b. Pre-storm proton spectrum variations of the ring current for six L-shells.

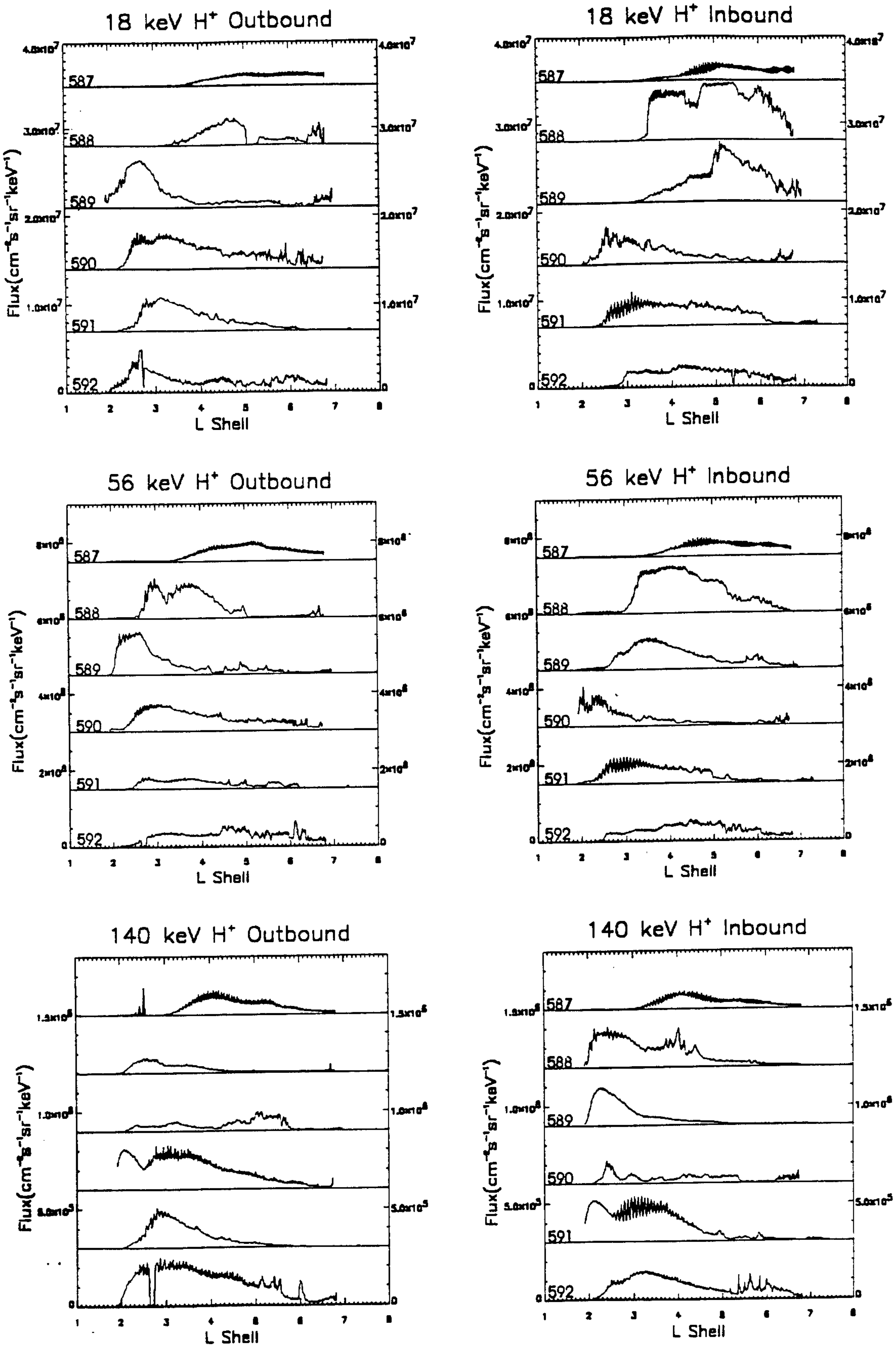

Figure 9a. Fluxes for $H^+$ of energy 18, 56, and 140 keV for orbits 587 to 592. Orbit 592 is shown on the lower panel of each figure. The other profiles are offset by a constant value to easy visualization.

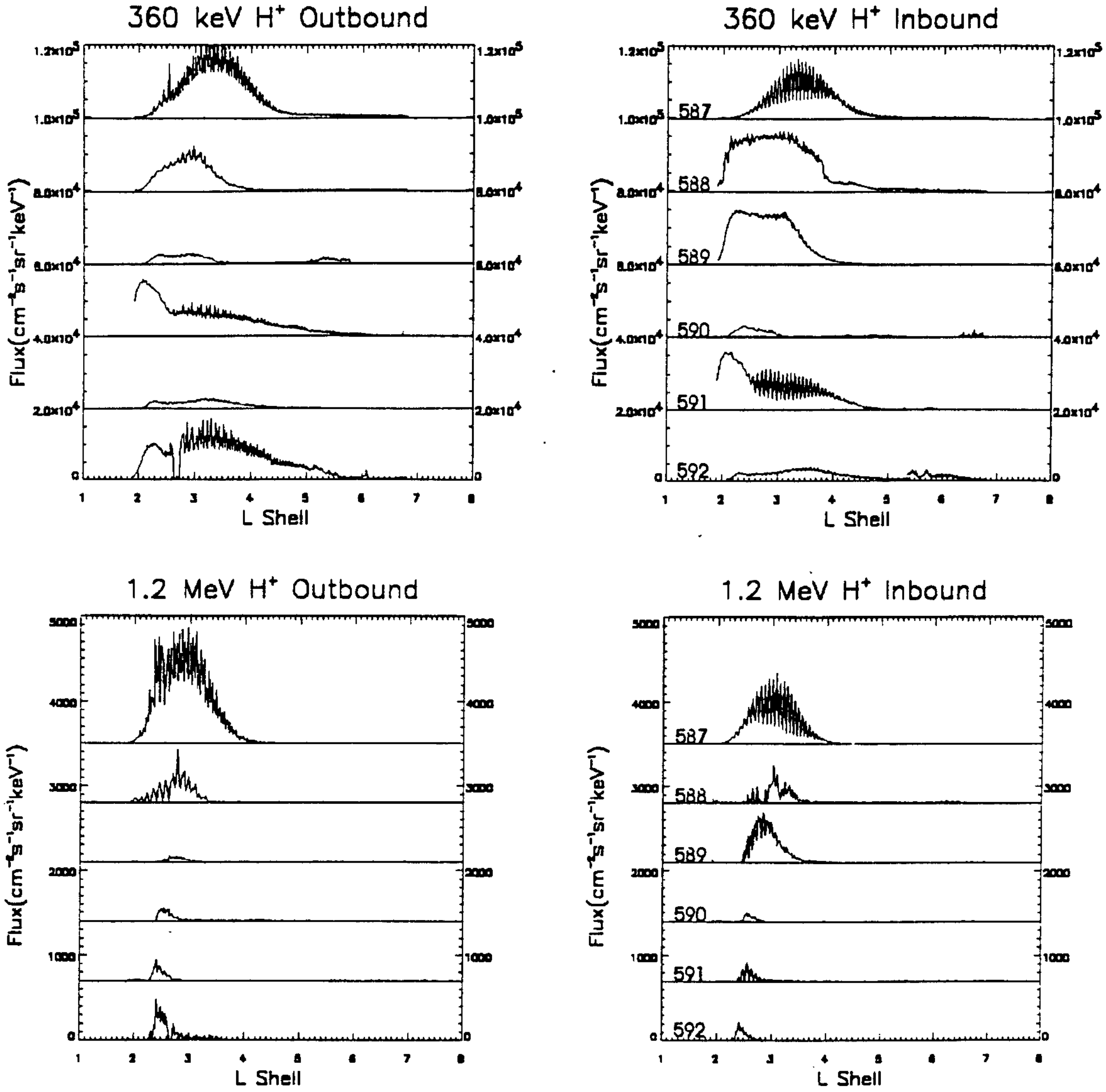

Figure 9b. Fluxes for $H^+$ of energy 360 and 1200 keV for orbits 587 to 592. Orbit 592 is shown on the lower panael of each figure. The other profiles are offset by a constant value to easy visualization..

flux increased by about a factor of two while the 1.2 MeV hydrogen flux decreased by over a factor of two. Only the 56 and 140 keV hydrogen, 90 and 300 keV, and 75 and 106 keV oxygen flux moved significantly inward by about 1.5 to 2 L-shell units while the 360 keV hydrogen flux moved inward by about 0.5 L-shell units. These observations are rather striking since the ring current($40<E<200$ keV) moved from an L shell of about 4 to 5 down to L shell between 2.5 and 3.5 in a period of less than about 3 hours. Hydrogen, helium, and oxygen with energy less than about 40 keV did not move inward significantly. During the main phase of the storm (orbits 588-590) the 18 keV flux moves back and forth and changes intensity. The inbound 588 orbit shows the build-up of hydrogen flux between L shells of 3.4 and 6.5. The outbound orbit 589 shows the deep penetration of the 18 keV ring current maximum to L=2.5 with little flux above L=4. The inbound orbit 589 shows that the ring current is back to higher L shells and peaks at L=5.5. The next orbit shows again that the peak of the 18 keV ring current moves inward to about L=3 and stays inward.

While past observations have revealed the general structure of the ion ring current region, the details of the inner edge are poorly understood because of the low sensitivity of ion composition measurements and because of the sensitivity of instruments to radiation belt backgrounds. The data collected by IMS-HI clearly show that the hydrogen, helium, and oxygen fluxes can abruptly drop-off by several orders in less than 0.5 L shell. The data suggest that strong loss processes, such as ion-cyclotron waves, other wave-particle interactions, and charge exchange, are active and can precipitate ions out of the lower ring current..

This study can be summarized by the following:

a. A sharp inner L-shell boundary can exist for protons, helium, and oxygen ions. This boundary is marked by a decrease in flux of greater than 3 orders of magnitude for $2<L<4$. The 18 keV boundary moves to within an L=1.6 on the noon side during the magnetic storm of March 25, 1991.

b. For quite pre-storm times the inner edge of the ring current differential flux is consistent with a double charge exchange loss process, while the outer edge is consistent with radial diffusion. The differential flux maximizes at L=5 for 56 keV, at L=4 for 140 keV, at L=3 for 360 keV, at L=2.5 for 1.2 MeV, and at L=2 for 1.7 MeV protons.

c. During the magnetic storm the proton, helium, and oxygen fluxes intensified and moved inward at different times. The storm was dominated by protons.

d. The measured energy content of the ring current was consistent with the Dessler-Park-Sckopke relation. The energy content of the ring current increased by a factor of 15 in the energy range 10 to 400 keV.

*CRRES - UARS Instrument Comparison*

The opportunity to compare measurements of the high-energy particle spectrometers on CRRES and the NASA Upper Atmosphere Research Satellite (UARS) [Reber, 1993] was available for data collected from October 1, 1991, when the High Energy Particle Spectrometer

(HEPS) instrument, a part of the Particle Environment Monitor (PEM) [Winningham et al., 1993] on UARS was activated, until October 12, 1991 when CRRES failed.

The SEP (ONR 307-3) instrument on CRRES and the HEPS instrument on UARS shared a common heritage having been designed and built by the Space Sciences Laboratory of Lockheed Martin. There were major differences in the instruments, however, including geometric factors and the methods of data accumulation. It is of interest, therefore, to compare spectral measurements from the two spectrometers at times when the spacecraft were in close conjunction.

Since the orbits of the spacecraft were very different, comparisons of spectral measurements involve transforming pitch angles from one spacecraft to the other, as well as finding the time(s) of closest conjunction as a function of geomagnetic coordinates and magnetic local time. To obtain the times (UT) of conjunctions, coordinates (latitude, longitude and altitude) from both CRRES and UARS were used to calculate the magnetic field intensity, B, and the magnetic L-shell parameter utilizing the same code [Olson and Pfitzer, 1974]. Data for comparison were taken from the times corresponding to the nearest L-shell values with the smallest time differences. The results from a previous calculation of the conjunctions between CRRES and UARS were used to select the most likely cases for this study.

The particle telescope instruments from both spacecraft covered the same nominal energy ranges of 0.04 to 5 MeV for electrons and 1 to > 100 MeV for protons using silicon solid-state detectors. Because the orbit of CRRES went to high altitudes, the geometric factors of the SEP sensors were much smaller than those of the four heads of HEPS ($3 \times 10^{-3}$ $cm^2$-sr versus 0.54 $cm^2$-sr, respectively). Signal processing was also significantly different in the two instruments. SEP analyzed one energy range of electrons or protons at a time for 32 seconds, which is approximately one spin of the spacecraft. HEPS simultaneously collected all incident particles over the entire energy range from four separate detector systems, each viewing with non-overlapping 30° fields-of-view in the upward hemisphere centered at -15°, +15°, 45°, and 90° with respect to the zenith direction.

Conjunctions between CRRES and UARS were selected from the first two days of the overlap period, October 1 - 2, 1991. The superposed spectra (shown in Figure 10) for the first conjunction on October 1 at a high L-shell value (L ~ 6.6) are similar in shape, but more than one order of magnitude different in absolute flux. This may be due to the pitch-angle sampling of SEP, which sweeps four degrees during the 0.75 second data accumulation period, and it may include HEPS electrons from pitch angles that mirror above UARS and have higher intensities. The high-energy fluxes greater than 0.5 MeV are probably due in part to cosmic rays that penetrate into the energy loss detector of the telescope and are not eliminated by the anticoincidence system. Proton spectra were also compared, but are not shown because HEPS appears to observe solar protons, while CRRES, not having crossed the magnetopause, is measuring locally trapped proton fluxes.

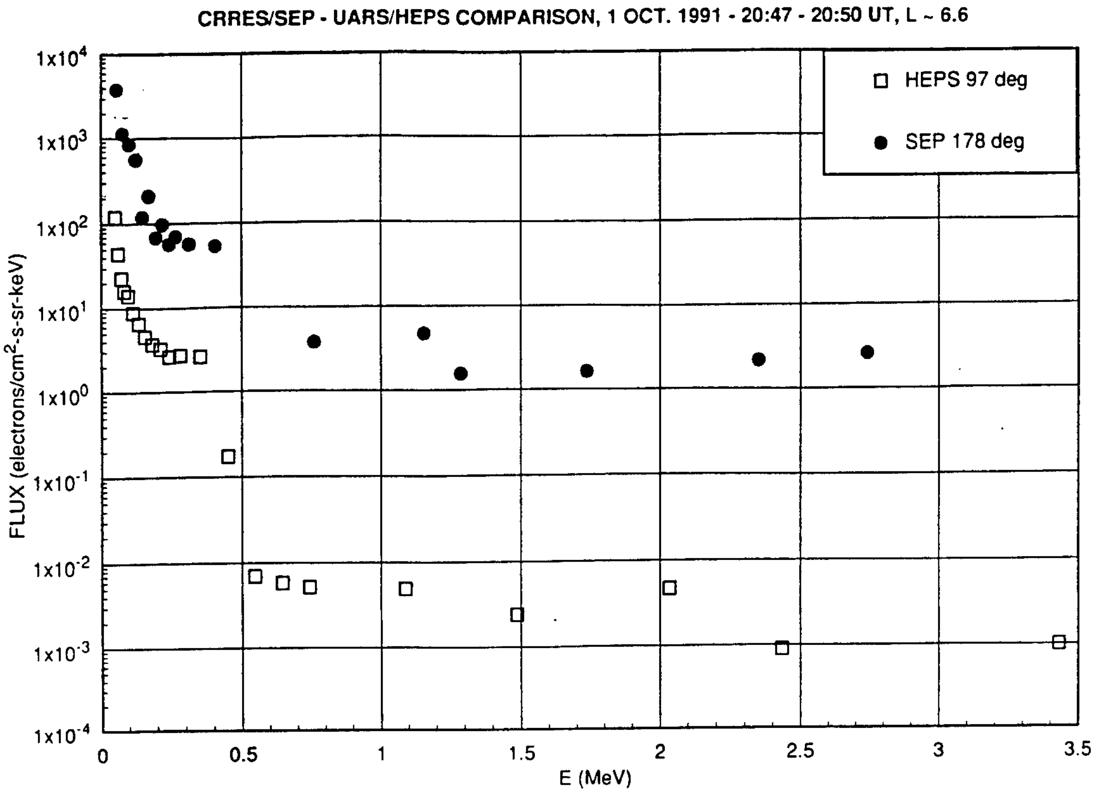

Figure 10. Superposed SEP and HEPS electron spectra from the conjunction of CRRES and UARS at 20:47 - 20:50 UT and L ~ 6.6 on October 1, 1991.

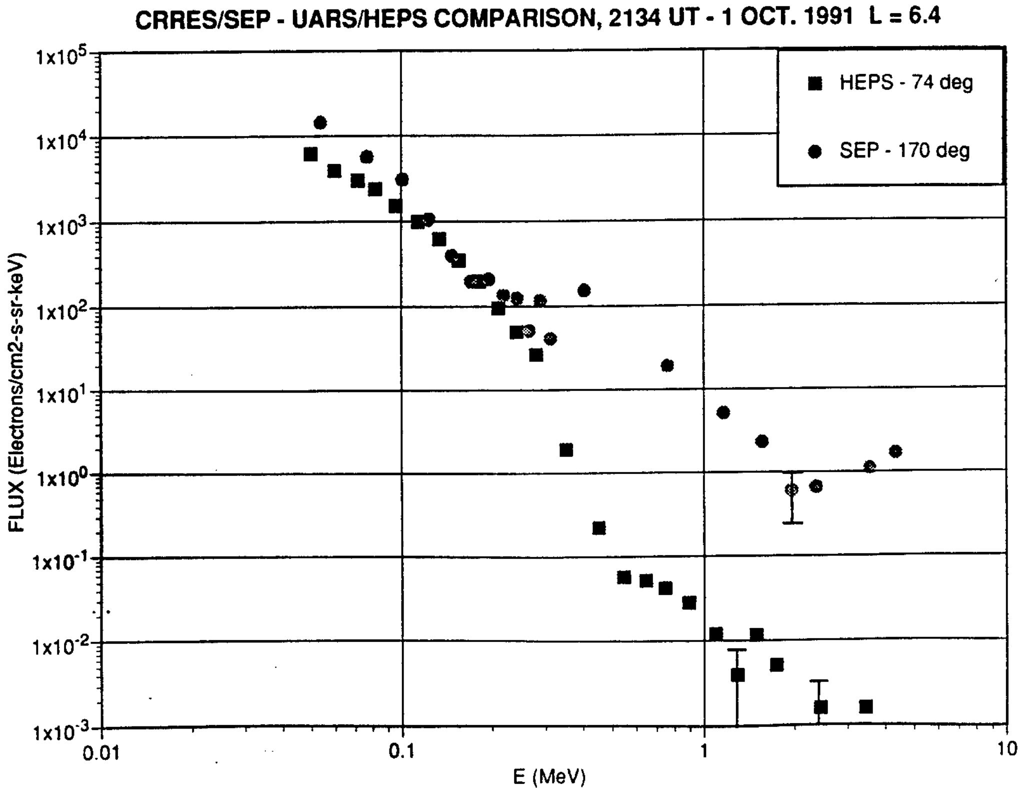

Figure 11. Superposed SEP and HEPS electron spectra at 21:34 UT and L = 6.4 on October 1, 1991.

Another time period was chosen on October 1 at 21:34 UT when the spacecraft were not in conjunction but were at high L shells, such that UARS observed solar particles outside the magnetosphere. CRRES did not cross the magnetopause, however, so spectral comparison was made near the trapping boundary even though the magnetic local time was different at the two spacecraft. As can be seen in Figure 11 the electron spectra at this time were very similar at energies below ~ 300 keV, but this may be fortuitous given the flux differences exhibited in the conjunctions. The noticeably high flux at 0.4 MeV in the SEP data is probably due to bremsstrahlung, which can occur in the lowest channel of the energy loss detector. Differences at higher energies may again be due to cosmic rays in SEP.

The second conjunction, shown in Figure 12, occurred on October 2 in the inner radiation belt at L=1.39. Plotted is the net flux in the pitch-angle range of 44° to 48° with the flux at 4° to 8° subtracted as background. The high-energy electrons from SEP are not plotted because the spectrum at 4° to 8° is higher in intensity than at 90°, indicating that the response is due to penetrating protons that overwhelm the electron fluxes. A pitch angle of 48° at the CRRES location transforms to 90° at UARS. SEP spectra for two pitch angles are plotted to show the variation that occurs with pitch angle. Magnetic local times at the two spacecraft differed by about two hours. Proton fluxes can be seen in Figure 13 from the two spins of CRRES following the electron data at 12:14 UT and from the coordinated HEPS data. The differences seen in the 1 to 5 MeV range may be due to the HEPS data not being corrected for high intensity electron effects. The spectra do agree fairly well in the 5 to 20 MeV range. Above ~ 25 MeV the expected fall off of the SEP protons can be seen due to the high threshold setting in the SEP dE/dx detectors.

The electron spectra from both high and low L-shell regions showed good agrement in shape and variable closeness in absolute flux levels. Some of the differences are likely to be due to uncertainties in matching pitch angles transformed from the higher-altitude spacecraft to the position of the low-altitude UARS and/or possible inaccuracies in the calculation of pitch angles at CRRES. The proton spectral comparison in the anomaly region (Figure 13) exhibited good agreement in both spectral shape and flux intensity over the higher-energy range of 5 to 20 MeV, for which both instruments should have the best response characteristics. With a suitable correction for the electron effects, the HEPS spectra in the 1 to 5 MeV energy range would probably move closer to that of SEP.

### *Testing of the Rice Magnetospheric Specification and Forecast Model*

Ion data from the IMS-LO payload have been provided to support the extensive testing of the Rice Magnetospheric Specification and Forecast Model. The Rice University model is designed to be an operational model of electron and ion fluxes at energies of 100eV to 100 keV and at radial distances from 2 to 10 earth radii. IMS-LO $H^+$ and $O^+$ ions at several energies were used for comparisons with the model for 4 magnetic storm periods in 1990 and 1991. Results for the

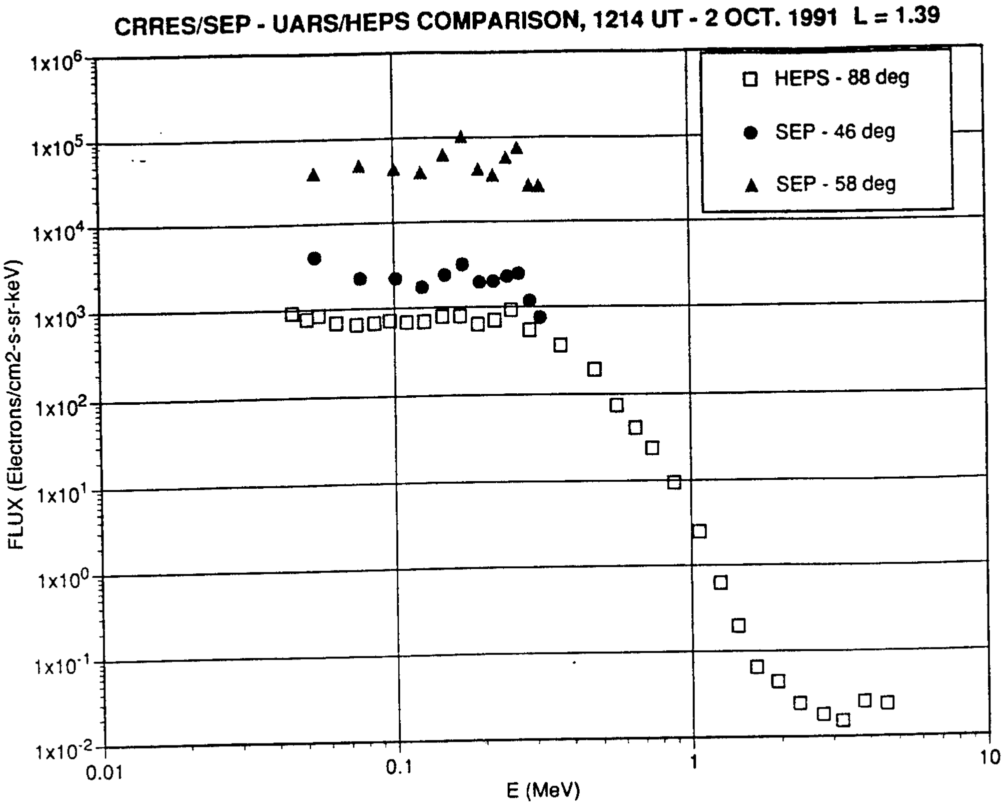

Figure 12. Superposed SEP and HEPS electron spectra from the conjunction of CRRES and UARS at 12:14 UT and L = 1.39 on October 2, 1991.

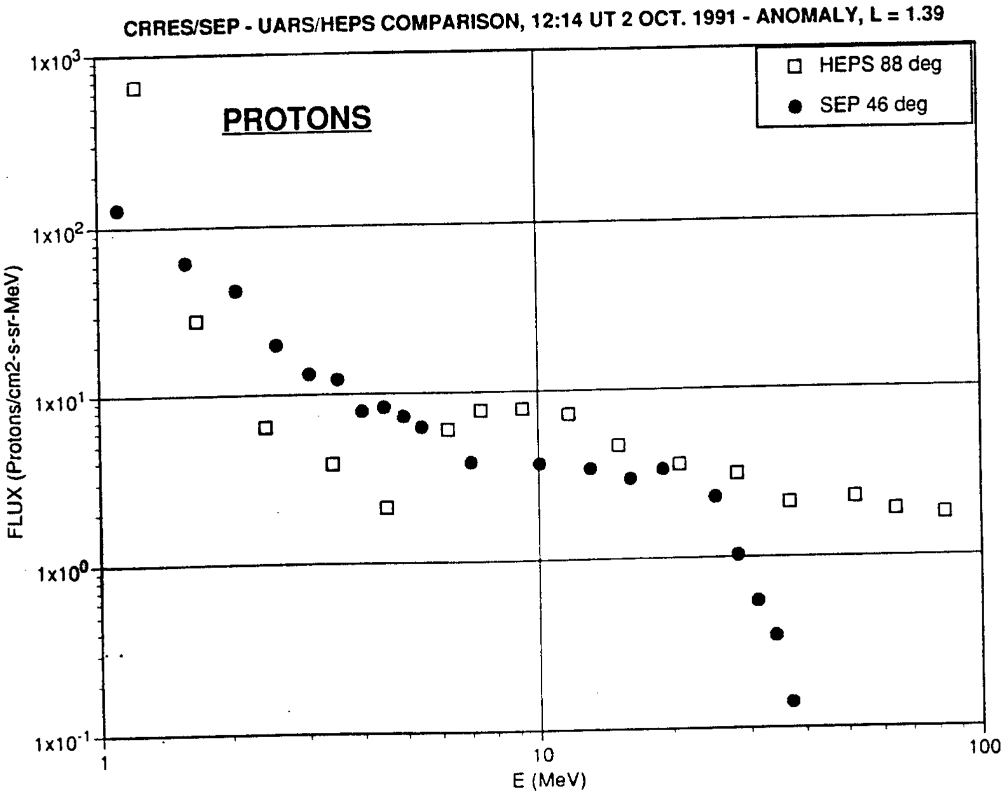

Figure 13. Superposed SEP and HEPS proton spectra from the conjunction of CRRES and UARS in the anomaly region at 12:14 UT and L = 1.39 on October 2, 1991.

testing were presented at the spring 1994 meeting of the American Geophysical Union by Lambour et al. The abstract for the paper appears in Appendix B.

## Dynamic Event Studies

The ONR-307 data set is well suited to the study of very dynamic processes that are responsible for the energization and transport of magnetospheric plasma and particle populations. By their nature, many of these processes are impulsive. In order to understand better the key physical processes we have used the summary data to identify events in which the satellite and instrumentation were well positioned to record these transient phenomena. Within the CRRES database we have identified a number of very interesting events for further analysis. Some of them are summarized below.

### *Observations and Analysis of Long-Term Ion Pitch-Angle Asymmetries near the Equator*

Significant measurements were obtained with the IMS-LO instruments that imply the action of new dynamical processes in the magnetosphere during magnetic storms. Such measurements have not previously been reported in the literature. This study makes use of the IMS-LO directional fluxes of $H^+$, $He^+$, and $O^+$ ions from 0.11 to 35 keV over nearly the entire pitch-angle range, $0° \leq \alpha \leq 180°$. During sixteen magnetic storms, highly asymmetric pitch-angle distributions of these ions — especially $O^+$ ions — were measured at L shells > 4. Although the magnitude of the asymmetry and the energies of the affected ions varied with time, the sense of the ion flow, implied by the Asymmetric Pitch-Angle DistributionS (APADS), remained the same for periods much longer than the ion bounce times. These distributions have been referred to as "clipped wing butterfly" distributions in our previous reports.

To make sure these unusual measurements were not due to a flaw in the instrument or the electronics, we examined data obtained with a similar instrument— the Hot Plasma Composition Experiment (HPCE) [Shelley et al., 1985] on the AMPTE/CCE satellite. Indeed, we found an event of APADS under similarly disturbed conditions.

Normally during disturbed times the pitch-angle distributions of $O^+$ ions of energy less than about 6 keV are cigar shaped; i.e., the directional flux has a minimum value at the pitch angle $\alpha = 90°$ and it steadily increases symmetrically toward lower and higher pitch angles. However, during these unusual events, the pitch-angle distributions of these ions were highly asymmetric about 90: the directional flux increased monotonically from one end of the pitch-angle range to the other (from 0° to 180° or from 180° to 0°).

One event, for which solar-wind data (plasma and magnetic-field measurements) from the IMP 8 satellite were available, was analyzed in detail. This event occurred during the magnetic storm of 26 August 1990. The $O^+$ APADS were observed from about 13:00 to 15:59 UT, while the CRRES satellite moved through L-shell values from 4.6 to 6.8, magnetic local times from 04:31 to 06:37, and magnetic latitudes from 9.3° to 16.3° along its outgoing leg. Twenty-six minute averages of the ion pitch-angle distributions (directional flux vs. pitch angle) at various energies are shown in panels a–f of Figure 14. The L-shell values and times over which the distributions were averaged are given in the panels. Note that the magnitude of the asymmetry of the distributions at a given energy, as well as the energy range of the APADS, were variable in time, yet the sense of the asymmetry remained the same during this entire period.

Toward lower ion masses, the pitch-angle asymmetry decreased rapidly. The asymmetry of the $He^+$ ions was much smaller than that of the $O^+$ ions at the same energies, and the asymmetry of the $H^+$ ions was so small that it was not easily perceptible. At energies less than about 4.9 keV, the directional flux of the $H^+$ ions was nearly constant over the entire pitch-angle range of the measurements. However, the $H^+$ energy spectrum became harder, and the integrated flux decreased, as the maximum energy of the $O^+$ APADS increased.

The behavior of the electrons also changed appreciably when the $O^+$ APADS appeared. Prior to 1300 UT, the electron pitch-angle distributions that were measured with the IMS-LO instrument (67 eV to 20 keV) were "rounded" in a manner typical of trapped particles, with maximums at $\alpha = 90°$. Afterward, the distributions of electrons with energies between 1.7 to 20 keV suddenly became flat over the pitch-angle range of the measurements (0° to 135°), and remained flat until they again became "rounded" near 16:00 UT. During the same time period, electrons of energy less than about 1.7 keV developed "winged" distributions (cigar shapes), in which the directional flux increased rapidly from 90° to 0° and from 90° to the limit (135°) of the observations. Moreover, the 0°-flux relative to the 90°-flux increased rapidly toward lower energies. The energy spectrum of the electrons also became harder during this time period.

The events in which the $O^+$ ions were asymmetric for periods greater than 2 hours, and the conditions under which they were observed, are listed in Tables 2 and 3. Note in the 3rd column of Table 2 that the APADS observed on July 13 (Orbit 856) persisted for 4 hours. Comparison of columns 4 and 6 shows that the ion flows were antiparallel to the magnetic field $\boldsymbol{B}$ in the dawn sector and parallel to $\boldsymbol{B}$ in the dusk sector. Column 5 shows that these APADS were observed at L-shell values higher than 4.6. Note from Table 3 that the dipole-tilt angles (the complement of the angle between the Earth's magnetic dipole and the solar-wind velocity) were large and that the extreme solar-wind parameters and *Kp* and *D*st indices imply highly disturbed magnetospheric conditions. Moreover, the solar 10.7 cm flux was high, implying a high photoionization rate of the sunlit polar atmosphere. All 17 of the events were observed in the dawn or dusk sectors during similar conditions. The dawn and dusk ion-flow directions of the 16 events observed with CRRES were the same as those shown in Table 2, but the ion-flow direction of the event observed near dawn with AMPTE/CCE was in the opposite direction ($\hat{\boldsymbol{B}}$).

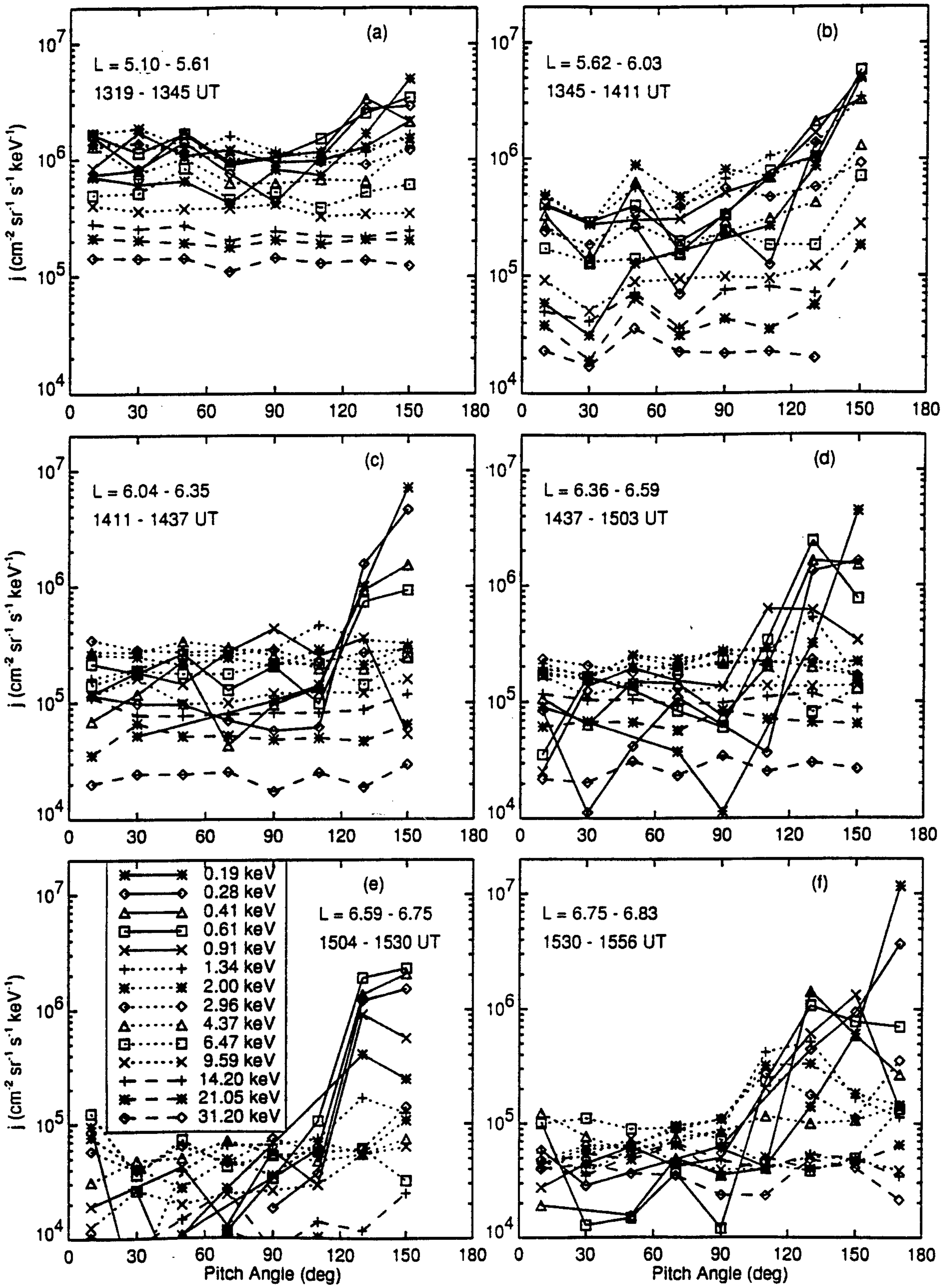

Figure 14. Measurements of the pitch-angle distributions of $O^+$ ions made on the CRRES satellite on August 26, 1990. The L-shell value and time intervals of the measurements are given in the panels.

Table 2. Observations of Asymmetric Pitch-Angle Distributions of duration exceeding 2 hours

| CRRES Orbit | Date | Time (UT) | Ion-Flow Direction along Field | L Value | Magnetic Local Time (hr) |
|---|---|---|---|---|---|
| 50 | 8/15/90 | 1130 to 1400 | $-\hat{B}$ | 5.4 to 7.2 | 6.7 to 7.2 |
| 77 | 8/26/90 | 1300 to 1600 | $-\hat{B}$ | 4.6 to 6.2 | 4.6 to 6.8 |
| 766 | 6/5/91 | 0400 to 0740 | $+\hat{B}$ | 5.7 to 7.3 | 17.4 to 19.5 |
| 767 | 6/5/91 | 1445 to 1820 | $+\hat{B}$ | 6.7 to 7.0 | 18.2 to 20.2 |
| 846 | 7/9/91 | 0800 to 1020 | $+\hat{B}$ | 5.2 to 7.8 | 18.2 to 19.9 |
| 856 | 7/13/91 | 1100 to 1500 | $+\hat{B}$ | 6.2 to 7.6 | 15.5 to 18.1 |
| 858 | 7/14/91 | 0800 to 1100 | $+\hat{B}$ | 7.0 to 8.1 | 15.9 to 17.8 |

Table 3. Conditions at Times of Events

| CRRES Orbit | Dipole-Tilt Angle | Solar Wind Conditions | | Kp | *D*st(nT) | Solar 10.7 cm Flux |
|---|---|---|---|---|---|---|
| | | Den. (cm$^{-3}$) | Vel.(km/s) | | | |
| 50 | 16.72° to 21.98° | 6 | 580 | > 4.7 | –50 | 155.9 |
| 77 | 16.29° to 20.86° | 12 | 740 | > 6 | –100 | 285.1 |
| 766 | 11.78° to 14.57° | 34 | 600 | 7.3 | –120 | 258.1 |
| 767 | 32.20° to 32.31° | 30 | 560 | 8.7 | –180 | 258.1 |
| 846 | 14.93° to 20.64° | 2 | 700 | > 7 | –150 | 200.6 |
| 856 | 21.96° to 31.38° | No Data | | > 8 | –170 | 202.3 |
| 858 | 14.25° to 21.82° | No Data | | > 6 | –120 | 194.8 |

Our analysis indicates this asymmetry was caused by a parallel electric field, $\boldsymbol{E}_{//}$, that extended from one hemisphere to the other and generally increased with time. Because ions are accelerated by such a field toward the equator in one of the hemispheres, the directional flux, $j(w,\alpha)$, of the ions, which increases as the ion energy increases, is the highest at the equator in the direction of $\boldsymbol{E}_{//}$. In the other hemisphere, ions are either (1) lost (precipitated in the atmosphere because of their continued acceleration by $\boldsymbol{E}_{//}$), (2) stored (trapped by the opposing electric and magnetic forces), or (3) returned to the equator with lower energies, hence with lower directional fluxes if $\boldsymbol{E}_{//}$ increases with time.

Additional processes can accelerate particles along the magnetic field direction, such as the centrifugal force arising from the $\boldsymbol{E} \times \boldsymbol{B}$ drift [Cladis, 1986; Horwitz, 1987; Delcourt et al., 1990], the ponderomotive force [e. g., Li and Temerin, 1993], and Fermi acceleration. Moreover, if trapped particles drift onto distended field lines, their equatorial parallel velocities increase adiabatically as discussed by Tsyganenko [1989]. However, these processes alone would not cause a long-term asymmetry of the ion pitch-angle distribution because they would increase $v_{//}$ by nearly the same magnitude in both directions, $\hat{\boldsymbol{B}}$ and $-\hat{\boldsymbol{B}}$, near the equator.

Our detailed analysis of the event of August 26, 1990 is described in the paper entitled, "Observations of Long-Term Field-Aligned Flow of $O^+$ Ions near Equator during Summer and Winter", by J. B. Cladis and H. L. Collin [1994], a preprint of which is in Appendix B. This paper has been submitted to the Journal of Geophysical Review for publication. According to this analysis the electric field was induced by the time-varying external currents (magnetopause, magnetotail, and Birkeland currents) during times when the dipole-tilt angle was appreciably greater than, or less than, zero. A symmetrical ring current does not induce such a field. Moreover, Birkeland currents do not produce a net flux through areas enclosed by field lines when the currents are symmetrical about the equator. They do so only when the dipole is tilted because, then they are stronger in the summer hemisphere than in the winter hemisphere [Fujii et al., 1981]. Because of this Birkeland-current asymmetry, a net magnetic flux, westward on the dawn side – and eastward on the dusk side – of the inner magnetosphere, is enclosed by geomagnetic field lines. Hence, when the dipole-tilt angle is positive (northern summer), increasing Birkeland currents induce electric fields that are directed along $-\hat{\boldsymbol{B}}$ in the dawn sector and along $\hat{\boldsymbol{B}}$ in the dusk sector. These directions are consistent with the ion-flow directions of the 16 events observed on CRRES, which were all observed during northern summer. During northern winter, the directions of the fields induced by increasing Birkeland currents are in the opposite direction; and this result is consistent with the direction of the ions observed during northern winter with the AMPTE/CCE satellite. When the magnetopause and magnetotail currents decrease, as implied by the decreasing solar-wind pressure during the August event, the magnetic flux through the inclined (to $Z_{GSM}$) areas bounded by near dawn and dusk geomagnetic field lines increases, generally along the $Z_{GSM}$ direction. The parallel electric fields induced by this flux change are in the same directions in the dawn and dusk sectors during northern summer and winter as those produced by increasing Birkeland currents.

The magnetopause currents produce flux through these inclined areas that is in the opposite direction to that produced by the tail current. However, while the standoff distance is increasing, as it was during this event, the net change in the flux produced by the magnetopause currents through the dawn and dusk magnetic loops is less than that produced by the magnetotail currents.

Our estimate of the EMF produced by the growth of the Birkeland currents, based on the time variations of these currents inferred from the onboard magnetometer and interplanetary conditions, was found to be appropriate to account for the asymmetry of the ions. By using Tsyganenko's 1989 model [Tsyganenko, 1989], with his activity parameter, IKP, set to 8 and 1, respectively, the flux change produced by the magnetopause and magnetotail currents through the areas enclosed by the field lines was estimated for a jump of the standoff distance from its minimum to its maximum values allowed by the field model. This flux change was found to be about an order of magnitude lower than that produced by the full range of the Birkeland currents. Nevertheless, the tail current is regarded to be an important source of the electric field because the disturbance of the magnetic field during this storm was far beyond the range covered by Tsyganenko's model.

The essential features of the $O^+$ APADS were reproduced with a computer-simulation program that simulated the motion of initially-trapped ions in the presence of a parallel electric field. An increasing electric field, except for periods of about half the ion bounce time, was found necessary to account for the persistency of the ion flow direction. Although the APADS shown in Figure 14 imply time variations of the magnitude of the electric field, the ion flow remained in the same direction for about 3 hours. Therefore, the flux linkages connecting the Birkeland currents with those at lower latitudes must have increased faster than linearly during the event. Indeed, the onboard magnetometer suggests that the portion of the total magnetic field ascribed to the external currents (the part beyond the modeled field) generally increased faster than linearly during the period of the $O^+$ APADS (13:19 UT–15:56 UT).

The pitch-angle asymmetries of the $He^+$ and $H^+$ ions, which were measured in the same energy/charge range as the $O^+$ ions, were progressively less pronounced than those of $O^+$ because their velocities were progressively higher.

The computer-simulation results reveal that the asymmetric pitch-angle distributions observed near the equator with the CRRES and AMPTE/CCE satellites were caused by parallel electric fields that generally increased with time and extended from one hemisphere to the other. According to the detailed analysis of the event observed on August 26, 1990, the electric field was induced by increasing Birkeland currents, which are stronger in the summer hemisphere than in the winter hemisphere, and by the decreasing tail current implied by the decreasing solar-wind pressure. Since the directions of this electric field in the dawn and dusk sectors, during northern summer and winter, are consistent with the directions of all the observed inter-hemispheric ion flows, one or both of these current sources may have been responsible for all these events. The absence of flows in the opposite directions may imply that the time variations of decaying Birkeland currents and increasing tail currents are not sufficient to produce appreciable electric fields.

*Analysis of Further Obervations of Asymmetric Ion Pitch-Angle Distributions*

After the paper on the event observed on August 26, 1990 was submitted, analysis was continued on additional APADS events listed in Tables 2 and 3. Unfortunately, interplanetary data were not available for the events observed on July 13-14, 1991 and incomplete data were available for the June 5 event. The interplanetary data for the other events are presented below.

The $O^+$ APADS were observed from 1130 UT to 1400 UT on August 15, 1990. The IMP 8 measurements of the number density and speed of the solar wind, and the magnetic field components ($B_x$, $B_y$, and $B_z$) and total IMF, $B_T$, from 0 to 16 hours UT on that day, are shown in Figures 15 and 16, respectively. Based on these data, the time variations of the Birkeland current density were estimated from the work of Iijima and Potemra [1982]. These authors used a linear least-squares technique to correlate a variety of interplanetary quantities, involving hourly values of solar wind density, speed, and IMF components, with the Triad satellite measurements of the region 1 Birkeland-current densities. They also computed the "best" straight-line fit of the current densities to these interplanetary quantities. On the dawn side of the magnetosphere, they found the highest correlation (0.66) for the relationship,

$$J = 0.0328\xi + 1.4\ \mu A / m^2 \tag{1}$$

where

$$\xi = [N^{1/2} V (B_y{}^2 + B_z{}^2)^{1/2} \sin(\theta / 2)]^{1/2} \tag{2}$$

Here, $N$ (cm$^{-3}$) and $V$ (km/s) are the solar-wind density and speed, and $\theta$ is the angle between the $z$ axis and the transverse component $(B_y{}^2 + B_z{}^2)^{1/2}$ (nT) of the IMF (GSM coordinates). By using these equations, we computed the current density versus time shown in Figure 17. The APADS event occurred during the time interval between the vertical lines. Since this current density was decreasing during this interval, it appears that the electric field responsible for the APADS was not induced by the Birkeland currents.

The solar-wind pressure was very high, but it was fairly steady during this event. However, the $B_T$ vector rotated slowly to the south from 9 to 11.5 hours UT and away from the south from 11.5 to 14 hours. This rotation of the field is indicated in Figure 18, in which the total field $B_T$ (solid line) and the $-B_z$ component are drawn versus time. The negative value of the $B_z$ component is drawn so the magnitudes of these fields can be compared. It is clear that the total IMF was almost entirely southward at 11.5 hours. As discussed below, the electric field was

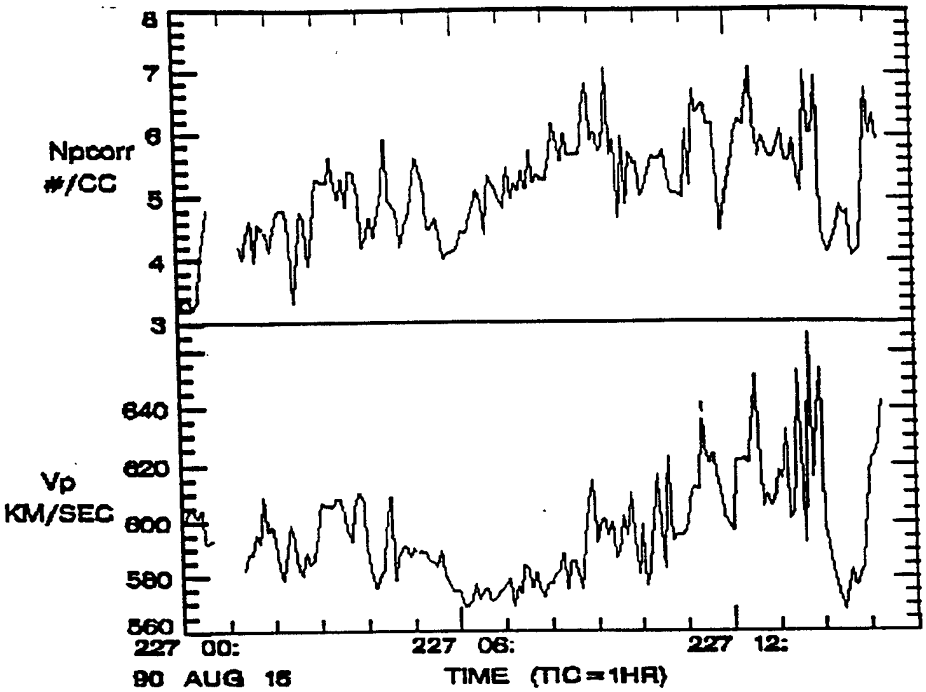

Figure 15. IMP 8 data on the number density and speed of the solar wind from 0 to 16 hours UT on August 15, 1990.

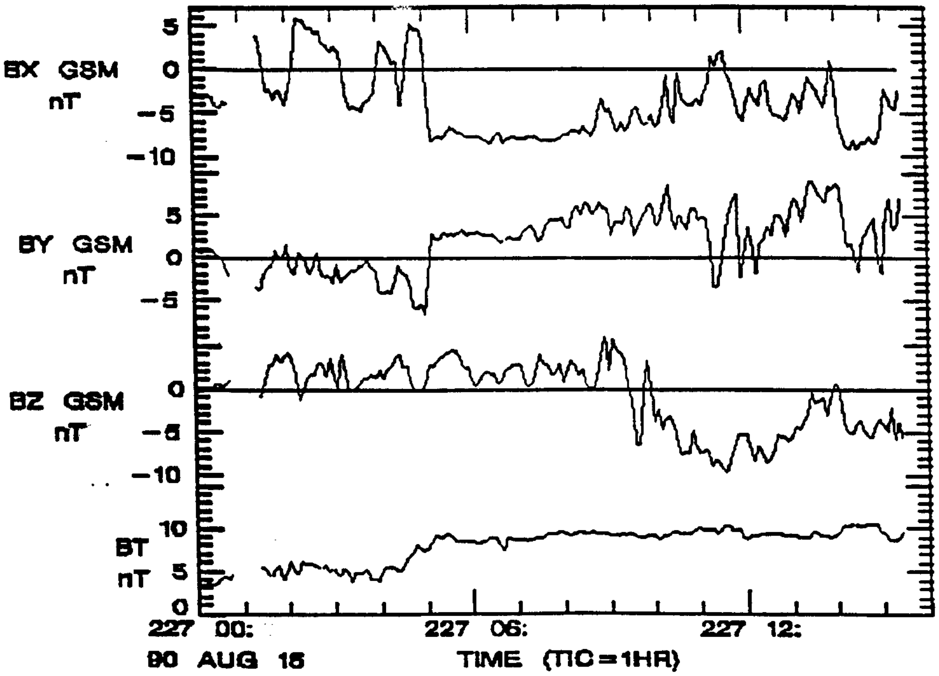

Figure 16. IMP 8 data on the interplanetary magnetic field components $B_x$, $B_y$, and $B_z$ and the total field, $B_T$, from 0 to 16 hours UT on August 15, 1990.

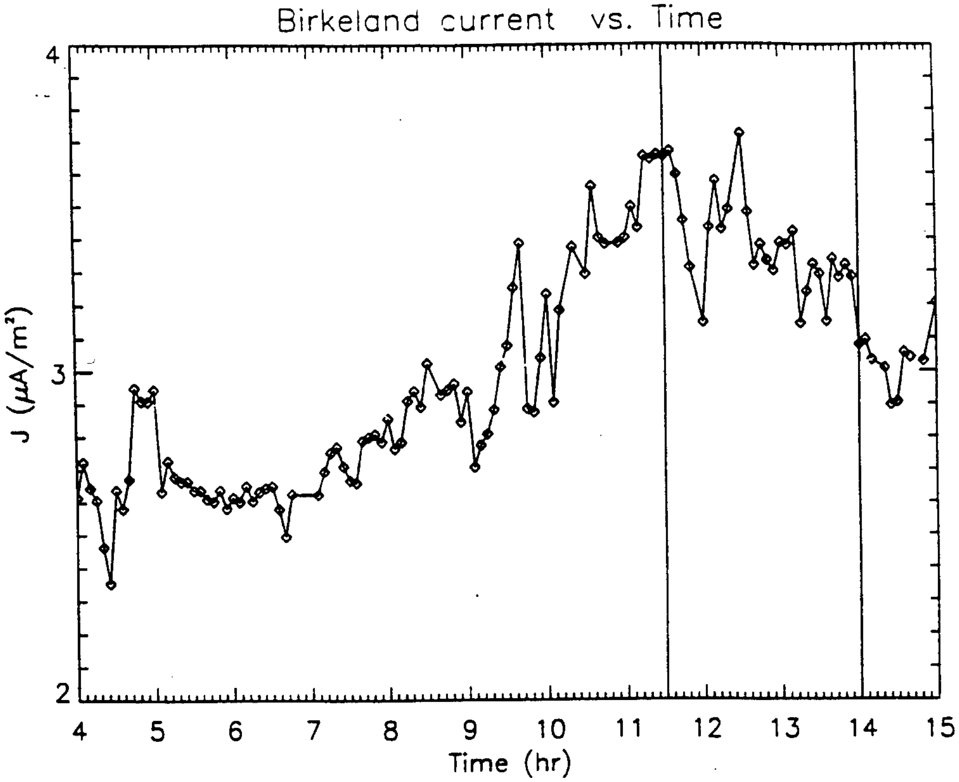

Figure 17. Current density of the Region 1 Birkeland current as implied by the solar-wind conditions (see Equations (1) and (2)).

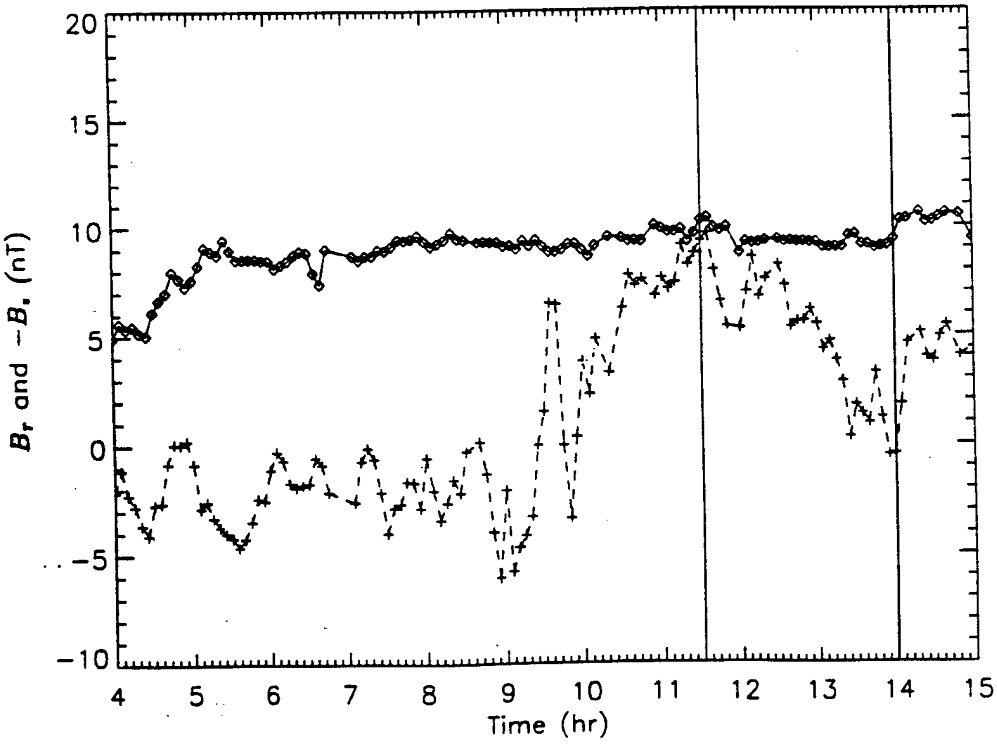

Figure 18. Total interplanetary magnetic field (solid line) and the negative value of $B_z$ the component (broken line) on August 15, 1990. The APADS occurred during the time interval between the vertical lines.

most likely induced by the response of the tail current to this rotation of the IMF. First, the interplanetary conditions during the other events will be described.

On June 5, 1991 the $O^+$ APADS were observed from 14:45 UT to 18:20 UT. The IMP 8 measurements of the magnetic field components ($B_x$, $B_y$, and $B_z$), the total IMF, $B_T$, and the solar-wind number density and speed were available from 10 to 18 hours UT on that day. The solar wind pressure was increasing steadily during this event. Moreover, the Birkeland currents were probably increasing because the Birkeland current density, which was computed using Equations (1) and (2), was increasing with time. All these data indicate that the electric field responsible for the APADS may have been induced by the increasing Birkeland currents. However, the $B_T$ vector again rotated toward the south prior to the event, from 13:25 to 14:45 UT; then it remained closely southward as $B_z$ slowly increased in magnitude. Therefore, these data indicate that the change in the tail field also contributed to the induced electric field.

An orbit earlier, on June 5 also, the $O^+$ APADS were observed from 08:00 UT to 10:20 UT. The IMP 8 measurements of the magnetic field components ($B_x$, $B_y$, and $B_z$) and the total IMF field were available during this event, but there were large gaps in the solar wind data. Only three data points were available, from 09:21UT to 10:32 UT. These data points indicate the solar-wind pressure was high (number density ≈ few protons per $cm^2$, and velocity ≈ 700 km/s), but steady. The $B_T$ vector quickly rotated southward just prior to 06:00 UT, and it remained closely southward until about 13:10. The close tracking of the magnitudes of $B_T$ and $B_z$ can be seen in Figure 19. After 06:25 UT, $B_z$ steadily increases until at least 16:20 UT. Note that while the APADS of the previous events occurred during the entire time that the IMF was southward and $B_z$ was increasing, the period, 08:00 UT to 10:20 UT, over which the APADS were identified in the CRRES data, lies well within the time over which $B_z$ was increasing, as shown in Figure 19. Because of this discrepancy, we reexamined the CRRES data and found that the data does not show the APADS were **not** present from 06:10 UT to 15:00 UT at sufficiently high L-shell values. The CRRES satellite was inbound during this time interval. Prior to 08:00 UT, the APADS could not be identified because of the limited pitch-angle coverage; and after 10:20 UT, the satellite moved to L-shell values lower than 5, where the induced electric field is small.

All these APADS occurred, as shown above, after the IMF turned southward and while $B_z$ was increasing with time. These conditions indicate the electric field responsible for the APADS was more likely induced by changes of the magnetotail neutral-sheet current than the Birkeland currents. Field line merging at the dayside magnetopause is favored when the IMF is directed southward. Then, geomagnetic field lines are drawn tailward at a high rate, especially when the solar-wind speed is high. As a result the flaring angle of the tail field increases, which causes the pressure of the magnetic field against the neutral sheet to increase. The dawn-to-dusk tail current therefore increases, and the magnetic field produced by this current decreases the $(B_z)_{GSM}$ component in the inner magnetosphere. As the tail field tends to relax, reconnection increases and the field lines are convected sunward at an enhanced rate. Later, when the $B_z$ component of the IMF increases, the rate of field line merging decreases,and the end result is that the $(B_z)_{GSM}$

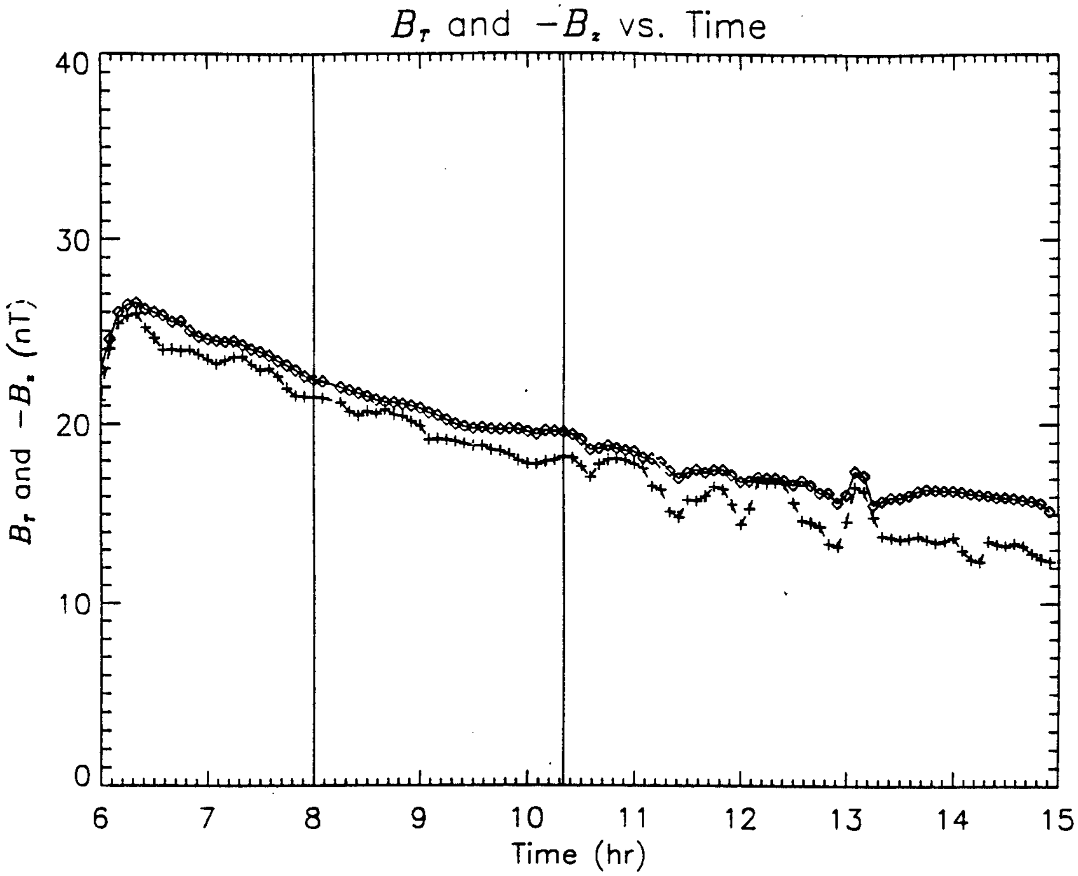

Figure 19. Total interplanetary magnetic field (solid line) and the negative value of $B_z$ the component (broken line) on July 9, 1991. The APADS were evident in the data during the time interval between the vertical lines; they probably began near 0600 UT, but could not be identified because of the limited pitch-angle coverage from 0600 to 0800 UT.

component due to the tail current increases. Hence, the resulting increase of the flux through the inclined "dipole-field lines" near dawn and dusk induces the electric field along those field lines in the proper direction to account for the APADS. It is not clear why APADS were not observed with asymmetries in the opposite direction while the $(B_z)_{GSM}$ component was decreasing due to the increasing tail current. Perhaps APADS were produced in the opposite direction, but were not observed. They may have been averaged out because the integration time necessary to obtain sufficient statistics was large (on the order of hours), or perhaps the pitch-angle coverage was not favorable.

The computer simulation program revealed that the parallel electric field must have been increasing in time to explain the duration of the APADS beyond their bounce times. It can easily be shown that such an increase in the induced electric field may occur, even if the $(B_z)_{GSM}$ component increases only linearly with time, because the area enclosed by the field lines on which the electric field appears also depends on $(B_z)_{GSM}$. As $(B_z)_{GSM}$ decreases/increases the equatorial crossing point of a field line moves outward/inward. At high L-shell values this displacement of the equatorial crossing points is appreciable. From Faraday's law of induction, the EMF (the integral of the electric field over the closed path bounding the area) is equal to $-\partial\Phi_m / \partial t$, and the magnetic flux $\Phi_m$ is equal to the integral of $(B_z)_{GSM}$ over the enclosed area projected in the plane perpendicular to the $Z_{GSM}$ axis. Therefore, the electric field increases in time when the partial time derivative of $(B_z)_{GSM}$ is constant because of the attendant time variation of the area.

Our investigations of these additional events support the findings of the paper on the APADS discussed in the previous section. However, these events indicate that the tail current may be more effective than the Birkeland currents in producing parallel electric fields on field lines in the dawn and dusk sectors. Moreover, in these events all the APADS began when the IMF was entirely southward and persisted while the $B_z$ component of the IMF was increasing.

## Conclusions

The data analysis and scientific research using the ONR-307 the ion, proton, and electron data sets have shown new and exciting results in all of the three key areas of investigation: particle precipitation and wave-particle interactions, radiation belt and ring current modeling, and dynamic event studies.

Our research utilizing the CRRES database has produced a number of first time observations. We have seen good correlation between precipitating particles and plasma waves in the outer radiation belt region, both observed by instrumentation on the same spacecraft, a first for spacecraft in this region. Mapping of the detailed structure of the ring current has been accomplished for the first time during a large magnetic storm. Another first was the observation of the asymmetric pitch-angle distributions (APADS) of $O^+$ ions, which lasted up to several hours during geomagnetic storms after the $B_z$ had turned southward and continued to increase in intensity.

Under the previous CRRES investigation for ONR (contract N00014-83-C-0476) we made the following important findings regarding particle precipitation and wave-particle interactions:

- Simultaneous wave-electron bursts occurred near the equator.
- The observations of wave-electron interactions occurred at energies as low as 1.7 keV and as high as 288 keV.
- It was found that the wave frequencies and precipitating electron energies were generally consistant with each other.

In the present study we found that the wave fields were often associated with narrow electron flux decreases. The conclusions of that work are summarized below:

- There is a general correlation between wave intensities and electron fluxes. Higher fluxes accompany higher wave intensities.
- The sudden, short electron dropouts usually, but not always, include both electrons and ions, as well as the thermal plasma.
- Hiss and chorus are usually enhanced near the boundaries of the particle dropouts or where particle gradients are large. However, similar wave enhancements are sometimes seen without particle dropouts. Presumably in those cases a flux gradient exists somewhat removed from the satellite, and the waves generated at the gradient propagate to the satellite location.
- On short time scales (<30 min) features in the wave and particle profiles are sometimes correlated, but frequently are independent. Again the localized nature of the particle characteristics compared to the more widespread wave fields may be responsible for the lack of detailed correlation.
- Because of the rapid loss of particles during dropouts, it is concluded that these dropouts cannot be caused by the mechanism of plasma waves scattering the particles into the

atmospheric loss cone. At the L-shell values considered the loss cone is so small that even with strong diffusion, a particle requires many bounces to enter the atmosphere through the loss cone.

Investigation of the ion composition data during the large magnetic storm of March 1991 revealed the detailed structure of the ring current, allowed mapping of the structure for the first time, and showed dynamic transport of the hydrogen, helium, and oxygen ions to lower L-shells.

As part of our dynamic event studies we have investigated ion pitch-angle distributions during geomagnetic storms. The findings are as follows:

- The CRRES observations of the long-term asymmetries of ion pitch-angle distributions near the equator are new. They have not been previously reported in the literature.
- They reveal important interactions of the solar wind and the magnetosphere, and they imply significant inter-hemispheric asymmetries and dynamics.
- A computer-simulation of the APADS reveals that the asymmetric pitch-angle distributions observed near the equator with the CRRES and AMPTE/CCE satellites were caused by parallel electric fields that generally increase with time and extend from one hemisphere to the other.
- A detailed analysis of the event observed on August 26, 1990 reveals that the electric field was induced by increasing Birkeland currents, which are stronger in the summer hemisphere than in the winter hemisphere, and by the decreasing tail current implied by the decreasing solar-wind pressure. Since the directions of these electric fields in the dawn and dusk sectors, during northern summer and winter, are consistent with the directions of all the observed inter-hemispheric ion flows, one or both of these current sources may have been responsible for all these events.
- The absence of flows in the opposite directions may imply that the time variations of decaying Birkeland currents and increasing tail currents are not sufficient to produce appreciable electric fields.
- The electric fields, through the asymmetric precipitation of ions and electrons in the northern and southern hemispheres and the trapping of ions between magnetic and electric mirrors in one of the hemispheres, may also produce differences in inter-hemispherical high-latitude phenomena, such as ionospheric convection and auroras.
- Our investigations of the additional events may also indicate that the tail current may be more effective than the Birkeland currents in producing parallel electric fields on field lines in the dawn and dusk sectors. Moreover, all the APADS began when the IMF was entirely southward and persisted while the $B_z$ component of the IMF was increasing.

The CRRES ONR-307 database is rich in examples of particle precipitation, wave-particle interactions, and geomagnetic storms that have a dynamic effect on the radiation belt and ring current regions. The CRRES program has made this invaluable data set of complicated observations available. As each analysis is performed, potential new studies appear.

The variety of wave-particle phenomena illustrated in Figure 6 for just two orbits, such as the exchange of hiss for chorus at the plasmapause and the variations of chorus frequency with L, suggest that this data set contains many additional features that can lead to a better understanding of wave-particle relationships. Since many of these features are frequently observed in other orbits, it is believed that these relationships have general validity. One such example that was discussed above is our recent initial investigation of the narrow proton flux events that are as short as one second. Another is a more rigorous analysis of the chorus feature seen on orbit 279 (November 17, 1990) that needs to be done using the energetic electron data to obtain the electron parallel velocities and using the wave data projected to the equator to get the gyrofrequency at the location where chorus is generated. Such a study could be used to test the theory that was proposed some time ago by Helliwell [1967], but never confirmed. (see recent paper by Skoug et al., [1996])

More analysis of the asymmetric pitch-angle distribution events should be performed in detail to illuminate the primary current systems responsible for this new dynamic feature found during geomagnetic storms. Moreover, the behavior of all the particles that were measured by CRRES ONR-307 instrumentation during these events should be studied to improve our understanding of the response of the diverse populations of magnetospheric charged particles to parallel electric fields.

Our studies of the CRRES ONR-307 database have yielded new results, each of which contributes to our better understanding of the radiation belt and ring current regions and to improving the models of these regions. Additional studies of the unique CRRES database would continue this effort.

## References

Anderson, R. R, D. A. Gurnett, and D. L. Odem, "CRRES plasma wave experiment," *J. Spacecr. Rockets, 29,* 570, 1992.

Cladis, J. B., "Parallel acceleration and transport of ions from polar ionosphere to plasma sheet," *Geophys. Res. Lett., 13,* 893, 1986.

Cladis, J. B., and H. L. Collin, "Observations of long-term field-aligned flow of $O^+$ ions near equator during summer and winter," (submitted to *J. Geophys. Res.*, 1997).

Collin, H. L., J. M. Quinn, G. R. Smith, E. Hertzberg, S. Roselle, and S. J. Battel, "The low energy ion mass spectrometer (ONR-307-8-1, 2) on CRRES," *J. Spacecr Rockets, 29,* 617, 1992.

Delcourt, D. C., J. A. Sauvaud, and A. Pedersen, "Dynamics of single-particle orbits during substorm expansion phase," *J. Geophys. Res., 95,* 20853, 1990.

Dungey, J. W., "Loss of Van Allen electrons due to whistlers," *Plant. Space Sci., 11,* 591, 1963.

Fujii, R., T. Iijima, T. A. Potemra, and M. Sugiura, "Seasonal dependence of large-scale Birkeland currents," *Geophys. Res. Lett, 8,* 1103, 1981.

Gloeckler, G. and D. C. Hamilton, "AMPTE ion composition results", Physica Scripta, T18, 73, 1987.

Hamilton, D. C., G. Gloeckler, F. M. Ipavich, W. Studemann, B. Wilken, and G. Kremser, "Ring current development during the great geomagnetic gtorm of February 1986," *J. Geophys. Res., 93,* 14343, 1988.

Helliwell, R. A. "A theory of discrete VLF emissions from the magnetosphere," *J. Geophys. Res. 72,* 4773, 1967.

Horwitz, J. L., "Parabolic heavy ion flow in the polar magnetosphere," *J. Geophys. Res., 92,* 175, 1987.

Iijima, T., and T. A. Potemra, "The relationship between interplanetary quantities and Birkeland current densities," *Geophys. Res. Lett., 9,* 442, 1982.

Imhof, W. L., J. Mobilia, H. D. Voss, H. L. Collin, M. Walt, and R. R. Anderson, "Association of waves with narrow particle dropouts in the outer radiation belt," (in press, *J. Geophys. Res.*, 1997).

Imhof, W. L., R. M. Robinson, H. L. Collin, J. R. Wygant, and R. R. Anderson, "Simultaneous measurements of waves and precipitating electrons near the equator in the outer radiation belt," *J. Geophys. Res., 99,* 2415, 1994.

Imhof, W. L., R. M. Robinson, R. W. Nightingale, E. E. Gaines, and R. R. Vondrak, "The outer boundary of the earth's electron radiation belt: Dependence upon L, energy, and equatorial pitch angle," *J. Geophys. Res., 98,* 5925, 1993.

Imhof, W. L., R. M. Robinson, H. L. Collin, J. R. Wygant, and R. R. Anderson, "Simultaneous equatorial measurements of waves and precipitating electrons near in the outer radiation belt," *Geophys. Res. Lett., 19,* 2437, 1992.

Imhof, W. L., H. D. Voss, M. Walt, E. E. Gaines, J. Mobilia, D. W. Datlowe, and J. B. Reagan, "Slot region electron precipitation by lightning, VLF chorus, and plasmaspheric hiss," *J. Geophys. Res., 91,* 8883, 1986.

Imhof, W. L., R. R. Anderson, J. B. Reagan, and E. E. Gaines, "Coordinated measurements of slot region electron precipitation by plasmaspheric wave bands," *J. Geophys. Res., 89,* 2217, 1984.

Johnson, M. H. and J. Kierein, "Combined Release and Radiation Effects Satellite (CRRES) spacecraft and mission," *J. Spacecr. Rockets, 29,* 556, 1992.

Kaufman, R. L., J. T. Horng, and A. Konradi, "Trapping boundary and field-line motion during geomagnetic storms," *J. Geophys. Res., 77,* 2780, 1972.

Kennel, C. F., and H. E. Petschek, "Limit on stably trapped particle fluxes," *J. Geophys. Res., 71,* 1, 1966.

Li, X., and M. Temerin, "Ponderomotive effects on ion acceleration in the auroral zone," *Geophys. Res. Lett., 20,* 13, 1993.

Nightingale, R. W., R. R. Vondrak, E. E. Gaines, W. L. Imhof, R. M. Robinson, S. J. Battel, D. A. Simpson, and J. B. Reagan, "CRRES spectrometer for electrons and protons," *J. Spacecr. Rockets, 29,* 614, 1992.

Olson, W. P., and K. A. Pfitzer, "A quantitative model of the magnetospheric magnetic field," *J. Geophys. Res., 79,* 3739, 1974.

Reber, C. A., "The Upper Atmosphere Research Satellite (UARS)," *Geophys. Res. Lett., 20,* 1215, 1993.

Shawhan, S. D., "Magnetospheric Plasma Waves" in *Space Plasma Physics: The Study of Solar-system Plasmas, Vol 2,* Space Science Board, National Academy of Science, Washington D. C. 1979.

Shelley, E. G., A. Ghielmetti, E. Hertzberg, S. J. Battel, K. Altwegg-Von Burg, and H. Balsiger, "The AMPTE/CCE hot-plasma composition experiment (HPCE)," *IEEE Trans. Geosci. Remote Sensing, GE-23,* 243, 1985.

Skoug, R. M., S. Datta, M. P. McCarthy, and G. K. Parks, "A cyclotron resonance model of VLF chorus emissions detected during electron microburst precipitation," *J. Geophys. Res., 101,* 21481, 1996.

Tsyganenko, N. A., "A model of the magnetospheric magnetic field with a warped tail current sheet," *Planet. Space Sci., 37,* 5, 1989.

Voss, H. D., E. Hertzberg, A. G. Ghielmetti, S. J. Battel, K. L. Appert, B. R. Higgins, D. O. Murray, and R. R. Vondrak, "Medium energy ion mass and neutral atom spectrometer," *J. Spacecr. Rockets, 29,* 566, 1992.

Voss, H. D., et al., "Lightning-induced electron precipitation," *Nature, 312,* 740, 1984.

Winningham, J. D., et al., "The UARS particle environment monitor," *J. Geophys. Res., 98,* 10649, 1993.

Wygant, J. R., P. R. Harvey, D. Pankow, F. S. Mozer, N. Maynard, H. Singer, M. Smiddy, W. Sullivan, and P. Anderson, "The CRRES electric field/Langmuir probe instrument," *J. Spacecr. Rockets, 29,* 601, 1992.

## List of Figures

Figure 12. Superposed SEP and HEPS electron spectra from the conjunction of CRRES and UARS at 12:14 UT and L = 1.39 on October 2, 1991.

Figure 13. Superposed SEP and HEPS proton spectra from the conjunction of CRRES and UARS in the anomaly region at 12:14 UT and L = 1.39 on October 2, 1991.

Figure 14. Measurements of the pitch-angle distributions of $O^+$ ions made on the CRRES satellite on August 26, 1990. The L-shell value and time intervals of the measurements are given in the panels.

Figure 15. IMP 8 data on the number density and speed of the solar wind from 0 to 16 hours UT on August 15, 1990.

Figure 16. IMP 8 data on the interplanetary magnetic field components $B_x$, $B_y$, and $B_z$ and the total field, $B_T$, from 0 to 16 hours UT on August 15, 1990.

Figure 17. Current density of the Region 1 Birkeland current as implied by the solar-wind conditions (see Equations (1) and (2)).

Figure 18. Total interplanetary magnetic field (solid line) and the negative value of $B_z$ the component (broken line) on August 15, 1990. The APADS occurred during the time interval between the vertical lines.

Figure 19. Total interplanetary magnetic field (solid line) and the negative value of $B_z$ the component (broken line) on July 9, 1991. The APADS were evident in the data during the time interval between the vertical lines; they probably began near 0600 UT, but could not be identified because of the limited pitch-angle coverage from 0600 to 0800 UT.

## List of Tables

## Appendix A: List of Publications and Presentations

**Publications** (since April 1994)

"Simultaneous Measurements of Waves and Precipitating Electrons near the Equator in the Outer Radiation Belt," W. L. Imhof, R. M. Robinson, H. L. Collin, J. R. Wygant, and R. R. Anderson, *J. Geophys. Res., 99,* 2415, 1994.

"Observations of Possible Wave-Particle Interactions Identified by the CRRES Particle Correlator: Preliminary Comparison with Kennel-Petschek Theory," N. W. Watkins, P. J. Christensen, C. G. Mouikis, S. C. Chapman, M. P. Gough, J. R. Wygant, D. A. Hardy, K. J. Kerns, H. Singer, C. Paranicas, M. Popecki, H. L. Collin, A. D. Johnstone, and R. R. Anderson, in *Physics of Space Plasma, No. 13,* edited by T. Chang and J. R. Jasperse, P. 547, Scientific, Cambridge, MA, 1995.

"Suspected Wave-Particle Interactions Coincident with a Pancake Distribution as Seen by the CRRES Spacecraft," N. W. Watkins, J. A. Bather, S. C. Chapman, C. G. Mouikis, M. P. Gough, J. R. Wygant, D. A. Hardy, H. L. Collin, A. D. Johnstone, and R. R. Anderson, *Adv. Space Res., 17,* (10)83, 1996.

"Association of Waves with Narrow Particle Dropouts in the Outer Radiation Belt," W. L. Imhof, J. Mobilia, H. D. Voss, H. L. Collin, M. Walt, and R. R. Anderson, (in press, *J. Geophys. Res.,* 1997).

"Observations of Long-Term Field-Aligned Flow of $O^+$ Ions near Equator During Summer and Winter," J. B. Cladis and H. L. Collin, (submitted to *J. Geophys. Res.,* 1997).

**Presentations** (since April 1994)

"Rice Magnetospheric Specification and Forecast Model: Inner Magnetosphere Test Results," R. L. Lambour, J. W. Freeman, R. A. Wolf, R. Spiro, B. Hausman, A. Nagai, B. Bales, R. Hilmer, W. Denig, D. Hardy, D. McComas, M. Thomsen, and H. L. Collin, *EOS, Trans. Am. Geophys. Union, 75,* 318, 1994.

"Narrow Flux Drop-offs and Enhancements in the Outer Radiation Belt, Association With Waves and Magnetic Fields," W. L. Imhof, H. D. Voss, J. Mobilia, H. L. Collin, J. R. Wygant, R. R. Anderson and H. J. Singer, *EOS, Trans. Am. Geophys. Union, 75,* 542, 1994.

"Suspected Wave-Particle Interactions Coincident with a Pancake Distribution as Seen by the CRRES Spacecraft," N. W. Watkins, J. A. Bather, S. C. Chapman, C. G. Mouikis, M. P. Gough, J. R. Wygant, D. A. Hardy, H. L. Collin, A. D. Johnstone, and R. R. Anderson, COSPAR, 1994.

"Asymmetric Pitch-Angle Distributions and Birkeland Currents in the Outer Magnetosphere," J. B. Cladis and H. L. Collin, *EOS, Trans. Am. Geophys. Union, 76,* F488, 1995.

# Appendix B: Selected Publications

JOURNAL OF GEOPHYSICAL RESEARCH, VOL. 99, NO. A2, PAGES 2415–2427, FEBRUARY 1, 1994

# Simultaneous measurements of waves and precipitating electrons near the equator in the outer radiation belt

W. L. Imhof, R. M. Robinson, and H. L. Collin
Lockheed Palo Alto Research Laboratory, Palo Alto, California

J. R. Wygant
Space Sciences Laboratory, University of California, Berkeley

R. R. Anderson
Department of Physics and Astronomy, University of Iowa, Iowa City

**Abstract.** An investigation of wave-particle interactions is made using several simultaneous electron and wave measurements performed at near-equatorial positions from the CRRES satellite. Bursts of electron precipitation were observed, most frequently at local times near dawn. Examples of bursts are presented in which the fluxes of the precipitating electrons and the wave intensities are correlated with coefficients as high as 0.7. During bursts the frequencies of the enhanced waves spanned a wide range from 311 Hz to 3.11 kHz, and the energies of the enhanced electrons were in the range 1.7 keV to 288 keV. The changes of the precipitating fluxes were generally less pronounced at the lowest energies. On the basis of electron-cyclotron resonant calculations using the cold plasma densities and ambient magnetic fields taken from the CRRES measurements it was found that the wave frequencies and precipitating electron energies were generally consistent with those expected from electron resonance with parallel propagating whistler waves. The electron data of principal concern here were acquired in and about the loss cone with narrow angular resolution spectrometers covering the energy range 340 eV to 5 MeV. The wave data included electric field measurements spanning frequencies from 5 Hz to 400 kHz and magnetic field measurements from 5 Hz to 10 kHz.

## Introduction

Electrons trapped in the radiation belt can interact with waves that may be present and may consequently undergo a change in equatorial pitch angle such that their mirror point altitudes are lowered into the atmosphere, and the electrons are thereby lost from the radiation belt. The role of wave-particle interactions in the morphology of the electron radiation belt has been well established by many experimental and theoretical investigations.

From a low-altitude satellite, Injun 3, *Oliven and Gurnett* [1968] made simultaneous measurements of electron bursts and of VLF chorus emissions at high latitudes. They found that the bursts of precipitating electrons were always accompanied by chorus emissions. However, chorus bursts were not always accompanied by electron precipitation bursts. A one-to-one association between individual electron precipitation bursts and individual chorus emissions was not generally found. . .

Electron precipitation into the atmosphere can also be detected remotely with bremsstrahlung X ray detectors placed on a balloon, rocket, or satellite. Correlated bursts of X rays and whistler-triggered chorus observed at Siple Station, Antarctica ($L = 4.3$), by *Rosenberg et al.* [1971, 1990] are further evidence for the importance of waves in scattering electrons into the loss cone.

Plasma wave observations from the ISEE satellite revealed the frequent presence of monochromatic frequencies in the 10–25 kHz range that are attributed to ground-based VLF transmitters [*Imhof et al.*, 1981]. Narrow and sometimes multiple peaks in the energy spectra of precipitating electrons were observed from the P78-1 satellite. The peak energies varied with $L$ value in a characteristic pattern which, when combined with the nearly simultaneous occurrence of narrow band wave frequency, supported the conclusion that the narrow peaks in the electron spectra resulted from cyclotron resonance interactions with the waves produced by ground-based VLF transmitters.

Simultaneous measurements of the precipitating electron spectra, the wave frequency distributions, and the plasma density profiles in the slot region of the radiation belt were made for the first time by *Imhof et al.* [1982]. The plasma wave densities, which were obtained from the ISEE 1 data and the electron spectra measured on the P78-1 satellite were found to be consistent with each other, supporting the hypothesis of *Lyons et al.* [1972] that electrons in the slot region are precipitated by cyclotron resonance interaction with the plasmaspheric whistler mode wave bands.

In an experiment carried out in 1982, electrons precipitated from the radiation belt by the controlled injection of VLF signals from a ground-based transmitter were observed [*Imhof et al.*, 1983]. The measured energy spectra revealed

Copyright 1994 by the American Geophysical Union.

Paper number 93JA02828.
0148-0227/94/93JA-02828$05.00

that much of the enhanced electron flux was concentrated near the resonant energies for first-order cyclotron interactions occurring close to the magnetic equator with the nearly monochromatic waves emitted from the transmitter.

From a low-altitude satellite, *Voss et al.* [1984] reported the first satellite measurements of electron precipitation by lightning. A one-to-one correlation was found between ground-based measurements of VLF spherics and whistlers and the low-altitude satellite measurements of precipitating energetic electrons.

Although many of the past observations provided indirect evidence connecting pitch angle scattering into the loss cone and plasma waves, there remains a serious lack of simultaneous wave and electron measurements near the equator where most of the wave-particle interactions are believed to take place. Recently, examples of simultaneous electron and wave measurements from the CRRES satellite were presented by *Imhof et al* [1992]. The CRRES satellite offered the advantages of providing near-equatorial measurements at altitudes up to 35,786 km and therefore over a wide range of $L$ shells. The precipitating electron fluxes were obtained with fine angular resolution spectrometers oriented at various angles to the satellite spin axis. Using these fine angular resolution measurements, *Imhof et al* [1992] showed examples in which the variations in electron fluxes in the loss cone and the wave intensities were correlated.

Here we present the results of a more comprehensive analysis of the CRRES events. In particular, we provide the results of a quantitative study of the relative variations of particle and wave intensities. The results are discussed in the context of the *Kennel and Petschek* [1966] theory, and an evaluation is made of the occurrence frequency of the events in $L$ and local time.

## Description of Instrumentation

The CRRES satellite was launched on July 25, 1990, into a geosynchronous transfer orbit with an apogee of 35,786 km and a perigee of 350 km. The geosynchronous transfer orbit of CRRES and its inclination of 18° allowed the instruments to obtain extensive measurements of the radiation belts and magnetosphere near the equatorial plane throughout the 14-month mission. Apogee at launch was at about 0800 local time, and the spacecraft precessed toward earlier local times at a rate of about 15 hours per year.

One of the instruments in the payload, the Spectrometer for Electrons and Protons (SEP), had a fine angular resolution (±1.5°); covered the energy range 40 keV to 5 MeV; and had detectors oriented at 80°, 60°, and 40° to the satellite spin axis [*Nightingale et al.*, 1992]. Energy spectra were obtained by pulse height analysis of the signals from silicon detectors; the four lowest energy channels had center energies of 53 keV, 77 keV, 100 keV, and 124 keV and widths of 25 keV. The low-energy ion mass spectrometer (IMS-LO) instrument provided measurements of lower-energy electrons in three broad energy bands centered at 340 eV, 1.7 keV, and 8.9 keV at 75° to the satellite spin axis and with an angular resolution of ±2.5° [*Collin et al.*, 1992]. The angular resolution of these instruments is adequate for measurements of outer belt electrons in and about the equatorial loss cone which is about ±4° wide at $L = 6$.

The CRRES detectors scanned a range of pitch angles as the spacecraft rotated about its spin axis which pointed approximately sunward. The view direction of an instrument which is at an angle to the spin axis will sweep out a cone as the satellite rotates and will view pitch angles which are the angles between the cone surface and the field line. The range of pitch angles viewed is limited by the relative orientation of the field line and the axis of the cone, i.e., the spin axis. An instrument will view directly along the field line only when the spin axis is oriented such that the field line lies on the surface of the cone. All of the data needed for this study were taken from periods when the orientation allowed SEP to view within a few degrees of the field line.

The ac electric and magnetic field data used in this study were provided by the University of Iowa/Air Force Geophysics Laboratory (AFGL) Plasma Wave Experiment and the University of California at Berkeley/AFGL Electric Field/Langmuir Probe Experiment. These took electric field signals from a pair of orthogonal 100-m tip to tip booms in the spin plane of the spacecraft. The ac magnetic field measurements were from a search coil magnetometer located at the end of a 6-m mast extending out in the spin plane of the spacecraft. The Iowa/AFGL instrument included a sweep frequency receiver and multichannel spectrum analyzer which together provided ac electric field measurements from 5 Hz to 400 kHz and magnetic field measurements from 5 Hz to 10 kHz [*Anderson et al.*, 1992]. The Berkeley/AFGL experiment [*Wygant et al.*, 1992] measured electric and magnetic waveforms over frequencies ranging from quasi-static to 40 kHz. The instrument also provided continuous monitoring at several samples per second of the wave amplitudes measured through 3 broadband filters with maximum response at frequencies of 32 Hz, 256 Hz, and 2048 Hz.

## Presentation of Data

The SEP detectors viewed the loss cone no more than once during each 29-s spin of the CRRES satellite. The loss cone data indicated the frequent occurrence in the outer radiation belt of energetic precipitating electrons. An example is shown in Figure 1 of selected pitch angle distributions and of the precipitation fluxes at these energies plotted as a function of time. Enhanced electron precipitation was observed during short time intervals or bursts. In this and other examples, bursts were generally evident only at small equatorial pitch angles with the high-altitude measurements indicating that during bursts, very little change may occur in the fluxes of electrons mirroring near the equator.

In order to obtain a database for studying short-duration bursts of precipitating electrons, the SEP electron data were surveyed for bursts in the fluxes of electrons at pitch angles <4°. The bursts were identified on the basis of the degree to which they stood out above the ambient radiation fluxes. Because CRRES took several tens of minutes to pass through the outer radiation belt, all of the bursts had shorter durations with the longest being 18 min. For this reason, enhancements with durations exceeding 18 min were not included in the survey. Only pronounced events were considered, so it was required that during the burst the electron flux at 0° to 4° pitch angle increase by at least a factor of 2 with a subsequent decrease also of a factor of 2 or greater.

From the surveys, information was obtained on the dependence of the occurrence of electron bursts upon magnetic local time (MLT) and upon the value of $L$. The fraction of

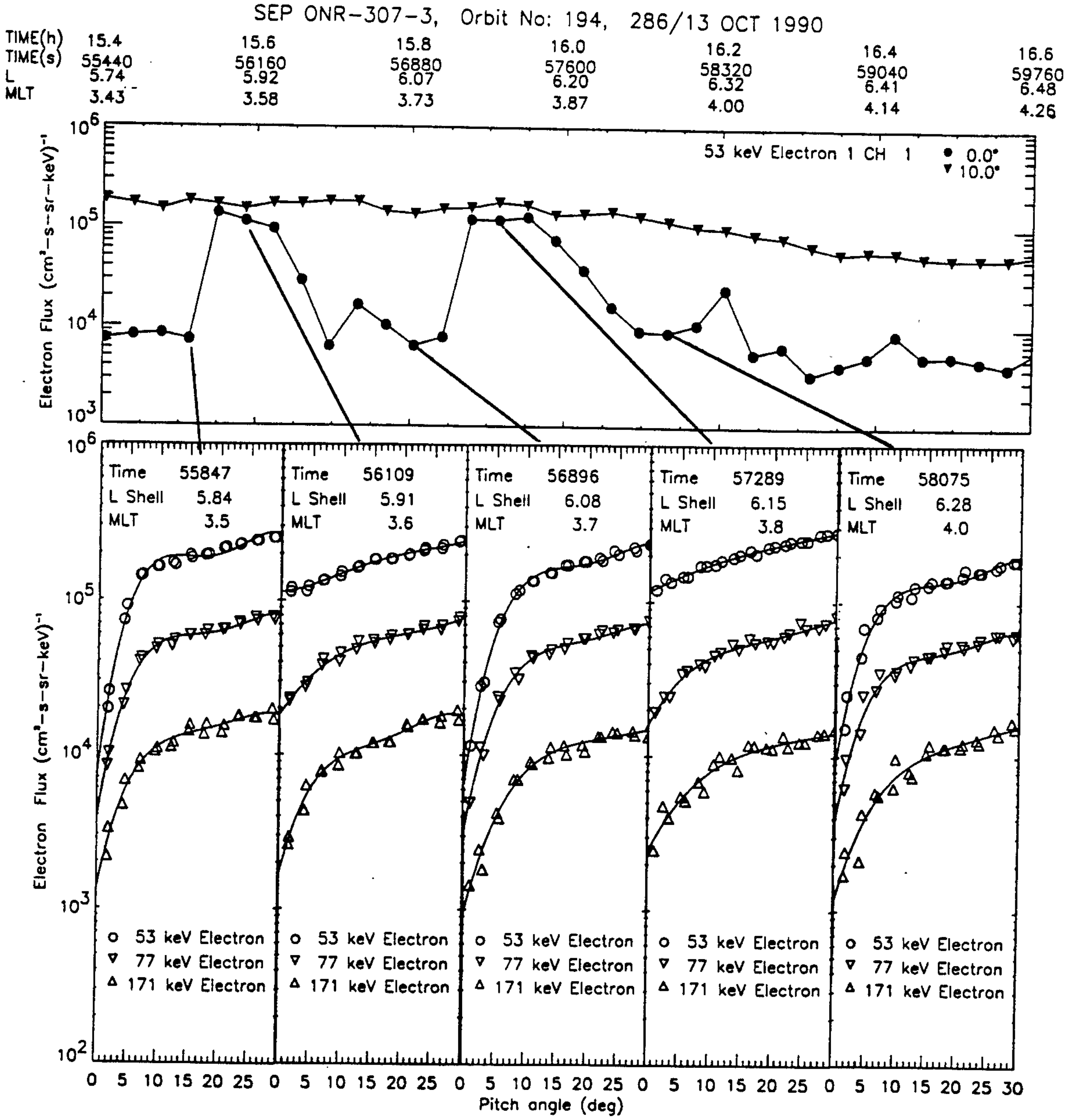

**Figure 1.** Selected pitch angle distributions and the fluxes at 0° and 10° pitch angle versus time and associated parameters.

the satellite passes in which electron bursts were observed from the equator is plotted as a function of MLT in Figure 2 (top). The average number of electron bursts observed per pass of the satellite is plotted versus MLT in Figure 2 (middle). The number of satellite passes through each 1-hour MLT interval in which observations were made is plotted in Figure 2 (bottom). The various MLT intervals were not sampled uniformly throughout the mission; in fact, no data were acquired in the near-equatorial positions at MLT values near 12. Also, bursts were rarely seen between 13 and 16 MLT. Over the local time interval covered it appears that electron bursts near the equator occurred most frequently near dawn. Such an MLT dependence was previously reported by *Oliven et al.* [1968] for electron bursts observed at low satellite altitudes.

The number of bursts observed in each half-unit *L* shell interval is presented in Figure 3 (top). Because of the nonuniform coverage of the various *L* shells, this plot does not represent the frequency of occurrence of bursts as a function of *L*. The majority of bursts in the database used for this investigation are in the vicinity of $L = 6$ to 7. The relative time durations in which the SEP detector scanned through pitch angles <4° in each of the *L* shell intervals are plotted in Figure 3 (middle). The burst observation frequency is plotted as a function of *L* in Figure 3 (bottom).

An investigation was made of passes in which the waves

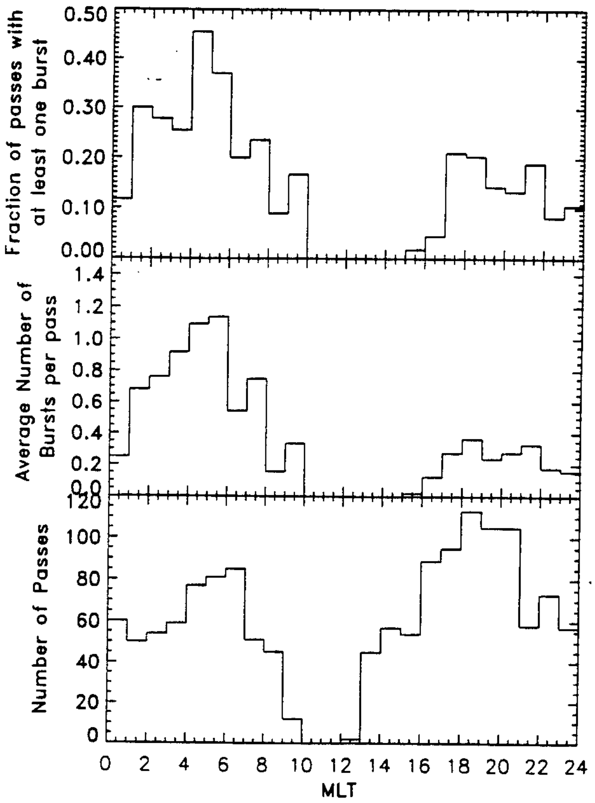

**Figure 2.** (top) The fraction of satellite passes through each 1-hour interval of MLT in which electron bursts were observed. (middle) The average number of electron bursts observed in each pass plotted as a function of MLT. (bottom) The number of satellite passes through each 1-hour MLT interval for which data were processed.

displayed good correlation with the fluxes of precipitating electrons. For this purpose the pitch angle for each 0.25-s sample was calculated using magnetic field data from the CRRES magnetometer. Because the pitch angle coverage of the detectors was not always complete, a method was developed to extrapolate the measured distribution to small pitch angles that may not have been sampled. The method is to fit the fluxes measured between 0° and 30° pitch angle to a fourth-order polynomial. The fluxes given by the polynomial fit were then used to study the variations with time of fluxes at a given pitch angle. The fit was also used to integrate the distributions over arbitrary pitch angle ranges. Although the fourth-order polynomial fit may not be the most accurate way to fit fluxes within the loss cone, the fitting procedure was never used to extrapolate the measured distributions by more than a few degrees. Because we are primarily concerned with the temporal variation in the fluxes, the errors produced by this simplified approach do not affect our conclusions. Visual inspection of each of the fits was made to ensure that no unrealistic extrapolation of fluxes resulted from this procedure. Flux measurements within the loss cone are compromised to some extent, in any case, because the angular resolution of the detectors, although very fine, is comparable to the angular width of the loss cone for the near-equatorial measurements. For this study, no attempt has been made to correct for the finite acceptance angle of the detector and to unfold the true angular variation of the fluxes. The absolute fluxes at various pitch angles would be affected, but here we are concerned with changes in intensity with time. When processed in this manner, the data provide information about flux variations in the loss cone that are relatively insensitive to the pitch angle coverage during each spin.

An example of the flux variations obtained in the manner described above is shown in Figure 4. The data were acquired at $L$ values between 5 and 6 near dusk magnetic local time. Figure 4d shows the fluxes of 53-keV electrons at 0° and 10° pitch angles derived from the polynomial fits. The striking features in this display are the two isolated enhancements at 0° pitch angle with no corresponding variation at 10°. Each spike consists of one measurement in which the pitch angle distributions became more isotropic for that sampling interval.

Various ephemeris parameters are listed in Figure 4 (bottom), including $L$, MLT, and the ratio of the local magnetic field strength to that at the equator ($B/B_0$). The value of $B/B_0$ was generally very close to 1.0, indicating the measurements were performed close to the equator. It is also noteworthy that in all of the burst events described here the enhanced precipitating electrons were moving in directions away from the equator. We were unable to compare electron fluxes directed toward and away from the equator because SEP and IMS-LO did not view both loss cones during any spin.

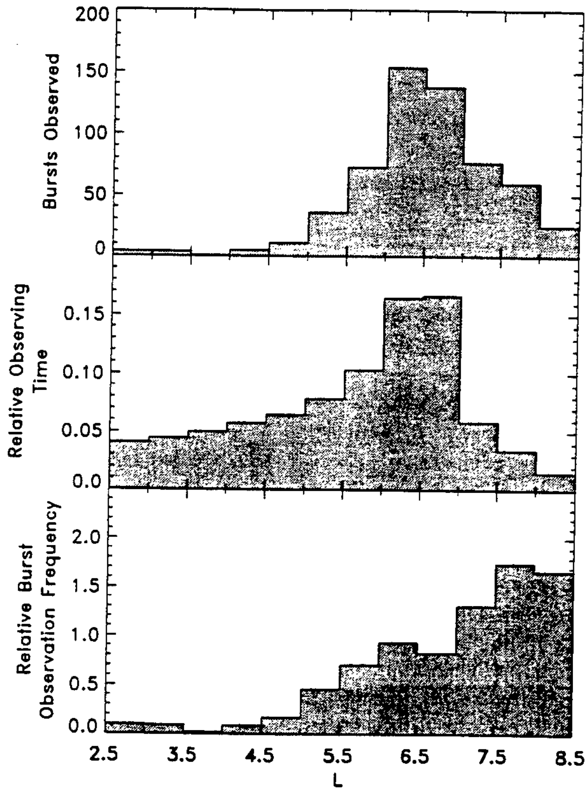

**Figure 3.** (top) The number of electron bursts observed in each half-unit $L$ shell interval. (middle) The relative durations of time for which data were analyzed. (bottom) The number of bursts observed per unit time.

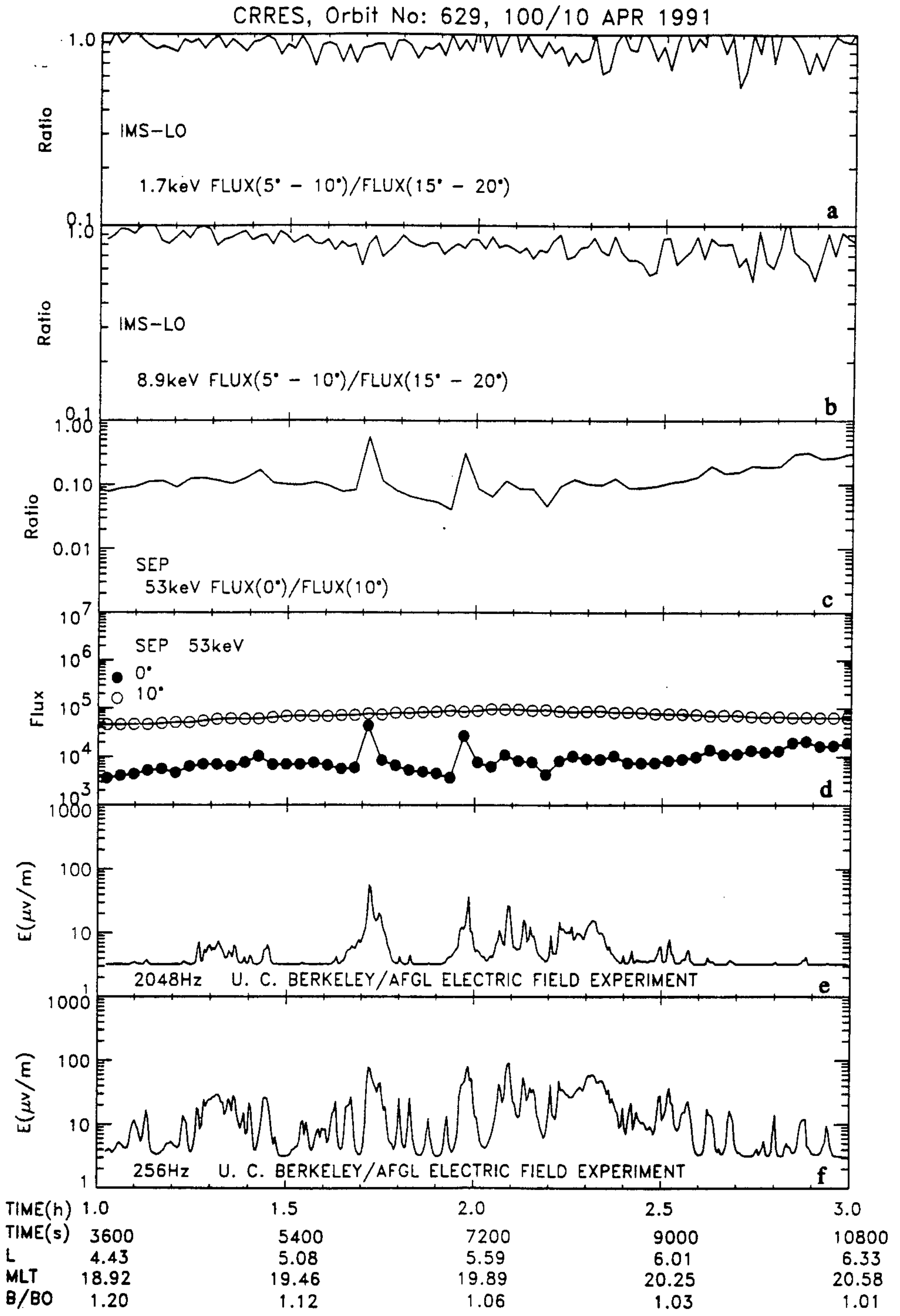

**Figure 4.** (a)–(d) Fluxes and ratios of various energy electrons at different pitch angles and (e)–(f) electric field intensities $E$ ($\mu$v/m) at two frequencies.

Before proceeding with the presentation of the data it is important to discuss the sampling characteristics of the SEP data when analyzed by the method described above. The polynomial fits used the data measured during a half spin of the satellite, about 15 s, but the fluxes near the loss cone that are most important for the calculation of the 0° fluxes were measured during an interval of only a few seconds. Because of instrument mode changes, it took about 132 s before another electron flux measurement near the loss cone was made. Thus adjacent points in Figure 4 are about 2 min apart, whereas each measurement has an intrinsic temporal resolution of several seconds.

Each of the flux enhancements in Figure 4 is accompanied by correlated enhancements in the ac electric field wave

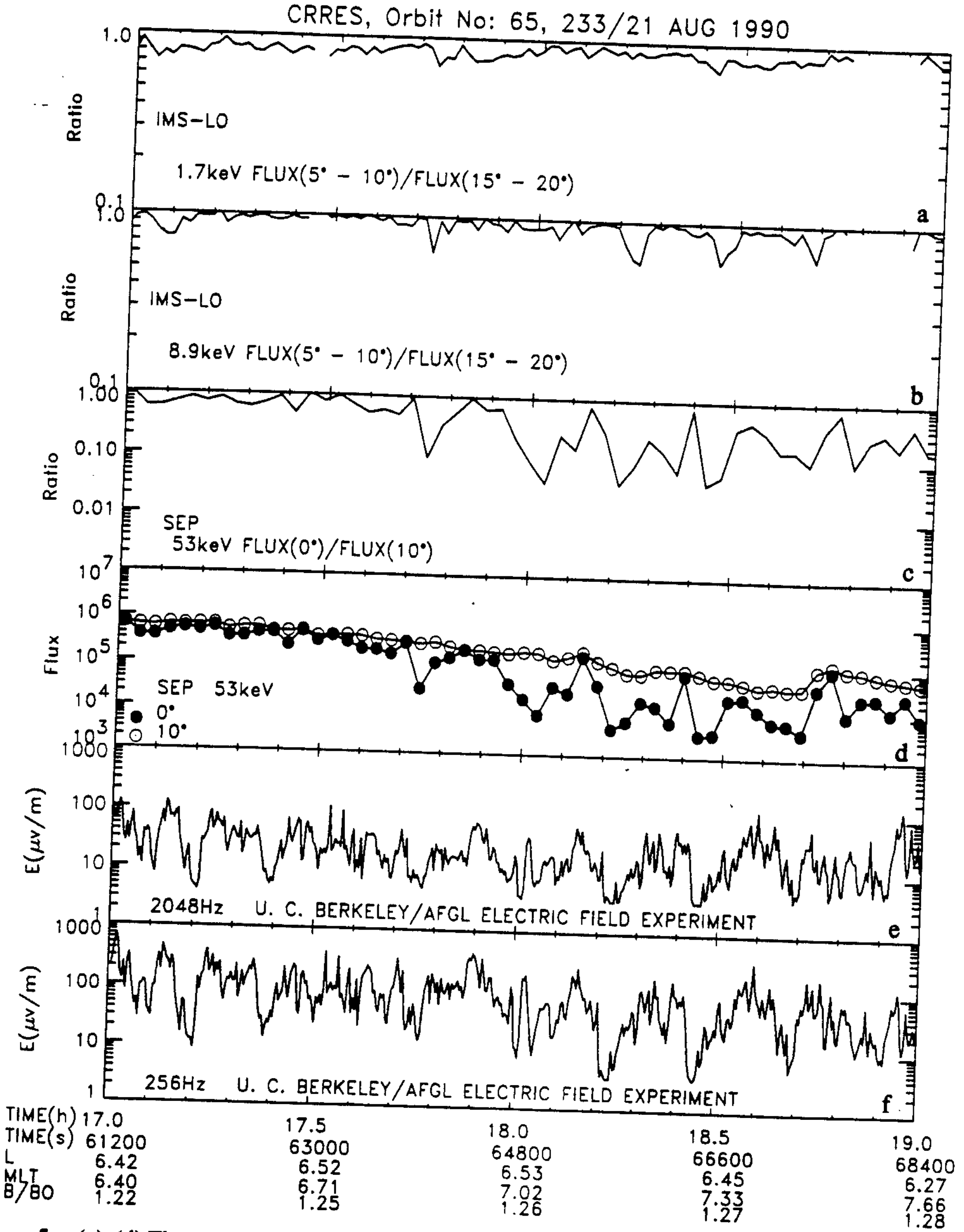

**Figure 5.** (a)–(d) Fluxes and ratios of various energy electrons at different pitch angles and (e)–(f) electric field intensities $E$ ($\mu$v/m) at two frequencies.

intensities as measured by both the Berkeley and Iowa instruments, although only Berkeley data are shown in Figure 4. Figures 4e and 4f show the wave intensities in two broad frequency bands.

Figures 4a, 4b, and 4c show the ratio of fluxes at or near 0° pitch angle to those outside the loss cone at about 10° at three different energies. These quantities were computed to bring out subtle enhancements in isotropy that may otherwise be too difficult to distinguish. This was particularly important for the IMS-LO data which extended the electron energy coverage down to tens of eV. Because the events were selected on the basis of good loss cone coverage by the SEP instrument, the pitch angle coverage of these events by IMS-LO was not always optimal. The IMS-LO field of view was displaced from the SEP field of view by 5° relative to the spin axis. This difference and the wider intrinsic angular resolution of the IMS-LO instrument meant that there was no advantage in performing the same polynomial fitting technique for the IMS-LO pitch angle distributions. Accordingly, average fluxes for IMS-LO over appropriate pitch angle intervals were used such as 0° to 5° or 5° to 10° for the precipitated electrons and 10° to 15° or 15° to 20° for the trapped electrons. The cyclotron resonance interaction causes electrons to lose energy as they diffuse from large pitch angles toward the loss cone. In consequence, it is not strictly correct to compare electrons of the identical energy at different pitch angles. However, over the range of pitch angles which we have used, 0° to 20°, the energy loss is relatively small and is within the energy band pass of the instruments.

Figure 5 shows data from another type of correlation event in a similar format to Figure 4. The data from this dawn sector pass of the spacecraft show isotropy approaching apogee. Beginning at 1742 UT, the fluxes at 0° shown in Figure 5d exhibit large variations, while fluxes at 10° are smoothly varying with time. In this case both the minima in the 0° fluxes and the maxima where isotropy occurs are correlated with features in the Berkeley wave data. It is interesting to note that no noticeable change in the character of the wave intensities is observed at 1742 UT, the point at which the dropouts in 0° fluxes become large. The flux ratios in Figures 5a, 5b, and 5c show that some of the dropouts in field-aligned fluxes extend to energies as low as 8.9 keV. Note the difference in vertical scale between Figures 5a and 5b and Figure 5c. The flux ratio at 53 keV decreases almost an order of magnitude for the event between 1742 and 1748 UT, whereas the fluxes at 8.9 keV only decrease by about a factor of 2. At 1.7 keV there are only suggestions of dropouts at 1745 and 1824 UT. Some of the precipitating electron fluxes are correlated well with the measured waves, but in other cases the data suggest that the interactions did not occur near the satellite or that other mechanisms are involved.

Figure 6 shows data from another dawn sector pass. The most dramatic feature in this pass is the broad region of enhancement in wave power and electron flux ratio between 0600 and 0618 UT. The enhancement is just apparent in the 1.7-keV data. Two other similar enhancements can be seen after 0630 UT and before 0700 UT. They differ from those shown in Figure 4 because they are not spiky in nature, and they differ from those shown in Figure 5 because of the absence of isotropy over most of the pass. Comparing the wave data between the three bursts in Figure 6 shows that the first burst is most intense at 2048 Hz. Also, this is the only one of the three bursts that is apparent in the 1.7-keV flux channel. The second burst is most obvious in the 32-Hz channel of the wave detector and in the higher-energy channels of the electron detectors. However, although an enhancement in the 53- and 288-keV flux ratios can be seen in connection with this burst, the pitch angle distributions are far from being isotropic. In the third burst the most intense wave channel is 256 Hz, and the enhancement in flux ratio can be seen down to 8.9 keV. Examination of the pitch angle coverage for SEP and IMS-LO for this pass shows that the absence of enhancements in the 1.7-keV flux channel for the second two bursts cannot be explained in terms of a difference in loss cone coverage. In almost all of the events identified in this study, wave-associated electron enhancements are less pronounced or absent completely at the lower-energy electron channels. In fact, a significant depletion was observed in the lowest-energy channel in the first of these bursts. Thus the burst after 0600 UT is unusual in that the signature in the lower-electron energy channels was very distinct. In association with this event we note the more intense wave power in the 2048-Hz channel.

It is important to note that the enhancements in the August 23, 1990, event have a different nature in the IMS-LO and SEP data. This is shown in Figure 7 where the fluxes of precipitating electrons and those trapped near the equator are plotted separately in addition to their ratios. Clearly, there is a pronounced depletion in the precipitating and trapped fluxes of the lower-energy electrons at the time and/or position of the pronounced enhancement in the intensities of the electrons ≥53 keV. For the passes through this same $L$ shell region on previous and subsequent orbits we have investigated the flux variations and established that the depletion in the low-energy electron flux was seen only on that orbit. The depletion may be due to wave-particle interactions occurring at locations far from the satellite or to other mechanisms.

The ac electric field measurements from the Berkeley instrument are fairly broadband, and a more detailed indication of the spectral distribution of the waves can be seen from the Iowa wave data. In the following paragraphs we describe the results of a more detailed analysis of the data obtained during orbits 65 and 69 (Figures 5 and 6, respectively).

Figure 8 shows the electric field wave intensities at many frequencies acquired by the Iowa instrument for the August 23 event. For the event beginning at about 0600 UT the wave intensity at 3.11 kHz is very pronounced, in agreement with the Berkeley data at 2.048 kHz. On the other hand, the other two enhancements observed during this pass are more pronounced in the 300–600 Hz range.

Plate 1 contains a color spectrogram from the Iowa electric field wave data during the pass on August 23. The striped patterns are due to cycling between two types of electric field antennas. As evident in Plate 1, the wave intensities at times shortly after 0530 UT are more pronounced at the higher frequencies than are the later enhancements. It is to be noted that the lower-energy electron flux ratios are enhanced at times earlier than 0618 hours UT.

The upper hybrid resonance frequency in the color spectrogram allows determination of the cold plasma density. Knowing the density and the electron-cyclotron frequency obtained from $B$, we can calculate the resonant energy of different frequency waves, assuming the interaction between electrons and waves is via parallel-propagating whistler mode waves. For this mode the electron cyclotron resonance energy is

$$E_r = \frac{f_c}{f}(1 - f/f_c)^3 E_c$$

In this equation $f$ is the wave frequency, $fc$ is the electron cyclotron frequency and $E_c = B^2/8\pi n = 255.4 \text{ keV } f_c^2/f_p^2$, where $f_p$ is the electron plasma frequency and $n$ is the electron density [*Kennel and Petschek*, 1966].

Figure 9 contains plots of wave intensity versus the equivalent electron resonance energy at selected times during the August 23, 1990, pass. This shows that for the event just after 0600 UT, there was significantly more wave power at frequencies resonating with electrons of energy in the ~10–100 keV range, in agreement with the observed enhancements seen in the IMS-LO data. On the other hand, the event at 0655 UT has a well-defined peak at resonance energies in the 100–300 keV range. Correspondingly, this was the event with a very clear signature in the 288-keV electron energy channel.

Another way to demonstrate the correlation between wave power and precipitating flux enhancements is illustrated in Figure 10. Here we used the fact that the 256-Hz waves measured by the Berkeley instrument in the orbit 65 and 69 events resonate with electrons having energies near

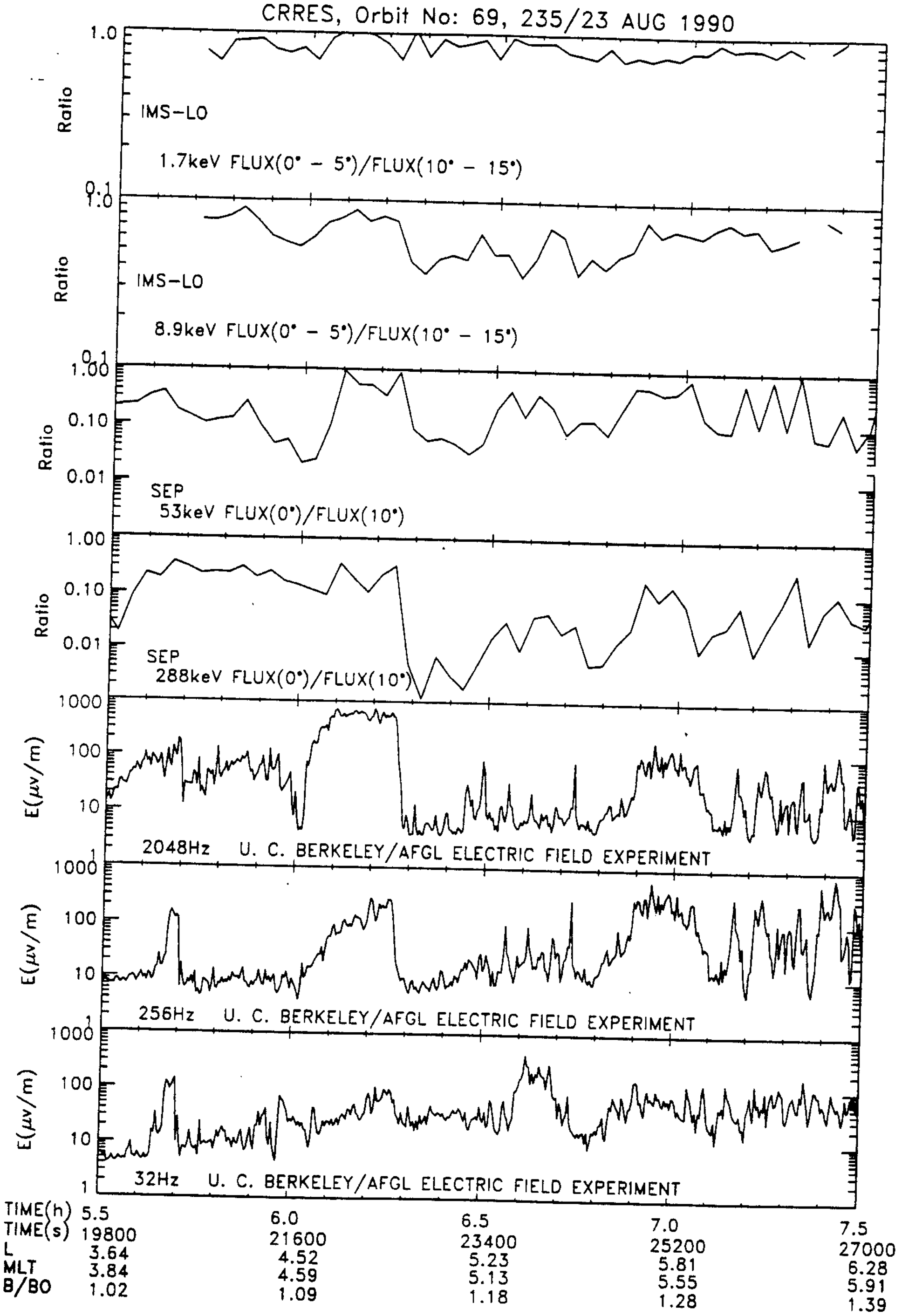

**Figure 6.** Ratios of various energy electrons at different pitch angles and electric field intensities $E$ ($\mu$v/m) at three frequencies.

53 keV. Figure 10 shows the electric field strength at this frequency versus the ratio of precipitating to trapped electron flux at 53 keV. In both cases there is a significant correlation between the two quantities.

The analysis shown in Figure 10 was also performed for 32-Hz and 2048-Hz waves, each time correlating the electric field strengths with the flux ratio for electrons at the appropriate resonant energies. The correlation coefficients derived in this manner are shown in Figure 11. Here we show only results for two of the bursts observed during orbit 69. The data in Figure 11 show that the highest correlation in both events is in the 256-Hz channel. Thus, although these two events differed in the frequency range over which the wave powers were enhanced, they were similar in that the most efficient coupling between waves and particles occurred at frequencies that resonated with the 53-keV energy channel.

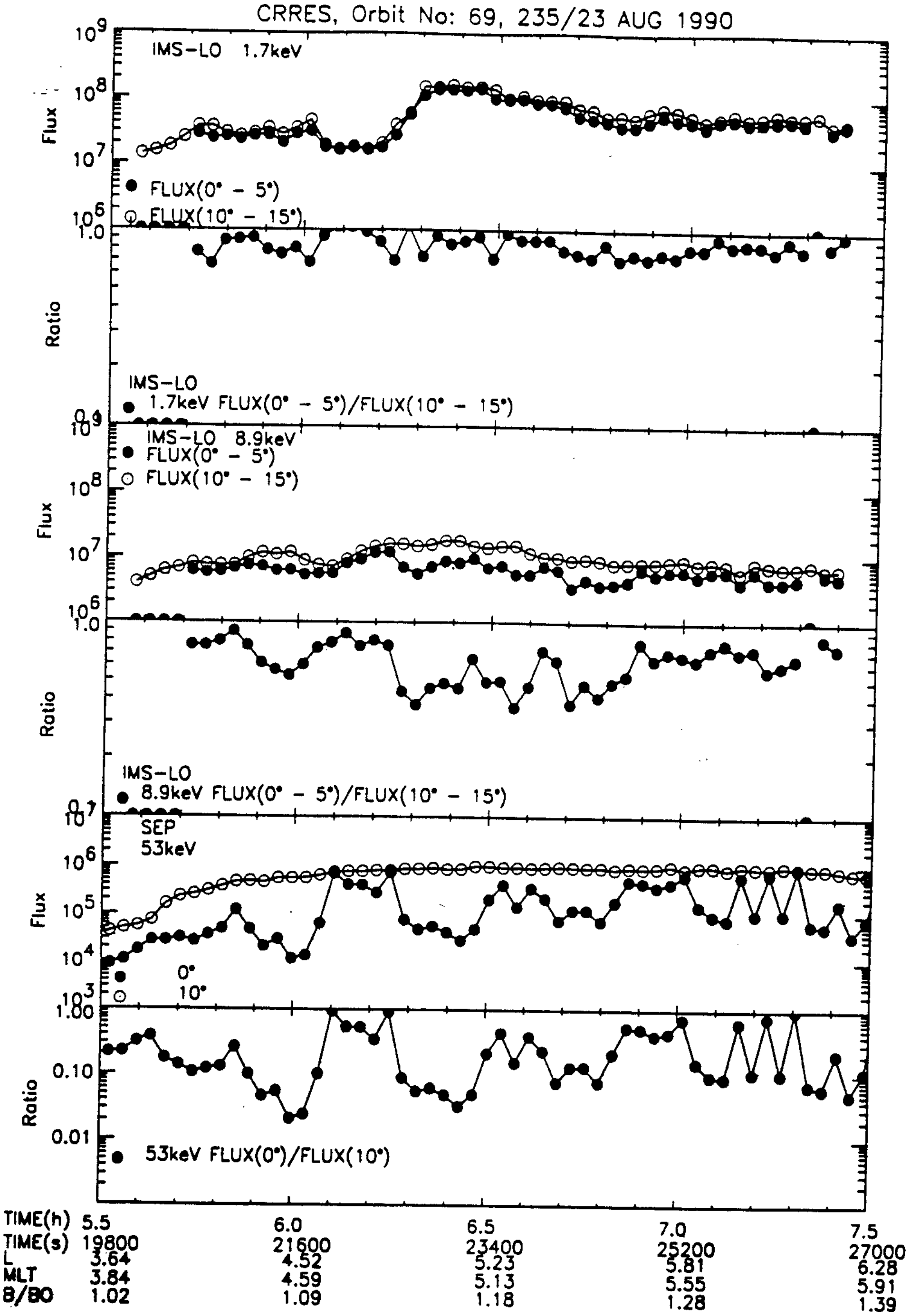

**Figure 7.** Fluxes of precipitating and trapped electrons in addition to the corresponding ratios.

The characteristics of these events can be summarized as follows.

1. Electron precipitation bursts were observed most frequently at local times near dawn.

2. The bursts were generally evident only at small equatorial pitch angles with little change occurring in the fluxes of electrons mirroring at high altitudes.

3. Simultaneous wave-electron bursts occurred near the equator, with the wave and electron intensities often displaying correlation coefficients as high as 0.7.

4. The observations of wave-electron interactions occurred at energies as high as 288 keV.

5. Variations connected with the waves were sometimes observed at energies as low as 1.7 keV.

6. On the basis of the cold plasma densities and electron-cyclotron frequencies taken from the CRRES measurements

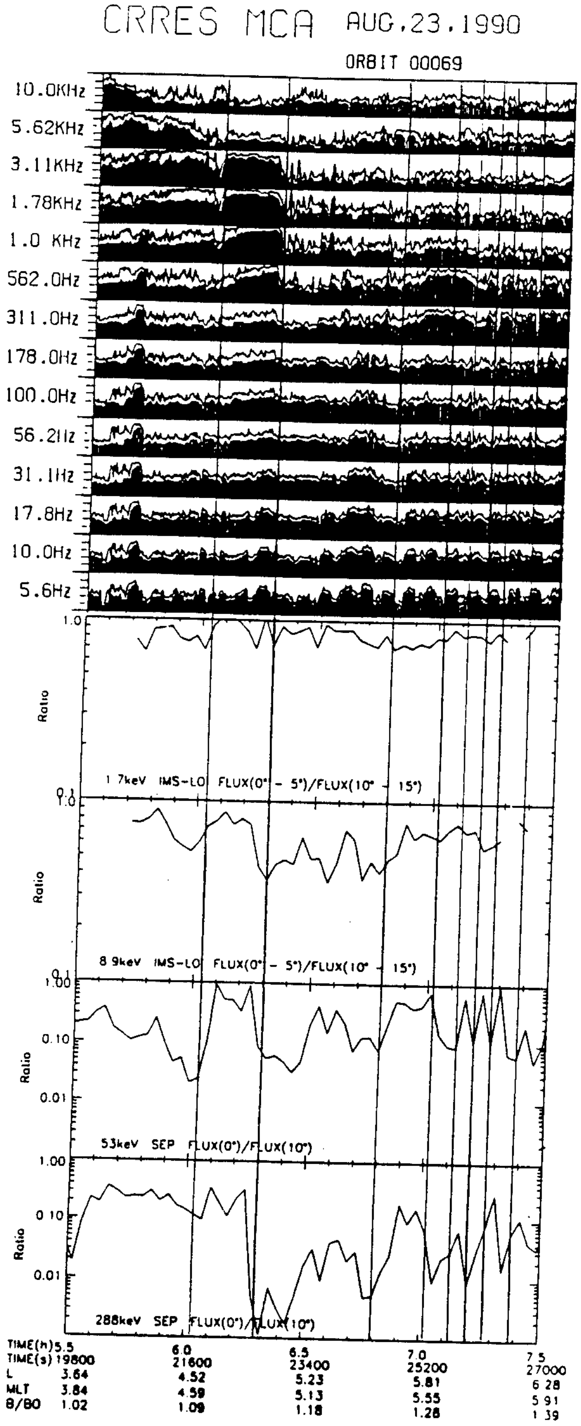

**Figure 8.** The wave intensities at various frequencies in addition to the ratios of electron fluxes at various pitch angles.

it was found that the wave frequencies and precipitating electron energies were generally consistent with each other.

7. On one satellite pass when wave bursts were observed with peak intensities at different frequencies the electron bursts were most dominant at lower energies when the waves peaked at higher frequencies.

8. Some of the wave-particle interactions were observed to occur over time intervals of many minutes.

9. Some low-energy bursts occurred only in the ratios of the fluxes at 0° to those at higher angles, there being a depression in the fluxes over all pitch angles at the time of the event.

## Discussion

The results presented here provide new insights into the nature of the transient precipitation events previously reported by *Imhof et al.* [1992]. In a search through the entire CRRES data set, 590 such events were identified. Many of the events are characterized by correlated enhancements in precipitating electron fluxes and ac electric field intensities. Because of the great variability observed in the energies of the electrons and wave intensities in the enhancements, we have studied several events in detail to see if they can be understood within the context of the *Kennel and Petschek* [1966] theory. The results shown in Figure 6 support the theory quite well in terms of the relative enhancements in the lower- and higher-electron energy channels. Our general impression from examining all of the events leads to the conclusion that the interaction between bursts of higher-frequency waves and lower-energy electrons is much weaker. The low-energy electrons appear to have many variations that may not be associated with the wave bursts.

*Kennel et al.* [1970] pointed out that since whistlers interact primarily with high-energy electrons, it is doubtful that they could also be responsible for the copious loss of softer (<1 to 10 keV) electrons from the nightside auroral lines of force. Subsequently, this suggestion was investigated extensively; for example, *Lyons* [1974] calculated diffusion coefficients for resonance with the type of intense electrostatic waves observed by *Kennel et al.* [1970]. Recently, *Johnstone et al.* [1993] found that wave-particle interactions occur at energies below 10 keV. Although enhancements at low-electron energies were not observed in most of the events studied here, the few events that were identified indicate that wave-particle interactions at energies below 10 keV occasionally occur.

For one event during orbit 69 it was found that the enhancement in the ratio of precipitating to trapped fluxes at low-electron energies occurred in association with an overall flux decrease. This is different from the behavior observed for the high-energy electrons, where these events invariably accompany an overall increase in flux. The events that occur in association with an overall increase in flux can be understood in terms of pitch angle scattering into the loss cone alone. However, the events in which the precipitating to trapped electron flux ratio increases at a time when the overall fluxes are decreasing may indicate the presence of other mechanisms.

It is desirable to compare the measured fluxes of precipitating electrons with those expected theoretically from cyclotron interactions near the equator, calculated using the wave intensities measured at those positions in space. Such calculations have been performed under a variety of conditions [e.g., *Inan*, 1987] for single wave-particle interactions. However, in this paper the experimental data have mainly applied to bursts of waves lasting several minutes. The precipitation fluxes might therefore result from multiple wave-particle interactions in the near-equatorial region. The

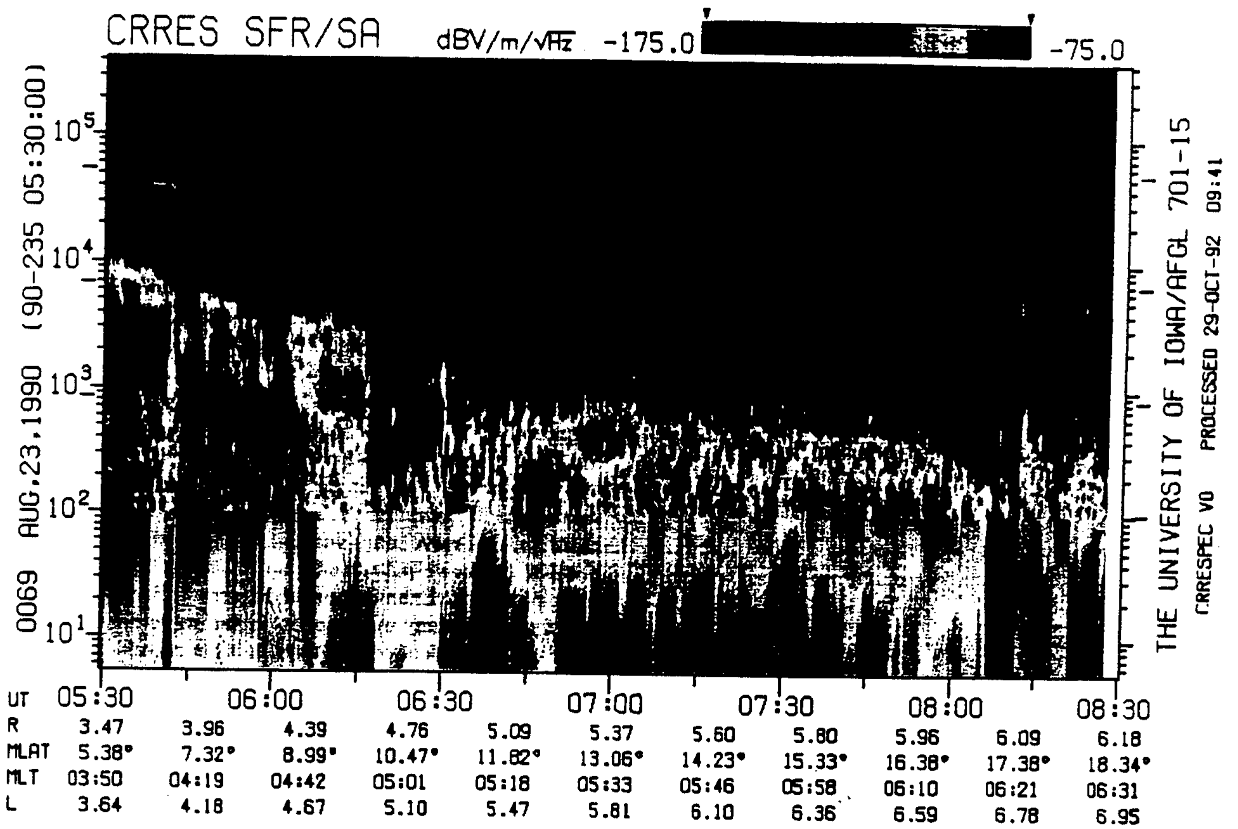

**Plate 1.** A spectrogram from the University of Iowa wave data.

latter processes may lead to enhanced fluxes at small equatorial pitch angles where the fluxes may be quite low and perhaps to a depletion in the fluxes mirroring nearer to the equator where the fluxes are higher. The latter situation may apply to the low-energy electron fluxes observed on orbit 69. To our knowledge, calculations of the expected precipitating fluxes for multiple wave-particle interactions have not been made, and therefore this comparison is considered to be beyond the scope of this paper.

The statistical results shown in Figures 2 and 3 indicate that these events occur most commonly in the dawn sector at *L* values >6. This distribution, when mapped to the ionosphere, is similar to the electron precipitation pattern mapped out by *Berkey et al.* [1974] using ground-based

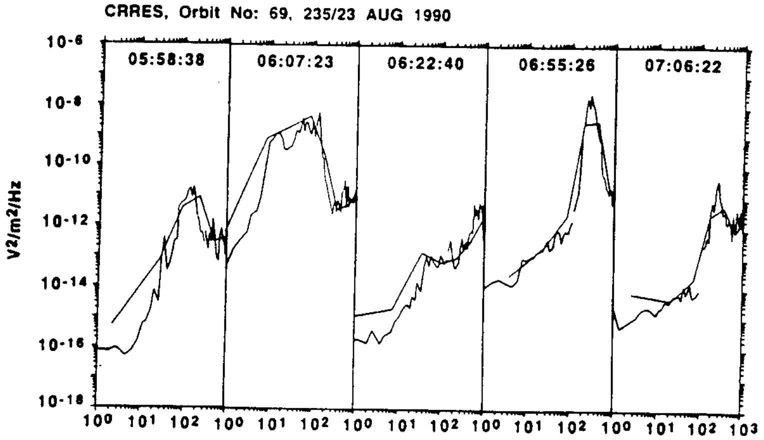

**Figure 9.** Plots of wave intensity versus the equivalent electron energy at selected times. The lines with fine structure represent the output from the sweep frequency receiver, whereas the other lines represent measurements from the multichannel spectrum analyzer.

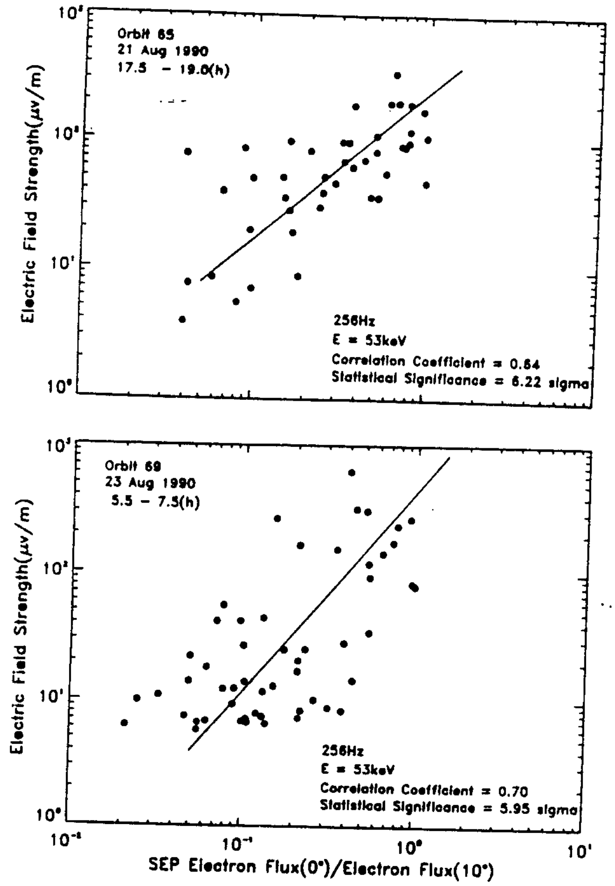

**Figure 10.** Electron fluxes versus the simultaneous electric field intensity.

riometer measurements. The riometers monitor $D$ region absorption resulting from precipitation of electrons with energies of several tens of keV. *Berkey et al.* [1974] showed that these electrons precipitate following substorm onsets in the midnight sector. The subsequent temporal development of the absorption is consistent with that expected from the eastward drift of a population of energetic electrons. These drifts follow approximately lines of equal $L$ value remaining roughly centered at $L = 6$. Furthermore, the distribution resulting from an isolated substorm very quickly reaches a configuration in which most of the precipitation is in the morningside auroral zone. Thus we speculate that the transient bursts described here are associated with the mechanism that precipitates energetic electrons injected at midnight during substorms. Typically, this precipitation takes the form of pulsating aurora, and it is tempting to account for the burstiness of the events described here in terms of individual pulsations. However, pulsating aurora typically display periodicity of the order of 15 s. No such periodicity is observed in the data presented here. On the other hand, the limitations set by the irregular sampling of the loss cone and the 132 s between adjacent samples could easily mask such periodic behavior. It would be more reasonable to examine the wave data for evidence of this periodicity because the wave instruments do not suffer from the sampling problems. Examination of Figures 4, 5, and 6 shows that there are many more spikes in the wave data than are apparent in the electron flux data. It is conceivable that each of these spikes is associated with an enhancement in the precipitating fluxes over the trapped fluxes, but because of the incomplete pitch angle coverage and the unfortuitous timing of the sampling interval, the enhancements do not show up in the particle data.

## Conclusions

The data presented here provide support for the *Kennel-Petschek* [1966] theory for pitch angle scattering of energetic electrons into the atmospheric loss cone. The high-angular resolution electron flux measurements show enhancements in fluxes near the loss cone relative to the trapped fluxes. When higher-frequency waves are present, the flux enhancements are seen at lower-electron energies in agreement with

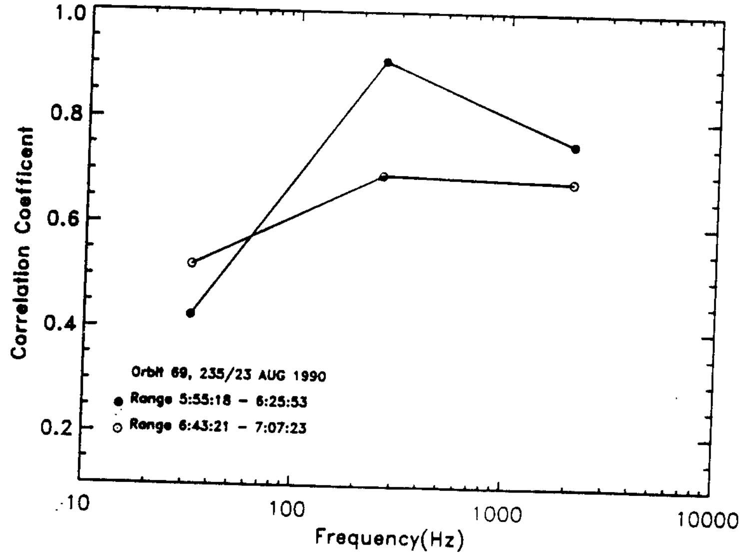

**Figure 11.** The wave-electron correlation coefficient versus the wave frequency.

the theory. In general, the best correlation between waves and particles is seen for wave frequencies near 256 Hz and for electron energies near 50 keV. Enhancements of electrons with energies as low as 1.7 keV are seen occasionally. The spatial distribution of the bursts is consistent with that expected from energetic electrons injected near midnight in association with auroral substorms.

**Acknowledgments.** The SEP and IMS-LO instruments are part of the ONR 307 experiment on CRRES, and much of the data analysis presented here was sponsored by the Office of Naval Research (contract N00014-83-C-0476). The Lockheed Independent Research Program provided partial support for the analysis. Special thanks are extended to J. P. McGlennon for his dedicated data analysis contributions. Appreciation is given for the contribution of R. R. Vondrak. Our thanks are owed to M. Schulz for helpful discussions. We would like to thank the referees for valuable comments. The Iowa effort was supported by NASA subcontract 9-X29-D9711-1 with Los Alamos National Laboratory. Special thanks are given to R. W. Lane from the University of Iowa, who did specialized programming. The U. C. Berkeley work was performed under Air Force contract F19628-92-K-0009.

The Editor thanks T. J. Rosenberg and A. D. Johnstone for their assistance in evaluating this paper.

## References

Anderson, R. R., D. A. Gurnett, and D. L. Odem, The CRRES plasma wave experiment, *J. Spacecr. Rockets*, *29*, 570–573, 1992.

Berkey, F. T., V. M. Driatskiy, K. Henricksen, B. Hultquist, C. Jelly, T. I. Shehuka, A. Theander, and J. Yliniemi, A synoptic investigation of particle precipitation dynamics for 60 substorms in IQSY (1964–65) and IASY (1969), *Planet. Space Sci.*, *22*, 255–307, 1974.

Collin, H. L., J. M. Quinn, G. R. Smith, E. Hertzberg, S. Roselle, and S. J. Battel, The low energy ion spectrometer (ONR-307-8-1, 2) on CRRES, *J. Spacecr. Rockets*, *29*, 617–620, 1992.

Imhof, W. L., R. R. Anderson, J. B. Reagan, and E. E. Gaines, The significance of VLF transmitters in the precipitation of inner belt electrons, *J. Geophys. Res.*, *86*, 11,225–11,234, 1981.

Imhof, W. L., R. R. Anderson, J. B. Reagan, and E. E. Gaines, Coordinated measurements of slot region electron precipitation by plasmaspheric wave bands, *J. Geophys. Res.*, *87*, 4418–4426, 1982.

Imhof, W. L., J. B. Reagan, H. D. Voss, E. E. Gaines, D. W. Datlowe, J. Mobilia, R. A. Helliwell, U. S. Inan, J. Katsufrakis, and R. C. Joiner, Direct observation of radiation belt electrons precipitated by the controlled injection of VLF signals from a ground-based transmitter, *Geophys. Res. Lett.*, *10*, 361–364, 1983.

Imhof, W. L., R. M. Robinson, H. L. Collin, J. R. Wygant, and R. R. Anderson, Simultaneous equatorial measurements of waves and precipitating electrons in the outer radiation belt, *Geophys. Res. Lett.*, *19*, 2437–2440, 1992.

Inan, U. S., Gyroresonant pitch angle scattering by coherent and incoherent whistler mode waves in the magnetosphere, *J. Geophys. Res.*, *92*, 127–142, 1987.

Johnstone, A. D., D. M. Walton, R. Liu, and D. A. Hardy, Pitch angle diffusion of low-energy electrons by whistler mode waves, *J. Geophys. Res.*, *98*, 5959–5967, 1993.

Kennel, C. F., and H. E. Petschek, Limit on stably trapped particle fluxes, *J. Geophys. Res.*, *71*, 1–28, 1966.

Kennel, C. F., F. L. Scarf, R. W. Fredericks, J. H. McGehee, and F. V. Coroniti, VLF electric field observations in the magnetosphere, *J. Geophys. Res.*, *75*, 6136–6152, 1970.

Lyons, L. R., Electron diffusion driven by magnetospheric electrostatic waves, *J. Geophys. Res.*, *79*, 575–580, 1974.

Lyons, L. R., R. M. Thorne, and C. F. Kennel, Pitch-angle diffusion of radiation belt electrons within the plasmasphere, *J. Geophys. Res.*, *77*, 3455–3474, 1972.

Nightingale, R. W., R. R. Vondrak, E. E. Gaines, W. L. Imhof, R. M. Robinson, S. J. Battel, D. A. Simpson, and J. B. Reagan, The ONR-307-3 spectrometer for electrons and protons on the CRRES Satellite, *J. Spacecr. Rockets*, *29*, 614–617, 1992.

Oliven, M. N., and D. A. Gurnett, Microburst phenomena, 3, An association between microbursts and VLF chorus, *J. Geophys. Res.*, *73*, 2355–2362, 1968.

Oliven, M. N., D. Venkatesan, and K. G. McCracken, Microburst phenomena, 2, Auroral-zone electrons, *J. Geophys. Res.*, *73*, 2345–2353, 1968.

Rosenberg, T. J., R. A. Helliwell, and J. P. Katsufrakis, Electron precipitation associated with discrete very low frequency emissions, *J. Geophys. Res.*, *76*, 8445–8452, 1971.

Rosenberg, T. J., R. Wei, D. L. Detrick, and U. S. Inan, Observations and modeling of wave-induced microburst electron precipitation, *J. Geophys. Res.*, *95*, 6467–6475, 1990.

Voss, H. D., et al., Lightning-induced electron precipitation, *Nature*, *312*, 740–743, 1984.

Wygant, J. R., P. R. Harvey, D. Pankow, F. S. Mozer, N. Maynard, H. Singer, M. Smiddy, W. Sullivan, and P. Anderson, The CRRES electric field/Langmuir probe instrument, *J. Spacecr. Rockets*, *29*, 601–604, 1992.

---

R. R. Anderson, Department of Physics and Astronomy, University of Iowa, Iowa City, IA 52242. (e.mail:SPAN:: IOWAVE::ANDERSON)

H. L. Collin, W. L. Imhof, and R. M. Robinson, Lockheed Palo Alto Research Laboratory, Department 91-20, Building 255, 3251 Hanover Street, Palo Alto, CA 94304 (e.mail:SPAN: lockhd::collin;SPAN:lockhd::imhof; SPAN:lockhd::robinson)

J. R. Wygant, Space Sciences Laboratory, University of California, Berkeley, CA 94720. (e.mail:SPAN:ucbsp::wygant).

(Received July 12, 1993; revised September 16, 1993; accepted October 5, 1993.)

Published in Physics of Space Plasma, No. 13, p.547, 1995.

# OBSERVATIONS OF POSSIBLE WAVE-PARTICLE INTERACTIONS IDENTIFIED BY THE CRRES PARTICLE CORRELATOR: PRELIMINARY COMPARISON WITH KENNEL-PETSCHEK THEORY

N. W. Watkins, P. J. Christiansen[1], C. G. Mouikis, S. C. Chapman
Space Science Centre (MaPS), University of Sussex, UK
M. P. Gough
Space Science Centre (ENGG), University of Sussex, UK,
J. R. Wygant
Space Sciences Laboratory, University of California, Berkeley, CA 94720
D. A. Hardy, K. J. Kerns and H. Singer[2]
USAF Phillips Laboratory, Bedford, MA 01731
C. Paranicas and M. Popecki[3],
Center for Space Physics, Boston University
H. L. Collin
Lockheed Palo Alto Research Labs., Palo Alto, CA 94304
A. D. Johnstone
Mullard Space Science Laboratory, University College London, UK
R. R. Anderson,
University of Iowa, Iowa City,

## ABSTRACT

We show preliminary direct observations of wave-particle interactions detected by the Sussex Particle Correlator Experiment (SPACE) on the CRRES satellite. The instrument performed real time in-situ cross correlations between electrons below 20 keV (later 30 keV) and waves in the 0 to 5 kHz region. As an illustration of the methodology in use we show an event during 13 October 1990, a moderately quiet day, when CRRES was in the post-midnight sector. Correlations appear to be observed between the electrons and wave emissions in the region of 1/3 of the electron gyrofrequency. At this time electrons measured by the Lockheed IMS-LO instrument showed shoulders (suggestive of positive $\partial f/\partial\alpha$ ) developing on the flanks of trapped distributions. Comparisons are shown between the correlator, wave and electron data. These results are discussed in terms of wave-particle resonance conditions and wave dispersion relation. Provisional results indicate that the

---

[1] deceased, 30 July 1992

[2] Now with NOAA Space Environment Laboratory, Boulder , Colorado

[3] Now at Institute for the Study of Earth, Oceans and Space, University of New Hampshire, Durham, NH 03824

fit of an n = −1 whistler mode resonance to the data is not good (assuming 10 keV as the critical energy) and hence that an alternative explanation is required. This hypothesis is qualified by reference to the particle count rate.

## I. PURPOSE OF SPACECRAFT PARTICLE CORRELATION

The wave particle-correlator (WPC) technique is aimed at the detailed in-situ exploration of wave particle interactions in space plasmas. The indirect approach previously applied [1] used particle data to infer distributions which could then, via dispersion solvers such as WHAMP, be used to predict observable wave modes. In contrast the WPC can, in principle, directly identify a region of two dimensional $(v_\perp, v_\parallel)$ particle phase space in which wave particle interactions are occuring, while returning the resonant wave frequency $\omega$ and a measure of the degree to which the particles are modulated by the waves. The linear resonance condition

$$\omega - k_\parallel v_\parallel = n\Omega_e \tag{1}$$

(where $\Omega_e$ is the electron gyrofrequency) then gives the value of $k_\parallel$, provided that $n$ can be deduced from the appropriate dispersion relation.

In the particular case of the USAF/NASA Combined Release and Radiation Effects Satellite (CRRES), launched in July 1990 and discussed here, the version of the WPC implemented can detect electron resonance with waves of intrinsic frequencies as high as 5 kHz (in the cross correlation function mode) or up to 30 kHz ( in "filter" mode), and as low as 250 Hz. On CRRES, the WPC estimates the direct cross correlation between the particles and the wave signal so the the degree of particle modulation by waves can be measured. The principal limitation of this technique is that it requires "sufficiently good" statistics, a constraint which must be defined for each implementation of the WPC.

The geometric factor of the electron detector is a function of energy (and, more weakly, of pitch angle) so that a greater differential number flux is required to make a measurement at lower energies, for example. This is shown for the specific case of CRRES in figure 1. The count rate also depends on $f(v)$ which in turn typically depends strongly on pitch angle [4], so unless a dedicated particle detector is used, it will not necessarily be possible to make statistically significant estimates of the extent of modulation over the whole $(v_\parallel, v_\perp)$ range.

---

[4] See for example the low energy electron data for CRRES illustrated in figure 3 which shows differential number flux peaked around 90 degrees pitch angle.

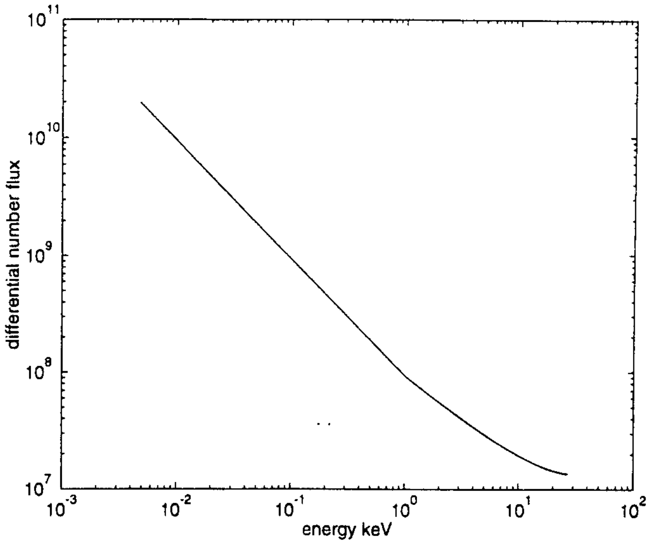

Figure 1: Differential number flux required to produce $10^4$ counts per second in three adjacent coarse zones of the CRRES correlator i.e. 1 every CCF bin, plotted as a function of incident electron energy.

The WPC technique was developed originally at Sussex [2] and has since been developed and modified both at Sussex and at Berkeley, the Max Planck Institute and the University of New Hampshire. First used on sounding rockets [3], the Sussex correlator has been used on more recent rocket experiments such as CAESAR 2 [4] on which bunching was observed on the primary auroral beam at the local $f_{UH}$ ( $\approx$ 3 MHz ) and on the satellites UOSAT 2, AMPTE-UKS and CRRES. It has most recently flown on Shuttle Tether [5]. The different implementations of the WPC are described in [9]

The **S**ussex **PA**rticle **C**orrelator **E**xperiment (SPACE) on CRRES was designed to perform in situ correlation of the particle counts from the Low Energy Plasma Analyser (LEPA) and the onboard electric field signal from the Berkeley wave instrument. SPACE was a programmable instrument and two types of operating mode were used during the lifetime of CRRES. We first consider those features of the instrument which were common to both. The Low Energy Plasma Analyser measured protons, and electrons from approximately 100 eV ( 10 eV for protons) to 30 KeV (for both). SPACE took as one input the electron signal from LEPA. The **E** - field wave signal was taken in from the Berkeley wave experiment via a wideband ( $< 30$ kHz) filter. It was then saturated using an operational amplifier to produce a square wave at the frequency of the highest amplitude wave mode present. This square wave was then used as a predictive filter on the particle counts by one of 2 methods. The square wave was either used as a frequency at which to bin the particle counts ( mode 0) or the 1 bit time series itself was used as a signal to correlate with a 1 bit particle count series (mode 9).

*SPACE MODE 0:* SPACE Operated for CRRES orbits through 416, all but 5 orbit pairs were mode 0 or the closely related mode 5. Mode 0 returned a calculated modulation significance by binning particle counts (in a given energy and pitch angle range) using a square wave at the frequency associated with the highest amplitude obtained from the above method. In this mode samples were taken of both particle counts and the square wave at a fixed rate (every $16\mu s$) for 4 ms. (allowing for frequencies up to 30kHz ). Although the frequency of the strongest wave could vary during that period the binning method is still valid. The result was the counts when the wave is high $N_H$ and the counts when the wave is low $N_L$. Modulation significance was then calculated, on the assumption of Poisson statistics, on board by:

$$Sig(E,\omega,\theta) = \frac{N_H - N_L}{\sqrt{(N_H + N_L)/2}}. \tag{2}$$

As there is less telemetry available than that required to send all the calculated significances, the highest recorded in each energy level is sent for each of 32 energy levels, 4 times per half spin [5].

Analysis of the mode 9 data is being used to "calibrate" the mode 0 data which is held currently at Sussex. In particular the dependence on frequency of the phase angle obtained from the FFTs can be assessed in mode 9 because phase angle as well as amplitude is returned, and this in turn can be used to assess the likely effectiveness of mode 0.

*SPACE MODE 9:* Here we consider data from mode 9 - the "cross correlation" mode. In this mode the particle counts, $Cp$, were recorded in $10^{-4}$ second bins. After 128 time bins the mean level was calculated, and used to set a particle bit "high" if the count in a given bin was greater than the mean, "low" if less than the mean, thus producing a square wave signal representing particle count rate, recorded as a 1 bit time series $Cp_i, i = 1, 2, ..., 128$. The saturated wave input, $Cw$, was measured at the end of each bin and the wave bit was set high if displacement is positive, zero otherwise, to produce a second 1 bit time series $Cw_i, i = 1, 2, ..., 128$. The result was thus two one bit time series, from which the correlator formed a direct one bit cross correlation function (CCF):

$$CCF(\tau) = \Sigma_{i=1}^{64} Cp_i Cw_{i+\tau} \tag{3}$$

and sent down the data at regular intervals corresponding to summation of

---

[5] 8 times in mode 5

not more than 23 individual CCFs [6] as 1 summed CCF. 15 of these summed CCFs were returned during every half spin ( approximately 15 seconds ) of CRRES, to give an indication of the variation of cross correlation with pitch angle. The pitch angle sensitivity of the technique is limited in practise because of the greater counts in the 90 degree direction.

The meaning of the 1 bit CCF may not be physically transparent, so we consider two artificial but illustrative examples. One is where the particles show no modulation by the waves, and the particle count rate is exactly $2 \times 10^4$ counts per second so $Cp_i$ is 1,1,1,1,1, ... If the wave frequency is 5kHz, [7] over the whole sampling interval, then the wave series is $1, 0, 1, 0, 1, \ldots$. We can see from equation (3) that $CCF(0) = CCF(2\tau) = CCF(4\tau) = 32$, but also that $CCF(\tau) = CCF(3\tau) = 32$ also, i.e. the resultant CCF is flat.

At another extreme is the case where a particle time series is strongly with the wave so that the particle counts correspond with the wave peaks only, i.e. the counts are $2, 0, 2, 0, 2, \ldots$ giving a particle time series $Cp_i$ of $1, 0, 1, 0, 1, \ldots$. The CCF then becomes $CCF(0) = CCF(2\tau)\ldots = 32$ whereas $CCF(\tau) = 0$. The mean value is thus 16, lower than before, but the degree of modulation is high, ie $max(CCF) - min(CCF) = 32 - 0 = 32$. The CCF is seen to be modulated at $1/(2\tau)$ ie 5kHz in this case.

Viewed in terms of sampling both the filter modes and mode 9 take near simultaneous ( of order $\mu s$ apart) samples of particle and waves at a fixed frequency. Mode 9 samples at 10 kHz to produce the CCF, while mode 0 samples at about 60Khz to produce the significance.

## II. MODE 9 OBSERVATIONS OF WAVE PARTICLE INTERACTIONS

We present an illustrative event observed by the Sussex Particle Correlator (SPACE) during orbit 194 on 1990 October 13, while operating in its wave-particle cross correlation mode (LEPA mode 9). Figure 2a) shows the correlator survey data from orbit 194 with the corresponding Iowa wave instrument survey plot given as Figure 2b). The energy of the electron input to SPACE from LEPA is shown plotted versus UT in the lowermost panel of figure 2a) , in mode 9 the instrument swept down from 20 keV[8] to 10 eV in 120 steps dwelling on one energy level during each half spin (14.3 seconds). In both types of plot the electron gyrofrequency calculated from the Phillips Laboratory **B** field data is shown as a solid black line. The top panel of figure 2a) shows the natural logarithm of the square of the amplitude (arbitrary units ) of the Fourier Transform (FFT) of the CCFs displayed on

---

[6] no onboard record of the number was calculated.

[7] the highest which can be resolved by a sampling frequency of 10kHz

[8] At this point the instrument had not been set to its maximum energy sweep range

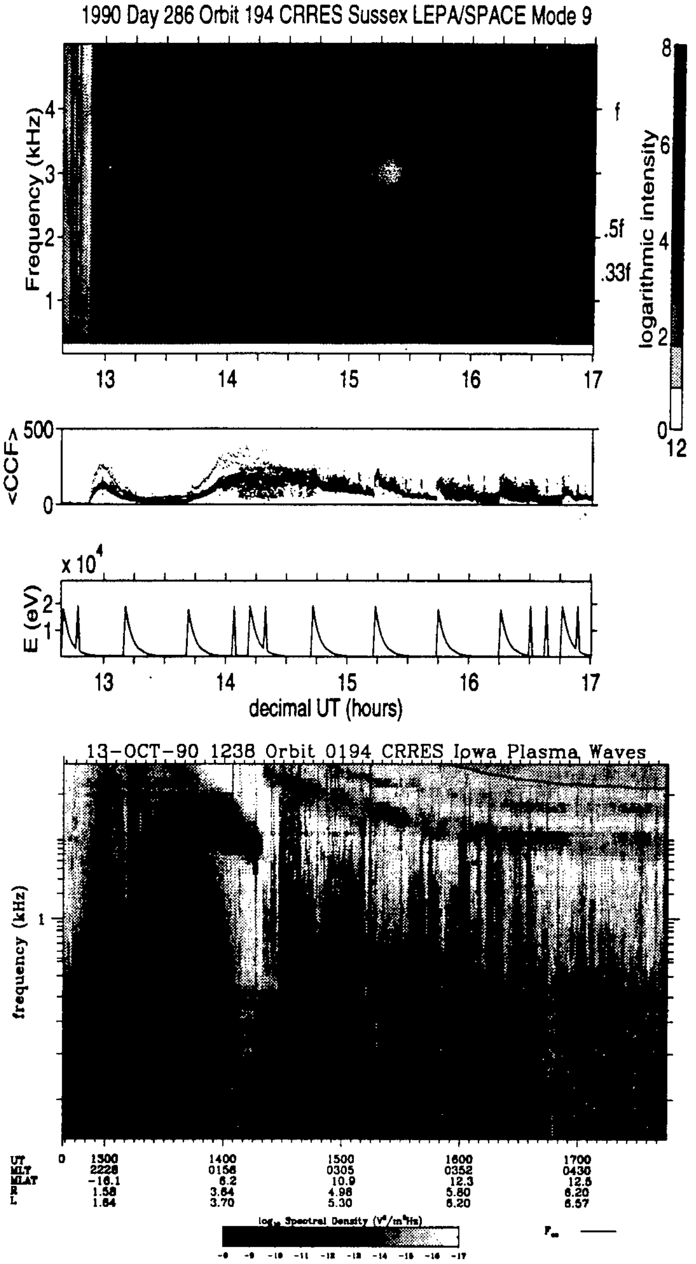

Figure 2: (a) Sussex Correlator Survey data from Orbit 194. (b) Iowa Wave Experiment survey data from orbit 194.

a plot of frequency (linear scale) versus UT and provides a measure of the spectral intensity [9] of the wave particle correlations observed by SPACE. The first correlator angular sector in each half spin is omitted as the particle detector voltage was still stabilising in this period. Each vertical stripe is an average over 4 successive half spins, approximately 1 minute. This can be directly compared with the wave spectrum as seen by the Iowa instrument plot, which shows E-field power density (again colour coded on a logarithmic scale) in a (logarithmic) frequency versus time plot, for the more extensive frequency range .01 to 400 KHz. On inspection of the survey plots we note that similar spectral features can be seen in both the WPC and wave plots but also that they are not identical. Note, however, that the correlator did not always receive E-field input throughout this orbit, during some of which the Berkeley instrument was in its Langmuir probe mode.

## III.OVERVIEW OF ORBIT 194

Figures 2a) and 2b) give an overview in UT for the event. It was a moderately quiet day ($K_p = 2+$), and a large negative bay in $D_{st}$ had occurred 3 days before. The spacecraft exited the plasmasphere at around 14:00 UT. Strong electromagnetic emissions below the electron gyrofrequency ( the dark line on the wave plot) appeared as early as 13:50 UT. The electromagnetic emissions fell in frequency as the spacecraft moved to increasing L value until at 14:45 UT they are both within the frequency range of the correlator and are being used as its input. The correlator then detects evidence of wave particle interactions in the form of large values of the amplitude of the FFT. Correlations with these emissions continue until around 1545. The energy of the particle input to SPACE from LEPA is shown plotted versus UT in the bottom panel of figure 2a), and we see that each burst in CCF "spectral intensity" occurs during a single 30 minute duration sweep in energy of the particle detector, suggesting that resonant particles may only detected in a restricted range of energies.

## IV.PRESENTLY KNOWN INSTRUMENTAL EFFECTS

Some artefacts are currently known to be present on the CCF plot (figure 2a). The correlator survey plots show high amplitudes associated

---

[9] The spectral intensity plotted here is analogous to the power density which would be obtained from an ACF

with the lowest Fourier mode, around the 200 Hz region. This is unlikely to be physical because any time dependence in the wave or particle inputs will produce a response in the first Fourier mode. This effect is probably a result of the count rate variation with time resulting from the continual scanning of pitch angle. Also just visible are regular downward sweeping features which pass through the gyrofrequency and which relate to the periods when the particle instrument is reset to 20 keV [10] This latter effect is caused by a small, $\approx 1\%$, voltage ripple remaining on the electrostatic analyser plates. When the spectrum has a significant change of count rate with selected energy this ripple will cause the detected counts to be modulated because of the sensitivity of the correlation technique. There is also the possibility of aliasing due to fixed sampling rate. We can only guard against this by comparison with the wave data.

## V.HIGH RESOLUTION PLOTS

We will focus on the time from 14h 45m to 15h 45m UT. The SPACE data from all energy sweeps between the plasmapause crossing at about 14:00 UT [11] and 17:00 UT where the LEPA instrument changed mode have been examined, and a high amplitude in the "spectral density" is found during two sweeps, at 14:40 -15:10 UT and then at 15:10 - 15:40 UT. The spacecraft moves from L $\approx 5-6$ and through magnetic latitudes $\lambda \approx 10-12^o$ over the interval spanning the events. The wave plot shows a persistent sub-cyclotron feature throughout this period with no gross change in the type of emissions.

The properties of a given CCF can be characterized by the frequency at which the amplitude of the FFT of the cross correlation function between the wave and particle signals is at its greatest. As we have already stated that the wave with which the CCF is formed is effectively square because of the "clipping" operation that has been performed on it, it is only the maximum amplitude that is likely to be physical.

In addition, the measurement provides the energy and pitch angle of the particles apparently resonant at this frequency.

See figure 4a and 4b for the periods 14.76 to 15.23 decimal UT, and where SPACE data is shown at medium resolution. The top panels simply show each energy sweep at higher resolution, the axes are Fourier mode (32 corresponding to 5 kHz) versus the number of spin pairs since the beginning

---

[10] three times over a full energy sweep. This is not always visible in the energy panel of the correlator survey plot - figure 2a) but is visible in the mean level of the CCF in the panel above.

[11] See fiducial marks on figure 2b)

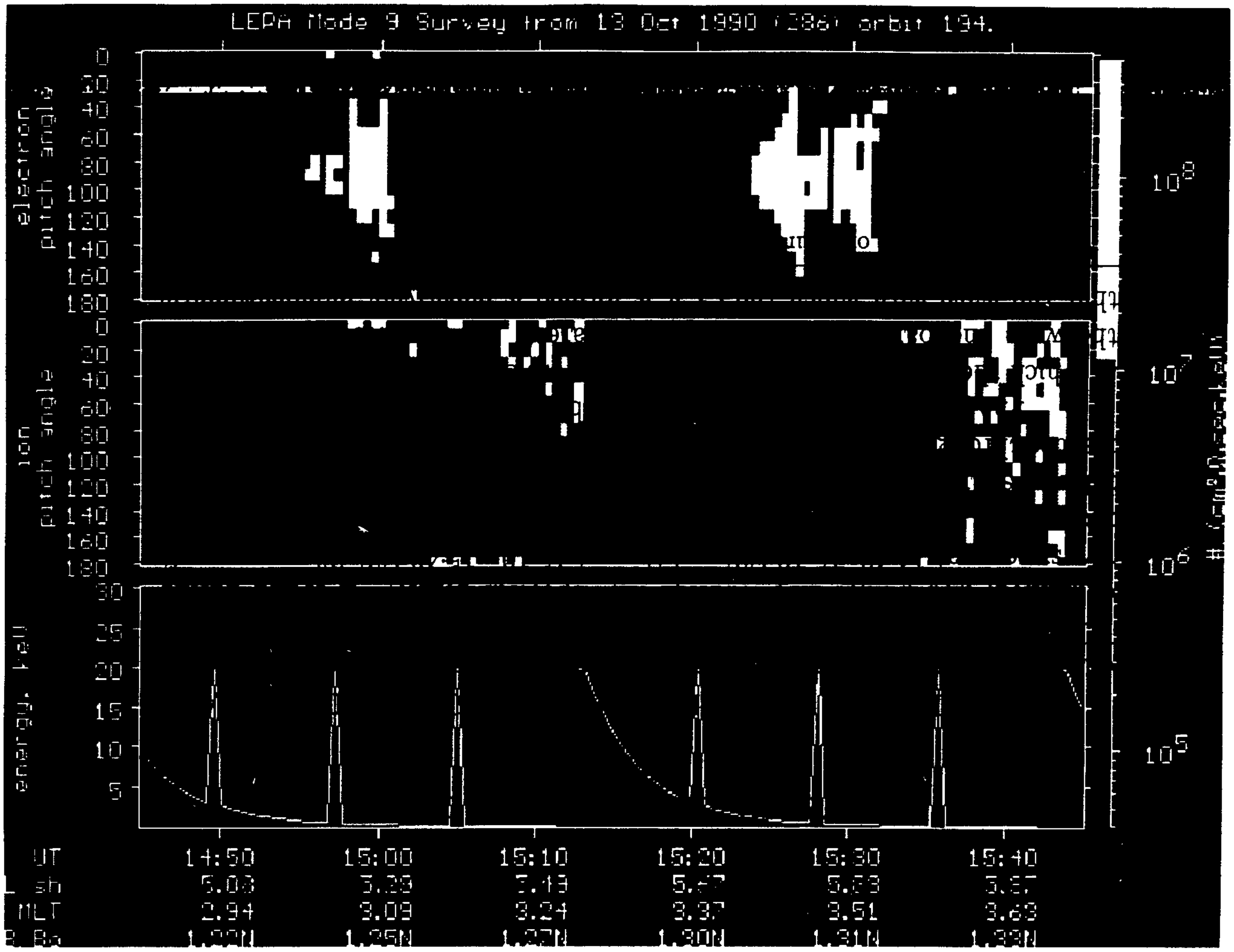

Figure 3: LEPA mode 9 Survey data for 1445 to 1545 UT on orbit 194

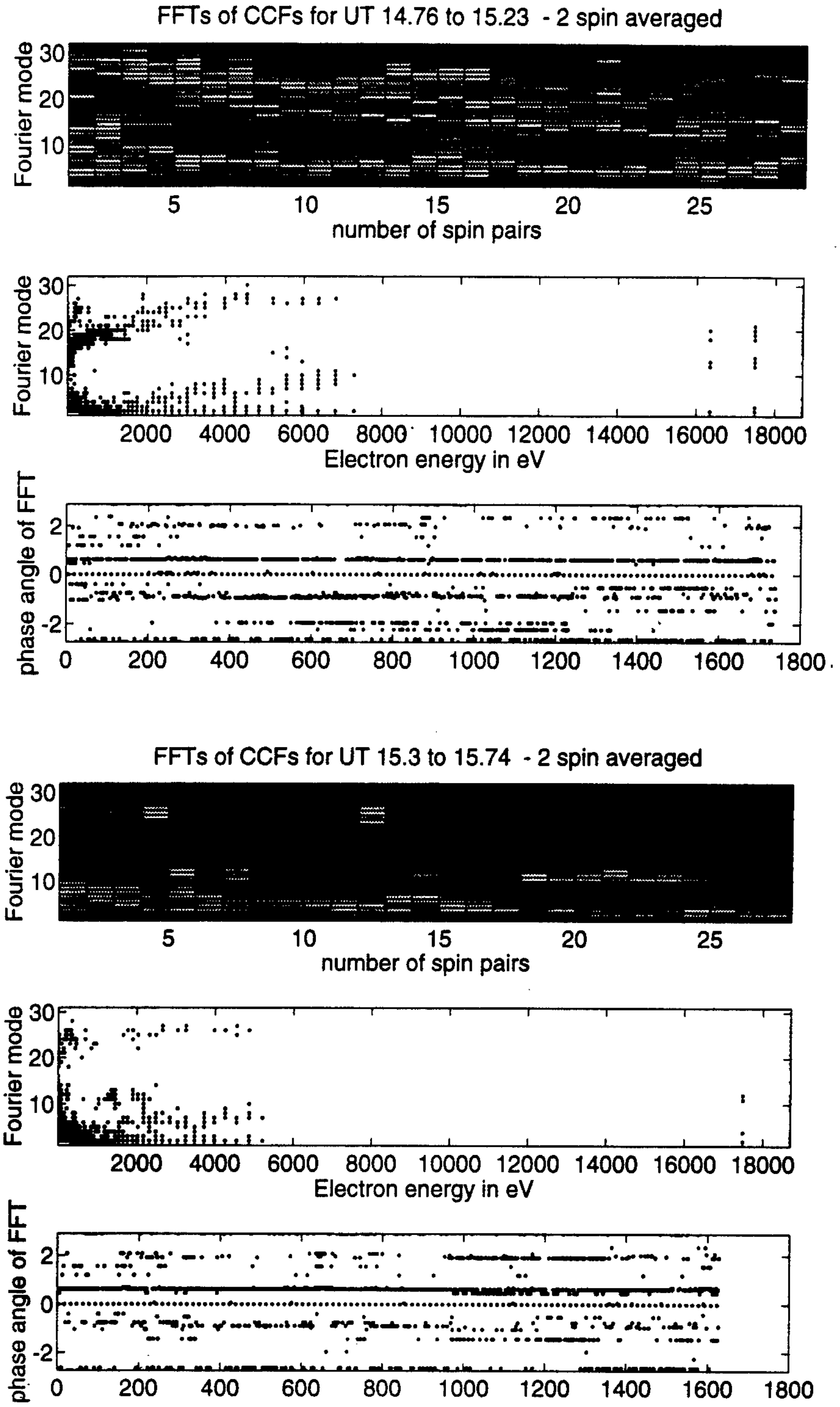

Figure 4: a)Sussex Correlator data from Orbit 194 - medium resolution . First event b) Second event

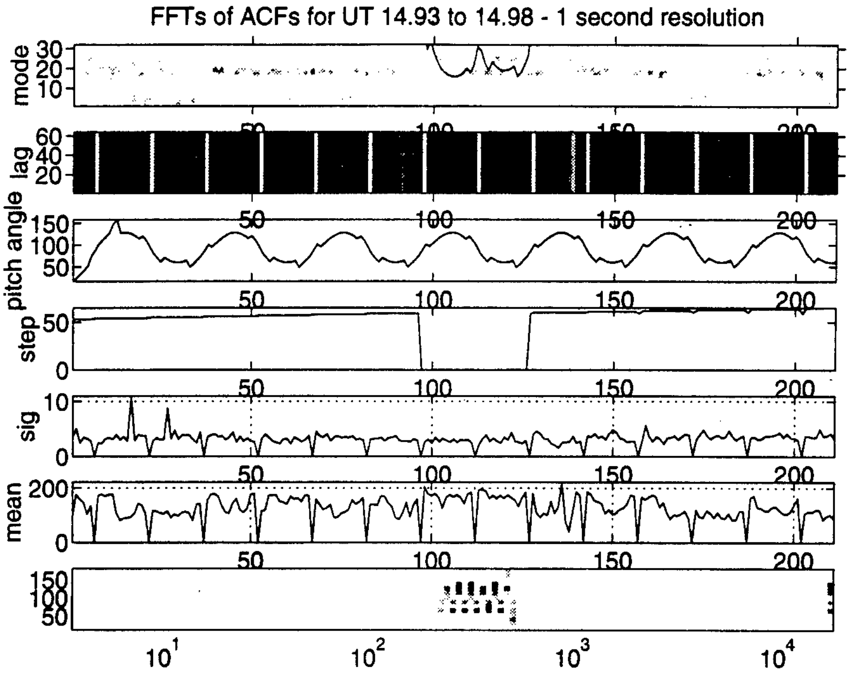

Figure 5: Sussex Correlator data from Orbit 194 - fine resolution

of the period shown, one spin pair is approximately 1 minute. The third panel of each figure is on the same time axis, here expressed in terms of seconds (ie the approximate length of each summed CCF). The y-axis is the phase angle associated with the maximum value of the amplitude. The middle panel of both figures shows the relation of the frequency at which the maximum amplitude of each FFT was recorded, and the electron energy. For an electron of energy $E$ there will be a series of possible resonant $\omega$s on the $(\omega, E)$ surface depending on pitch angle and the wave mode.

The two periods of SPACE data, which show similar wave data, appear to show noticeably dissimilar patterns here, and this may be evidence of wave particle interactions occurring. This hypothesis is under further investigation.

Figure 5 shows a high resolution plot of SPACE data from 14.93 to 14.98 UT. The top panel 5a) shows the FFT of the CCF, the second, 5b) shows the original raw CCFs. The third 5c) shows the pitch angle range swept out by the 3 zones from which correlator data is taken. The next 5d) shows the energy step of LEPA [12], the fifth, 5e), shows a crude measure of the degree of modulation of the CCF ie

$$max(CCF) - min(CCF)/\sqrt{mean(CCF)}. \tag{4}$$

In fact we will need a better measure of significance involving the actual particle count rate, as the meaning of $max(CCF) - min(CCF)$ depends on how many counts were taken in the interval, ie how "difficult" it would be to obtain this configuration purely randomly.

The sixth 4f) shows the mean level of the cross correlation function and the seventh shows a pitch angle versus energy versus summed modulation plot .

Figure 5f) at first sight suggests that the event may have a resonant population which is strongly collimated perpendicular to the magnetic field (the scatter from the perpendicular direction is of order the $\pm 5^o$ error in determining the pitch angle). We must however also consider electron counts as revealed by LEPA survey data (Figure 3) and that from IMS-LO (Figure 6) which show evidence of electrons scattering into the loss cone just before 1500, and "shoulders" developing on trapped distributions at 1450 onwards, respectively.

## VI. COMPARISON WITH KENNEL AND PETSCHEK

---

[12] Energy $E$ in keV is obtained from the step $n$ by $E = 20(0.9349)^{n+1}$

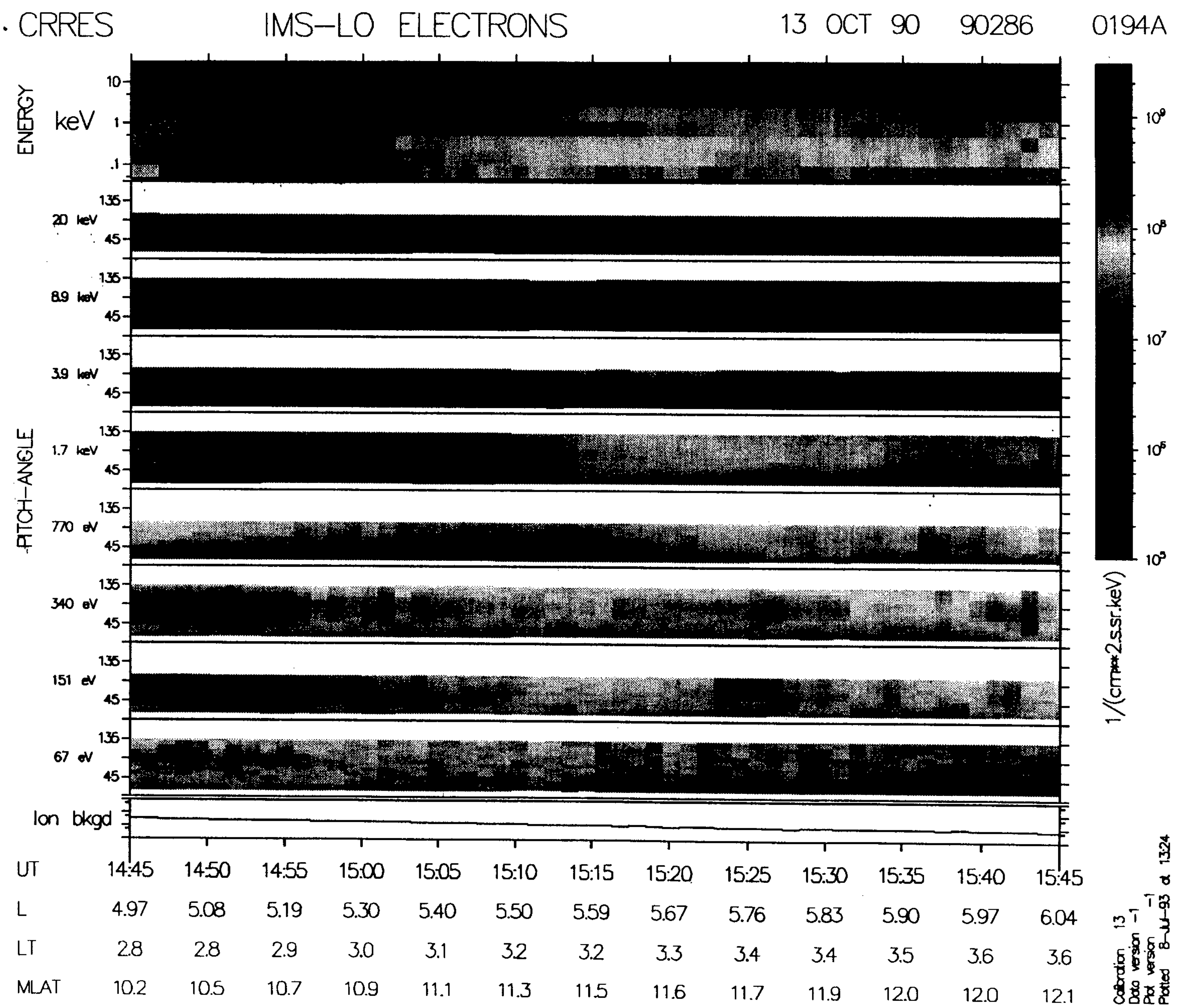

CRRES
IMS-LO ELECTRONS
13 OCT 90
90286
0194A
ENERGY
keV
10
1
.1
PITCH-ANGLE
135
20 keV
45
135
8.9 keV
45
135
3.9 keV
45
135
1.7 keV
45
135
770 eV
45
135
340 eV
45
135
151 eV
45
135
67 eV
45
Ion bkgd
$10^9$
$10^8$
$10^7$
$10^6$
$10^5$
1/(cm**2.s.sr.keV)
UT 14:45 14:50 14:55 15:00 15:05 15:10 15:15 15:20 15:25 15:30 15:35 15:40 15:45
L 4.97 5.08 5.19 5.30 5.40 5.50 5.59 5.67 5.76 5.83 5.90 5.97 6.04
LT 2.8 2.8 2.9 3.0 3.1 3.2 3.2 3.3 3.4 3.4 3.5 3.6 3.6
MLAT 10.2 10.5 10.7 10.9 11.1 11.3 11.5 11.6 11.7 11.9 12.0 12.0 12.1
Calibration 13
Data version -1
Plot version -1
Plotted 8-Jul-93 at 13:24

We have attempted to fit a whistler $n = 1$ resonance to our data (as first done in [6]), using Kennel-Petschek [7] methods as recently described by Johnstone et al [8]. Our method is to calculate resonant energy $E_R$ from electron data and pitch angle, and estimate the "critical" energy $E_C$ as 10 keV (we do not yet have the estimate of cold plasma density from the Iowa wave instrument which would give us a better value here ). We then calculate resonant frequency $\omega/\Omega_e$ and plot it - see figure 5f). The fit is not convincing but at this preliminary level of analysis this is not surprising and further efforts in this direction will proceed in parallel with a detailed examination of the data.

## VII. CONCLUSIONS.

We know that linear resonance can occur at any perpendicular velocity, but only at a specific parallel velocity, given by the resonance condition (See eg [7]).

More detailed analysis is required to determine the wave modes that could be in resonance with these particles, but here the cross-correlation technique has been shown in use in the context of an apparent wave particle interaction event.

Detailed modelling of the instrument response is being undertaken (see [9]), to refine the threshold above which a measured CCF can be considered significant.

Simulation using a 2D EM PIC code is underway ( see P Devine, S C Chapman, J W Eastwood, "Simulation of Whistler Mode waves in an isotropic plasma" in this volume), which will have applications to this programme.

## ACKNOWLEDGEMENTS

We are grateful to Tim Yeoman for providing activity indices. NWW has been supported by SERC Grant GR/J02438 to Sussex University, and CGM and NWW acknowledge support from the USAF Window on Science programme, under grant WOS WOS-93-2038.

This paper is dedicated to the memory of Peter Christiansen.

## REFERENCES

[1] Ronmark K and Christiansen P. J., Nature, **294**, 335 (1981)

[2] M. P. Gough M. P., Nucl. Inst. Meth., **177**, 581 (1980)

[3] Gough M. P., Nature, **287**, 15, (1980)

[4] Gough M. P., Christiansen P. J. and K. Wilhelm J. Geophys. Res., **95**, 1287 (1990)

[5] Gough M.P. et. al., EOS Trans. AGU., **73**, No. 43, 425, (1992)

[6] Christiansen P.J. et. al., EOS, Trans. AGU, **72**, No. 44, 408 (1991)

[7] Kennel C.F and Petschek H. E., J. Geophys. Res., **71**, 1, (1966)

[8] Johnstone, A.D., Walton, D.M., Liu, R. & Hardy D.A., J. Geophys. Res. , Vol. 98, pp 5959 - 5968 (1993).

[9] C. G. Mouikis, P.J. Christiansen, S. C. Chapman, and N.W. Watkins, "The University of Sussex wave-Particle Correlator: Computer Simulation of Instrument Response", in Proceedings of START Conference, Aussois, France, 31 January- 5 February, ESA WPP-047, pp. 409-412 (1993)

Pergamon

*Adv. Space Res.* Vol. 17, No. 10, pp. (10)83–(10)87, 1996
Copyright © 1995 COSPAR
Printed in Great Britain. All rights reserved
0273–1177/96 $9.50 + 0.00

0273-1177(95)00698-2

# SUSPECTED WAVE–PARTICLE INTERACTIONS COINCIDENT WITH A PANCAKE DISTRIBUTION AS SEEN BY THE CRRES SPACECRAFT

N. W. Watkins,[1] J. A. Bather,[1] S. C. Chapman,[1]
C. G. Mouikis,[1] M. P. Gough,[2] J. R. Wygant,[3] D. A. Hardy,[4]
H. L. Collin,[5] A. D. Johnstone[6] and R. R. Anderson[7]

[1] *Space Science Center (MAPS), University of Sussex, Falmer, Brighton BN1 9QH, U.K.*
[2] *Space Science Center (ENGG), University of Sussex, Falmer, Brighton BN1 9QH, U.K.*
[3] *School of Physics and Astronomy, University of Minnesota, MN, U.S.A.*
[4] *USAF Phillips Laboratory/GPSG, Bedford, MA, U.S.A.*
[5] *Lockheed Palo Alto Research Center, Palo Alto, CA, U.S.A.*
[6] *Mullard Space Science Laboratory, University College London, U.K.*
[7] *Space Science Laboratory, University of Iowa, U.S.A.*

## ABSTRACT

On 1990 October 13 the Sussex Particle Correlator Experiment on the USAF/NASA Combined Release and Radiation Effects Satellite (CRRES) observed modulation in the onboard wave-particle correlation functions at frequencies between one third and one half of the electron gyrofrequency during the period from 14:45 UT to 15:45 UT. At this time the Iowa plasma wave experiment measured chorus emissions in the region of one third of the local electron gyrofrequency, and the Lockheed IMS-LO electron instrument observed an apparent velocity dispersion event in electrons between 770eV and 20 keV, beginning at about 15:12 UT. We describe the particle correlation technique, briefly present this event, and then describe an approach to testing the hypothesis that wave-particle interactions were responsible for the large modulation seen in the particle correlator. Recent work on the statistical analysis of such data is presented.

## 1. INTRODUCTION

An outstanding problem in space plasma physics is to demonstrate directly the occurence of wave particle interactions (WPIs) in the magnetosphere, because of their expected importance in the transfer of energy and momentum in space plasmas, which are essentially collisionless. The family of particle correlation techniques all aim to perform in-situ measurement of linear, resonant wave particle interactions (WPI) in space plasmas. The particle autocorrelator (PAC) technique originated at Sussex /1/, and was first used on sounding rockets /e.g. 5/ although the earlier work of /2/ had measured the frequency spectrum of a fixed energy electron detector. The correlator concept was since developed and modified both at Sussex and at Berkeley -where it is also referred to as the phase correlator - (eg /3,4/ and references therein), the Max Planck Institute and the University of New Hampshire. All correlator designs have in common that they look for periodicities in the input of a particle detector that match those of a component or components of the input of a wave detector. What differentiates the second generation wave-particle correlators (WPCs) is that they use a wave detector as a predictive input, whereas the PAC, in calculating an autocorrelation function is estimating one of a more general class of structure functions on the particle time series produced by the detector. WPC designs differ in the type of amplitude and phase information they can return about the degree of particle modulation by the waves (e.g. the percentage of particle bunching if any).

From linear theory, for a wave mode of frequency $\omega$, resonance can occur only at specific electron parallel velocities $v_{\parallel}$ in the electron frame, given by the resonance condition

$$v_{\parallel} = \frac{(n\Omega_e + \omega)}{k_{\parallel}} \tag{1}$$

where $\Omega_e$ is the electron gyrofrequency, and $n$ is an integer.

From quasi-linear theory, the consequence of near-resonance is bunching of the particles about a given phase /10/. The aim of the correlator is to evaluate a structure function (such as the autocorrelation function (ACF)), or an estimate of cross correlation on the available particle and wave time series, over given regions in energy-pitch angle space, in order to detect this bunching. As a low energy electron instrument samples a range of energies and pitch angles the WPC can, in principle, directly identify a region of phase space in which wave particle interactions are occuring. The resolution in phase space depends on how the electron instrument is dividing up the energy and pitch angle space, and on the $\Delta E/E$ of electron instrument, which governs the intrinsic resolution of $v_{\parallel}$. One must also consider $\Delta\omega/\omega$ which is more subtle in effect and dependent on the mode in which the correlator instrument is being operated. The strengths of the instrument include that it can measure wave phenomena with intrinsic frequencies as high as 5 kHz in the cross correlation mode discussed in this paper, with a frequency resolution of 160 Hz. A general problem is that comparison of measurements made at different points in the energy-pitch angle space requires that the count rate must be high enough to allow statistically significant measurements. The counts will however, for a real particle distribution, depend on pitch angle, and so one cannot compare all of phase space in practice unless the particle counter provides enough counts at the lowest particle densities. unlikely for other than a dedicated particle instrument. Other limitations are specific to the type of correlator employed, in the case discussed below a cross correlation function is only capable of looking at linear relationship between waves and particles /8/. In our case we have a 64 point cross correlation function so significant $\sqrt{N}/N$ statistical noise is inevitable. Despite all these caveats the experiment can in principle perform in situ measurement of wave-particle interactions, and so represents a potential advance over the indirect methods used so far.

## 2. THE SPACE INSTRUMENT FOR CRRES

The SPACE experiment on CRRES was designed to perform in situ correlation of the particle counts from the Low Energy Plasma Analyser (LEPA) and the onboard wave signal from the Berkeley electric field/Langmuir probe instrument. The $E$ - field wave signal was taken in from the electric field experiment via a wideband ( less than 30 kHz) filter and then put into an operational amplifier in order to extract the highest amplitude wave mode by clipping. The wave signal was then used as a predictive filter on the particle counts. In the mode considered here and at this stage in the mission LEPA detected electrons from $\approx$ 100 eV to 20 KeV. The correlator used fixed rate sampling of the square wave (at $10kHz$ in the mode considered here) to form a 1 bit time series corresponding to wave displacement. At this point several different types of correlation estimators were then possible, depending on the mode of operation.

We present observations from the correlator's cross correlation mode. in which the raw particle counts including background, $C_p$, were recorded in 128 bins each $10^{-4}$ seconds in duration. At this point. provided that there was at least 1 count in each bin [corresponding to a count rate of $10^4$ per second] the average level was used to set the corresponding bit of $C_p$ high (1) if the counts in that bin were greater than the mean, low (0) if less than mean. The saturated wave input. $C_w$, was measured at the end of each time bin and wave bit set "high" if displacement was positive, zero otherwise. The result was two 1 bit time series which could be cross correlated. If counts were on average less than one per bin however the original time series was not replaced, but any $C_p$ that was greater than 1 was replaced by one. The count rate into what was not a dedicated particle instrument was usually less than $10^4$ per second including background and so this was usually the applicable regime.

Frequently the un-normalised linear cross-correlation function between these two time series would be estimated by (see for example, /8,9/ ) :

$$s_k^{(l)} = \sum_{i=0}^{128-|k|-1} Cp_i Cw_{i+k} \tag{2}$$

The notation $|k|$ indicates that time lags of $\pm k$ are defined, and $k$ runs from 0 (the zero lag), to 127. This means that there will be $2 * 128 - 1$ i.e 255 terms in the function. Unlike an autocorrelation function it will not be symmetric in $k$. It also means that the $kth$ term is formed from $128 - k - 1$ terms. However, if we instead consider only postive lags up to 63 we can have an alternative one-sided direct one bit cross correlation function (CCF) where the 64 terms $s_k^{(c)}, k = 1, 64$ are given by:

$$s_k^{(c)} = \sum_{i=1}^{64} Cp_i Cw_{i+k}. \tag{3}$$

These two estimators would be equivalent (see /6/ p.270) in the limit $N \to \infty$. $s_k^{(c)}$ is calculated on CRRES. and 23 of the above functions are then transmitted as 1 accumulated CCF denoted by $S_k$, once per second i.e approximately 15 times per half spin. Note that the zero lag is not sent.

## 3. MODE 9 OBSERVATIONS OF WAVE PARTICLE INTERACTIONS

We will consider an example of an observation made by the Sussex Particle Correlator (SPACE) while operating in its wave-particle cross correlation mode. This was during orbit 194 on 1990 October 13. Figure 1 (a) the shows WPC survey data from orbit 194 with the corresponding Iowa wave instrument survey plot as Figure 1 (b). The energy of the particle input to SPACE from LEPA is shown plotted versus UT in the lowermost panel of figure 1 (a). We see that the instrument sweeps down from 20 keV to 10 eV in 120 steps dwelling on one energy level during each half spin (14.3 seconds). The top panel of figure 1 (a) shows the magnitude ( the square root of the modulus squared ) of the Fourier Transform of the summed CCFs (divided by 32) displayed on a plot of frequency (linear scale) versus decimal UT. This provides a measure of the relative spectral intensity of the wave particle correlations observed by SPACE The first WPC angular sector is omitted as the voltage is still stabilising in this period. Each vertical stripe is an average over 4 successive half spins, approximately 1 minute. It should be noted that the WPC did not always receive E-field input throughout this orbit, during some of which the Berkeley instrument was in Langmuir probe mode.

Strong chorus emissions below the electron gyrofrequency (the continuous dark line on figure 1(b)) appeared as early as 13:50 UT. The electromagnetic emissions fall in frequency as the spacecraft moves to increasing L value. The two highest values of the magnitude of the spectral density can be seen at 14:30 and 15:15 on figure 1 (a). In only one case, however, is the input into the correlator known to be a valid periodic wave signal, the later of the two points. The earlier is from the Langmuir probe. We want to determine if either of these two events is likely to be due to a wave particle interaction. Because the magnitude of the associated spectral power is not sufficient to discriminate (as borne out by the modelling performed in /11/) between these two cases, we seek a more unambiguous indicator.

## 4. ANALYSIS AND MODELLING

The WPC is operating in a regime where the ratio of count rate to characteristic wave frequency is less than or of order unity. The typical maximum quiet-time electron count rate for LEPA (including background) on CRRES was 2 or 3 times $10^3$ per second, which has been established from a systematic survey of LEPA data. This implies that the instrument is usually in the second of the 2 régimes discussed above. Confirmation of this is the dependence of the mean value of the cross correlation functions on the energy of the electrons, and thus on the count rate, which can be seen

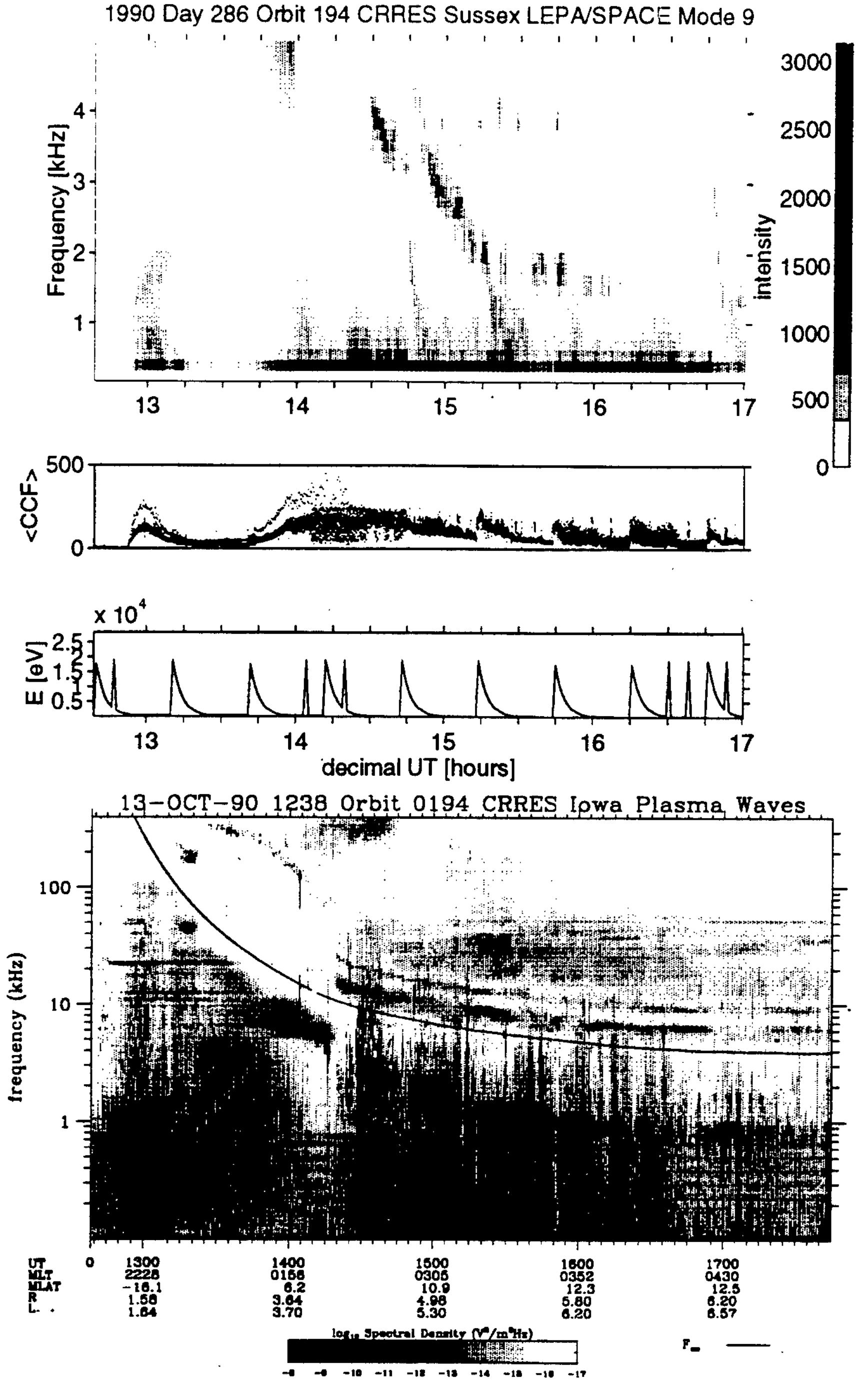

Figure 1: (a) Top panels: Sussex Correlator Survey data from Orbit 194. (b) Bottom panel: Iowa Wave Experiment survey data from orbit 194. The gyrofrequency is marked by a solid line.

in figure 1 (a).

We thus need to design a statistical test that will help us to decide whether the interactions apparently observed by the WPC are statistically significant. We test the hypothesis $H_0$ ie that the random arrival times of the particles are completely independent of each other against the hypotheses $H_k$ that there is a modulation of period $2k$.

This can be done by calculating the set of test statistics

$$t_k = (S_1 - S_k)^2/(S_1 + S_k) \tag{4}$$

where the $S_k$ are defined as above and $k$ runs from 1 to 33. Preliminary testing using simulated data and 5 kHz modulation suggests that this is a valid approach /7/. This is now being generalised to other frequencies and to real WPC data from this and other events. The technique relies on our ability to independently estimate the $k$ at which we should be testing, which we can do by examining the wave data. Providing that we can establish through simulation the characteristic distributions for values of $t_k$ taken from unmodulated and modulated particle series, we should be able to compare these with the values obtained from real data and thus, by consideration of individual observations, ascertain whether there are indeed wave-particle interactions being observed. It is intended to report the detailed results of these tests, for several CRRES orbits, in a future paper.

More detailed analysis is required to determine the wave modes that could be in resonance with these particles, here the cross-correlation technique has been shown in use in the context of a possible wave-particle interaction events.

## ACKNOWLEDGEMENTS

We would like to acknowledge the help of Chris Paranicas and Mark Popecki in producing the wave plot used as figure 1(b), and Kevin Kerns in analysing and reducing the LEPA data. NWW acknowledges the support of PPARC grant GR/J 02438 and NWW and CGM acknowledge the assistance of the USAF office of Aerospace Research under the Window on Science Programme.

This paper is dedicated to the memory of Peter Christiansen.

## REFERENCES

1. Gough M. P.,*Nucl. Inst. Meth.*, 177, 581, 1980
2. Spiger R.J., et al,*Rev. Sci. Instrum*, 45, 10,1974
3. R.E.Ergun, *J. Geophys. Res*, 96, 225, 1991
4. Muschetti L., Roth I. and R.E.Ergun., *Phys. Plasmas*, 1(4), 1008, 1994.
5. Gough M. P., *Nature*, 287, 15, 1980
6. Bendat J.S. and A. G. Piersol, *Random Data: Analysis and Measurement Procedures*, 2nd Edition, Wiley, 1986.
7. Watkins N.W., Mouikis C. G., Chapman S.C., Christiansen P.J., Gough M.P., Wygant J.R., Hardy D.A. and A.D.Johnstone, in *Current Topics in Astrophysical and Fusion Plasma Research*, Proceedings of International Workshop and Winterschool in Plasma Physics, Pichl/Schladming, Austria, 28 February - 5th March 1994, eds. M. F. Heyn, W. Kernbichler and H. K. Biernat, 1994
8. Lynn P.A., *Digital Signals, Processors and Noise*, Macmillan, 1992.
9. Krauss T.P., Shure L. and J. N. Little, *Signal Processing Toolbox Users Guide*, The Mathworks Inc., 1993.
10. Melrose D. B., *Instabilities in Space and Laboratory Plasmas*, Cambridge University Press, 1986.
11. Mouikis C.G., *The University of Sussex Particle Correlator: Computer Simulation of Instrument Response and Observations in the Foreshock and the Magnetopause*, D Phil thesis, Sussex University,1994.)

# Association of Waves with Narrow Particle Dropouts in the Outer Radiation Belt

W. L. Imhof, J. Mobilia, H. D. Voss*, H. L. Collin
Lockheed Martin Palo Alto Research Laboratory
Palo Alto, California 94304

M. Walt
STARLAB, Stanford University
Stanford, California 94305

R. R. Anderson
Department of Physics and Astronomy
University of Iowa, Iowa City, Iowa 52242

J. R. Wygant*
School of Physics and Astronomy
University of Minnesota, Minneapolis, Minnesota 55455

4/7/97

# Association of Waves with Narrow Particle Dropouts in the Outer Radiation Belt

W. L. Imhof, J. Mobilia, H. D. Voss*, H. L. Collin
Lockheed Martin Palo Alto Research Laboratory
Palo Alto, California 94304

M. Walt, STARLAB, Stanford University, Stanford, California 94305

R. R. Anderson, Department of Physics and Astronomy, University of Iowa,
Iowa City, Iowa 52242

J. R. Wygant+, School of Physics and Astronomy, University of Minnesota,
Minneapolis, Minnesota 55455

## Abstract

An investigation has been made of the association of plasma waves with narrow dropouts (<30 minute observation time) in the fluxes of trapped energetic electrons and protons within the radiation belts. The experiment, conducted with instruments on the CRRES satellite, indicates that 5 Hz <frequency< 1 kHz waves are nearly always produced at the times and positions of narrow energetic

electron flux dropouts. The waves may be produced at the positions of steep particle flux gradients. This phenomenon is best studied during short duration events that provide measurements on both sides of a boundary in a relatively quiescent state. In addition to an investigation of the waves associated with narrow dropouts the data presented here show the general correlations between waves and particle fluxes, particularly after new injections or plasmapause crossings. In some cases energetic proton dropouts also occur and may contribute to the generation of waves.

* Now at Physics Dept, Taylor University, Upland, Indiana

+ Formerly at Space Sciences Laboratory, University of California, Berkeley, California

## Introduction

At synchronous or near-synchronous orbit long duration (≥30 minutes) decreases in the fluxes of energetic electrons and protons have been observed followed by very rapid increases (e.g. Walker et al., 1976; Erickson et al., 1979; Sauvaud and Winckler, 1980; Nagai, 1982; Baker and McPherron, 1990; Baker et al., 1993; Nakamura et al., 1994; Thomsen, et al., 1994; Moldwin, et al., 1995; Fennell et al., 1996). Most of these decreases have been interpreted as resulting from the relative motion of the satellite with respect to various boundaries such as (a) the outer trapping boundary, (b) the boundary between closed field lines and the open field lines in the tail lobes, or (c) the magnetopause. Flux dropouts associated with the growth phase of substorms have also been attributed to betatron deceleration in the changing geomagnetic field (Sauvaud et al., 1996). The subsequent flux recoveries, especially cases when the flux increased above the pre-dropout level, have often been associated with the expansion phase onset of magnetospheric substorms. Most of these observations have been made from satellites in geosynchronous orbit, which is nominally at L = 6.6.

In addition, short duration (<30 minute) flux dropouts have been observed both at synchronous altitude (Su et al., 1976; Sergeev et al., 1992, Kopanyi and Korth, 1995) and on lower L shells (Yeager and Frank, 1969; Kaufmann et al., 1972; Korth et al., 1995). None of the above studies included data on the local plasma wave environment which might be expected to change as the satellites crossed boundaries or encountered currents or strong flux gradients.

The short duration dropouts at lower L values have not been studied as thoroughly as the more prolonged events, and their source mechanism(s) is (are) not as well understood as those of longer duration. Short duration events, particularly those in which the particle fluxes return to their pre-dropout values, are more likely due to the transit and subsequent return of the satellite across a plasma boundary than due to a major deformation of the magnetosphere accompanying a substorm injection of particles. In many of the long duration dropouts the plasma and wave environment at the end of the dropout may be quite different from conditions at the start. Thus, the short duration events offer a better possibility of studying the particle and wave environment on each side of a boundary in a relatively quiescent state.

Waves are known to cause particle precipitation from the radiation belts through wave-particle interactions, but based on the fact that both electrons and protons over a wide range of energies are involved in the dropouts it is not likely that the particle dropouts are caused by such processes. However, VLF and ELF waves may still play an important role in the overall structure of dropouts. In particular, plasma instabilities such as drift wave instabilities in inhomogeneous plasmas are expected to occur at strong particle flux gradients. Also, electron and ion pitch angle distributions should be different on each side of the plasma boundary, and the waves produced by pitch angle anisotropies should reflect this difference. It is therefore of interest to investigate whether dropouts are associated with the generation of waves in the magnetosphere. The waves can be used as a diagnostic of the boundary motion and of the plasmas involved.

The primary purpose of this paper is to present coordinated data on trapped particle fluxes and plasma wave intensities at the times of narrow particle dropouts. As the comparisons will show, these quantities are not related in any simple way although simultaneous changes in both particle and wave intensities occur frequently. This research therefore provides data against which theories of wave and particle energy exchange can be tested. Here we make use of VLF and ELF wave and energetic particle measurements performed from the CRRES (Combined Release and Radiation Effects Satellite) which had a highly eccentric, nearly equatorial orbit. The wave environment in and near the regions of narrow particle dropouts is investigated for evidence that the large gradients in particle flux are also regions of enhanced plasma waves. To identify times of observation of particle gradients the entire data set from the Spectrometer for Electrons and Protons (SEP) was surveyed for narrow (<30 minutes observation time) pronounced dropouts in the electron fluxes within the outer radiation belt. At the times of such events data from other detectors in the CRRES payload were examined.

## Instrumentation

The CRRES satellite was launched on July 25, 1990 into an orbit with an apogee of 35,786 km, a perigee of 350 km, and an inclination of 18°. Apogee at launch was at about 0800 local time, and the spacecraft precessed toward earlier local times at a rate of about 15 hours per year. The satellite spin axis was kept pointed within 15 degrees of the sun.

The particle data used here were acquired with the ONR 307 instruments on CRRES. One of the instruments in the payload was the Spectrometer for Electrons and Protons (SEP). This instrument measured the energy spectra of electrons over the range 40 keV to 5 MeV with silicon solid-state detectors oriented at 80°, 60°, and 40° to the satellite spin axis. The spectrometer had an angular resolution of ± 1.5°(Nightingale et al., 1992). In normal operations the instrument was configured in four different modes, two for electrons and two for protons. It remained in each mode for 32 seconds. Electron data were also obtained from the Ion Mass Spectrometer-Lower Energy (IMS-LO) spectrometer in three broad energy bands centered at 1.7, 3.9, and 8.9 keV at 75° to the satellite spin axis and with an angular resolution of ± 2.5° (Collin et al., 1992). Further details on these electron spectrometers are available in the referenced papers.

The Ion Mass Spectrometer-Higher Energy (IMS-HI) instrument (Voss et al., 1992) measured the energy spectra and pitch angle distributions of ions and neutral particles from a few tens of keV to a few hundred keV. The IMS-HI instrument was based on ion momentum separation in a magnetic field followed by a measurement of total energy deposition in a solid-state detector. After exiting the collimators, ions entered a 7000-G magnetic field where they were deflected into various sensors depending on their momentum. Seven cooled (-50° C) solid-state sensors were used in an array at various deflection angles. The instrument featured simultaneous momentum and energy analysis at relatively large geometric factors (between $10^{-3}$ and $10^{-2}$ $cm^2$ sr). The look direction from the spin axis was 75° with a pitch angle resolution of ± 2°. The energy range for the proton measurements used here was 18 to 360 keV.

In the inner radiation belt both SEP and IMS-HI may be sensitive to penetrating protons. Therefore, at $L \leq 2$ the particle fluxes measured by these detectors may have a poorly defined background. Since none of the events discussed in this paper are in the inner zone, this background is not important here.

The electric and magnetic field wave data used in this study were provided by the University of Iowa/Air Force Geophysics Laboratory (AFGL) Plasma Wave Experiment and the University of California at Berkeley/AFGL Electric

Field/Langmuir Probe Experiment. The Iowa/AFGL instrument included a Sweep Frequency Receiver (SFR) and Multichannel Spectrum Analyzer (MCA) which together provided electric field wave measurements from 5 Hz to 400 kHz and magnetic field measurements from 5 Hz to 10 kHz (Anderson et al., 1992). The Berkeley/ AFGL experiment (Wygant et al., 1992) measured electric and magnetic waveforms over frequencies ranging from quasistatic to 40 kHz. The instrument also provided continuous monitoring at several samples per second of the wave amplitudes measured through 3 broadband filters with maximum responses at frequencies of 32 Hz, 256 Hz, and 2048 Hz.

Electric field wave data in the frequency range 5 Hz to 400 kHz were available during most orbits. Due to an instrument failure the magnetic component of the waves was not measured after orbit 602. Thus, while both electric and magnetic wave amplitudes were compared with particle dropouts up to orbit 602, only electric field intensities could be compared with dropout cases after that orbit.

## Examples of Wave and Particle Variations

Since the flux falloffs and recoveries associated with the dropouts have a variety of shapes and amplitudes, a single criterion was used in the selection of narrow dropouts from the electron survey plots. The investigation presented in this paper has been limited to dropouts having an intensity decrease of at least a factor of 10 and an observed duration time for electrons of less than 30 minutes. Associations of the waves with broader particle dropouts are also observed to occur, but that aspect of the phenomenon has not been studied in this investigation. The selection of dropout cases was made from electron data only and was completed before any comparisons were made with the proton and wave data.

### A. *Data from Orbit 186, October 10, 1990*

An example of correlated particle and wave data is shown in Figure 1 where selected energetic electron and proton fluxes for the full 10-hour time interval of orbit 186 are plotted in the middle sections of Figure 1. The particle fluxes shown are averaged over the full range of pitch angles. The bottom section of the figure is a spectrogram (frequency versus time with a color code for intensity) from the Iowa electric field wave instrument during the satellite pass. The electron cyclotron frequency, Fce, determined from the magnitude of the ambient magnetic field measured by the CRRES Magnetometer Experiment (Singer et al., 1992) is indicated by the thin red line drawn across the plot. The magnetic and electric field wave data in 14 frequency channels are plotted separately in different sections. On this orbit CRRES exited the plasmasphere through a very steep plasmapause at 0638 UT when L = 3.0, R = 2.70 Re, Magnetic Local Time (MLT) = 1.0 hours, and the magnetic latitude was 15 degrees. It re-entered the plasmasphere through a very steep plasmapause at 1458 UT when L = 2.8, R = 2.40 Re, MLT = 10.0 hours, and the magnetic latitude was 20 degrees. Geomagnetic activity was high throughout orbit 186. The NOAA World Data Center A for Solar Terrestrial Physics geomagnetic and solar data (Coffey, 1991) in fact identified October 10 as the most geomagnetically disturbed day of the month with the 24-hour sum of Kp being 37+. October 8 had been the second quietest day of the month with the 24-hour sum of Kp being 8+ and the 24-hour sum of Kp was 19 for October 9.

The high-time resolution electric and magnetic field spectrum analyzer plots from 5 Hz to 10 kHz and electric field spectrograms that extend to 400 kHz show the following features. The primary naturally occurring electromagnetic phenomenon inside the plasmasphere is a broadband isotropic plasmaspheric hiss band between 100 Hz and a few kHz. The whistler mode hiss emissions are most likely amplified by anisotropies in the radiation belt electrons. A band of chorus between 100 hz and 10 kHz extends across the plamaspause crossing at 0638 UT. This band intensified at the leading edge of the dropout at 0735 UT. It did not continue after the dropout as is best seen in the uppermost section of Figure 1. Beginning at about 0705 UT the electron cyclotron harmonic (ECH) waves in the band just above Fce and electrostatic ELF waves from 5 Hz to a few hundred Hz intensified. Sporadic electrostatic bursts in the 1 kHz to 10 kHz range also began around 0705 UT. Around 0725 UT, immediately before the particle dropout, the electrostatic ELF band disappeared or diminished in intensity by more than two orders of magnitude. This band re-appeared 10 minutes later at the leading edge of the narrow particle dropout. In fact, at 0735 UT there was a broadband peak in both the electric field noise and the magnetic field noise from 5 Hz up to 10 kHz. These narrow bursts of noise are probably related to the currents which are responsible for a noticeable deflection in the magnetic field at 0735 UT (Singer, personal communication, 1995). The electrostatic ELF band and higher frequency electrostatic noise continued after the dropout. Weak impulsive bursts of electromagnetic noise across much of the spectrum analyzer band (5 Hz to 10 kHz) occurred occasionally after the dropout.

The intensification of the ECH waves and the electrostatic ELF waves as well as the occurrence of the sporadic electrostatic waves and electromagnetic chorus in the period from around 0705 UT to nearly 0735 UT is most likely related to the injection of electrons as indicated at that time in the 77 keV electron data shown in Figure 1.

Many wave aspects near the inbound plasmapause crossing at 1458 UT were similar to those previously noted at the outbound crossing. An electromagnetic broadband hiss band extending from around 30 Hz to above 5 kHz was in its mid-frequency range one to two orders of magnitude more intense inside the plasmasphere than it was immediately outside the plasmapause. A strong chorus band began near 1300 UT and rose in frequency from 200 Hz at 1300 UT to 20 kHz at the plasmapause where it ended. This band varied in frequency roughly as $r^{-6}$. It was especially intense from 1355 UT to 1420 UT. The second short term dropout in the electron data was centered on 1250 UT. For nearly one hour prior to the dropout only a narrow electromagnetic band from 56 Hz to 311 Hz was evident in the magnetic field data. The strong chorus band with the $r^{-6}$ dependence began immediately following the narrowband dropout. The electron data show that a weak electron injection occurred around 1100 UT when the narrowband electromagnetic emissions began. Immediately following the narrowband dropout another electron injection occurred that increased the fluxes several orders of magnitude over the previous injection. These electron fluxes are probably responsible for the chorus band.

### *B. Other Examples of Waves Associated with Dropouts*

A detailed examination of the wave and particle data has just been made for one complete orbit in which several pronounced variations were observed. In order to achieve a larger statistical sample for the wave and particle comparisons, data are now presented from twelve orbits in which electron flux dropouts with short observation times occurred. These data are provided in Figures 2 to 5. The electric field wave data are presented in the bottom sections in the form of spectrograms from the Sweep Frequency Receiver and in other panels as plots of the output of the Multichannel Spectrum Analyzer. For the orbits before 602 the magnetic field wave data are presented in an upper section. Fluxes of particles at selected energies averaged over the full range of pitch angles are plotted. Arrows are shown below the Sweep Frequency Receiver data to indicate the times of the selected narrow electron flux dropouts. At these times vertical lines are drawn through much of the data. It should be noted that on occasion one or more of the instruments are not acquiring data due to spacecraft moding. The electric field wave and electron flux data are plotted on an expanded time scale in Figure 6 for four orbits.

The criteria used for selection of dropouts were that they be very pronounced and of short duration (<30 min). This restriction led to a very limited number of cases such that it was not practical to analyze different categories of dropouts separately in various Kp and MLT intervals. Since the maximum Kp over the previous 24 hours was 4 or greater in all of the cases, it is reasonable to identify all of the events as occurring during geomagnetically disturbed times. The MLT range of the dropouts was also limited, being concentrated in the midnight sector. Consequently, information on the MLT distribution of the short dropout phenomena is not available.

The examples of Figures 2 to 6 illustrate the general correlation of waves with particle dropouts as well as the lack of consistent one-to-one correspondence of individual wave bursts with particle fluctuations. The proton flux reductions often took place simultaneously with the electron dropouts, for example in orbits 279, 542 and 766 but not in 583 and 902. Wave enhancements occurred in the regions of isolated particle dropouts as well as in other regions where the particle fluxes varied rapidly. For example, orbit 615 had multiple occurrences of wave bursts over a three hour period during which time the proton and electron fluxes changed erratically.

In almost every case, strong low frequency electric field turbulence was observed at or very near the time of the narrow dropouts as is most easily seen in the spectrograms. All of the orbits with dropouts prior to orbit 602 showed enhanced low frequency electromagnetic bursts at or near the time of the dropouts except for orbit 583, as shown in Figure 3. On orbit 583 strong low frequency electrostatic and electromagnetic emissions were observed associated with what appears to be the start of a narrow flux dropout in the electron data about 0830 UT. The electromagnetic bursts evident around 0930 UT began higher in frequency than those observed for the majority of the narrow dropouts. Inspection of the high time resolution data for all of the orbits showed that the most intense wave activity usually occurred at steep flux density gradients at the leading and trailing edges of the narrow dropouts.

Frequently bands of chorus were observed either just prior to or just after the narrow dropouts. This phenomenon is illustrated in Figure 3 for orbits 547 and 583 (and for orbit 547 in Figure 6) where chorus begins immediately after the narrow dropouts. The appearance or disappearance of chorus after a narrow dropout may indicate that the spacecraft has crossed a boundary into a different region.

On orbit 186 shown in Figure 1 electromagnetic chorus preceded the first narrow dropout (see MAG ANTENNA panel) and did not continue immediately after the dropout. For the second dropout, chorus was sharply enhanced after the narrow dropout. On orbits 279 and 542 shown in Figure 2 (also in Figure 6 for orbit 542) chorus was not associated with the dropouts. On orbit 279 the chorus ended near 1330 UT as the fluxes of the highest energy electrons fell dramatically. It reappeared about 1530 UT when the fluxes of highest energy electrons increased dramatically. On orbit 542 the chorus ended around 1100 UT when the electron fluxes gradually dropped as the spacecraft moved to the outer portion of the outer radiation belt. The chorus reappeared suddenly about 1200 UT at the time electron flux levels increased enough to sustain chorus generation. Then chorus deminished again around 1300 UT as the flux levels continued to fall. During these injections the outer magnetosphere apparently has sufficient plasma to support intense electromagnetic waves.

For orbit 615 shown in Figure 4 it is clear that the electric field emissions associated with the boundaries of the narrow dropouts just after 1100 UT are very similar to various emissions throughout the interval 1100 UT to 1300 UT including those associated with the narrow spike in the electron flux just after 1000 UT. In Figure 4, orbits 615 and 666 show examples of narrow dropouts occurring in the middle of a region of plasma generating strong electric field noise. Orbits 686 and 737 (in both Figure 4 and Figure 6) also show examples of narrow dropouts at the boundary leading into a region generating intense electric field noise.

The data for orbit 759 in Figure 5 illustrate the similarity of the electric field waves in a narrow dropout region to those associated with a sudden injection of plasma. For orbit 766 we see how intense the electric field waves are for strong and continuous injections of both electrons and protons. For orbit 766 we see that a period of very little wave activity also preceded the plasma injection occurring just before 0730 UT.

## *C. Short Term Fluctuations*

For investigation of shorter time scales ($\Delta t < 30$ min) the electric field wave data at three different frequencies are plotted in the upper sections of Figures 7 and 8 for a one hour interval. For the investigation of short term fluctuations the proton measurements from IMS-HI were used in preference to the electrons measured with the SEP instrument whose time resolution was 2 minutes. In the lower two sections of Figure 7 are plotted the fluxes of protons at 18 and 56 keV averaged over the full range of pitch angles.

While some individual wave bursts occur simultaneously (within ≈ 15 sec) with the proton changes (for example the bursts at 14:00:30 in Figure 7 and at 5:15:15 in Figure 8), numerous wave bursts of about 30 seconds duration have no association with proton changes.

The data from the three filters presented in Figures 7 and 8 indicate that the rms amplitude of the electric field is often stronger in the lower frequency filters than the higher frequency filters. The electric field fluctuations reach amplitudes of 5 to 10 mV/m during periods of peak power. Comparisons of the sinusoidal modulation of the filter outputs (at twice the spacecraft spin period) to the orientation of the electric field booms relative to the ambient magnetic field direction indicate that the fluctuation amplitude is greatest when the booms are perpendicular to the magnetic field direction. These comparisons imply that the waves are predominantly polarized perpendicular to the magnetic field during these events. It should be noted that the filters average the fluctuation amplitude of the electric field over one second, and the peak amplitudes measured with higher time resolution can be significantly higher.

Each of the narrow energetic electron dropouts selected in the survey of the CRRES data is listed in Table 1. All of these narrow dropouts had observation durations of less than 30 minutes. The table lists several quantities associated with the start of recovery from the dropout: UT in hours, MLT, L, Kp, and Dst. The presence or absence of a dropout in the ions is indicated. Two columns indicate whether there was a change in the VLF electrostatic or electromagnetic wave intensity. High energy ion dropouts occurred simultaneously with electron dropouts in more than half of the cases whereas low energy ion dropouts were present during only about a quarter of the electron dropouts.

## Discussion

The data presented here have shown the general correlations between wave intensities and particle fluxes. The most pronounced correlations occurred at the times of new particle injections or plasmapause crossings. Strong wave intensities frequently occurred in association with broad dropouts at the time of substorms. However, the principal objective of this paper has been to study the interesting phenomena of narrow particle dropouts which have been found frequently to be associated with wave enhancements.

The energetic particle dropouts are caused by the satellite suddenly entering a substantially different plasma environment having much less ($<10^{-1}$)

particle flux than experienced immediately before or after the dropout. These flux changes often but not always occurred for all energetic particle types observed. However, the time profiles of the particle flux are sometimes quite different for electrons and protons. One would expect slightly different boundaries for the various species and energies since the different populations have different gyroradii and drift velocities. Also the ions and electrons drift in opposite directions. In some cases the thermal plasma also showed a strong density reduction, as would be expected if the satellite passed into field lines leading to the tail. The magnetic field frequently increased during the particle dropouts in agreement with the expected diamagnetic behavior of the plasma.

A coarse time scale ($\Delta t \geq 30$ min) comparison of wave and particle intensities during the time interval surrounding the dropout events reveals that a general increase in wave intensity for 5 Hz <freq<1 kHz occurs at or near the time of each dropout. The occurrence of wave bursts is so infrequent that their association with particle flux changes cannot be by chance. In the course of this investigation of narrow dropouts some broad dropouts were also examined, and it was discovered that wave enhancements often occurred near the edges of the broad dropout at times of sharp decreases or increases in energetic particle flux. The association of waves and particle dropouts is not perfect, however. While wave enhancements almost always occur near the dropouts, bursts of wave activity are sometimes seen at times when there are no observable changes in particle fluxes. This finding may be attributed to the narrow localization of the particle fluxes in comparison with the more widespread nature of the waves.

A detailed comparison of waves and particles on very short time scales ($\Delta t<30$ sec) shows a much weaker correlation. In some cases a sudden change in particle flux (at the edge of the dropout) coincided with a pronounced change in the wave environment (see for example orbits 279 and 542), although in many cases the initial times were several seconds apart. Some flux features, peaks or valleys, as short as 15 seconds duration appeared to coincide with enhanced or reduced wave amplitude. In these cases, an increased particle flux sometimes accompanied an increase in wave amplitude and sometimes a reduced wave amplitude. Most of the time, however, the detailed structure of the particle fluxes (feature less than 30 seconds long ) did not correspond consistently with wave data.

We interpret the coarse time scale observations in association with narrow particle dropouts as indicative that waves are produced at or near the particle boundaries which define the sudden flux changes. These waves propagate some distance from the generation site and hence only a general correlation with particle boundaries is observed. The probability of detecting the waves depends both on the generation strength as well as the propagation path and will therefore depend on the detailed plasma properties and geometry in particular cases. For fine scale observations the lack of a consistent correlation between the waves and the particle fluxes may result from the difference in spatial extent of the two quantities.

An alternate interpretation might be constructed in which the waves scattered the particles and thereby produced the sudden reductions in trapped flux. This possibility appears very unlikely in that a resonance interaction would not be expected to affect all particle types over a broad range of energies simultaneously. Furthermore, even in the strong diffusion limit with the loss cone filled, the overall particle loss rate is limited by the number of particles in the loss cone as they reach the atmosphere. Because of the small size of the loss cone at the satellite position for these data, over 1.5 minutes would be required to deplete the electron population and several hours would be needed for the protons.

## Acknowledgments

The SEP, IMS-LO, and IMS-HI instruments are part of the ONR307 experiment on CRRES, and much of the data analysis presented here was sponsored by the Office of Naval Research (contracts N00014-83-C-0476 and N00014-94-C-0042). The Lockheed Independent Research Program provided partial support for the analysis. Special thanks are extended to J. P. McGlennon and J. Beeler for their dedicated data analysis contributions. Interactions with H. J. Singer were very helpful. Appreciation is given for the contribution of R. R. Vondrak. The research effort at the University of Iowa has been supported by NASA under subcontract 9-X29-D9711-1 with Los Alamos National Laboratory. Special thanks go to R. W. Lane for his programming efforts and to M. D. Brown for producing the wave data plots. The U. C. Berkeley work was performed under Air Force contract F19628-92-K-0009.

## References

Anderson, R. R., D. A. Gurnett, and D. L. Odem, CRRES plasma wave experiment, J. Spacecr. Rockets, 29, 570-573, 1992.

Baker, D. N., and R. L. McPherron, Extreme energetic particle decreases near geostationary orbit: a manifestation of current diversion within the inner plasma sheet, J. Geophys. Res., 95, 6591-6599, 1990.

Baker, D. N., T. I. Pulkkinen, R. L. McPherron, J. D. Craven, L. A. Frank, R. D. Elphinstone, J. S. Murphree, J. F. Fennell, R. E. Lopez, and T. Nagai, CDAW 9 analysis of magnetospheric events on May 3, 1986: event C, J. Geophys. Res., 98, 3815-3834, 1993.

Coffey, H. E., Geomagnetic and solar data, J. Geophys. Res., 96, 1885, 1991.

Collin, H. L., J. M. Quinn, G. R. Smith, E. Hertzberg, S. Roselle, and S. J. Battel, The low-energy ion spectrometer on CRRES, J. Spacecr. Rockets, 29, 617-620, 1992.

Erickson, K. N., R. L. Swanson, R. J. Walker, and J. R. Winckler, A study of magnetosphere dynamics during auroral electrojet events by observations of energetic electron intensity changes at synchronous orbit, J. Geophys. Res., 84, 931-942, 1979.

Fennell, J. F., J. L. Roeder, H. E. Spence, H. Singer, A. Korth, M. Grande, and A. Vampola, CRRES observations of particle flux dropout events, Adv. Space Res., Vol. 18, No. 8, 217-228, 1996.

Kaufmann, R. L., J. T. Horng, and A. Konradi, Trapping boundary and field-line motion during geomagnetic storms, J. Geophys. Res., 77, 2780-2798, 1972.

Kopanyi, V. and A. Korth, Energetic particle dropouts observed in the morning sector by the geostationary satellites GEOS - 2, Geophys, Res. Lett; 22, 73-76, 1995.

Korth, A., R. Friedel, D. N. Baker, H. Luhr, S. L. Ullaland, J. F. Fennell, and G. D. Reeves, Dynamics of the plasma sheet in the dawn sector of the magnetosphere: observations from CRRES. Proceedings of International Conference on Substorms 2 ed. by J. R. Kan, J. D. Craven, and S. I. Akasofu, Geophysical Institute, Fairbanks, Alaska, p315, 1995.

Moldwin, M. B., M. F. Thomsen, S. J. Bame, D. J. McComas, and J. Birn, Flux dropouts of plasma and energetic particles at geosynchronous orbit during large geomagnetic storms: Entry into lobes, J. Geophys. Res., 100, 8031-8043, 1995.

Nagai, T., Local time dependence of electron flux changes during substorms derived from multi-satellite observations at synchronous orbit, J. Geophys. Res., 87, 3456-3468, 1982.

Nakamura, R., D. N. Baker, T. Yamamoto, R. D. Belian, E. A. Bering III, J. R. Benbrook, and J. R. Theall, Particle and field signatures during pseudobreakup and major expansion onset, J. Geophys. Res., 99, 207-221, 1994.

Nightingale, R. W., R. R. Vondrak, E. E. Gaines, W. L. Imhof, R. M. Robinson, S. J. Battel, D. A. Simpson, and J. B. Reagan, The ONR-307-3 spectrometer for electrons and protons on the CRRES Satellite, J. Spacecr. Rockets, 29, 614-617, 1992.

Sauvaud, J. A., and J. R. Winckler, Dynamics of plasma, energetic particles, and fields near synchronous orbit in the nighttime sector during magnetospheric substorms, J. Geophys. Res., 85, 2043-2056, 1980.

Sauvaud, J.-A., and T. Beutier, On the origins of flux dropouts near geosynchronous orbit during the growth phase of substorms 1. Betatron effects, J. Geophys. Res., 101, 19911, 1996.

Sergeev, V. A., T. Bosinger, R.D. Belian, G. D. Reeves, and T. E. Cayton, Drifting holes in the energetic electron flux at geosynchronous orbit following substorm onset, J. Geophy. Res., 97, 6541-6548, 1992.

Singer, H. J., W. P. Sullivan, P. Anderson, F. Mozer, P. Harvey, J. Wygant, and W. McNeil, Fluxgate magnetometer instrument on the CRRES, J. Spacecr. Rockets, 29, 599-601, 1992.

Su, Shin-yi, T. A. Fritz, and A. Konradi, Repeated sharp flux dropouts observed at 6.6 $R_E$ during a geomagnetic storm, J. Geophys. Res., 81, 245-252, 1976.

Thomsen, M. F., S. J. Bame, D. J. McComas, M. B. Moldwin, and K. R. Moore, The magnetospheric lobes at geosynchronous orbit, J. Geophys. Res., 99, 17,283-17,293, 1994.

Voss, H. D., E. Hertzberg, A. G. Ghielmetti, S. J. Battel, K. L. Appert, B. R. Higgins, D. O. Murray, and R. R. Vondrak, Medium energy ion mass and neutral atom spectrometer, J. Spacecr. Rockets, 29, 566-569, 1992.

Walker, R. J., K. N. Erickson, R. L. Swanson, and J. R. Winckler, Substorm-associated particle boundary motion at synchronous orbit, J. Geophys. Res., 81, 5541- 5550, 1976.

Wygant, J. R., P. R. Harvey, D. Pankow, F. S. Mozer, N. Maynard, H. Singer, M. Smiddy, W. Sullivan, and P. Anderson, The CRRES electric field/Langmuir probe instrument, J. Spacecr. Rockets, 29, 601-604, 1992.

Yeager, D. M. and L. A. Frank, Large temporal variations of energetic electron intensities at midlatitudes in the outer radiation zone, J. Geophys. Res., 74, 5697-5708, 1969.

## Figure Captions

1. Charged particle and wave data for orbit 186. The bottom sections contain a sweep frequency receiver spectrogram and the output of the multichannel spectrum analyzer for the electric field wave data. Two other sections contain plots of the fluxes of protons and electrons at various energies averaged over the full range of pitch angles. In an upper section the magnetic component of the wave data is plotted.

2. Charged particle and wave data for orbits 279 and 542. The bottom sections contain a sweep frequency receiver spectrogram and the output of the multichannel spectrum analyzer for the electric field wave data. Two other sections contain plots of the fluxes of protons and electrons at various energies averaged over the full range of pitch angles. In an upper section the magnetic component of the wave data is plotted. Vertical lines are drawn to show the alignment at the times of special interest.

3. Charged particle and wave data for orbits 547 and 583. The bottom sections contain a sweep frequency receiver spectrogram and the output of the multichannel spectrum analyzer for the electric field wave data. Two other sections contain plots of the fluxes of protons and electrons at various energies averaged over the full range of pitch angles. In an upper section the magnetic

component of the wave data is plotted. Vertical lines are drawn to show the alignment at the times of special interest.

4. Charged particle and wave data for orbits 615, 666, 686, and 737. The bottom sections contain a sweep frequency receiver spectrogram and the output of the multichannel spectrum analyzer for the electric field wave data. Two other sections contain plots of the fluxes of protons and electrons at various energies averaged over the full range of pitch angles. Vertical lines are drawn to show the alignment at the times of special interest.

5. Charged particle and wave data for orbits 759, 766, 768, and 902. The bottom sections contain a sweep frequency receiver spectrogram and the output of the multichannel spectrum analyzer for the electric field wave data. Two other sections contain plots of the fluxes of protons and electrons at various energies averaged over the full range of pitch angles. Vertical lines are drawn to show the alignment at the times of special interest.

6. Sweep Frequency Receiver Spectrograms and electron flux at 77 keV on orbits 542, 547, 686, and 737 for two-hour periods roughly centered on the times of the narrow particle dropouts.

7. Proton and wave data for a portion of orbit 542. In the upper sections the electric field wave intensities at three different frequencies are plotted. In the lower sections are plotted the fluxes of protons at 18 and 56 keV averaged over the full range of pitch angles. Vertical lines are drawn to show the alignment at times of special interest.

8. Proton and wave data for a portion of orbit 712. In the upper sections the electric field wave intensities at three different frequencies are plotted. In the lower sections are plotted the fluxes of protons at 18 and 56 keV averaged over the full range of pitch angles. Vertical lines are drawn to show the alignment at times of special interest.

Table 1. Characteristics of Narrow Electron Dropouts (< 30 min )

| At start of recovery from electron dropout | | | | | | | MAX Kp IN PREV 24 HOURS | VLF ELECTRIC FIELD WAVE CHANGE | VLF MAGNETIC FIELD WAVE CHANGE | >18 keV ION DROPOUT | <10 keV ION DROPOUT |
|---|---|---|---|---|---|---|---|---|---|---|---|
| ORBIT | DATE | UT | MLT | L | Dst | Kp | | | | | |
| 186 | 10/10/90 | 07:37 | 02:54 | 5.41 | -114 | 6 | 6 | yes | yes | yes | yes |
| 186 | 10/10/90 | 12:49 | 06:30 | 7.20 | -88 | 5 | 6 | no | no | no | no |
| 279 | 11/17/90 | 14:24 | 02:54 | 6.76 | -36 | 4 | 4 | yes | yes | yes | * |
| 542 | 03/05/91 | 14:02 | 23:24 | 6.76 | -30 | 4 | 5- | yes | yes | yes | no |
| 547 | 03/07/91 | 14:43 | 23:00 | 6.96 | -20 | 4- | 5 | yes | yes | no | no |
| 552 | 03/09/91 | 17:34 | 23:54 | 6.24 | -30 | 3+ | 4+ | yes | yes | yes | no |
| 583 | 03/22/91 | 09:25 | 22:54 | 6.43 | -38 | 4 | 7- | weak | yes | no | * |
| 615 | 04/04/91 | 11:13 | 21:54 | 7.22 | -3 | 6+ | 6+ | yes | na | yes | no |
| 666 | 04/25/91 | 09:30 | 21:54 | 6.75 | -21 | 3 | 5- | yes | na | yes | yes |
| 686 | 05/03/91 | 12:23 | 20:18 | 8.05 | -22 | 3 | 6 | yes | na | yes | * |
| 712 | 05/14/91 | 05:17 | 21:06 | 6.29 | -28 | 3+ | 5 | weak | na | yes | no |
| 719 | 05/17/91 | 00:46 | 20:12 | 6.61 | 13 | 6 | 6 | no | na | no | no |
| 737 | 05/24/91 | 11:25 | 20:54 | 7.07 | -19 | 2+ | 5- | yes | na | no | no |
| 759 | 06/02/91 | 10:29 | 19:48 | 7.89 | -43 | 4 | 7+ | yes | na | no | * |
| 766 | 06/05/91 | 04:13 | 17:48 | 5.95 | -76 | 7+ | 7+ | yes | na | yes | no |
| 768 | 06/06/91 | 03:54 | 18:30 | 6.68 | -147 | 6- | 9- | yes | na | yes | yes |
| 902 | 08/02/91 | 09:53 | 18:00 | 5.98 | -91 | 5+ | 6+ | yes | na | no | no |

* Insufficient ion flux to establish the presence of a dropout.
na = data not acquired

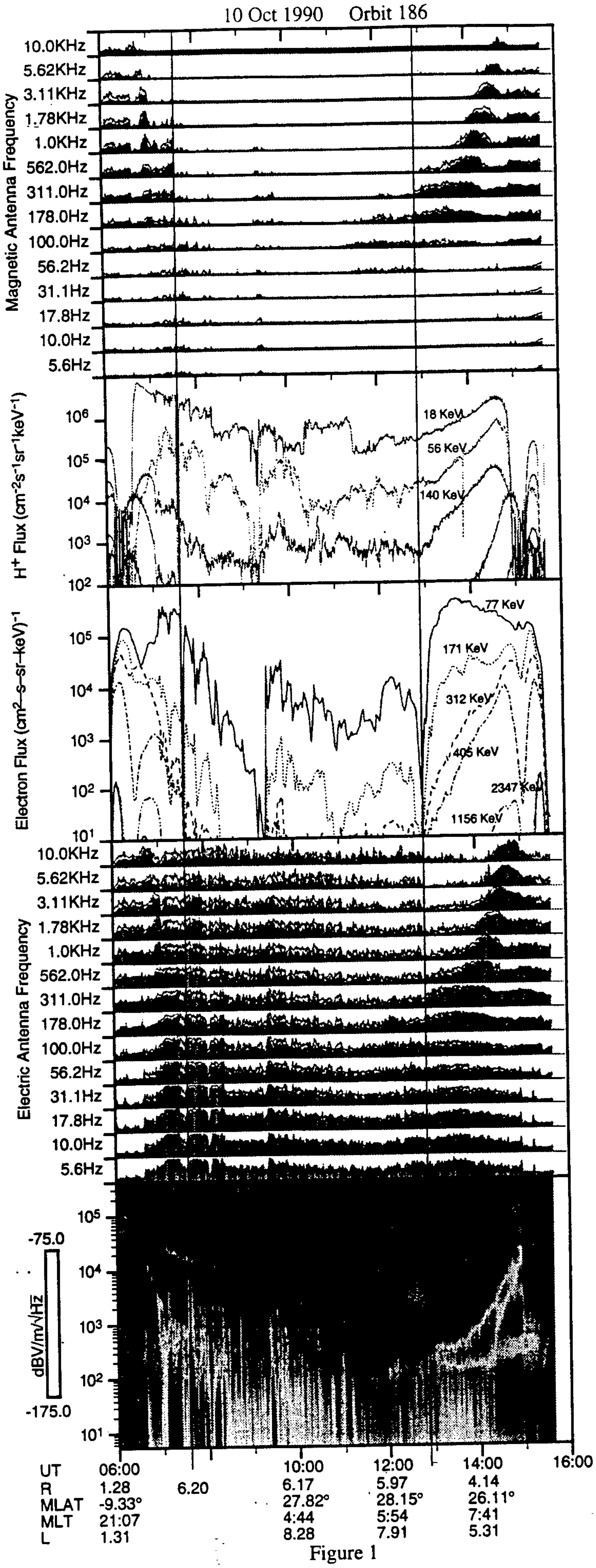
10 Oct 1990 Orbit 186
Magnetic Antenna Frequency
10.0KHz
5.62KHz
3.11KHz
1.78KHz
1.0KHz
562.0Hz
311.0Hz
178.0Hz
100.0Hz
56.2Hz
31.1Hz
17.8Hz
10.0Hz
5.6Hz
H+ Flux (cm-2s-1sr-1keV-1)
10^6
10^5
10^4
10^3
10^2
18 KeV
56 KeV
140 KeV
Electron Flux (cm2-s-sr-keV)-1
10^5
10^4
10^3
10^2
10^1
77 KeV
171 KeV
312 KeV
405 KeV
2347 KeV
1156 KeV
Electric Antenna Frequency
10.0KHz
5.62KHz
3.11KHz
1.78KHz
1.0KHz
562.0Hz
311.0Hz
178.0Hz
100.0Hz
56.2Hz
31.1Hz
17.8Hz
10.0Hz
5.6Hz
-75.0
dBV/m/√Hz
-175.0
10^5
10^4
10^3
10^2
10^1
UT 06:00 10:00 12:00 14:00 16:00
R 1.28 6.20 6.17 5.97 4.14
MLAT -9.33° 27.82° 28.15° 26.11°
MLT 21:07 4:44 5:54 7:41
L 1.31 8.28 7.91 5.31

Figure 1

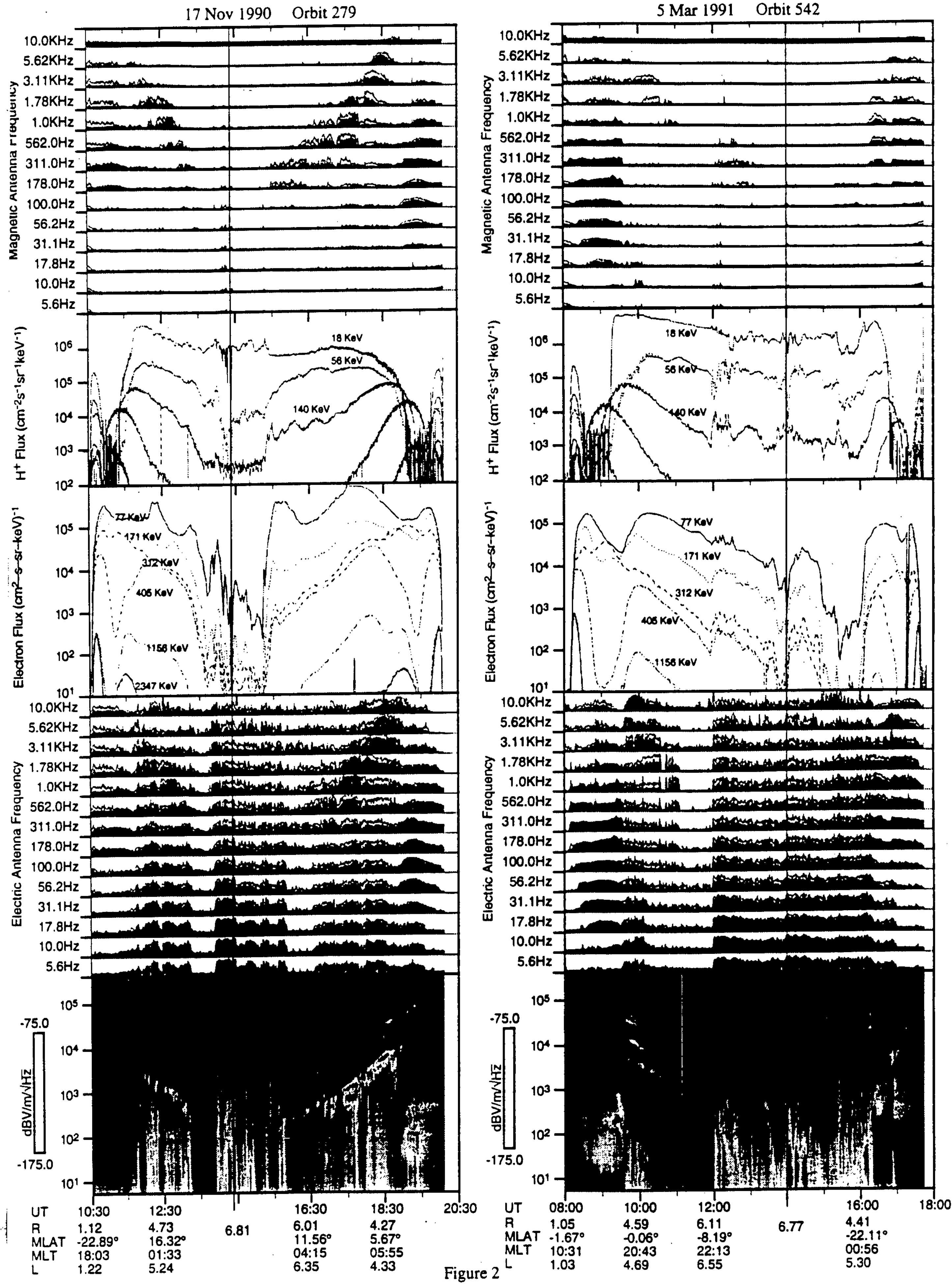
17 Nov 1990 Orbit 279
5 Mar 1991 Orbit 542
Magnetic Antenna Frequency
10.0KHz
5.62KHz
3.11KHz
1.78KHz
1.0KHz
562.0Hz
311.0Hz
178.0Hz
100.0Hz
56.2Hz
31.1Hz
17.8Hz
10.0Hz
5.6Hz
H+ Flux (cm-2s-1sr-1keV-1)
10^6
10^5
10^4
10^3
10^2
18 KeV
56 KeV
140 KeV
Electron Flux (cm2-s-sr-keV)-1
10^5
10^4
10^3
10^2
10^1
77 KeV
171 KeV
312 KeV
405 KeV
1156 KeV
2347 KeV
Electric Antenna Frequency
dBV/m/√Hz
-75.0
-175.0
10^5
10^4
10^3
10^2
10^1
UT 10:30 12:30 16:30 18:30 20:30
R 1.12 4.73 6.81 6.01 4.27
MLAT -22.89° 16.32° 11.56° 5.67°
MLT 18:03 01:33 04:15 05:55
L 1.22 5.24 6.35 4.33
UT 08:00 10:00 12:00 16:00 18:00
R 1.05 4.59 6.11 6.77 4.41
MLAT -1.67° -0.06° -8.19° -22.11°
MLT 10:31 20:43 22:13 00:56
L 1.03 4.69 6.55 5.30

Figure 2

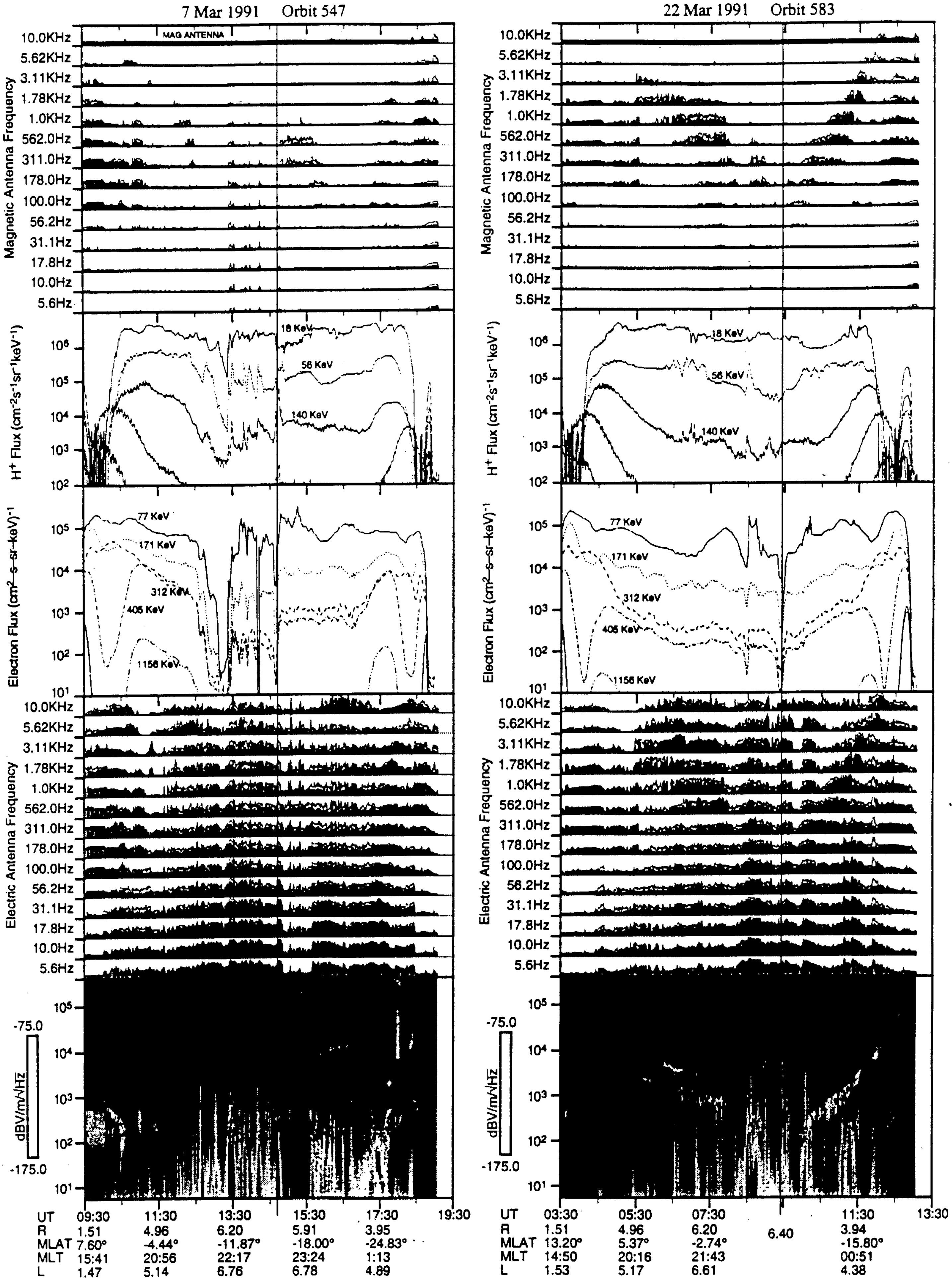
7 Mar 1991 Orbit 547
22 Mar 1991 Orbit 583
MAG ANTENNA
Magnetic Antenna Frequency
10.0KHz
5.62KHz
3.11KHz
1.78KHz
1.0KHz
562.0Hz
311.0Hz
178.0Hz
100.0Hz
56.2Hz
31.1Hz
17.8Hz
10.0Hz
5.6Hz
H+ Flux (cm-2s-1sr-1keV-1)
18 KeV
56 KeV
140 KeV
Electron Flux (cm2-s-sr-keV)-1
77 KeV
171 KeV
312 KeV
405 KeV
1156 KeV
Electric Antenna Frequency
dBV/m/√Hz
-75.0
-175.0
UT 09:30 11:30 13:30 15:30 17:30 19:30
R 1.51 4.96 6.20 5.91 3.95
MLAT 7.60° -4.44° -11.87° -18.00° -24.83°
MLT 15:41 20:56 22:17 23:24 1:13
L 1.47 5.14 6.76 6.78 4.89
UT 03:30 05:30 07:30 11:30 13:30
R 1.51 4.96 6.20 6.40 3.94
MLAT 13.20° 5.37° -2.74° -15.80°
MLT 14:50 20:16 21:43 00:51
L 1.53 5.17 6.61 4.38

Figure 3

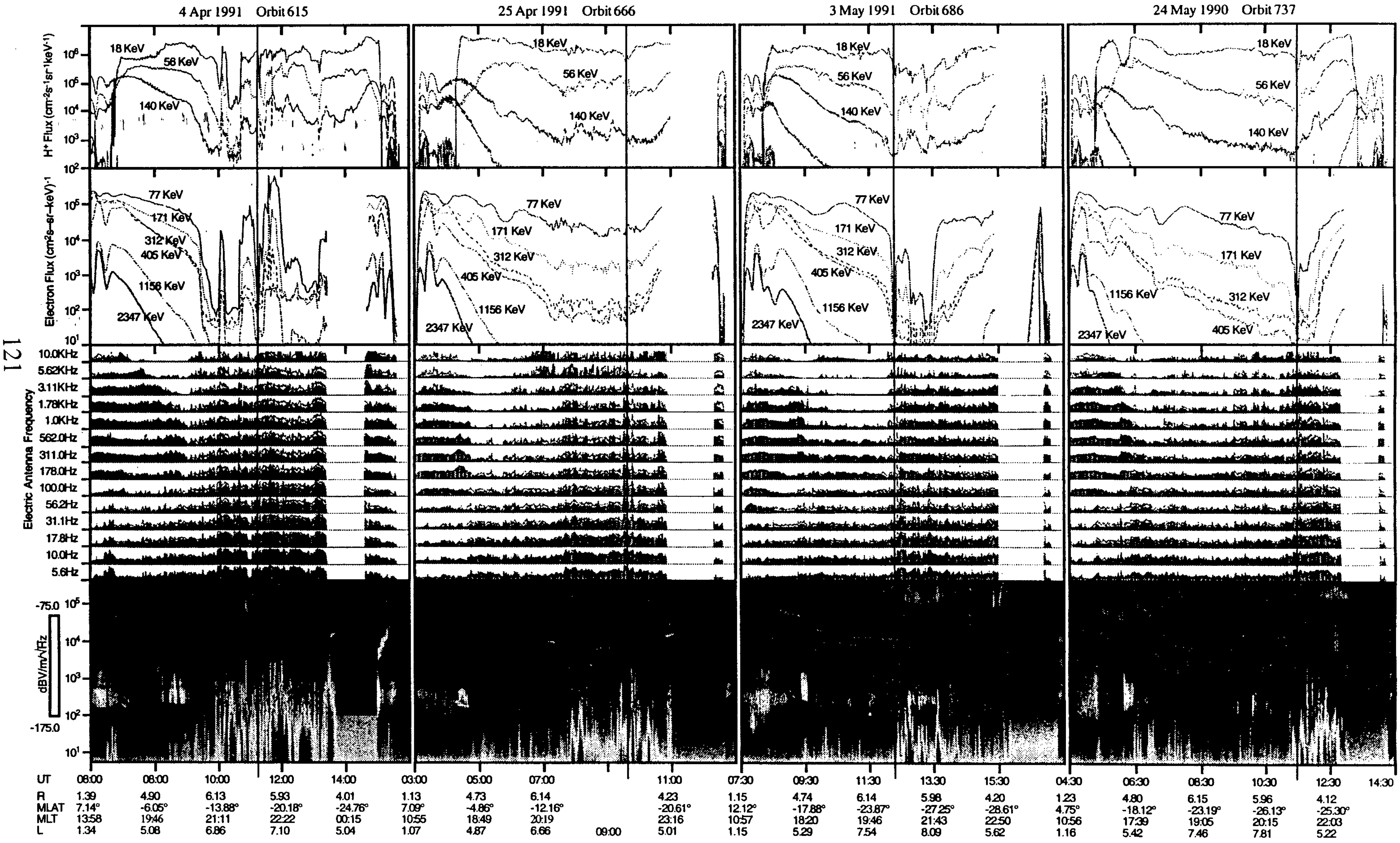
4 Apr 1991 Orbit 615
25 Apr 1991 Orbit 666
3 May 1991 Orbit 686
24 May 1990 Orbit 737
H+ Flux (cm-2s-1sr-1keV-1)
10^6
10^5
10^4
10^3
10^2
18 KeV
56 KeV
140 KeV
Electron Flux (cm2s-sr-keV)-1
10^5
10^4
10^3
10^2
10^1
77 KeV
171 KeV
312 KeV
405 KeV
1156 KeV
2347 KeV
Electric Antenna Frequency
10.0KHz
5.62KHz
3.11KHz
1.78KHz
1.0KHz
562.0Hz
311.0Hz
178.0Hz
100.0Hz
56.2Hz
31.1Hz
17.8Hz
10.0Hz
5.6Hz
-75.0
dBV/m/√Hz
-175.0
10^5
10^4
10^3
10^2
10^1
UT
R
MLAT
MLT
L
08:00 1.39 7.14° 13:58 1.34
08:00 4.90 -6.05° 19:46 5.08
10:00 6.13 -13.88° 21:11 6.86
12:00 5.93 -20.18° 22:22 7.10
14:00 4.01 -24.76° 00:15 5.04
03:00 1.13 7.09° 10:55 1.07
05:00 4.73 -4.86° 18:49 4.87
07:00 6.14 -12.16° 20:19 6.66
09:00
11:00 4.23 -20.61° 23:16 5.01
07:30 1.15 12.12° 10:57 1.15
09:30 4.74 -17.88° 18:20 5.29
11:30 6.14 -23.87° 19:46 7.54
13:30 5.98 -27.25° 21:43 8.09
15:30 4.20 -28.61° 22:50 5.62
04:30 1.23 4.75° 10:56 1.16
06:30 4.80 -18.12° 17:39 5.42
08:30 6.15 -23.19° 19:05 7.46
10:30 5.96 -26.13° 20:15 7.81
12:30 4.12 -25.30° 22:03 5.22
14:30

Figure 4

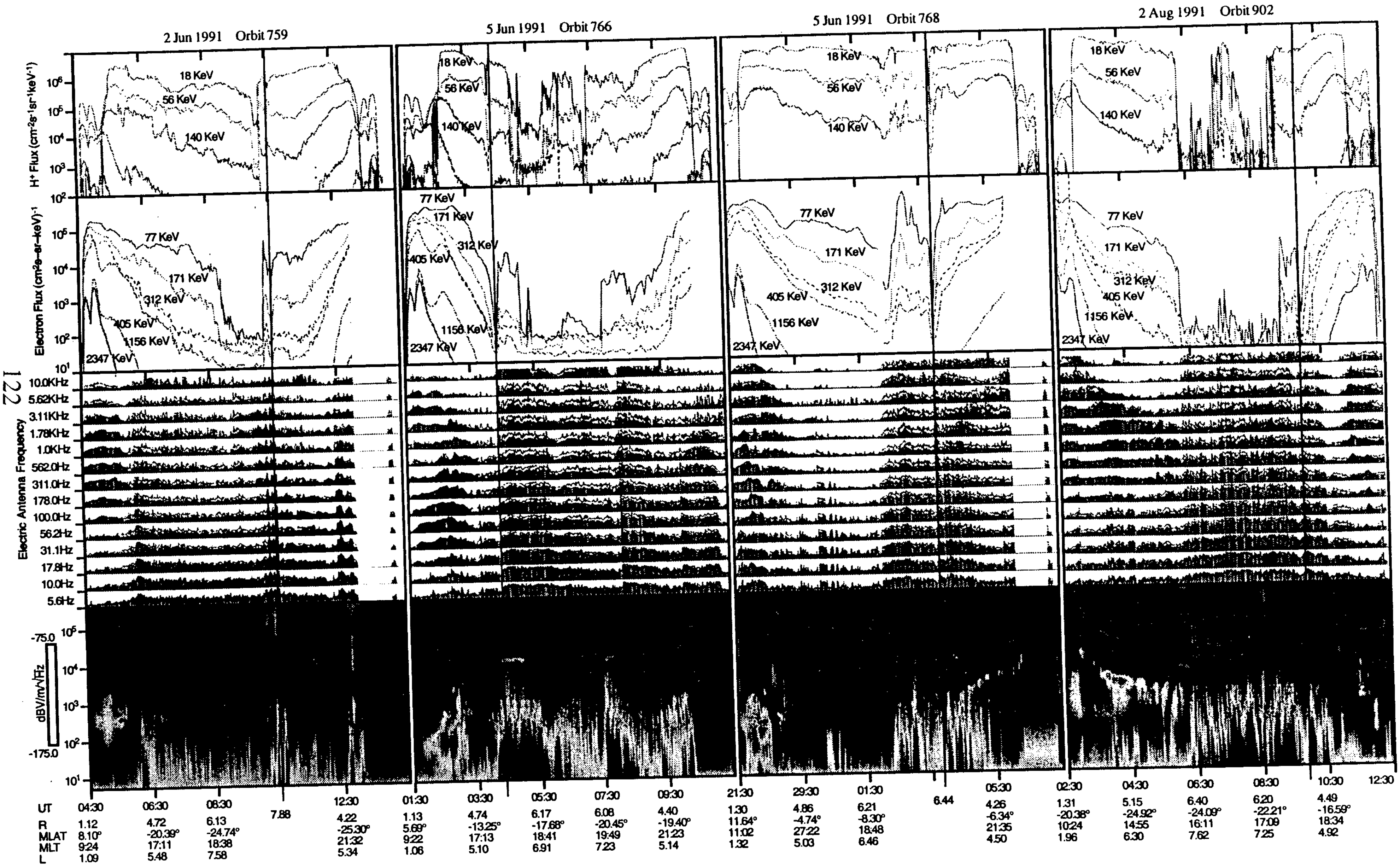
2 Jun 1991 Orbit 759
5 Jun 1991 Orbit 766
5 Jun 1991 Orbit 768
2 Aug 1991 Orbit 902
H+ Flux (cm-2s-1sr-1keV-1)
Electron Flux (cm2s-sr-keV)-1
18 KeV
56 KeV
140 KeV
77 KeV
171 KeV
312 KeV
405 KeV
1156 KeV
2347 KeV
Electric Antenna Frequency
10.0KHz
5.62KHz
3.11KHz
1.78KHz
1.0KHz
562.0Hz
311.0Hz
178.0Hz
100.0Hz
56.2Hz
31.1Hz
17.8Hz
10.0Hz
5.6Hz
-75.0
-175.0
dBV/m/√Hz
UT
R
MLAT
MLT
L
04:30 1.12 8.10° 9:24 1.09
06:30 4.72 -20.39° 17:11 5.48
08:30 6.13 -24.74° 18:38 7.58
7.88
12:30 4.22 -25.30° 21:32 5.34
01:30 1.13 5.69° 9:22 1.06
03:30 4.74 -13.25° 17:13 5.10
05:30 6.17 -17.68° 18:41 6.91
07:30 6.08 -20.45° 19:49 7.23
09:30 4.40 -19.40° 21:23 5.14
21:30 1.30 11.64° 11:02 1.32
29:30 4.86 -4.74° 27:22 5.03
01:30 6.21 -8.30° 18:48 6.46
6.44
05:30 4.26 -6.34° 21:35 4.50
02:30 1.31 -20.38° 10:24 1.96
04:30 5.15 -24.92° 14:55 6.30
06:30 6.40 -24.09° 16:11 7.62
08:30 6.20 -22.21° 17:09 7.25
10:30 4.49 -16.59° 18:34 4.92
12:30

Figure 5

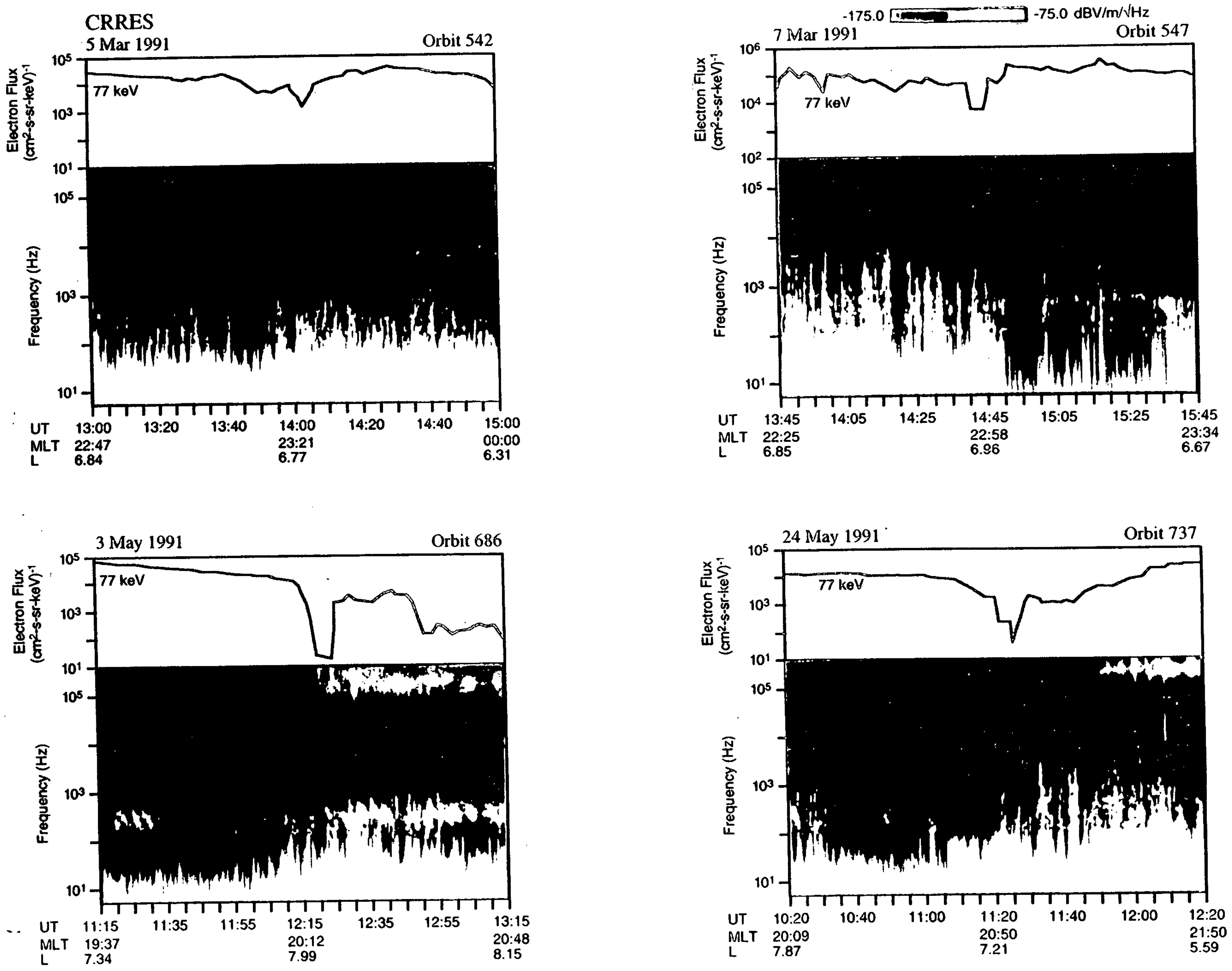
CRRES
5 Mar 1991
Orbit 542
77 keV
Electron Flux (cm²-s-sr-keV)⁻¹
Frequency (Hz)
10⁵
10³
10¹
UT 13:00 13:20 13:40 14:00 14:20 14:40 15:00
MLT 22:47 23:21 00:00
L 6.84 6.77 6.31
-175.0 -75.0 dBV/m/√Hz
7 Mar 1991
Orbit 547
10⁶
10⁴
10²
UT 13:45 14:05 14:25 14:45 15:05 15:25 15:45
MLT 22:25 22:58 23:34
L 6.85 6.96 6.67
3 May 1991
Orbit 686
UT 11:15 11:35 11:55 12:15 12:35 12:55 13:15
MLT 19:37 20:12 20:48
L 7.34 7.99 8.15
24 May 1991
Orbit 737
UT 10:20 10:40 11:00 11:20 11:40 12:00 12:20
MLT 20:09 20:50 21:50
L 7.87 7.21 5.59

**Figure 6**

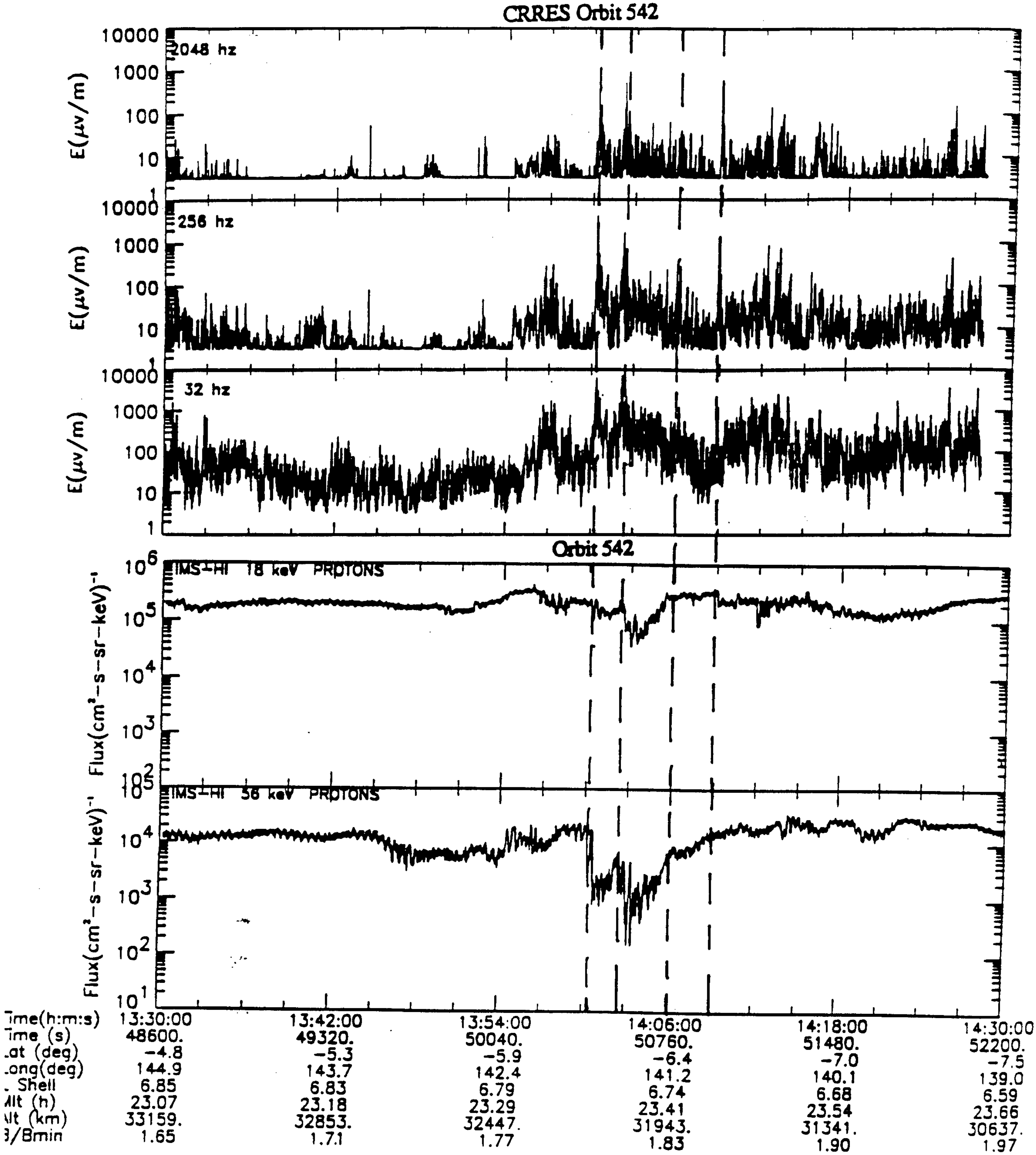
CRRES Orbit 542
2048 hz
256 hz
32 hz
E(μv/m)
10000
1000
100
10
1
Orbit 542
IMS-HI 18 keV PROTONS
IMS-HI 56 keV PROTONS
Flux(cm²-s-sr-keV)⁻¹
10⁶
10⁵
10⁴
10³
10²
10¹
ime(h:m:s) 13:30:00 13:42:00 13:54:00 14:06:00 14:18:00 14:30:00
ime (s) 48600. 49320. 50040. 50760. 51480. 52200.
at (deg) -4.8 -5.3 -5.9 -6.4 -7.0 -7.5
ong(deg) 144.9 143.7 142.4 141.2 140.1 139.0
. Shell 6.85 6.83 6.79 6.74 6.68 6.59
lt (h) 23.07 23.18 23.29 23.41 23.54 23.66
lt (km) 33159. 32853. 32447. 31943. 31341. 30637.
3/Bmin 1.65 1.71 1.77 1.83 1.90 1.97

Figure 7

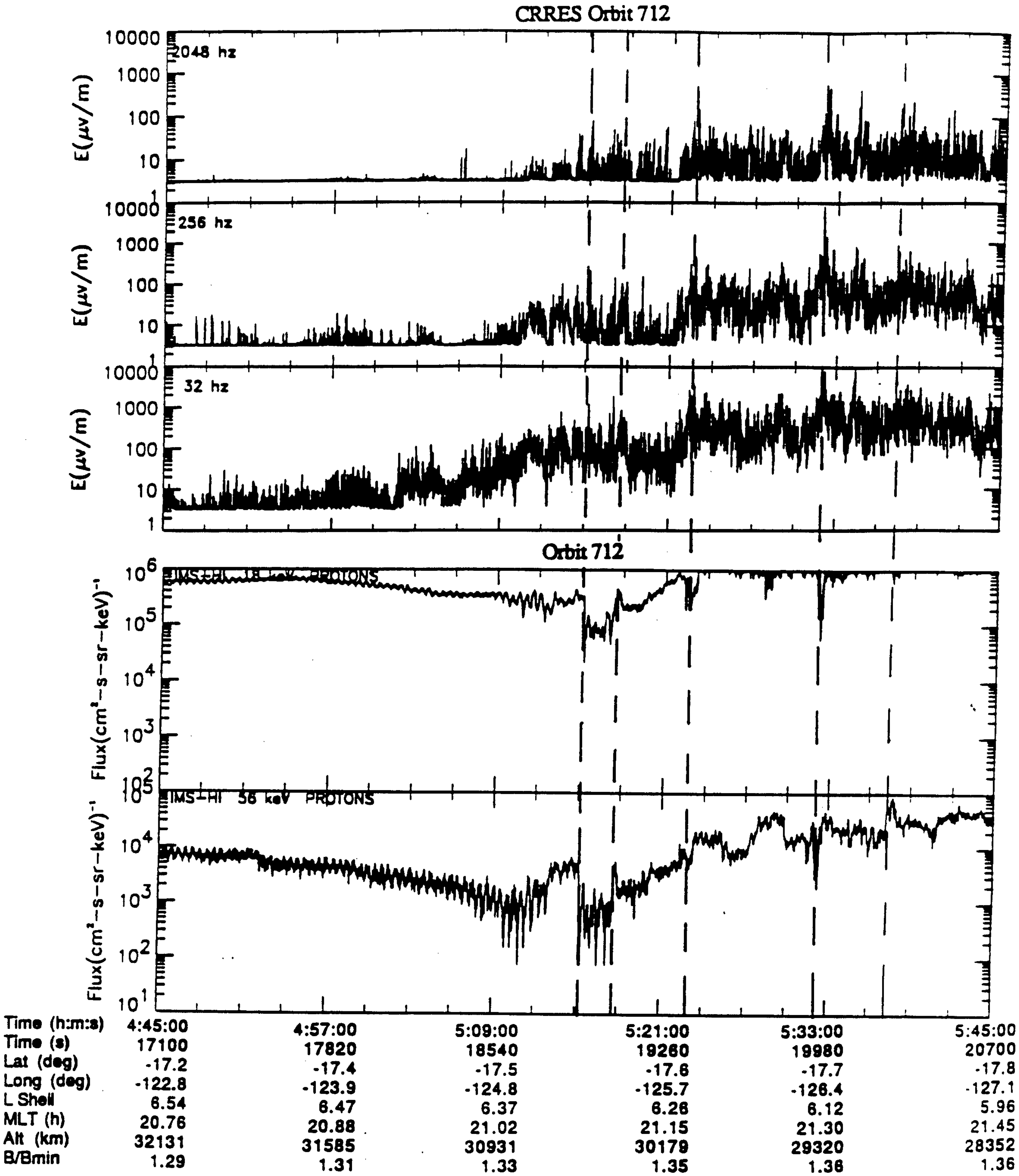
CRRES Orbit 712
2048 hz
256 hz
32 hz
E(μv/m)
10000
1000
100
10
1
Orbit 712
IMS-HI 18 keV PROTONS
IMS-HI 56 keV PROTONS
Flux(cm²-s-sr-keV)⁻¹
10⁶
10⁵
10⁴
10³
10²
10¹
Time (h:m:s) 4:45:00 4:57:00 5:09:00 5:21:00 5:33:00 5:45:00
Time (s) 17100 17820 18540 19260 19980 20700
Lat (deg) -17.2 -17.4 -17.5 -17.6 -17.7 -17.8
Long (deg) -122.8 -123.9 -124.8 -125.7 -126.4 -127.1
L Shell 6.54 6.47 6.37 6.26 6.12 5.96
MLT (h) 20.76 20.88 21.02 21.15 21.30 21.45
Alt (km) 32131 31585 30931 30179 29320 28352
B/Bmin 1.29 1.31 1.33 1.35 1.36 1.36

Figure 8

# OBSERVATIONS OF LONG-TERM FIELD-ALIGNED FLOW OF $O^+$ IONS NEAR EQUATOR DURING SUMMER AND WINTER

J. B. Cladis

Consultant, 2440 Sharon Oaks Dr., Menlo Park, CA 94025

H. L. Collin

Lockheed Martin Space Physics Laboratory, Palo Alto, CA 94304

*Abstract.* In the equatorial region of the outer magnetosphere ($R > 4\,R_E$), highly asymmetric storm-time pitch-angle distributions (0° vs. 180°) of $O^+$ ions (< 20 keV) have been observed near dawn and dusk during winter and summer seasons with ion spectrometers on-board the CRRES and AMPTE/CCE satellites. These ion asymmetries, although variable in magnitude and ion energy, persist in the same sense for periods up to 3 hours. The observed $O^+$ pitch-angle distributions suggest a net summer-to-winter ion flow in the dawn sector and a net winter-to-summer ion flow in the dusk sector. This is consistent with the direction of an induced parallel (to **B**) electric field that accompanies the growth of Region 1 and Region 2 Birkeland currents when the Earth's magnetic dipole is tilted toward or away from the sun. When the dipole is tilted, a net magnetic flux produced by these currents threads field lines in the dawn and dusk sectors of the inner magnetosphere. The net flux due to the Birkeland current arises because this current is asymmetric during summer and winter, being stronger in the hemisphere of the sun-lit polar ionosphere. To date one of the 17 observed events has been examined in detail. The time-variations of the Birkeland currents were estimated from on-board magnetic-field measurements and interplanetary conditions. By using a simple model of the Birkeland currents to compute the magnetic flux enclosed by field lines traversed by the CRRES satellite, the electromotive force (EMF) along these field lines was found to be in the range needed to account for the asymmetry

of the ions. The solar-wind pressure was decreasing during this event; hence the resulting changes of the magnetopause and magnetotail currents, which increased the net magnetic flux (mainly along the $z_{GSM}$ axis) through the areas enclosed by the inclined field lines, also must have contributed to this EMF. The general features of the observed pitch-angle distributions were confirmed with a computer program that simulated the response of initially-trapped ions to a parallel electric field.

## Introduction

Sixteen events of highly unusual ion pitch-angle distributions were measured at $L > 4$ during disturbed times with the IMS-LO instruments on the CRRES satellite. These instruments measure directional fluxes of $H^+$, $He^+$, and $O^+$ ions from 0.11 to 35 keV over nearly the entire pitch-angle range, $0° \leq \alpha \leq 180°$ [*Collin et al.*, 1992]. An additional event, with similar energy and pitch-angle coverage, was observed with the Hot Plasma Composition Experiment (HPCE) [*Shelley et al.*, 1985] on the AMPTE/CCE satellite. Both of these satellites are in highly eccentric, low inclination orbits; therefore, nearly the entire distribution of the ions along local field lines can be inferred from the near equatorial measurements.

During disturbed times the pitch-angle distributions of $O^+$ ions of energy less than about 6 keV are generally cigar shaped; i.e., the directional flux has a minimum value at the pitch angle $\alpha = 90°$ and steadily increases symmetrically toward lower and higher pitch angles. However, during these unusual events, the pitch-angle distributions of $O^+$ ions with energies generally less than a few keV were highly asymmetric about 90°. The directional flux increased monotonically from one end of the pitch-angle range to the other (from 0° to 180° or from 180° to 0°). Although the magnitude of the asymmetry – and the energies of the affected ions –varied with time, this general shape of the distribution was maintained for periods much longer than the ion bounce times. We will refer to these asymmetric pitch-angle distributions as APADS.

The events in which the $O^+$ ions were asymmetric for periods greater than 2 hours, and the conditions under which they were observed, are listed in Tables 1 and 2. Note in the 3rd column of Table 1 that the APADS observed on Orbit 856 persisted for 4 hours. Comparison of columns 4 and 6 shows that the ion flows were antiparallel to the magnetic field $\boldsymbol{B}$ in the dawn sector and parallel to $\boldsymbol{B}$ in the dusk sector. Column 5 shows that these APADS were observed at $L$ values higher than 4.6. Note from Table 2 that the dipole-tilt angles (the complement of the angle between the Earth's magnetic dipole and the solar-wind velocity) were large, and that the extreme solar-wind parameters and $Kp$ and $D$st indices imply highly disturbed magnetospheric conditions. Moreover, the solar 10.7–cm flux was high, implying a high photoionization rate of the sunlit polar atmosphere. All 17 of the events were observed in the dawn or dusk sectors during similar conditions. The dawn and dusk ion-flow directions of the 16 events observed with CRRES were the same as those shown in Table 1, but the ion-flow direction of the event observed near dawn with AMPTE/CCE was in the opposite direction ($\hat{\boldsymbol{B}}$). Furthermore, the on-board magnetic field measurements [*Singer et al.*, 1992], which were available to us for 5 of these events, all suggest the presence of Region 1 Birkeland currents that were generally increasing in time.

A detailed analysis of the event observed near dawn during the magnetic storm of August 26, 1990, is described below. This analysis indicates the ions were principally accelerated by an inter-hemispherical electric field, along $-\hat{\boldsymbol{B}}$, that was induced by the time-varying external magnetospheric currents: the growth of the Birkeland currents and the decrease of the magnetopause and magnetotail currents attending a decrease of the solar-wind pressure. During the summer and winter seasons, or more specifically, when the magnitude of the dipole-tilt angle is appreciable, Birkeland currents become asymmetric about the low-latitude boundary layer. In the summer hemisphere, this current is stronger mainly because the conductivity of the polar ionosphere is higher [*Fujii et al.*, 1981]. Because of this Birkeland-current asymmetry, a net magnetic flux, westward on the dawn side – and eastward on the dusk side – of the inner magnetosphere, is enclosed by geomagnetic field lines. Hence, when the dipole-tilt angle is positive (northern summer), increasing Birkeland currents induce electric fields that are directed along $-\hat{B}$ in the dawn sector and along $\hat{B}$ in the dusk sector. These directions are consistent with the ion-flow directions of the 16 events observed on CRRES, which were all observed during northern summer. During northern winter, the directions of the fields induced by increasing Birkeland currents are in the opposite direction; and this result is consistent with the direction of the ions observed during northern winter with the AMPTE/CCE satellite. When the magnetopause and magnetotail currents decrease, as implied by the decreasing solar-wind pressure during the August event, the magnetic flux through the inclined (to $Z_{GSM}$) areas bounded by geomagnetic field lines increases, generally along the $Z_{GSM}$ direction. The parallel electric fields induced by this flux change are in the same directions in the dawn and dusk sectors during northern summer and winter as those described above.

An electric field along the magnetic field affects all the charged particles in a magnetic tube. Generally, the particles are redistributed such that their charge-separation electric field tends to diminish the net electric field. However, as emphasized by *Heikkila and Pellinen* [1977], a charge-separation electric field, which is irrotational, cannot cancel an induced electric field, which is solenoidal. It can only redistribute the net field. The complex behavior of the lower-energy ions and electrons, which were counter-streaming and redistributed toward much-lower altitudes during this event, underscores the difficulties of understanding the distribution of the field.

In the next section the observations of the ions and electrons, as well as the on-board magnetic-field measurements and interplanetary conditions, during the storm of 26 August, 1990, are described. In the *Analysis* section, the EMF produced by the asymmetric Birkeland currents is computed using a simple model of the northern-summer Birkeland currents and estimating the time variations of the currents from the on-board magnetic-field measurements and interplanetary conditions. Also, a computer program is described that simulates of the effects of an applied parallel electric field on the equatorial pitch-angle distribution of initially trapped ions. In this work it was assumed that the full value of the induced EMF remained along the magnetic field and none of it was redistributed across the magnetic field. The principal features of the observed APADS were reproduced by this program.

## Observations During Storm of 26 August 1990

During the magnetic storm of 26 August 1990, the $O^+$ APADS were observed from about 1300 to 1559 UT while the CRRES satellite moved through $L$ values 4.6 to 6.8, magnetic local times 0431 to 0637, and magnetic latitudes 9.3° to 16.3° along its outgoing leg. Twenty-six minute averages of the ion pitch-angle distributions (directional flux vs. pitch angle) at various energies are shown in panels a–f of Figure 1. The $L$ values and times over which the distributions were averaged are given in the panels. Note that although the magnitude of the asymmetry of the distributions at a given energy, as well as the energy range of the APADS, were variable in time, the sense of the asymmetry remained the same during this entire period.

Toward lower ion masses, the pitch-angle asymmetry decreased rapidly. The asymmetry of the $He^+$ ions was much smaller than that of the $O^+$ ions at the same energies; and the asymmetry of the $H^+$ ions was so small that it was not easily perceptible. At energies less than about 4.9 keV, the directional flux of the $H^+$ ions was nearly constant over the entire pitch-angle range of the measurements. However, the $H^+$ energy spectrum became harder, and the integrated flux decreased, as the maximum energy of the $O^+$ APADS increased.

The behavior of the electrons also changed appreciably when the $O^+$ APADS appeared. Prior to 1300 UT, the electron pitch-angle distributions that were measured with the IMS-LO instrument (67 eV to 20 keV) were "rounded" in a manner typical of trapped particles, with maximums at $\alpha = 90°$. Afterward, the distributions of electrons with energies between 1.7 to 20 keV suddenly became flat over the pitch-angle range of the measurements (0° to 135°), and remained flat until they again became "rounded" near 1600 UT. During the same time period, electrons of energy less than about 1.7 keV developed "winged" distributions (cigar shapes) in which the directional flux increased rapidly from 90° to 0° and from 90° to the limit (135°) of the observations. Moreover, the 0°-flux relative to the 90°-flux increased rapidly toward lower energies. The energy spectrum of the electrons also became harder during this time period.

Fortunately, the IMP-8 spacecraft was in the solar wind during this storm and good measurements were obtained of the interplanetary magnetic field (IMF) and the solar-wind velocity and density. The components and magnitude of the IMF from 00–18 hours on 26 August 1990, and the solar-wind velocity and density over the same time period are shown in Figures 2 and 3, respectively, of *Jordan et al.* [1992]. The storm sudden commencement (SSC) occurred at 0543 UT, about 7 hours before the APADS were observed. As shown in Figure 3 of *Jordan et al.* [1992] the standoff distance of the sub-solar magnetopause decreased from 10.6 $R_E$ before the SSC to a minimum of 6.3 $R_E$ at 1230 UT. During the period of the APADS, the standoff distance generally increased from about 6.4 to 7.8 $R_E$. The *D*st index steadily became more negative from about 0 at 0700 UT, reaching its most negative value of about -110 nT at 1400 UT, and remaining near this level until 1750 UT. The three-hourly *Kp* index increased from 3+ before the SSC to 7– at 6-8 hours. Then it remained fairly constant through the end of the APADS event, and it decreased steadily from 6o at 15-17 hours to 3+ at 27-29 hours.

The CRRES satellite was near apogee, at $L = 6.6$, at the time of the SSC, and it remained at $L > 5.5$ until 0900 UT. Yet, even though the external currents change appreciably near the beginning of a storm, the ion pitch-angle distributions were symmetric about 90°. Our analysis indicates they were symmetric because the dipole-tilt angle was small (0°–3°) while CRRES was at $L > 5.5$; hence, all the external currents were nearly symmetrical about the magnetic equator.

Magnetic-field measurements were made on the CRRES satellite by *Singer et al.* [1992]. Their measurements on the orbit during which the APADS were observed are shown in Figure 2. In the upper 3 panels the VDH components of the field relative to the corresponding components derived from the Olson-Pfitzer dynamic magnetic field model [*Olson and Pfitzer*, 1977; *Walker*, 1979] are shown. $B_x$, $B_y$, and $B_z$, respectively denote the field components radially outward from the earth's dipole axis, eastward in magnetic coordinates, and antiparallel to the earth's magnetic dipole. The differences $\delta B_x$, $\delta B_y$, and $\delta B_z$ at the beginning of the traces are given at the left of the panels, under the ordinate labels. Note that if a trace extends below/above a panel it wraps to the top/bottom of the panel. The total magnetic field is given in the bottom panel, and the broken-line curve is the modeled field. Clearly, the magnetic field was highly disturbed.

During the period of the APADS (1300–1556 UT), the local magnetic field lines were distended, as indicated by the $\delta B_x$ and $\delta B_z$ components, and strong fluctuations of roughly one-hour periods were present in $\delta B_y$. The total magnetic field became increasingly higher than the expected field throughout the period of the APADS; then at 1545 UT, it decreased to its expected value at 1620 UT, at which time the magnetopause standoff distance had increased to about 10 $R_E$.

## Analysis

*Model of Birkeland Currents*

A simple model of the asymmetric Region 1 and Region 2 Birkeland current systems on the dawn side of the magnetosphere was constructed to estimate the EMF produced along the magnetic field lines on which the APADS were observed. As illustrated by the heavy lines in Figure 3, the Birkeland currents were simulated by current filaments (wires) along dipole magnetic field lines. (The directions of the ion-flows shown in this figure will be discussed later.) The filaments were spaced at intervals of 1 hour in magnetic-dipole local time from 0030 to 1030 MLT. In the ionosphere, the filaments simulating the Region 1 currents were located at the mean values of the colatitudes of the Region 1 currents given by the statistical model of *Ijima and Potemra* [1978] based on the Triad satellite data taken during disturbed conditions ($|AL| \geq 100\ \gamma$). The filaments simulating the Region 2 currents were locate at higher colatitudes by 3° in each meridional plane. Each filament $k$ carried the current

$$I_k = S_k j_k R \sin\theta_k \delta w \delta\varphi \tag{1}$$

where $j_k$ is the current density during disturbed times ($|AL| \geq 100\ \gamma$) of the Region 1 or Region 2 Birkeland currents at the magnetic local time of the filament, as given by Ijima and Potemra [1978]; $\theta_k$ is the colatitude; and $R$ is the geocentric distance to the altitude of 100 km in the ionosphere. The latitudinal widths $\delta w$ of the Region 1 and Region 2 currents in the ionosphere were taken to be 250 and 350 km, respectively; and $\delta\varphi$ was set equal to the longitudinal spacing of the filaments (15°).

The factors $S_k$ specify the seasonal inter-hemispherical asymmetries of the currents. Their values were primarily based on the results of *Fujii et al.* [1981], who used the Triad data acquired during the years 1973–1974 and 1976–1977 to investigate the seasonal dependence of the Birkeland currents. These authors found that the Birkeland currents on the dayside were about a factor of 2 higher during the summer than during the winter. Specifically, they found that the summer-to-winter ratios of the Region 1 and Region 2 currents were 1.8 and 1.9, respectively, from 0800 to 1200 MLT, and 1.1 for both these current systems from 0000 to 0800 MLT. Accordingly, the factors $S_k$ were set to 1 for all the filaments in the winter (southern) hemisphere, and to 1.1 for the filaments located from 0030 MLT to 0530 MLT in the northern hemisphere. However, the values of $S_k$ applied to the filaments located from 0630 MLT to 1030 MLT were increased by a factor of $\sqrt{3}$ beyond the summer-to-winter current ratios reported by Fujii et al. [1981] to account for the higher conductivity of the sun-lit ionosphere implied by the high solar 10.7-cm flux. *Fujii et al.* [1981] suggested that the higher conductivity of the sun-lit ionosphere was responsible for the enhanced Birkeland currents in the summer hemisphere. The Triad data used by *Fujii et al.* [1981] were acquired when the sun was very quiet. The first period (1973–1974) was at the very end of solar cycle 20 and the other (1976–1977) was at the beginning of solar cycle 21. Therefore, the solar EUV flux, which increases the conductivity of the ionosphere, was not as high during those years, on the average, than it was when the APADS were observed. The Triad data used in this study were taken when the solar 10.7-cm flux, which is well correlated with the solar EUV, was less than about 100. During the period of the APADS, the solar 10.7-cm flux was about 300. Since the conductivity is proportional to the square root of the solar 10.7-cm flux [*Robinson and Vondrak*, 1984], the values $S_k$ found by Fujii et al. [1981] were increased by $\sqrt{3}$ for the daytime filaments (0630–1030 MLT).

*Magnetic Flux Linkages*

Because of the symmetry of the geometry, as depicted in Figure 3, and the opposite flow directions of both the Region 1 and Region 2 currents in the northern and southern hemispheres, the net flux produced by these currents that link field lines at lower latitudes is zero if the currents are balanced. If the currents are not balanced, the net flux linkages may be determined by computing the magnetic flux produced by currents that are equal to the difference of the hemispherical currents and flow only in the hemisphere of the dominant current flow. Hence, the magnetic flux

$$\Phi_m(L) = \oint B_\varphi \mathrm{d}a \tag{2}$$

threading the area between the ionosphere and a dipole-field line at $L$ ($7 \geq L \geq 2$) in the 0600 MLT meridional plane was determined by using the Biot-Savart law to compute, at each element $\delta a$ of the enclosed area, the $\varphi$ component (eastward) of the magnetic field,

$$B_\varphi = -\frac{\mu_0}{4\pi}\sum_k \Delta I_k \int \frac{\mathrm{d}\bar{s}_k \times \bar{r}_k \cdot \hat{e}_2}{r_k^{\,3}} \tag{3}$$

produced by the difference of the hemispherical currents,

$$\Delta I_k = (S_k - 1)\, j_k R \sin\theta_k \delta w \delta\varphi \tag{4}$$

flowing in the northern-hemisphere filaments. In (3) $\mu_0$ is the permeability of free space ($4\pi \times 10^{-7}$ h/m), $\mathrm{d}\bar{s}_k$ is an incremental arc length along filament $k$ in the direction of the current, and $\bar{r}_k$ is the distance vector from the current element to $\delta a$. The unit vector $\hat{e}_2$ is directed eastward.

The magnitude of the magnetic flux, $\Phi_m(L)$, resulting from the integral of (2) over the areas enclosed by field lines increased rapidly from $2.04 \times 10^5$ T at $L$ = 1.95 to $2.34 \times 10^6$ T at $L$ = 3.45; then it increased more slowly to $2.19 \times 10^7$ T at $L$ = 7.07.

Since the standoff of the subsolar magnetopause, as implied by the solar-wind pressure, increased substantially during this event, the effect of the changing magnetopause and magnetotail currents on the parallel electric fields was explored. Tsyganenko's 1989 magnetic-field model [*Tsyganenko*, 1989] was used to the estimate the resulting change of the magnetic flux, $\Delta\Phi_m(L)$, threading the inclined areas bounded by dipole-field lines. This flux change was estimated by taking the difference of the flux linkages computed with the magnetic-disturbance parameter (IKP) of the model set to its extreme values, 1 and 8. The resulting value of $\Delta\Phi_m(L)$ was found to be $1.86 \times 10^6$T at $L$ =7, which is about an order of magnitude smaller than the flux $\Phi_m(7)$ produced by the Birkeland currents. The actual change of the magnetic flux was probably much higher because the geomagnetic-field disturbance during the August storm was far beyond the range of validity of the Tsyganenko model. Moreover, as discussed below, the time variation of this flux, as estimated from the change of the solar-wind pressure, was appreciable during this event.

*Time Variations of Currents*

Faraday's law of induction was used to compute the EMF, which is equal to the integral over the closed path along *s(L)*,

$$\oint \bar{E} \cdot \mathrm{d}\bar{s} = -\frac{\partial \Phi_{\mathrm{m}}(L)}{\partial t} \tag{5}$$

The time variations of the Birkeland currents were estimated from the on-board magnetometer data and the IMP-8 data in the solar wind. As shown in Figure 2, all three components of the local magnetic were different from the components given by the Olson-Pfitzer model [*Olson and Pfitzer*, 1977; *Walker*, 1979]. Moreover, the total magnetic field generally increased from its modeled value at 1300 UT to about 40 nT higher than its modeled value at 1545 UT. Although the distribution and closure of the Birkeland currents in the outer magnetosphere are uncertain, it seems that these currents may account for $\delta B_x$ and part of $\delta B_z$. Surely, the decreasing external currents, other than the Birkeland currents, also contribute to the increasing value of $\delta B_z$. The

$\delta B_y$ (eastward) component appears to be due principally to a combination of the Birkeland currents, which mainly contribute to a westward component, and the field-aligned $O^+$ ions, which probably contribute an eastward component because most of the $O^+$ current is expected to flow along field lines above the satellite. The ~ 1 hour fluctuations may have been due to temporal or spatial variations of the currents produced by multiple substorms. If we assume the total magnetic field above the modeled value, as shown in the bottom panel of Figure 2, was produced by Birkeland currents, and that the currents increased linearly from 0 at 1300 UT to the value given by (1) at 1545 UT, then from (5) the resulting EMFs at $L$ values of 5, 6, and 7 would be 0.76, 1.31, and 2.08 kV, respectively. These values are comparable to the average energy/charge ratios of the asymmetric $O^+$ ions.

The time variations of the Birkeland currents were also estimated from the work of *Iijima and Potmra* [1982], who used a linear least-squares technique to correlate a variety of interplanetary quantities, involving hourly values of solar wind density, speed, and IMF components, with Triad measurements of the Region 1 Birkeland-current densities. They also computed the "best" straight-line fit of the current densities to these interplanetary quantities. On the dawn side of the magnetosphere, they found the highest correlation (0.66) for the relationship,

$$J = 0.0328\xi + 1.4\ \mu A/m^2 \tag{6}$$

where

$$\xi = [N^{1/2}V(B_y^2 + B_z^2)^{1/2}\sin(\theta/2)]^{1/2} \tag{7}$$

Here, $N$ (cm$^{-3}$) and $V$ (km/s) are the solar-wind density and speed, and $\theta$ is the angle between the $z$ axis and the transverse component $(B_y^2 + B_z^2)^{1/2}$ (nT) of the IMF (GSM coordinates).

Figure 4 shows the time variation of the current density from (6) that was computed using 10-minute averages of the IMP 8 solar wind and IMF data for the time period of the observed $O^+$ APADS. At 1200 UT the IMP 8 satellite was located in the solar wind, being at $(X, Y, Z)_{GSM}$ = (5, -27, 12) $R_E$. In evaluating these results, the limitations of (6) must be kept in mind: the correlation coefficient was 0.66, the rms fit to the data was 0.68 $\mu A / m^2$, and the local times of the Triad data sere not specified. A significant feature of Figure 4 is that the current density of the Region 1 current was very high during the entire period of the APADS. Such high densities during this storm-time period appear plausible in view of the range of densities used by Iijima and Potemra, [1982] in this correlation analysis (see their Figure 4).

Another significant feature is the time variation of these current densities, which imply a similar variation of the Birkeland currents. The two pairs of vertical dotted lines drawn in the figure denote the time intervals during which the energies of the APADS, as shown in panels (b) and (f) of Figure 1, were much higher than those in the other panels. In panel (b) $O^+$ ions of energies up to 21 keV were asymmetric. Note that the sharpest increase of the Birkeland current density occurred during the measurement of these APADS. In fact, the jump in the current density from 1400 to 1411 UT is 2.55 $\mu A / m^2$, which is comparable to the highest density that was used for the computation of the flux linkages $\Phi_m (L)$ in (2). Such an increase of the flux in 11 minutes at $L = 6$ induces an EMF of 20 kV along the magnetic field! Notice in Figure 4 that the time interval of the APADS in panel (f), with respect to period of the second increase of the current density, is early by about 10 minutes. The highest energy of the asymmetric ions in panel (f) is about 10 keV, but the current density at that time interval is near a valley. If the interplanetary conditions changed earlier near the earth by 10 minutes than they did at the IMP8 spacecraft, both cases would have been in good agreement. However, it is more likely that the magnetopause and magnetotail currents also contributed to the electric fields responsible for both of these APADS, and probably for the entire event because, as shown in Figure 3 of *Jordan et al.* [1992], the **standoff distance** of the subsolar magnetosphere was increasing throughout this event, but it **increased especially** rapidly from about 1340 UT to 1500 UT and again toward the end of the event.

The persistence of ion flow in the same direction during the entire event also implies that all these external currents contributed importantly to the electric field. The computer experiments described below, which simulate the response of ions to a parallel electric field, reveal that the ion flow remains in the same direction as long as the electric field generally increases in time, except for periods comparable to half a bounce time of ions. Hence, the ion-flow direction should have reversed when the Birkeland currents decreased from 1433 UT to 1542 UT, as suggested by Figure 4. Since the ion-flow direction did not change, it appears that the magnetopause and magnetotail currents, which were decreasing during that time, continued the growth of the electric field.

*Response of Trapped Ions to Parallel Electric Field*

A computer program was written to simulate the motion of magnetically-trapped ions in the presence of a parallel electric field. The initial equatorial pitch-angle distribution of the flux, $j(t_0,w,\alpha_0)$, at $t_0 = 0$, energy $w$, and equatorial pitch angle, $\alpha_0$, was specified as input to the program. For non-relativistic particles, the quantity $j(t_0,w,\alpha_0)/w$ is conserved along the particle motion. Therefore, the equatorial flux at a later time, $t$, was taken to be $j(t,w',\alpha_0') = (w'/w)\,j(t_0,w,\alpha_0)$, where the time $t$, $w'$, and $\alpha_0'$ were determined by tracing the motion of an ion of initial energy $w$ and pitch angle $\alpha_0$ in the electric and magnetic fields. Actually, 16 ions were traced for each pair of the sampled initial conditions $w$, $\alpha_0$ in order to sample the spatial distribution of the ions at the onset time of the electric field. Each ion was started at the equator with specified values of $w$ and $\alpha_0$, and the electric field was turned on (at $t$ =0) when the ion reached one of 16 equally-spaced spatial bounce-phase positions. The ion case histories ($t$, $w'$, and $\alpha_0'$) and the sum of the flux values, $j(t,w',\alpha_0') = (w'/w)\,j(t_0,w,\alpha_0)$, were tallied in bins of widths $\Delta t$, $\Delta w'$, and $\Delta\alpha_0'$ each time the ion reached the equator. The average flux in a bin was then determined by dividing the sum of the flux values by the number of tallies in the bin.

The ion motion was computed by numerically integrating the equation,

$$\frac{dv_{//}}{dt} = -\frac{\mu}{m}\frac{dB}{ds} - \frac{q}{m}\frac{d\Psi}{ds} \tag{8}$$

where $v_{//}$ is the parallel ion velocity component (> 0 in the direction $\hat{B}$ and < 0 in the opposite direction); $s$ is the distance along the magnetic field measured from the equator (> 0 in the northern hemisphere and < 0 in the southern hemisphere); $\mu$ is the ion magnetic moment, which was assumed to be conserved; q and m are the charge and mass of the ion; and $\Psi(t, s)$ is the electric potential. The maximum value of the potential along a field line, $\Psi(t, s_{\text{lim}})$, where $s_{\text{lim}}$ is the field-line length to the altitude of 500 km in the northern hemisphere, was set equal to the EMF on that field line at the time $t$.

The initial equatorial pitch-angle distributions at $L$=6.67 of ions of various energies, which were specified as input for all the runs described here, were identically reproduced by the program when $\Psi(t, s_{\text{lim}})$ was set to zero for all values of $t$. These distributions are shown in panel (a) of Figure 5. The energy intervals of the ions are given in the insert.

The distributions at $L$=6.67 computed by using the step-function potential,

$$\Psi(t, s_{\text{lim}}) = \begin{cases} 0, & t = 0 \\ 2\,kV, & t > 0 \end{cases} \tag{9}$$

are shown in panels (b), (c), and (d) of Figure 5, averaged over the time periods 0–0.30, 0.30–0.60, and 0.60–0.90 hours, respectively. At $t > 0$, the magnitude of the electric field was constant, equal to 0.01924 mV/m, along the magnetic field. Notice in panel (b) of Figure 5 that the directional fluxes are lower than the initial fluxes at pitch angles less than about 90° and that they generally increase toward higher pitch angles. These features, which are similar to those of the measured APADS shown in Figure 1, are expected at early times because the parallel electric field, which extends from the northern to the southern hemispheres, accelerates the ions toward the equator in the northern hemisphere and precipitates or traps the lower-energy ions in the southern hemisphere. Ions, which are trapped by the opposing electric and magnetic forces in the southern hemisphere, are constrained to oscillate between magnetic (below) and the electric (above) mirrors. Since, in the present case, the electric field was uniform along $s$ at $t > 0$, it follows from (8) that an ion in the southern hemisphere at the position $s_i$ with energy $w = \mu B_m$ at $t = 0$ will be trapped if

$$w \leq \frac{q[\Psi_0 - \Psi(s_i)]}{1 - \dfrac{B_0}{B_m}} \tag{10}$$

The subscript 0 refers to quantities at the equator, $\boldsymbol{B_m}$ is the mirror-point field of the ion prior to the application of the electric field, and $\Psi(s_i)$ is the potential at $s_i$ at $t = 0$. This equation holds whether the ion moves toward or away from its initial mirror point at $t = 0$.

Notice that the ions of energies in the ranges 0.335–0.500, 0.500–0.745, and 0.745–1.105 keV, which have the highest directional fluxes at $\alpha = 171^\circ$ in panel (b) of Figure 5, have nearly equal fluxes at the supplementary pitch angle, 9°, in panel (c); and they return with similar fluxes at $\alpha = 171^\circ$ in panel (d). These oscillating ions had low mirror points in the northern hemisphere when the electric field was applied. They resemble the "bouncing ion clusters" observed by *Quinn and McIlwain* [1979] with the ATS 6 satellite. Of course, such bouncing clusters can also be produced by a parallel electric field of short duration.

If the potential increases with time, ions that cross the equator from the North may also become trapped between the electric and magnetic mirrors in the southern hemisphere. They will be trapped if, during the excursion time $t$ of the ion in the southern hemisphere, the potential at the equator increases by an amount that exceeds $w_{//}(t_0,0)/q$, the parallel energy/$q$ of the ion at its equatorial-crossing time, $t_0$. That is, if

$$q\Psi(t + t_0,0) - q\Psi(t_0,0) > w_{//}(t_0,0) \tag{11}$$

Moreover, since the distance between the electric and magnetic mirrors decreases as the electric field increases with time, the trapped ions are accelerated parallel to the magnetic field by the Fermi process. In the simulation program, ions were found to bounce between the electric and magnetic mirrors as many as 16 times before being precipitated into the atmosphere.

An increasing electric field also decreases the equatorial fluxes at pitch angles less than 90° because ions that cross the equator from the north move against an increasing electric field as they return to the equator from the south; hence their energies and directional fluxes at the equator are reduced.

The equatorial pitch-angle distributions at $L$=6.67, averaged over the time interval 0–0.5 hour, which were computed using the time-varying potential,

$$\Psi\,(t, s_{\text{lim}}) = \Psi\,(t = \infty, s_{\text{lim}})\,(1 - e^{-t/\tau}) \tag{9}$$

where $\tau$ = 0.5 hour and $\Psi\,(t = \infty, s_{\text{lim}})$ was set to 2 kV and 6 kV, are shown in panels (a) and (b), respectively, of Figure 6. The electric field was constant along the field line at each value of $t$, and at $t = \infty$, it was equal to 0.01924 mV/m and 0.05772 mV/m in panels (a) and (b), respectively.

Notice in panel (a) that ions in the energy range 0.335–0.500 keV are the most asymmetric, but in panel (b) ions in the range 0.745–1.105 keV are the most asymmetric. Computer runs with different values of $\Psi\,(t = \infty, s_{\text{lim}})$ revealed that, as $\Psi\,(t = \infty, s_{\text{lim}})$ increases from zero, the energy of the most asymmetric ions steadily increases. Moreover, the order of the ion energies from the most- to the least-asymmetric distribution change as follows: (1) at small values of $\Psi\,(t = \infty, s_{\text{lim}})$, the energies increase steadily from the lowest to the highest values, with the lowest-energy ions being the most asymmetric; (2) at the largest value of $\Psi\,(t = \infty, s_{\text{lim}})$, which was 15 kV, the order reverses: the energies decrease steadily from the highest to the lowest values, with the highest-energy ions being the most asymmetric; and (3) at intermediate values of $\Psi\,(t = \infty, s_{\text{lim}})$, the order is not monotonic: the energies initially decrease steadily from an intermediate value, at which the ions are the most asymmetric, to the lowest value; then they increase from the step above the intermediate value to the highest energy. The characteristics of these pitch-angle distributions are similar to those of the $O^+$ APADS shown in Figure 1. These simulation results indicate the $O^+$ APADS may have been caused by such an electric field that was steadily increasing in time, except for time intervals of about 1/3 hour (half the bounce time of the asymmetric ions), which is the time required to sense a change in the ion distribution.

At later times – after the potential in (9) became approximately steady – the ion pitch-angle distributions "sloshed" back and forth a few times, with an amplitude much less than shown in panels (c) and (d) of Figure 5, before they became symmetric about 90°. It is not clear why such sloshing is not displayed by the $O^+$ APADS shown in Figure 1. However, such sloshing is undoubtedly dependent on the spatial distribution of the electric field, as well as the time variations as indicated by the simulations. Moreover, it is affected by processes that were not simulated, particularly by those such as the cross-$\boldsymbol{B}$ drift and pitch-angle diffusion that change the distribution of the ions that are trapped between the electric and magnetic mirrors in the southern hemisphere.

An attempt was not made to seek better agreement with the data by trying more sophisticated spatial and temporal distributions of the potential because of the limited scope of the simulation program. Certainly, the fluctuations shown in Figure 2 imply the presence of waves that may interact with the ions. Moreover, the ions may diffuse in pitch angle because of streaming instabilities associated with the acceleration of ions along the magnetic field. Ions from the local ionosphere are particularly subject to such pitch-angle diffusion. These ions were not included in the simulation because, in the absence of diffusion, they would have been precipitated in the southern hemisphere.

## Summary

All 17 of the equatorial pitch-angle distributions of ions (< 20 keV) reported here, which were asymmetric for periods much longer than the ion bounce times, were observed during highly-disturbed magnetospheric conditions, in the dawn and dusk sectors, and while the dipole-tilt was appreciably toward or away from the sun. The distributions of the $O^+$ ions were the most asymmetric; and the distributions of successively-lower asymmetry were those of the $He^+$ and $H^+$ ions. The study reported here indicates this asymmetry was caused by a parallel electric field, $\boldsymbol{E}_{//}$, that extended from one hemisphere to the other and generally increased with time. Because ions are accelerated by such a field toward the equator in one of the hemispheres, the directional flux, $j(w,\alpha)$, of the ions, which increases as the ion energy increases, is the highest at the equator in the direction of $E_{//}$. In the other hemisphere, ions are either (1) lost (precipitated in the atmosphere because of their continued acceleration by $E_{//}$), (2) stored (trapped by the opposing electric and magnetic forces), or (3) returned to the equator with lower energies, hence with lower directional fluxes if $E_{//}$ increases with time.

Additional processes can accelerate particles along the magnetic field, such as the centrifugal force arising from the $\boldsymbol{E} \times \boldsymbol{B}$ drift [*Cladis*, 1986; *Horwitz*, 1987; *Delcourt et al.*, 1990], the ponderomotive force [e. g., *Li and Temerin*, 1993], and Fermi acceleration. Moreover, if trapped particles drift onto distended field lines, their equatorial parallel velocities increase adiabatically as discussed by Tsyganenko [1989]. However, these processes alone would not cause a long-term asymmetry of the ion pitch-angle distribution because they would increase $v_{//}$ by nearly the same magnitude in both directions, $\hat{B}$ and $-\hat{B}$, near the equator.

The analysis of the event of August 26, 1990, indicates that the electric field was induced by the time-varying external currents (magnetopause, magnetotail, and Birkeland currents) during times when the dipole-tilt angle was appreciably greater than, or less than, zero. A symmetrical ring current does not induce such a field. In order to account for the direction of the ion flow, the electric field along a field line must have been induced by an increasing magnetic flux, toward the west in solar-magnetic coordinates, through the area enclosed by the field line. Such flux changes are produced by increasing Birkeland currents and decreasing tail currents, but only when the dipole-tilt angle is not zero. The Birkeland currents do not produce a net flux through the area enclosed by the field line when they are symmetrical across the equator; they do so only when the dipole is tilted because, then, they are stronger in the summer hemisphere than in the winter hemisphere. Moreover, the tail currents do not produce a net flux through such areas unless they are inclined with respect to the $z_{GSM}$ axis. The magnetopause currents produce flux through these inclined areas that is in the opposite direction to that produced by the tail current. However, while the standoff distance is increasing, the net change in the flux produced by the magnetopause currents is less than that produced by the magnetotail currents.

The estimate of the EMF produced by the growth of the Birkeland currents, based on the time variations of these currents inferred from the on-board magnetometer and interplanetary conditions, was found to be appropriate to account for the asymmetry of the ions. By using Tsyganenko's 1989 model [*Tsyganenko*, 1989], with his activity parameter, IKP, set to 8 and 1, respectively, the flux change produced by the magnetopause and magnetotail currents through the areas enclosed by the field lines was estimated for a jump of the standoff distance from its minimum to its maximum values allowed by the field model. This flux change was found to be about an order of magnitude lower than that produced by the full range of the Birkeland currents. Nevertheless, the tail current is regarded to be an important source of the electric field because the disturbance of the magnetic field during this storm was far beyond the range covered by Tsyganenko's model.

Both of these sources induce electric fields in directions that are consistent with the directions of the inter-hemispheric ion flows of all the observed events (17), which were from summer-to-winter in the dawn sector and from winter-to-summer in the dusk sector, as illustrated in Figure 3. These observations include the longer-lasting events listed in Table 1 ( 2 in the dawn sector and 5 in the dusk sector), and 9 shorter-term events (3 in the dawn sector and 6 in the dusk sector). Unfortunately, apogee of the CRRES satellite was near both flanks of the magnetosphere only during northern summer. The APMTE/CCE data on the $O^+$ APADS event, which were kindly provided by Dave Klumpar of the Lockheed-Martin Space Sciences Laboratory, were obtained near dawn during northern winter.

The essential features of the $O^+$ APADS were reproduced with the computer-simulation program when the electric field was increasing with time. An increasing electric field, except for periods of about half the ion bounce time, was found necessary to account for the persistency of the ion flow direction. Although the APADS shown in Figure 1 imply time variations of the magnitude of the electric field, the ion flow remained in the same direction for about 3 hours. Therefore, the flux linkages in (2) must have increased faster than linearly during the event. Indeed, Figure 2 suggests that the portion of the total magnetic field ascribed to the external currents (the part beyond the modeled field) generally increased faster than linearly during the period of the $O^+$ APADS (1319 UT–1556 UT). Although the estimate of the time variation of the Birkeland currents, based on the solar-wind conditions (Figure 4), suggests the Birkeland currents decreased for a short period of time, the electric field probably continued to increase in the same direction because the standoff distance was increasing during that period and, indeed, throughout the entire event.

The pitch-angle asymmetries of the $He^+$ and $H^+$ ions, which were measured in the same energy/charge range as the $O^+$ ions, were progressively less pronounced than those of $O^+$ because their velocities were progressively higher.

## Conclusions

The computer-simulation results reveal that the asymmetric pitch-angle distributions observed near the equator with the CRRES and AMPTE/CCE satellites were caused by parallel electric fields that generally increased with time and extended from one hemisphere to the other. According to the detailed analysis of the event observed on August 26, 1990, the electric field was induced by increasing Birkeland currents, which are stronger in the summer hemisphere than in the winter hemisphere, and by the decreasing tail current implied by the decreasing solar-wind pressure. Since the directions of this electric field in the dawn and dusk sectors, during northern summer and winter, is consistent with the directions of all the observed inter-hemispheric ion flows, one or both of these current sources may have been responsible for all these events. The absence of flows in the opposite directions may imply that the time variations of decaying Birkeland currents and increasing tail currents are not sufficient to produce appreciable electric fields.

These electric fields, through the asymmetric precipitation of ions and electrons in the northern and southern hemispheres and the trapping of ions between magnetic and electric mirrors in one of the hemispheres, may also produce differences in inter-hemispherical high-latitude phenomena such, as ionospheric convection and auroras.

More of the APADS events should be analyzed in detail to obtain additional information on the processes reported here. Moreover, the behavior of all the particles that were measured during these events should be studied to improve our understanding of the response of the diverse populations of magnetospheric charged particles to a parallel electric field.

*Acknowledgments*. We wish to thank J. M. Quinn for bringing the observation of the APADS to our attention and for helpful discussions regarding their interpretation. We also thank H. J. Singer for sending us the magnetic-field measurements made on the CRRES satellite during several of the observed APADS events and D. M. Klumpar for providing his data on the event observed with the AMPTE/CCE satellite. We are grateful to M. Schulz for valuable discussions in all phases of this study and R. W. Nightingale for his able assistance in the preparation of this report. This work was supported by The Office of Naval Research under contract N00014–94–C–0042.

# References

Cladis, J. B., Parallel acceleration and transport of ions from polar ionosphere to plasma sheet, *Geophys. Res. Lett., 13,* 893, 1986.

Collin, H. L., J. M. Quinn, J. M. Smith, E. Hertzberg, S. Roselle, and S. J. Battel, The low energy ion mass spectrometer (ONR-307-8-1, 2) on CRRES, *J. Spacecraft and Rockets, 29,* 617, 1992.

Delcourt, D. C., J. A. Sauvaud, and A. Pedersen, Dynamics of single-particle orbits during substorm expansion phase, *J. Geophys. Res., 95,* 20,853, 1990.

Fujii, R., T. Iijima, T. A. Potemra, and M. Sugiura, Seasonal dependence of large-scale Birkeland currents, *Geophys. Res. Lett, 8,* 1103, 1981.

Heikkila, W. J., and R. J. Pellinen, Localized induced electric field within the magnetotail, *J. Geophys. Res., 82,* 1610, 1977.

Horwitz, J. L., Parabolic heavy ion flow in the polar magnetosphere, *J. Geophys. Res., 92,* 175, 1987.

Iijima, T., and T. A. Potemra, Large-scale characteristics of field-aligned currents associated with substorms, *J. Geophys. Res., 83,* 599, 1978.

Iijima, T., and T. A. Potemra, The relationship between interplanetary quantities and Birkeland current densities, *Geophys. Res. Lett., 9,* 442, 1982.

Jordan, C. E., J. N. Bass, M. S. Gussenhoven, J. F. Singer, and R. V. Hilmer, Comparison of magnetospheric magnetic field models with CRRES observations during the August 26, 1990, storm, *J. Geophys. Res., 97,* 16,907, 1992.

Li, X., and M. Temerin, Ponderomotive effects on ion acceleration in the auroral zone, *Geophys. Res. Lett., 20,* 13, 1993.

Olson, W. P., and K. Pfitzer, Magnetospheric magnetic field modeling, annual scientific report, Air Force Off. of Sci. Res. Contract F44620-75-C-0033, 96 pp., McDonnell Douglas Astronautics Co., Huntington Beach, Calif., 1977.

Quinn, J. M., and C. E. McIlwain, Bouncing ion clusters in the Earth's magnetosphere, *J. Geophys. Res.*, *84*, 7365, 1979.

Robinson, R. M., and R. R. Vondrak, Measurements of E region ionization and conductivity produced by solar illumination at high latitudes, *J. Geophys. Res.*, *89*, 3951, 1984.

Shelley, E. G., A. Ghielmetti, E. Hertzberg, S. J. Battel, K. Altwegg-Von Burg, and H. Balsiger, The AMPTE/CCE hot-plasma composition experiment (HPCR), *IEEE Trans. Geosci. Remote Sensing*, *GE-23*, 243, 1985.

Singer, H. J., W. P. Sullivan, P. Anderson, F. S. Mozer, P. R. Harvey, J. R. Wygant, and W. McNeil, Fluxgate magnetometer instrument on the CRRES, *J. Spacecraft and Rockets*, *29*, 599, 1992.

Tsyganenko, N. A., A model of the magnetospheric magnetic field with a warped tail current sheet, *Planet. Space Sci.*, *37*, 5, 1989.

Tsyganenko, N. A., On the re-distribution of the magnetic field and plasma in the near nightside magnetosphere during a substorm growth phase, *Planet. Space Sci.*, *37*, 183, 1989.

Walker, R. J., Quantitative modeling of planetary magnetospheric magnetic fields, in *Quantitative Modeling of Magnetospheric Processes*, ed. by W. P. Olson, *Geophys. Monogr. Ser., Vol. 21*, AGU, Washington, D. C., pp 9-34, 1979.

# Figure Captions

Figure 1. Measurements of the pitch-angle distributions of $O^+$ ions made on the CRRES satellite on August 26, 1990. The $L$ and time intervals of the measurements are given in the panels.

Figure 2. Magnetic-field measurements made on the CRRES satellite [*Singer et al.*, 1992] during the APADS event of August 26, 1990. The top three panels show the differences between measured and modeled (*Olson and Pfitzer* [1977]) VDH magnetic-field components, and the bottom panel shows the measured (solid line) and modeled (dotted line) total magnetic field. Please see text.

Figure 3. Illustration of modeling of Birkeland Region 1 (outermost heavy field line) and Region 2 (inner heavy field line) with electric "wires" along dipole field lines. The innermost, light lines denote the predicted ion-flow directions during northern summer and northern winter at dawn and dusk. All the measured ion-flow directions were consistent with the predicted values.

Figure 4. Time variation of Birkeland 1 current density during the APADS event of August 26, 1990, based on straight-line fit given by *Iijima and Potmra* [1982] of measured current densities to the interplanetary quantities described in the text [see equations (6) and (7)].

Figure 5. Simulated equatorial pitch-angle distributions of $O^+$ ions at $L$ =6.67. The initial distributions are shown in panel (a) ($E$ = 0). In panels (b), (c), and (d), the computed distributions for $E(t{>}0)$ = 0.01923 mV/m (step-function electric field constant along $s$) are shown for the time intervals 0–0.30 hour, 0.30–0.60 hour, and 0.60–0.90 hour, respectively.

Figure 6. Simulated equatorial pitch-angle distributions at $L$ =6.67 in time interval 0–0.5 hour, computed for the time-varying potential $\Psi(t, s_{\lim}) = \Psi(t=\infty, s_{\lim})\,(1 - e^{-t/\tau})$, where $\tau =$ 0.5 hr and $E(t,s) = -\partial\Psi(t,s)/\partial s$ was constant along $s$. In (a), $\Psi(t=\infty, s_{\lim}) = 2$

kV and $E(t = \infty, s) = 0.01924$ mV/m, and in (b), $\Psi\,(t = \infty, s_{\mathrm{lim}}) = 6$ kV and $E(t = \infty, s) = 0.05772$ mV/m.

# Tables

Table 1. Observations of Asymmetric Pitch-Angle Distributions of duration exceeding 2 hours

| CRRES Orbit | Date | Time (UT) | Ion-Flow Direction along Field | L Value | Magnetic Local Time (hr) |
|---|---|---|---|---|---|
| 50 | 8/15/90 | 1150 to 1400 | $-\hat{B}$ | 5.4 to 7.2 | 6.7 to 7.2 |
| 77 | 8/26/90 | 1300 to 1600 | $-\hat{B}$ | 4.6 to 6.2 | 4.6 to 6.8 |
| 766 | 6/5/91 | 0400 to 0740 | $+\hat{B}$ | 5.7 to 7.3 | 17.4 to 19.5 |
| 767 | 6/5/91 | 1500 to 1820 | $+\hat{B}$ | 6.7 to 7.0 | 18.2 to 20.2 |
| 846 | 7/9/91 | 0800 to 1020 | $+\hat{B}$ | 5.2 to 7.8 | 18.2 to 19.9 |
| 856 | 7/13/91 | 1100 to 1500 | $+\hat{B}$ | 6.2 to 7.6 | 15.5 to 18.1 |
| 858 | 7/14/91 | 0800 to 1100 | $+\hat{B}$ | 7.0 to 8.1 | 15.9 to 17.8 |

Table 2. Conditions at Times of Events

| CRRES Orbit | Dipole-Tilt Angle | Solar Wind Conditions Den. (cm$^{-3}$) | Solar Wind Conditions Vel.(km/s) | Kp | *D*st(nT) | Solar 10.7 cm Flux |
|---|---|---|---|---|---|---|
| 50 | 16.72° to 21.98° | 6 | 580 | > 4.7 | −50 | 155.9 |
| 77 | 16.29° to 20.86° | 12 | 740 | > 6 | −100 | 285.1 |
| 766 | 11.78° to 14.57° | 34 | 600 | 7.3 | −120 | 258.1 |
| 767 | 32.20° to 32.31° | 30 | 560 | 8.7 | −180 | 258.1 |
| 846 | 14.93° to 20.64° | 2 | 700 | > 7 | −150 | 200.6 |
| 856 | 21.96° to 31.38° | No Data | | > 8 | −170 | 202.3 |
| 858 | 14.25° to 21.82° | No Data | | > 6 | −120 | 194.8 |

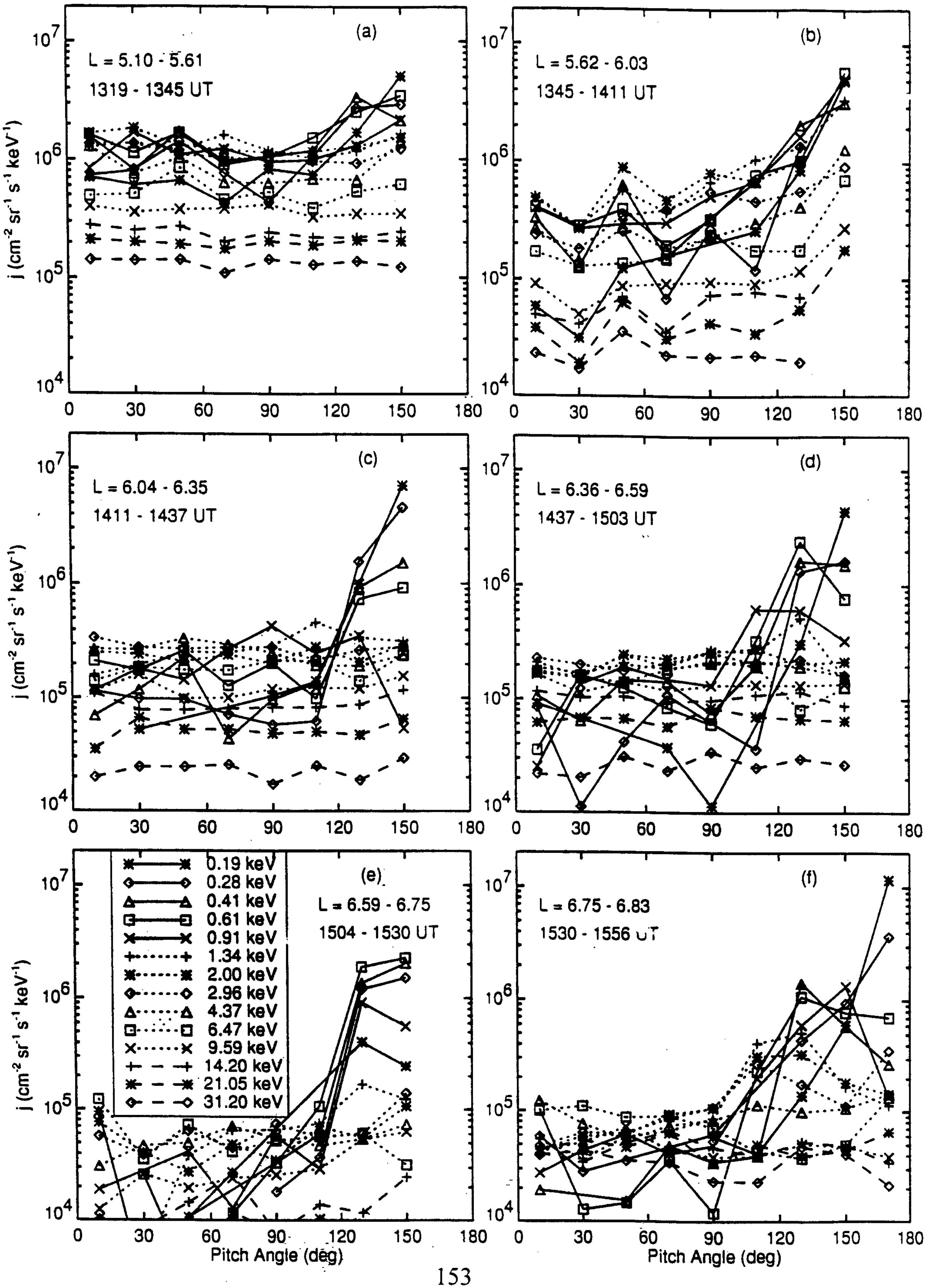(a)
L = 5.10 - 5.61
1319 - 1345 UT
(b)
L = 5.62 - 6.03
1345 - 1411 UT
(c)
L = 6.04 - 6.35
1411 - 1437 UT
(d)
L = 6.36 - 6.59
1437 - 1503 UT
(e)
L = 6.59 - 6.75
1504 - 1530 UT
(f)
L = 6.75 - 6.83
1530 - 1556 UT
j (cm⁻² sr⁻¹ s⁻¹ keV⁻¹)
10⁷
10⁶
10⁵
10⁴
0
30
60
90
120
150
180
Pitch Angle (deg)
0.19 keV
0.28 keV
0.41 keV
0.61 keV
0.91 keV
1.34 keV
2.00 keV
2.96 keV
4.37 keV
6.47 keV
9.59 keV
14.20 keV
21.05 keV
31.20 keV

Figure 1

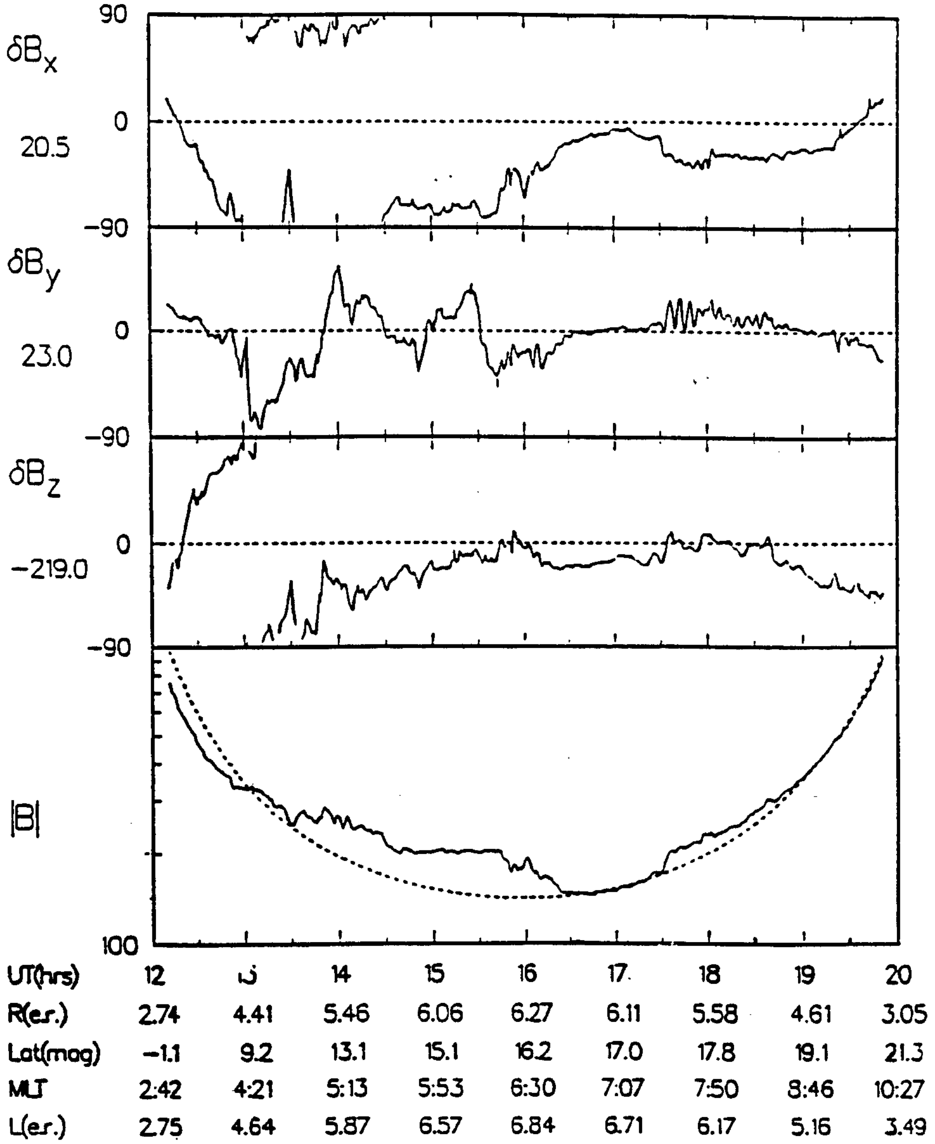
δBx
90
0
20.5
-90
δBy
0
23.0
-90
δBz
0
-219.0
-90
|B|
100
UT(hrs) 12 13 14 15 16 17 18 19 20
R(e.r.) 2.74 4.41 5.46 6.06 6.27 6.11 5.58 4.61 3.05
Lat(mag) -1.1 9.2 13.1 15.1 16.2 17.0 17.8 19.1 21.3
MLT 2:42 4:21 5:13 5:53 6:30 7:07 7:50 8:46 10:27
L(e.r.) 2.75 4.64 5.87 6.57 6.84 6.71 6.17 5.16 3.49

Figure 2

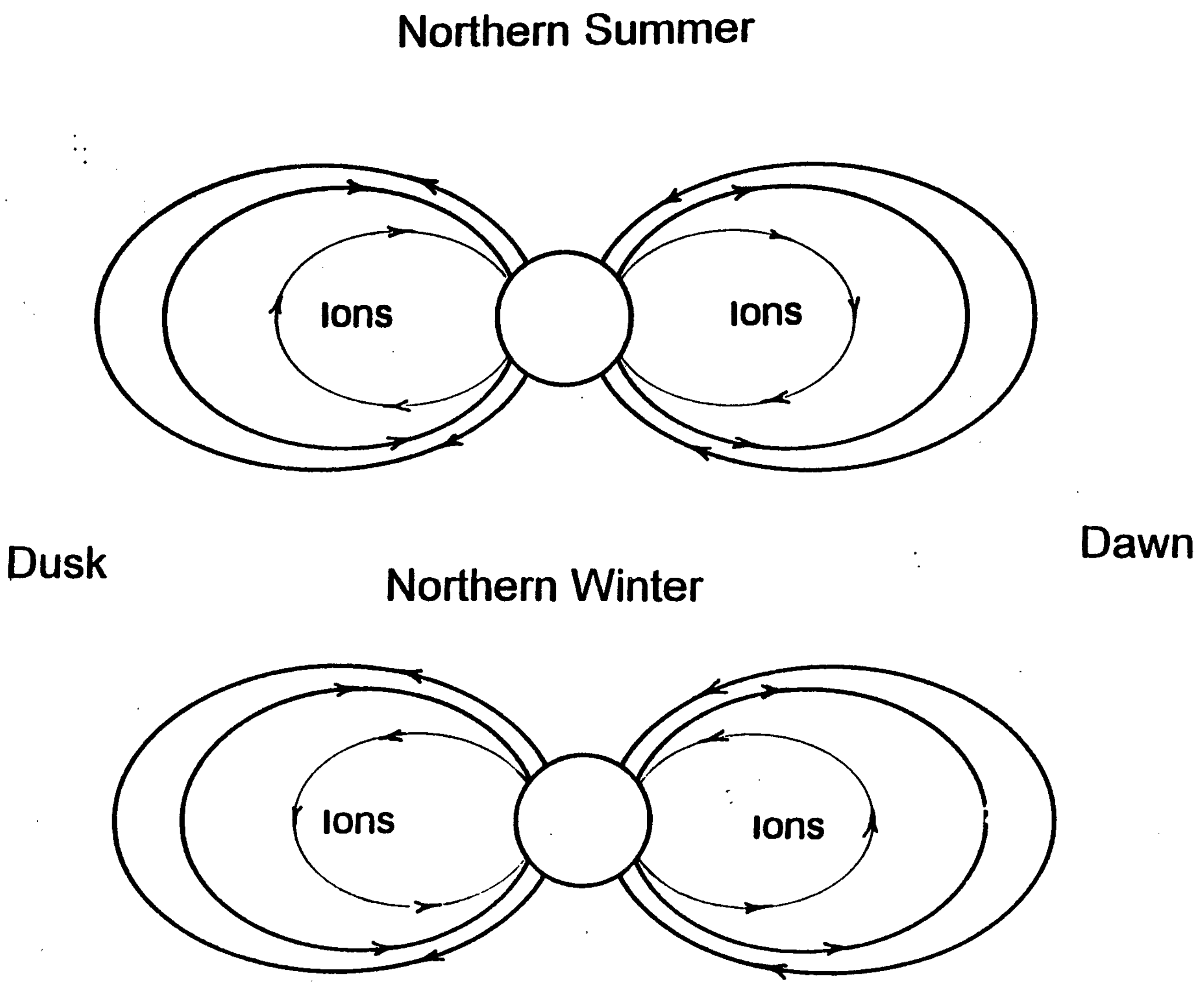
Northern Summer
Ions
Ions
Dusk
Dawn
Northern Winter
Ions
Ions

Figure 3

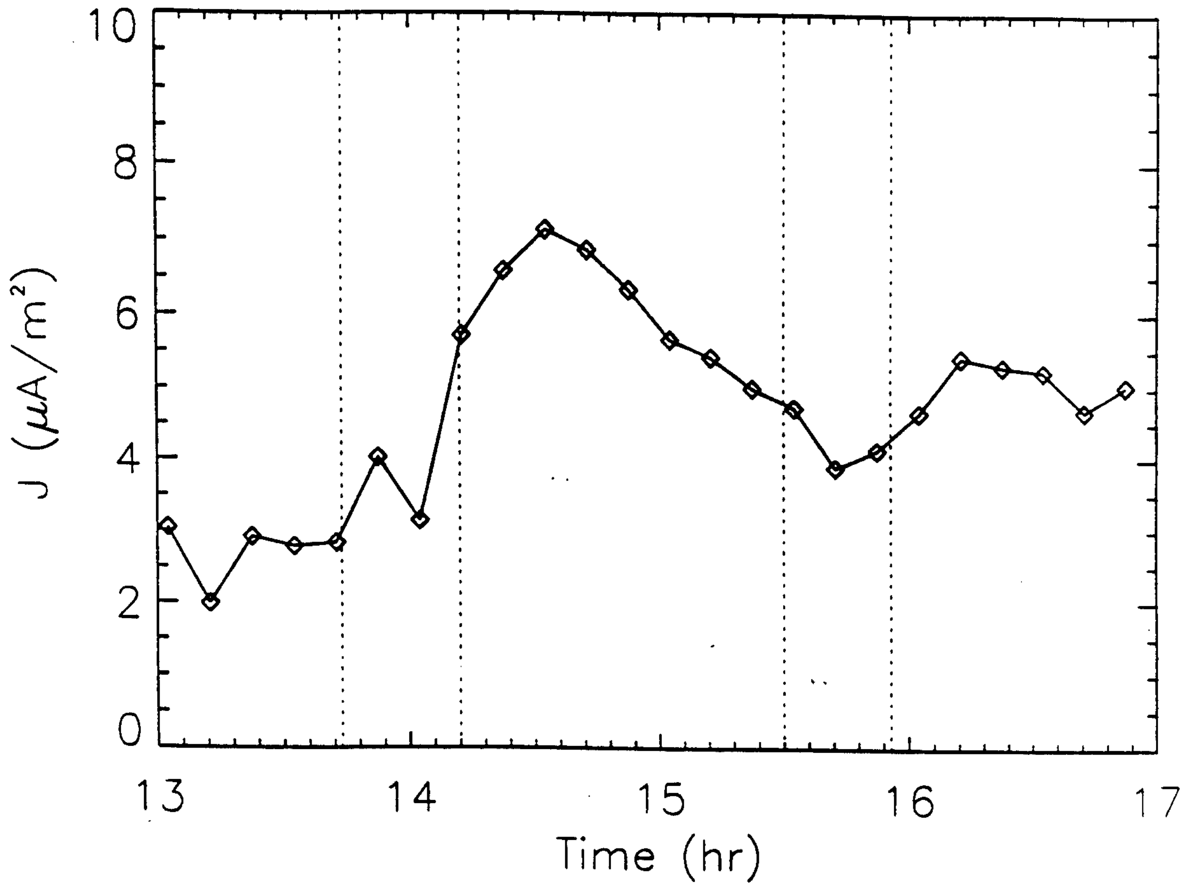

Figure 4

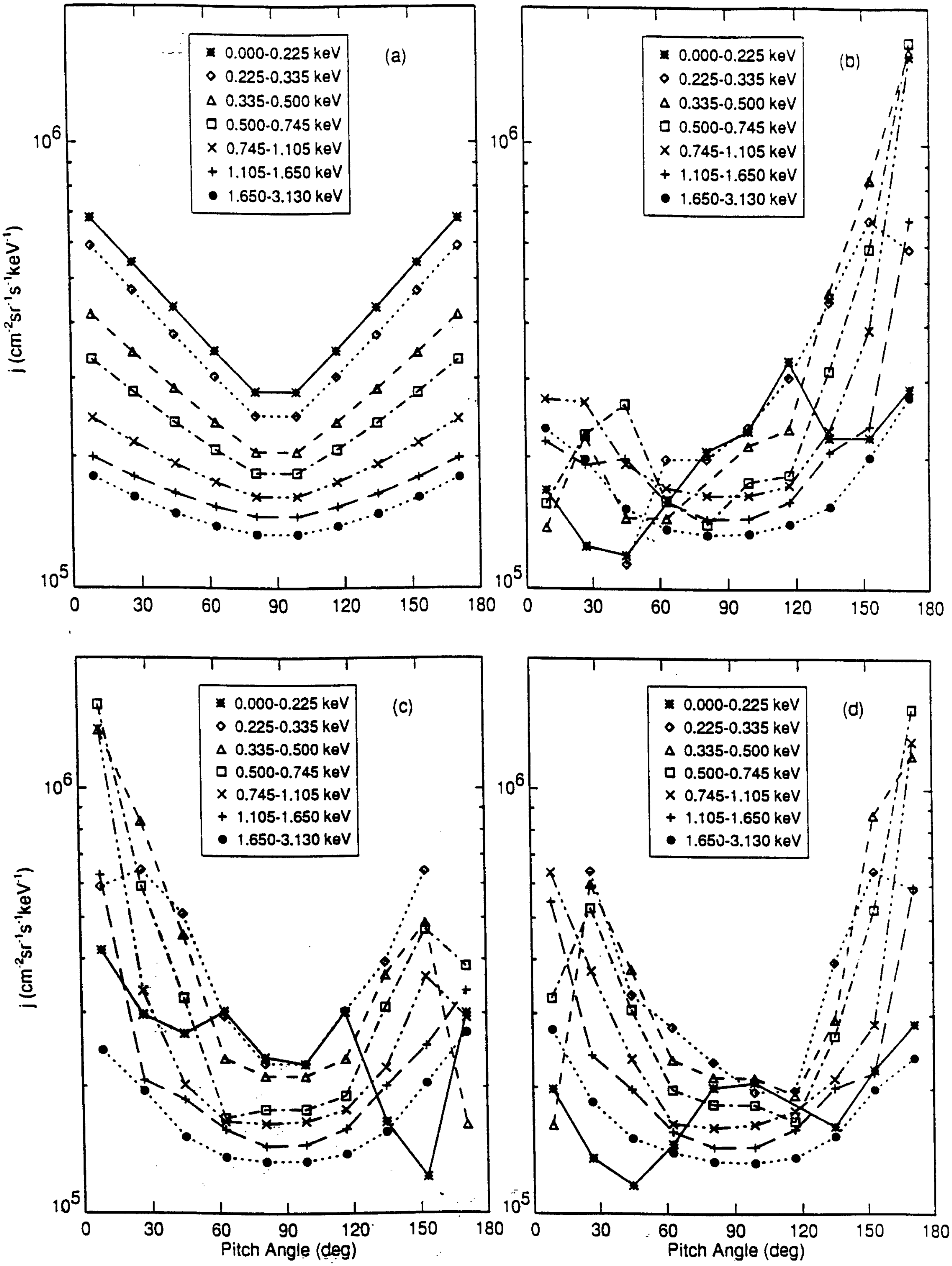
(a)
0.000-0.225 keV
0.225-0.335 keV
0.335-0.500 keV
0.500-0.745 keV
0.745-1.105 keV
1.105-1.650 keV
1.650-3.130 keV
(b)
0.000-0.225 keV
0.225-0.335 keV
0.335-0.500 keV
0.500-0.745 keV
0.745-1.105 keV
1.105-1.650 keV
1.650-3.130 keV
(c)
0.000-0.225 keV
0.225-0.335 keV
0.335-0.500 keV
0.500-0.745 keV
0.745-1.105 keV
1.105-1.650 keV
1.650-3.130 keV
(d)
0.000-0.225 keV
0.225-0.335 keV
0.335-0.500 keV
0.500-0.745 keV
0.745-1.105 keV
1.105-1.650 keV
1.650-3.130 keV
j (cm⁻²sr⁻¹s⁻¹keV⁻¹)
10⁶
10⁵
0
30
60
90
120
150
180
Pitch Angle (deg)

Figure 5

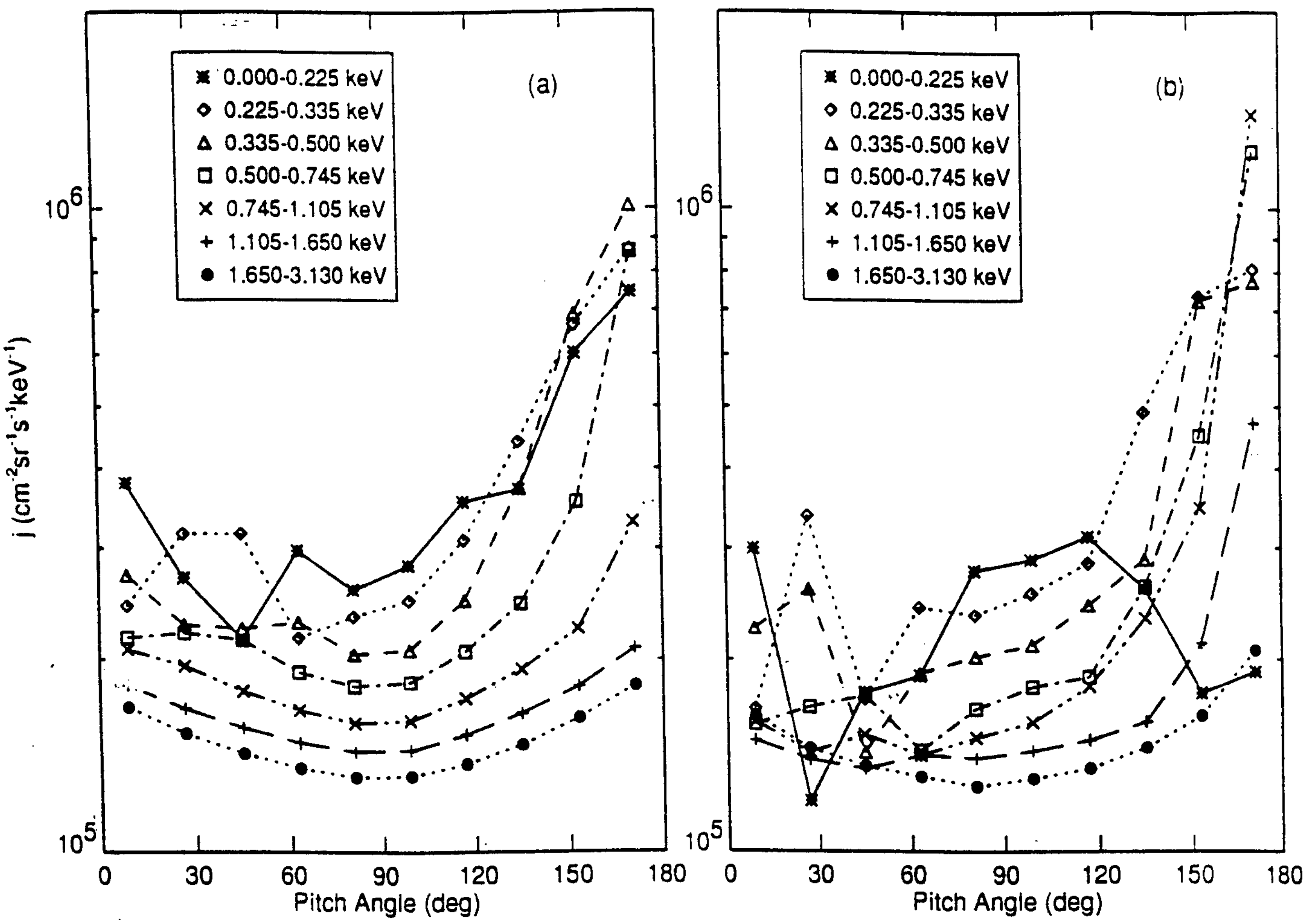

(a)
(b)
✱ 0.000-0.225 keV
◇ 0.225-0.335 keV
△ 0.335-0.500 keV
□ 0.500-0.745 keV
× 0.745-1.105 keV
+ 1.105-1.650 keV
● 1.650-3.130 keV
j (cm⁻²sr⁻¹s⁻¹keV⁻¹)
10⁶
10⁵
0
30
60
90
120
150
180
Pitch Angle (deg)

Figure 6

*AGU Spring 1994 Meeting SM52A-05*

# The Rice Magnetospheric Specification and Forecast Model: Inner Magnetosphere Test Results

R. L. Lambour, J. W. Freeman, R. A. Wolf, R. Spiro, B. Hausman, A. Nagai, B. Bales (All at Space Physics and Astronomy Department, Rice University, Houston, TX, 77251-1892)

R. Hilmer, W. Denig and D. Hardy (Phillips Laboratory, Geophysics Directorate, Hanscomb AFB, 01731)

D. McComas and M. Thomsen (Los Alamos National Laboratory, Los Alamos, NM 87545)

H. L. Collin (Lockheed Palo Alto Research, Palo Alto, CA, 94304-1911)

## Abstract

The Rice Magnetospheric Specification and Forecast Model (MSFM) is designed to be an operational model which will be used as a diagnostic tool for spacecraft charging and other operational spacecraft anomalies in post-event analysis and also for use in a real-time operational setting. The model specifies electron and ion ($H^+$ and $O^+$) fluxes of energies between 100 eV and 100 keV in the distance range from 2-10 $R_E$ on a two dimensional grid. We have completed intensive testing and calibration of the model using *in situ* observations from the CRRES satellite, data from the Los Alamos Magnetospheric Plasma Analyzer (MPA) aboard geosynchronous spacecraft 1989-046, the NASA trapped radiation models, and previously published observational data for comparison purposes. We have generated flux comparisons and root-mean square errors for six magnetic storm intervals. A brief summary of the results will be presented.

Abstract of paper presented at 1994 American Geophysical Union Fall Meeting

## Narrow Flux Drop-offs and Enhancements in the Outer Radiation Belt, Association With Waves and Magnetic Fields

W L Imhof H D Voss J Mobilia H L Collin (Lockheed Palo Alto Research Laboratory, Palo Alto, California 94304)
J R Wygant, (Space Sciences Laboratory, University of California, Berkeley, California 78228)
R R Anderson, (Department of Physics and Astronomy, University of Iowa, Iowa City, Iowa 52242)
H J Singer, (Space Environment Laboratory, NOAA R/E/SE, Boulder, Colorado 80303)

An investigation has been made of localized decreases and increases in the energetic particles, some at positions deep within the trapped population of the radiation belt. The study was performed with measurements of electrons, protons and He$^+$ particles at near equatorial position from the CRRES satellite. Electric field wave and magnetic field strength data recorded on CRRES were also used. Narrow observation time drop-offs near midnight with widths of only a few minutes well within the trapped population occurred at L shells as low as 5.4. Drop-offs occurred in both electrons and protons, and on some occasions with very similar flux profiles whereas in other cases there were major differences such as no proton flux decreases at the times of large changes in the electrons. Other events typically at higher L shells had slow decreases in particle flux followed by rapid increases, consistent with those often observed from synchronous orbit satellites and attributed to substorms, as substantiated by observations of AKR. Repeated narrow duration drop-offs and enhancements were sometimes observed around a broad event. The CRRES measurements of flux variations with L shell indicate that if the flux decreases are produced by a radial shift of the particle population, large spatial movements are required. Coordinated measurements of waves and magnetic field strengths are used to provide important information on the source(s) of fine-structure flux variations.

Abstract of paper presented at 1995 American Geophysical Union Fall Meeting

## Asymmetric Pitch-Angle Distributions and Birkeland Currents in the Outer Magnetosphere

J. B. Cladis (2440 Sharon Heights, Menlo Park, CA 94025; 415-854-0499; e-mail: cladis@rddvax.decnet.lockheed.com)
H. L. Collin (Lockheed Martin Palo Alto Research Laboratories, 3251 Hanover St., Palo Alto, CA 94304)

Ion spectrometers onboard AMPTE/CCE and CRRES have revealed highly asymmetric stormtime pitch-angle distributions (0° vs. 180°) for $O^+$ ions ~ 1 keV energy near dawn and dusk in the equatorial region of the outer magnetosphere ($R > 4\ R_e$) during the winter and summer seasons. These ion asymmetries persist for periods up to 4 hours. During these periods the pitch-angle distributions of electrons (< 20 keV) change toward isotropy. The observed $O^+$ pitch-angle distributions suggest a net summer-to-winter ion flow in the dawn sector and a net winter-to-summer ion flow in the dusk sector. This is consistent with the direction of the induced parallel (to B) electric field that accompanies the growth of the Region-1 Birkeland current, which is asymmetric during summer and winter because the current is stronger in the summer hemisphere. Simulation of the growth of the Birkeland currents inferred by the CRRES magnetometer during an event observed on August 26, 1990 indicates that the induced electromotive force along the magnetic field increased from about 1 kV at $L = 4$ to 8 kV at $L = 7$. These values are sufficient to account for the asymmetry of the $O^+$ ions.

## Symbols, Abbreviations, and Acronyms

| | |
|---|---|
| $\alpha$ | pitch-angle designation |
| AFGL | U.S. Air Force Geophysical Laboratory |
| AKR | Auroral Kilometric Radiation |
| AMPTE | Active Magnetospheric Particle Tracer Explorer |
| AMU | Atomic Mass Units of ion |
| APADS | Asymmetrical Pitch-Angle DistributionS |
| B, $\boldsymbol{B}$, $\hat{\boldsymbol{B}}$ | magnetic field intensity, vector, and unit vector |
| $B_x$, $B_y$, $B_z$, $B_t$ | magnetic field directional and total intensities |
| CCE | Charged Composition Explorer |
| cm | centimeter |
| COSPAR | international Committee On SPAce Research |
| CRRES | Combined Release and Radiation Effects Satellite |
| dE/dx | a thin silicon detector for measuring particle loss |
| DoD | Department of Defense |
| D region | region of ionosphere from ~70 - 90 km existing during daylight |
| *D*st | magnetic index of the ring current |
| e | charge of an electron |
| E | Energy of ion |
| ELF | Extreme Low Frequency |
| EMF | ElectroMagnetic Force |
| eq. | equation |
| et al. | et alii, Latin for "and others" |
| eV | electron Volt |
| GSM | Geocentric Solar-Magnetospheric coordinates |
| $H^+$ | Hydrogen ion |
| $He^+$ | Helium ion |
| HEO | High Earth Orbit |
| HEPS | High Energy Particle Spectrometer |
| HF | High Frequency |
| HPCE | Hot Plasma Composition Experiment on AMPTE |
| Hz | Hertz, a unit of frequency |
| i.e. | id est, Latin for "that is" |
| IMF | Interplanatary Magnetic Field |
| IMP | Interplanetary Monitoring Platform |
| IMS-HI | HIgh energy Ion Mass Spectrometer, an ONR-307 instrument on CRRES |
| IMS-LO | LOw energy Ion Mass Spectrometer, an ONR-307 instrument on CRRES |
| j | current density |
| $J$ | solar-wind current density |
| keV | kilo-electron Volts (= $10^3$ eV) |
| kHz | kilohertz (= $10^3$ Hz) |
| km | kilometer (= $10^3$ m) |

| | |
|---|---|
| $Kp$ | magnetic index geomagnetic activity in auroral region |
| LEO | Low Earth Orbit |
| L-shell, L | magnetic shell indicator |
| m | meter |
| M | Mass of ion |
| MCA | Multichannel Spectrum Analyzer,a part of Iowa/AFGL CRRES instrument |
| MeV | Mega-electron Volts (= $10^6$ eV) |
| $\mu$A | microAmpere (= $10^{-6}$ Ampere) |
| min | minute |
| nT | nanoTesla (=$10^{-9}$ Tesla), magnetic field unit |
| $N$ | solar-wind density ($cm^{-3}$) |
| NASA | National Aeronautics and Space Administration |
| $O^+$ | Oxygen ion |
| ONR | Office of Naval Research |
| ONR-307 | ONR sponsored experiment on CRRES |
| ONR-307-3 | designation of SEP |
| ONR-307-8 1,2 | designations of IMS-LO instruments 1 and 2 |
| ONR-307-8 3 | designation of IMS-HI |
| PEM | Particle Environment Monitor, an experiment on UARS |
| $\Phi_m$ | magnetic flux designator |
| q | electrical charge designator |
| s | second |
| s | the spin vector of CRRES |
| S3-3 | spacecraft designation |
| SC-3 | energetic electron and proton spectrometer on SCATHA sponsored by ONR |
| SCATHA | Spacecraft Charging AT High Altitudes |
| SEEP | Stimulated Energetic Electron Precipitation Experiment on P81-1 for ONR |
| SEP | Spectrometer for Electrons and Protons, an ONR-307 instrument on CRRES |
| SFR | Sweep Frequency Receiver, a part of Iowa/AFGL instrument on CRRES |
| sr | steradian, a unit of solid angle |
| SYNC | geoSYNChronous orbit |
| $\theta$ | angle between the $z$ axis |
| UARS | NASA Upper Atmosphere Research Satellite |
| ULF | Ultra Low Frequency |
| U.S. | United States (of America) |
| UT | Universal Time (= Greenwich Mean Time) |
| $V$ | solar-wind speed (km/s) |
| VLF | Very Low Frequency |
| w | particle energy designation |
| $Z_{GSM}$ | Z direction in Geocentric Solar-Magnetospheric coordinates |